ABSTRACT

MODELING OF TWO-DIMENSIONAL AND BIOLOGICAL MATERIALS TOWARDS DIVERSE NANO-SYSTEMS APPLICATIONS

by
Jatin Kashyap

This dissertation studies the demonstration of materials ranging from two-dimensional (2D) materials to small bio-molecules using various atomistic/molecular and sub-atomic particles (electron, hole, excitons) modeling techniques for multi-domain applications. Three categories of materials/systems are investigated as follows: 2D materials, biological materials, and complexes of 2D and biological materials.

The first problem demonstrates wrinkles' ubiquitous presence in two-dimensional materials significantly alters their properties. It is observed that water molecules, sourced from ambient humidity or transfer method, can get diffused in between Graphene and the substrate during the Graphene growth. The water diffusion causes/assists wrinkle formation in Graphene, which influences its properties. Among other observations, this study reveals that the initially distributed wrinkles tend to coalesce to form a localized wrinkle whose configuration depends on the initial wrinkle geometry and the quantity of the diffused water.

In the second problem, atomic and electron dynamics analysis is performed to study the impact of morphological and thickness changes of a MoS_2 multi-layered system on its tribological properties. Four different cases are considered, i.e., the number of layers (1-4 layers); and number (2-8 indents), radius (12Å, 16Å, 20Å, 24Å), and pattern (0°, 25°, 30°, 35°, 45°, 60°) of indents resulting into a total of 18 subcases. Changing the radius and number of indents are found to be the most effective, and the number of layers and indents'

pattern are the least effective way to tune the frictional characteristics of the MoS_2 system due to the resulting bond elongations. These results are further justified from Bethe–Salpeter model-based exciton's formations and recombination.

Same modeling tools are leveraged to study biological systems in Chapter four. The high liability cost of the pandemic caused by the SARS-CoV-2 molecule, which causes a disease known as COVID-19, has incentivized various private, government, and academic entities to work towards finding a cure for this and emerging diseases. As an outcome, multiple vaccine candidates are discovered to avoid the infection in the first place. However, so far there has been no success in finding fully effective therapeutic candidates. This project attempts to provide multiple therapy candidates based upon a sophisticated multi-scale in-silico framework, which increases the probability of the candidates surviving an in-vivo trial. A robust framework is used to screen the ligands (ZINC database); Step-I: high throughput molecular docking, Step-II: molecular dynamics analysis, Step-III: density functional theory analysis supported by machine learning predicted orbital's energy gap. In total, 242,000(ligands)*9(proteins) = 2.178 million unique protein binding site/ligand combinations were investigated. The proteins are selected based on recent experimental studies evaluating potential inhibitor binding sites. The project finally suggests three ligands attacking different binding sites of the same protein (7BV2). Finally, Chapter 5 discusses the potential usage of MXenes as a membrane for DNA sequencing and Brain-inspired neuromorphic computing.

MODELING OF TWO-DIMENSIONAL AND BIOLOGICAL MATERIALS TOWARDS DIVERSE NANO-SYSTEMS APPLICATIONS

by
Jatin Kashyap

A Dissertation
Submitted to the Faculty of
New Jersey Institute of Technology
in Partial Fulfillment of the Requirements for the Degree of
Doctor of Philosophy in Mechanical Engineering

Department of Mechanical and Industrial Engineering

August 2022

APPROVAL PAGE

MODELING OF TWO-DIMENSIONAL AND BIOLOGICAL MATERIALS TOWARDS DIVERSE NANO-SYSTEMS APPLICATIONS

Jatin Kashyap

Dr. Dibakar Datta, Dissertation Advisor — Date
Assistant Professor of Mechanical and Industrial Engineering, NJIT

Dr. Shawn A. Chester, Committee Member — Date
Associate Professor of Mechanical and Industrial Engineering, NJIT

Dr. Eon Soo Lee, Committee Member — Date
Associate Professor of Mechanical and Industrial Engineering, NJIT

Dr. Fatemeh Ahmadpoor, Committee Member — Date
Assistant Professor of Mechanical and Industrial Engineering, NJIT

Dr. Lin Dong, Committee Member — Date
Assistant Professor of Mechanical and Industrial Engineering, NJIT

Dr. Cristiano Dias, Committee Member — Date
Associate Professor of Physics, NJIT

BIOGRAPHICAL SKETCH

Author: Jatin Kashyap

Degree: Doctor of Philosophy

Date: August 2022

Undergraduate and Graduate Education:

- Doctor of Philosophy in Mechanical Engineering,
  New Jersey Institute of Technology, Newark, NJ, 2022

- Master of Engineering in Mechanical Engineering,
  Birla Institute of Technology and Science (BITS Pilani), Hyderabad, India, 2015

- Bachelor of Technology in Mechanical Engineering,
  Lovely Professional University, Jalandhar, Punjab, India, 2012

Major: Mechanical Engineering

Publications and Presentations:

J. Kashyap, E. H. Yang, and D. Datta, "Neuromorphic Computing Based Artificial Intelligence Using MXenes: Machine Learning Based Atomic Study and DFT Analysis" (in preparation).

J. Kashyap, V. Kumar, and D. Datta, "2D Membrane-Based DNA/RNA Sequencing Using TMD and MXenes by Machine Learning Molecular and Exciton Modeling" (in preparation).

J. Kashyap, J. Torsiello, Y. Kakehi, and D. Datta "Engineering Frictional Characteristics of MoS_2 Structure by Tuning Thickness and Morphology - An Atomic, Electronic Structure and Exciton Analysis" (submitted to Journals of 2D Materials- IOP).

J. Kashyap, and D. Datta, "Drug Repurposing for SARS-CoV-2: A High-Throughput Molecular Docking, Molecular Dynamics, Machine Learning, and DFT Study," Journal of Material Science, 2022. (Nature Publishing Group, an invited article in special issue on 'Computational Materials Design').

J. Kashyap, E. H. Yang, and D. Datta, "Computational Study of the Water-Driven Graphene Wrinkle Life-Cycle Towards Applications in Flexible Electronics", Scientific Reports (Nature Publishing Group), 10,11315,2020.

J. Kashyap, P. Solanky, V. Sharma, K. Ghatak, and D. Datta, “The Inherent Behavior of Graphene Flakes in Water: A Molecular Dynamics Study”, Computational Materials Science, 140-147,2019.

J. Kashyap, S. Nagesh, K. Narayan, and P. K. Pattnaik, “Design and Simulation of a Novel 3D MEMS Fabrication/Micro Cutting Facility by Thermally Actuated MEMS Device,” IEEE Region 10 Annual International Conference, Proceedings/TENCON, 2016, vol. 2016-January.

J. Kashyap, and D. Datta, "Understanding the Growth Mechanism of Transition Metal Dichalcogenides Heterostructures Using Molecular Dynamics Approach" 2019 Society of Engineering Science (SES) Conference 13 - 15 October 2019.

J. Kashyap, K. Ghatak, and D. Datta, “Characterizing the Morphology of the Different Grown Homo/Hetero TMD Structures by Controlling Parameters – a Multiscale Computational Approach,” Electrochemical Society (ECS) Meeting, 2019.

J. Kashyap, D. Datta, and K. Ghatak, “Growth Physics of MoS_2 Layer on the MoS_2 Surface: A Monte Carlo Approach,” Applied Physics Society (APS) March Meeting Abstracts, 2019, vol. 2019, p. F13.009.

J. Kashyap, and D. Datta, "Computational Modeling and Stress Analysis of Wrinkles in Graphene" World Conference on Computational Mechanics (WCCM) XIII, July 22-27, 2018, New York, NY, USA.

J. Kashyap, and D. Datta, "MD Simulation Study of Generation of Out-of-plane Graphene by Mechanical Deformation" #S318, 18th U.S. National Congress on Theoretical and Applied Mechanics June 4-9, 2018.

This dissertation is dedicated to the girls and boys of my tribe in India,
who will be the next generation of change-maker.

ACKNOWLEDGMENT

I sincerely express my gratitude and appreciation to my dissertation advisor, Dr. Dibakar Datta, for his help and support. His guidance at every step of my research at NJIT was conducive to the successful completion of my dissertation. I was able to leverage my understanding of molecular dynamics to start with from his extensive width of expertise in this field. He instilled confidence in me to conduct my computational studies, conferred faith in my abilities to make independent decisions related to my research, and inspired me. For the first year of my Ph.D. program, he would stress the importance of coursework and allowed me to prioritize them. I sincerely thank him for his invaluable mentorship.

I want to thank my dissertation committee members, Dr. Shawn Chester; Dr. Eon Soo Lee; Dr. Fatemeh Ahmadpoor; Dr. Lin Dong; and Dr. Cristiano Dias, for their guidance, expertise, and for providing unique perspectives to solve the problems whenever I have faced an obstacle in my graduate school research. Their knowledge and technical depth allowed me to sharpen my skills.

I would like to gratefully acknowledge the financial support from the Department of Mechanical and Industrial Engineering and from Dr. Datta's faculty start-up grant. Additionally, I would acknowledge the High Performance Computing (HPC) facilities provided by Academic and Research Computing Systems (ARCS) in the Department of Information Services and Technology (IST) of the NJIT and the support of the Extreme Science and Engineering Discovery Environment (XSEDE, Start-Up Allocation—DMR170065 and Research Allocation—DMR180013) for providing us their computational facilities and technical support.

I would like to extend my gratitude to my friends: Kirpal Singh, Money Sharma, Pankaj Anand, Harinder Singh, Amitpal Singh Khaira, Gurpreet Singh, Anuj Sood, Vikram Singh Chauhan, Chirag Bansal, Gurleen Singh, Dhruv Sood, Preet Lakhani, Jitendra Pant, Keven Alkhoury, Subhajit Rakshit, Abhishek Mukherjee, and Kamalika Ghatak for bestowing their faith in me, understanding me, guiding me to make the right decisions, cheering me up in uncertain circumstances, and always standing by me through life's ups and downs. In the end, words cannot express my love and deep gratitude to my partner, Raja (the cat), and my family, who have been with me from the beginning. A special thanks to Dr. Donna Peach (UK) and my colleagues from PhDForum.

TABLE OF CONTENTS

TABLE OF CONTENTS
(Continued)

TABLE OF CONTENTS
(Continued)

Chapter **Page**

LIST OF TABLES

LIST OF FIGURES

LIST OF FIGURES
(Continued)

LIST OF FIGURES
(Continued)

LIST OF FIGURES
(Continued)

LIST OF FIGURES
(Continued)

LIST OF FIGURES
(Continued)

LIST OF FIGURES
(Continued)

LIST OF FIGURES
(Continued)

LIST OF FIGURES
(Continued)

LIST OF ABBREVIATIONS

FG	Flat Graphene
GDW	Graphene with Distributed Wrinkles
GLW	Graphene with Localized Wrinkle
GNR	Graphene Nano-ribbons
WGNR	Wrinkled Graphene Nanoribbons
IAW	Initial Angle of Wrinkling (θ_{IAW})
FAW	Final Angle of Wrinkle (θ_{FAW})
PBC	Periodic Boundary Conditions
CR	Carbon Ratio
AR	Aspect Ratio

CHAPTER 1

INTRODUCTION

1.1 Introduction

In conformance with general landscape of research, this dissertation follows the pattern of studying a group of materials/structures (Two-dimensional materials and bio-molecules) by a group of methodologies (atomistic/molecular simulations) to demonstrate a group of applications (various structure-property relationships). The material being investigated is Graphene/MoS_2 and micro bio-molecules; the methodologies followed are Molecular Dynamics/Density Functional Theory/Machine Learning; and the applications being studied are structural perturbation-based properties/function changes. In the case of 2D materials, property tuning methods can be broadly classified in the category of structural and non-structural changes (electric/magnetic field, annealing, etc.), and further structural changes can be induced by directly applied strain, defects, step-edges, wrinkles, folds, indents (blisters), etc. In this dissertation, we are focusing on the wrinkles (Chapter 2) and folds (Chapter 3) based 2D materials' properties tuning because they fulfill the need for availability of controlling parameters (amplitude, wavelength, frequency) which can be fine-tuned to meet the requirements to produce desired strain field which in turn can generate desired property changes.

For biological materials, since a majority of nano bio-material do not exist in the form of layered structures (except lipids, etc.), it is difficult to control their properties by introducing step-edges or wrinkles or folds instead, their properties are primarily controlled by the fold configuration they acquire once they attached to another molecule or got detached from one. The fold configuration can be a primary source of mechanical strains

because folds cause a non-uniform strain field in the molecule, changing its functional properties like docking pose, binding strength, etc. In this study, we investigated the different sub-chains of Spike protein of SAR-CoV-2 (Chapter 4) using the same computational framework used for the in-depth investigation of Graphene and MoS_2. Small bio-molecules can also take advantage of strain induction. Because for biomolecules, their folding configuration is more important than their constituting atoms, i.e., two bio-molecules can have the same inhibitory effect if they can have the same fold configuration despite having different chemical/atomic compositions. Their folding and unfolding can be controlled by strain induced by the linked/docked molecules, i.e., substrates, etc. Given the application of using strain to control the various properties of materials of multiple domains, it becomes crucial to study it in detail while demonstrating the application of different materials in various fields.

In this dissertation, we aimed to use advanced modeling techniques, i.e., molecular dynamics, ab-initio-based electronic structure, and supervised machine learning properties modeling/force field generation to model the Two Dimensional(2D)/Nano and biological materials. Since all these modeling techniques compute the material at the atomic/electronic level, it becomes very computationally expensive to model large-scale materials, limiting us to nano-scale 2D materials and sub-micro scales bio-molecules. We can rationalize the dependencies of all of these methods as electron dynamics cause nuclei dynamics which in turn cause the change in the properties of the molecule/crystal bulk material under consideration. These techniques differ from classical constitutive modeling because their governing equations are based on the physics and thermodynamics of macro-scale bodies. The laws of physics change when materials' dimensions are brought down to

nano-scale level from macro level, for example, electrons floating around a material's nuclei can only occupy certain energy levels while baseball moving in a baseball field can possess any energy from infinite values on that energy spectra. Since nanoparticles are restricted to attain only discrete values for given properties, they are also called quantum particles as Quantum is the Latin word for "how much" i.e., something in finite quantity as opposed to infinite as in continuum spectrum. Since computationally investigated nano-scale materials only have a few hundred atoms, they show a significant change in the properties (and hence functional properties in the case of small bio-molecules) attributed to the change in electronic structure (electron orbitals) of the material. Thus, it becomes vital to take care of the non-continuum, i.e., quantum, nature of the particles and use the related modeling techniques, i.e., Schrodinger equation-based density functional theory (DFT) and experimental combined with DFT parameters-based force fields in case of molecular dynamics (MD). Advanced MD models are being fed force fields trained by empirical data (as experimental observations inherently take care of the quantum nature of the material) and DFT-based machine learning augmented data.

1.2 Background and Motivation

As seen in Figure 1.1, the 2D/nanomaterials have a wide range of applications. The ubiquitous presence of wrinkles in 2D materials alters their properties significantly. It is observed that during the growth process of Graphene, water molecules, sourced from ambient humidity or transferred method used, can get diffused in between Graphene and the substrate. The water diffusion causes/assists wrinkle formation in Graphene, which influences its properties. The diffused water eventually dries, altering the geometrical

parameters and properties of Wrinkled Graphene Nanoribbons (WGN). Initially, distributed wrinkles can be studied to whether they coalesce to form a localized wrinkle whose configuration depends on the initial wrinkle geometry and/or the quantity of the diffused water. Further bandgap (direct or indirect) and plastic limit of the stress dependencies can be investigated with the initial angle. The system stability can be checked with an increase in the initial angle of wrinkle and can be confirmed from the potential energy plots extracted from MD trajectories and the DOS plot.

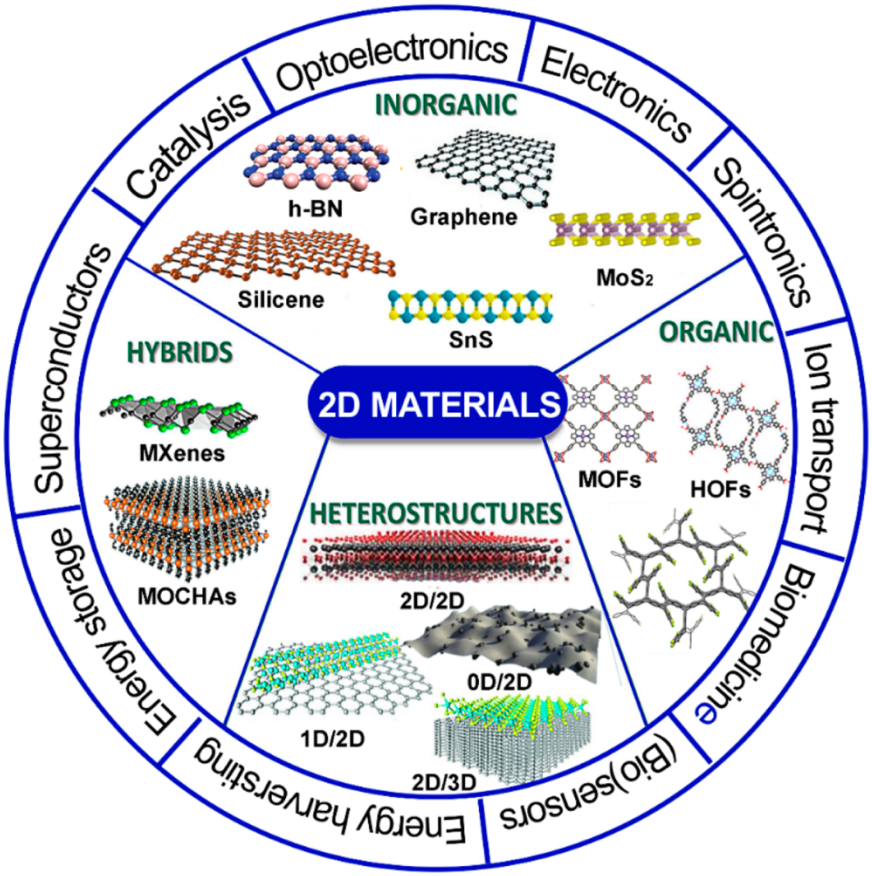

Figure 1.1 Different categories of non-bio nanomaterials.

*Source: Scarano, D., and Cesano, F., 2021, "Graphene and Other 2D Layered Nanomaterials and Hybrid Structures: Synthesis, Properties and Applications," Mater. , **14**(23).*

Furthermore, 2D materials are often used in cutting-edge optoelectronics applications, which makes it essential to study their mechanical properties. This motivates to study the impact of morphological and thickness changes of a MoS_2 multi-layered system on its tribological properties. Multiple parametrization factors can be investigated, i.e., number of layers (1-4 layers), number of indents, the radius of indents, pattern of indents, etc. An atomistic modeling code can be used to model the movement of a tip over the surface of the MoS_2 system. All considered parameter variables can be observed to find the most effective and the least effective way to tune the frictional characteristics in the MoS_2 system. The results can be further supported by a rationale based upon charge transfers and electron orbitals obtained from DFT-based code. To further investigate the effects, Transient Domain Density Functional Theory (TD-DFT) and Bethe–Salpeter equations-based calculation can be performed to study the dynamics of excitons (electron-hole pair) and whether they are being formed across the interface of layers and tip (interlayer excitons), which may result in stronger interlocking between the layer's surface and tip that can counterbalance any orbital shape induced weakness and/or interfacial bonds.

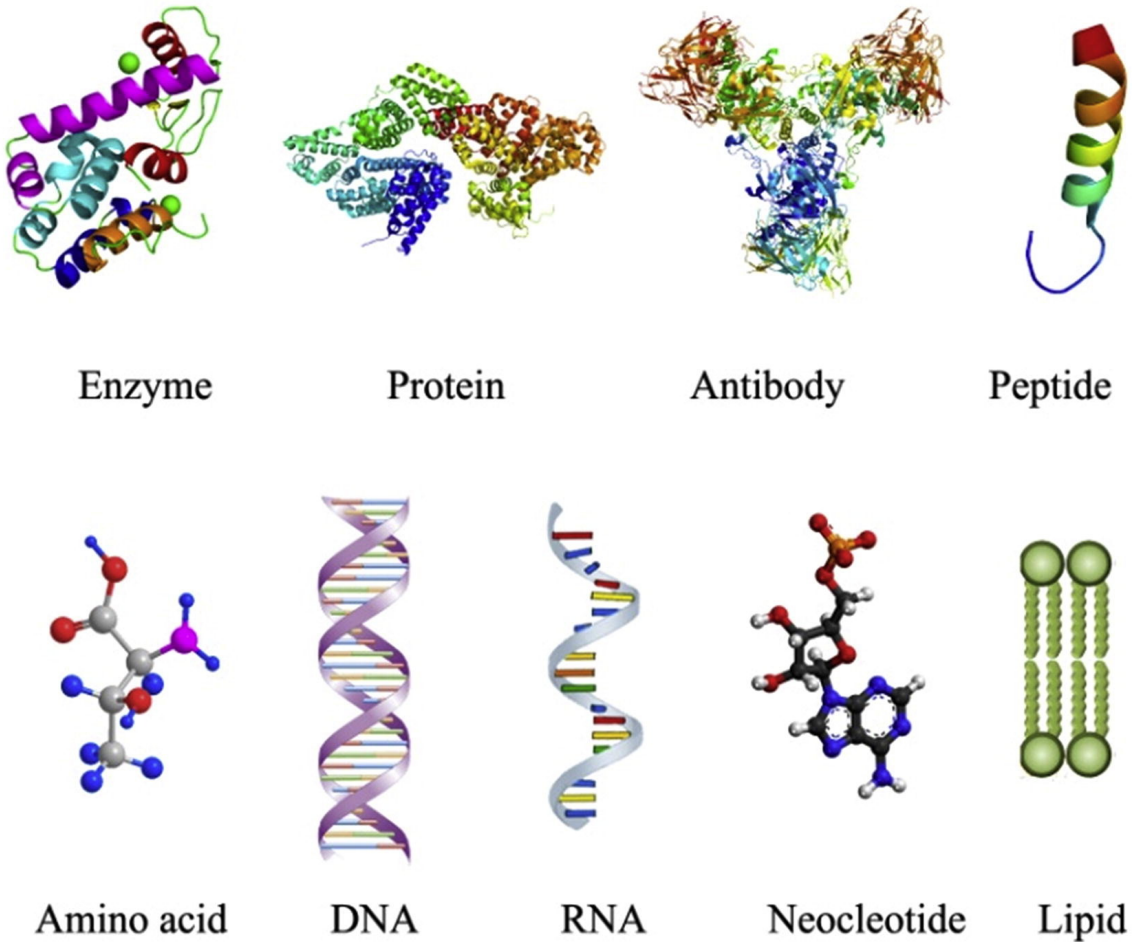

Figure 1.2 Different categories of biological nanomaterials.

Source: An, H., Li, M., Gao, J., Zhang, Z., Ma, S., and Chen, Y., 2019, "Incorporation of Biomolecules in Metal-Organic Frameworks for Advanced Applications," Coord. Chem. Rev., 384, pp. 90–106.

In this dissertation, only small molecules are investigated out of a wide range of bio-materials (Figure 1.2). A micro-molecule of dimension 125 nm has caused around 479 Million human infections (80 M for the USA) and 6.1 Million human deaths (977,000 for the USA) worldwide, and slashed the global economy by US$ 8.5 Trillion over two years period. The only other events in recent history that caused comparative human life loss through direct usage (either by (wo)man or nature, respectively) of structure-property relations of "nano-structures" (either (wo)man-made or nature, respectively) were nuclear bomb attacks of Japanese cities by the USA during World War II and 1918 Flu Pandemic.

This molecule is called SARS-CoV-2, which causes a disease known as COVID-19. The high liability cost of the pandemic had incentivized various private, government, and academic entities to work towards finding a cure for these and emerging diseases. As an outcome, multiple vaccine candidates are discovered to avoid the infection in the first place. So far, there has been no success in finding fully effective therapeutic candidates. This leads to motivation to provide multiple therapy candidates based upon a sophisticated multi-scale in-silico framework, which increases the probability of the candidates surviving an in-vivo trial. Ligands library can be selected from the ZINC database based upon previously partially successful candidates, i.e., Hydroxychloroquine, Lopinavir, Remdesivir, Ritonavir, etc. Following robust framework to screen the ligands can be adapted for such studies; Step-I: high throughput molecular docking, Step-II: molecular dynamics analysis, Step-III: density functional theory analysis. The proteins selected must be based on recent experimental studies evaluating potential inhibitor binding sites to ensure computational results are as reliable as possible. Step-I may filter the screened ligand number down to 10 ligands/protein based on molecular docking binding energy, and it can be further screened down to 2 ligands/protein based on drug-likeness analysis. Additionally, these two ligands per protein can be analyzed in Step-II with a molecular dynamic modeling-based RMSD filter of less than 1Å. Finally, Step III can be used to find the rationale behind comparatively higher ligand efficacy based upon electrons/sub-atomic particle dynamics.

1.3 Dissertation Outline

This dissertation is divided into the following segments: Chapter 1 describes the different categories of 2D/nanomaterial and small bio-molecules and why studying them using atomistic modeling approaches is helpful. It also highlights methodologies used in various molecular modeling techniques.

Chapter 2 explains the evolution of the life-cycle of wrinkles in Graphene nanoribbons exposed to moister content. It also studies the dynamics of the wrinkles under trapped water droplets.

Chapter 3 studies the nanofriction tuning in the MoS_2 system by engineering its surface morphology (in the form of indents) and thickness. In this Chapter, excitons pseudo particles were investigated across the interface of the system.

Chapter 4 presents the modeling of small bio-molecules to study the inhibition of SAR-CoV-2 by using similar methodologies followed in previous chapters in addition to machine learning-based molecular orbital gap prediction.

Chapter 5 provides a conclusion, and current and future work based upon the previous chapters of this dissertation.

CHAPTER 2

COMPUTATIONAL STUDY OF THE WATER-DRIVEN GRAPHENE WRINKLE LIFE-CYCLE TOWARDS APPLICATIONS IN FLEXIBLE ELECTRONICS

2.1 Introduction

Graphene like two dimensional (2D) materials are less resistant to buckling, and they tend to form surface corrugations such as wrinkles, ripples, crumples.[1] Depending upon applications, wrinkling can be "either boon or a bane". The ubiety of the surface textures significantly alters the mechanical, electronic, and optical properties. Which can be exploited in various applications in the fields of electronic[2], sensing and actuation[3], energy storage [4][5], chemical reactions [6][7][8], and bioelectronics [9]. Given the literature, applications in flexible electronics stand out among the others. Initially, wrinkles in Graphene were detected during the synthesis processes. [6][7] [10][11][12] Usually, amid the synthesis process of graphene, water molecules sourced from the ambient air/transfer process can get diffused in the system. The diffused water can significantly influence the geometrical parameters of the wrinkles, and consequently the properties of the Graphene [8] in addition to the substrate effect.[13] There are other ways for the water to get diffused in the system. For example, Raghav et al. had studied the wedging of a Graphene bilayer by water molecules.[14] The first on-purpose fabrication of the wrinkles was demonstrated in 2011[15], followed by multiple studies on modeling the wrinkle theoretically/numerically.[16][17]

Deformable Thin Film Transistors (TFTs) are core components in flexible electronics. Major obstacles in developing flexible TFTs are fragility and the current leakage. Surface instabilities in thin-film TFTs are exploited to overcome these

shortcomings. A Single-Walled Carbon Nanotube(SWCNT)/wrinkled Al_2O_3 TFT displayed minimum current leakage of 10-13 A, attributed to the airgaps present underneath the wrinkles.[12] Additionally, the In-Ga-Zn-O (IGZO), pentacene, reduced graphene oxide(rGO), and rGO/ Polydimethylsiloxane(PDMS) based TFTs are observed to preserve the electrical performance and mechanical stability under the strain of 20% due to wrinkles' existence.[18][19][20][21] Similar behavior was observed in silver, and rGO based interconnects.[17][18][22] It inspired the investigation of dependency of the device performance on individual geometrical parameters of the wrinkles. In an IGZO TFT and rGO interconnect, the wrinkle's wavelength and amplitude were controlled in a way so the device can be bent up to 13 μm and strained up to 5% while preserving the electrical performance. [17][23][24] Nirmalraj et al.[25] had demonstrated controlling the Pentacene growth on a MoS_2 substrate by tuning the wrinkle height. Furthermore, the non-uniformity of the wrinkled 2D material's topology can be used for photon trapping in between trough and vertex. This lead to the design of a wearable laser device with a threshold below than ever reported.[26] TFTs are usually decorated with mechanical sensors. A crumpled rGO based piezoresistive pressure sensor developed high stretchability, strain insensitive resistance profile, and increased sensitivity.[27] In another study, a wrinkled rGO sheet improved the sensitivity and range at non-stretched state too.[28] In addition to pressure and position detection, strain measurements are equally important in flexible electronics. Wrinkle assisted crack structures can be used to design strain sensors.[29] While subjected to bending stresses, the resulting sensor showed high sensitivity, high stretching range, low limit of detection, high durability, wider strain range. A Wrinkled 2D complex-based strain sensor is demonstrated to acquire a high gauge factor of 1071[30] and sustain the electrical

signals over a wide range of deformation.[15] The intrinsic piezoresistive property and electron tunneling effect(observed in our work in Section 2.3.2.1) in a graphene crystal were attributed to high sensitivity, wide range, and stretchability. [30] Additionally, the effect of engineering the wrinkle pattern in tuning adhesion, wetting, open-channel microfluidics, and responsive microlens arrays is studied experimentally.[31]

The presence of wrinkles in different 2D systems, including Co/Cu/PDMS has attributed to preserving Giant Magnetoresistance performance(GMR) even at strains as high as 4.5%.[32][33] The wrinkles patterns were observed to affect GMR and magnetic field sensitivity uniquely over a wide range of strain.[34] Often, there are sensitive parts of the device which should be shielded against the magnetic fields. A wrinkled polyurethane(PU)/MXene($Ti_3C_2T_x$) complex was tested for its electromagnetic wave interference(EMI) capability in flexible electronics.[35] The power storage components are also needed to be able to withstand mechanical deformations. Wrinkled/crumpled supercapacitors based upon graphene/rGO are demonstrated to have high capacitance at strains up to 300% and 5000 stretching cycles.[36][37]] Further, wrinkled 2D material based bioelectrodes seem to show no degradation in charge capacity and impedance while used for in-vivo measurements.[38] Wrinkles in Polyimide/Silbione system has resulted in low elastic modulus and high tangent modulus to avoid fracture and mechanical constraint on the movement of a biological tissue over a substrate, respectively.[39] Crumples in a 2D material can undergo a geometrical transformation for various reasons. A majority of systems acquired the same type of wrinkle as one can observe while growing graphene on a SiO_2 substrate. A related work by Lee et al. [40] revealed that during the transfer of exfoliated graphene onto a SiO_2 substrate, water molecules get diffuse between graphene

and substrate (Figure 2.1). The diffused water and subsequently its evaporation cause wrinkles and change in geometry of the wrinkles, respectively, resulting in Wrinkled Graphene Nanoribbon (WGNR). It may be essential to study wrinkle transformation lead by water diffusion and evaporation in the system.

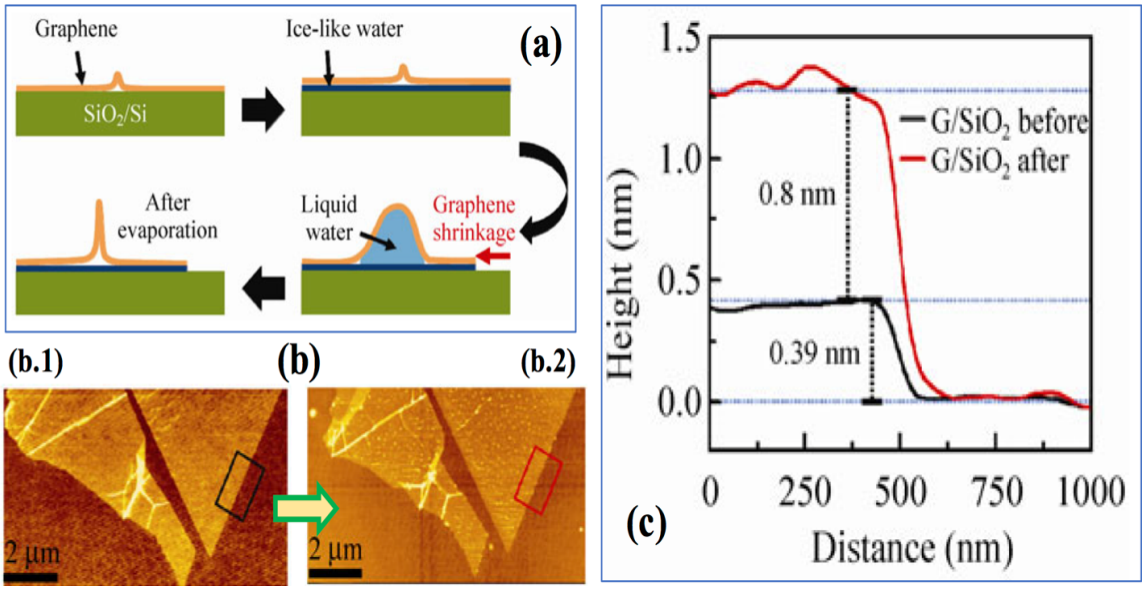

Figure 2.1 (a) Schematic diagram of the wrinkle formation process through the ice-like water formation and liquid water diffusion at high humidity, and liquid water evaporation in a dry environment. (b) Height changes in a graphene/SiO_2 structure after exposure to high humidity. AFM topographic images of a monolayer graphene mechanically exfoliated on SiO_2 (b.1) before and (b.2) after the high humidity exposure. (c) Averaged height profiles measured for the areas marked with black and red rectangle in (b.1) and (b.2), respectively. G denotes monolayer graphene.

Source: Springer Science + Business Media, Lee et al. Nano Res. 2012, 5(10):710-717

In this work, we provided a detailed explanation of water diffusion and its impact on a wrinkled bilayer graphene system characterized by geometrical parameters and electronic properties. Our results can explain the phenomenon of the water interaction with the graphene system[36][37], and change in electronic properties of different 2D materials caused by wrinkles [38][40]. Our study is composed of three phases. Phase I addresses the

wrinkle evolution due to diffused water in between graphene with distributed wrinkles and a graphene substrate. We had varied the amount of diffused water and the initial angle of the distributed wrinkles in graphene and studied the formation of final localized wrinkle configuration and the stress generated in wrinkled graphene. Lastly, Phase II uses Density Functional Theory (DFT) while considering the free-standing WGNR with four different initial angles and studies its influence on the electronic properties. Only quasi-periodic wrinkles are considered instead of a complex network of wrinkles that exist in the experimental setups. However, we believe that our studies will encourage researchers to study more complicated wrinkle structures.

2.2 Models and Methods

2.2.1 Molecular Dynamics (MD)

This study is divided into *three phases* based on which part of the wrinkle life-cycle is being studied, i.e., formation, evolution, collapse, and the approach used for analysis, i.e., MD or DFT. In the *first phase*, we investigated the wrinkle formation and evolution. In this phase (Figure 2.2a), we created a Graphene with Distributed Wrinkles (GDW) supported by a Flat Graphene (FG) with Periodic Boundary Conditions (PBC) (width = 20 Å) using the in-house MATLAB code. Here, we considered different Initial Angle of Wrinkle (IAW) denoted as θ_{IAW} (θ_{IAW} = 6°, 11°, 16°, 21°) to generate GDW with four different configurations. Figure 2.2a shows a representative case of $\theta_{IAW} = 11°$. While changing θ_{IAW}, we kept the number of carbon (C) atoms in GDW the same, the size of the FG is reduced. For example, if we take a flat graphene sheet and keep compressing to get wrinkles of different angles, the number of atoms in the sheet remains unchanged, while the overall length of the sheet is reduced. Table B.1 of the Appendix B shows the C atoms

for different θ_{IAW}. We define a parameter called Carbon Ratio (CR), which is the ratio of the number of C atoms in GDW to that of FG. For θ_{IAW} of 6°, 11°, 16°, 21°; CR values are 1.017, 1.053, 1.11, 1.20, respectively (Table B.1).

The Adaptive Intermolecular Reactive Bond Order (AIREBO) potential was used for the C-C interactions [42]. We performed an energy minimization of this system (Figure 2.2a) using the conjugate gradient method as implemented in the MD package LAMMPS [43]. While integrating Newton's Second Law of Motion equation to study the constant-energy surface of the system, it may be required to control a particular state variable of the system, i.e., Volume, Temperature, Pressure, etc., to replicate experimental conditions. Therefore, multiple statistical ensembles can be employed depending on controlling different state variables. For example, the constant-energy, constant volume ensemble (NVE) is used when the system is evolved in time, keeping the system's temperature and pressure free to change. This ensemble is also called as microcanonical ensemble.

Similarly, a constant-temperature, constant-volume ensemble (NVT) is known as canonical ensemble in which temperature is controlled through temperature-bath coupling and volume is kept constant. The constant-temperature, constant-pressure (NPT) ensembles control the system's pressure and temperature simultaneously while the system's volume is allowed to change. The simulations performed in this Chapter were successful with the NVE ensemble however tended to crash while using the NVT or NPT ensemble. Since the system is crashing in the first 1ns of the simulation run and after visually inspecting it, we believe the rationale may be the sharp vertex of wrinkles obtained from initial structures generated by the Matlab code. The Carbon atoms around the sharp vertex might have steric clashes that were exploding the simulation box if Newton's

Second Law was being solved with constant volume and temperature or constant pressure and temperature state variables.

Figure 2.2b shows the minimized/equilibrium configuration of GDW supported by the FG. At this point, we studied wrinkling evolution for four cases – (a) without water (Figure 2.2b), and (b) two-, (c) four-, and (d) six-layer of water in between the GDW and FG (Figure 2.2c,d,e). In-house MATLAB code was used to insert the water layer in the wrinkled system shown in Figure 2.2b. The density of the added water molecules, i.e., the number of water molecules per unit volume, is the same for all cases. Table B.1 of Appendix B shows the number of water molecules for different cases.

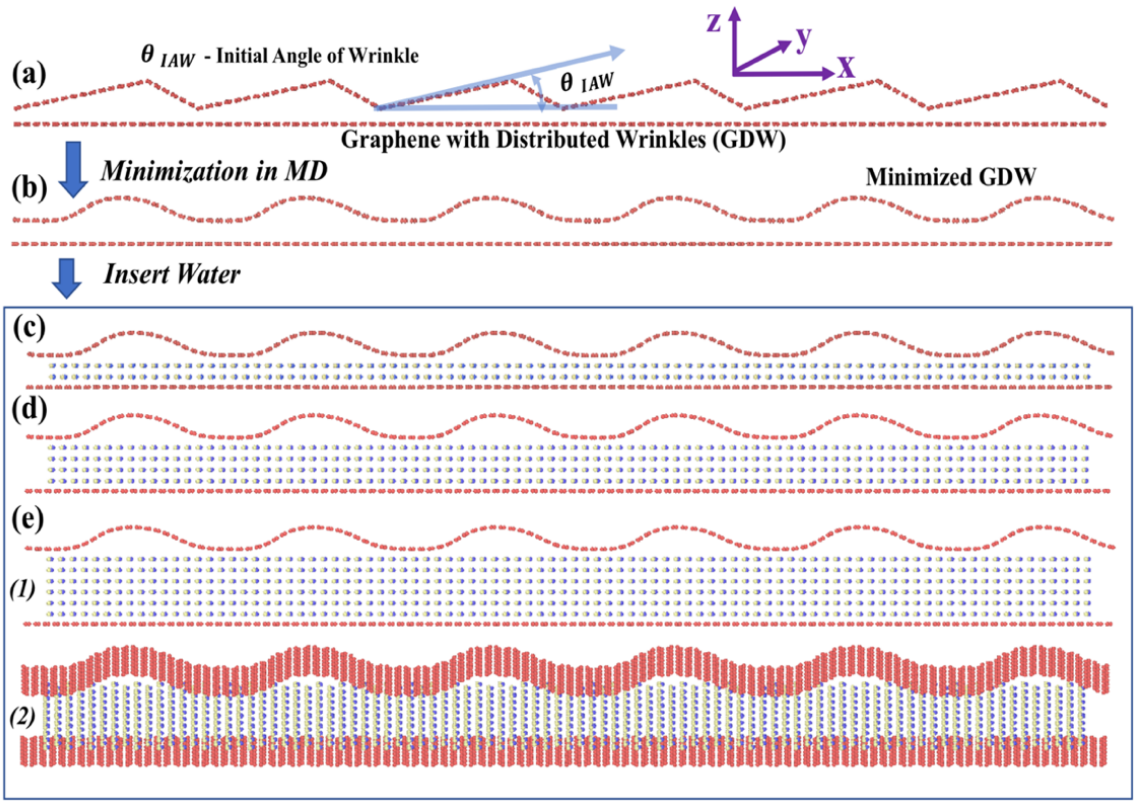

Figure 2.2 (a) V-shaped, hypothetical, wrinkling structure considered for the study (generated using Matlab code). Different Initial Angle of Wrinkling (IAW), $\theta_{IAW} = 6°$, 11°, 16°, 21°, are considered in this study. (b) Minimization of the system by MD (no water case). (c-e) Insertion of water for further studies. (c) two- (d) four-, and (e) six-layer of water. (e.1) side view and (e.2) inclined view. Simulation box is not visible.

The water molecules were added to the system (Figure 2.2b) in two different ways – (1) While adding the water, the gap between the graphene layers was increased to maintain a fixed distance between the water layers and the adjacent graphene sheet (Figure 2.2c, d, e). (2) Water layers were added while keeping the distance between GDW and FG to a fixed distance corresponding to the maximum water case considered (i.e., gap shown in Figure 2.2e is considered for all other cases). However, in both cases, we qualitatively observed the same results. Therefore, we only discuss the results for the cases shown in Figure 2.2b-e. We used TIP4P potential for water (H_2O)[44], and Lennard-Jones type of pair potential for C and H_2O interactions [45]. We used TIP4P potential before for water modeling [3,37], and our computational results were in good agreement with the experimental findings [3].

The methodology of *Phase I* is summarized in the 'Wrinkle Evolution' part of the flow-chart shown in Figure 2.3. The temperature of the system was controlled at 300 K using the Berendsen thermostat [46]. We then performed MD simulation using NVE ensemble with the timestep of 1 femtosecond. Sufficient MD steps (at least one million steps) were performed to make sure the system reached its lowest energy configurations (discussed later in detail).

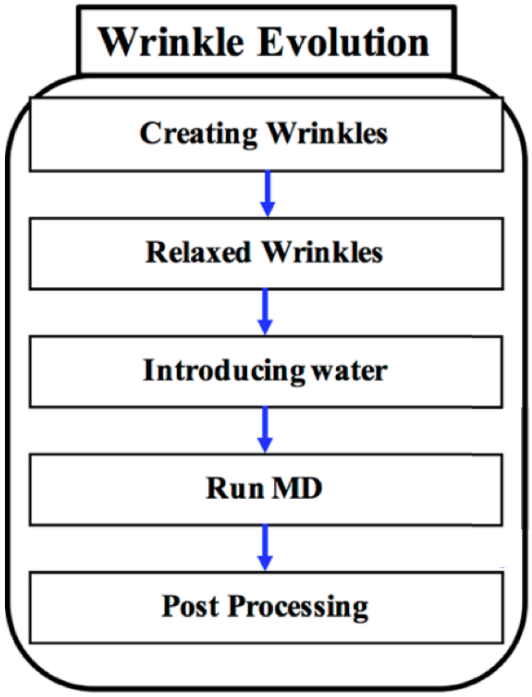

Figure 2.3 Flowchart showing the algorithm used for the Molecular Dynamics (MD) simulation for wrinkle evolution.

After the end of the first phase simulations, we stored the system configuration and reused it as the initial structure for the next phase of the project. We performed the stress analysis of the final stabilized graphene sheet with a localized wrinkle using the in-built LAMMPS stress computation algorithm [47]. The detail of the stress calculation methods is provided in the supplementary information (section D). Figure 2.3 displaces the algorithm used for the wrinkle evolution under water intercalation.

2.2.2 Density Functional Theory (DFT)

In *Phase II,* the DFT based analyses were performed on one frame from each case considered from Phase I. In this phase, we tried to understand the impact of geometrical parameters of WGNR on their fundamental electronic properties. We implemented first-principles DFT with plane-wave basis sets and pseudopotentials to describe the electron-

ion interactions as implemented in Quantum Espresso (QE) [48]. All calculations were done using the projector augmented wave (PAW) pseudopotentials and the Perdew–Burke–Ernzerhof (PBE) exchange-correlation functional [49]. The plane-wave basis sets were used with a plane-wave cutoff energy of 100 eV, and a kinetic energy cutoff for augmentation charges of 400 eV. The convergence threshold of Kohn-Sham equations was set to 1*e*-06. The gamma-centered *k*-point sampling grids obtained using the Monkhorst–Pack method, were 8x8x8 with a unit offset for the graphene unit cell. The valence electrons contain *s* and *p* orbitals for carbon. Before DFT calculations, all atoms in the cell, as well as the lattice dimensions and angles, were relaxed to the equilibrium configurations by using MD. For consistency, only one case corresponding to two water (H_2O) layers was studied from each considered IAW, i.e., 6°, 11°, 16°, 21°. Furthermore, the systems from all four cases were trimmed down to 120 atoms to eliminate the system size dependency, and conform to the available computational resources. For the band structure calculations, the symbols and coordinates of the high-symmetry points in the first Brillouin zone of the crystals were taken from Y Hinuma et al.[50]. MATLAB and VESTA codes were used for the post-processing of the results.

2.3 Results and Discussion

We discuss our results for three phases – (I) The formation and evolution of wrinkles for no-water, and water inside GDW and supported FG (without drying), and (II) The electronic structure of free-standing WGNR for four different geometries.

2.3.1 Phase I: The Formation and Evolution of Wrinkles Due to Diffused Water

As discussed in section 1 (introduction), during the synthesis [51] and/or transfer process[52], graphene can inherent distributed wrinkles, and they tend to coalescence to form a localized structures, i.e., from 'Graphene with Distributed Wrinkles (GDW)' to 'Graphene with Localized Wrinkle (GLW)'. For the simplicity of analysis, we considered here GDW only among other available morphologies (Figure 2.2b), i.e., ripples, crumples, folds, etc. First, we analyzed how GDW transforms into GLW when there is no diffused water (Figure 2.2b). Figure 2.4a shows the case of distributed wrinkles for the representative case of $\theta_{IAW} = 21°$ and CR=1.21. As mentioned earlier in section 2, Carbon Ratio (CR) is the ratio of C atoms in the upper sheet with wrinkles and the underlying flat sheet (see Table B.1 of Appendix B). The distributed wrinkles on same-side amalgamate to form a localized wrinkle, i.e., GDW transforms to GLW. In crystalline solids, same-sign dislocations repel according to Frank's rule [53]. However, in van der Waals (vdW) layered structures, such as graphene, same-sign (same-side) winkles attract each other to form a localized wrinkle. A similar observation was reported for the MoS_2 bilayer system [54]. As shown in Figure 2.4a, for $\theta_{IAW} = 21°$, first, the initially distributed wrinkles transform into intermediate wrinkle localization and finally single 'localized wrinkle'. During the intermediate steps (step = 10000, 25000), initially distributed wrinkles form three followed by two wrinkles and, finally, one 'localized wrinkle'. There is a drop in potential energy during the transformation of three to two and, finally, one wrinkle. In Appendix A, Figure A.1-A.3 show the evolution of initial wrinkle for three other cases – (1) $\theta_{IAW} = 6°$, CR = 1.017; (2) $\theta_{IAW} = 11°$, CR = 1.053; (3) $\theta_{IAW} = 16°$, CR = 1.11. As shown in Figure A.1 (Appendix A), when the θ_{IAW} is less (e.g., $\theta_{IAW} = 6°$), and CR is close to 1, initially

distributed wrinkles do not converge to single localized wrinkle, rather tries to transform into a highly strained flat sheet.

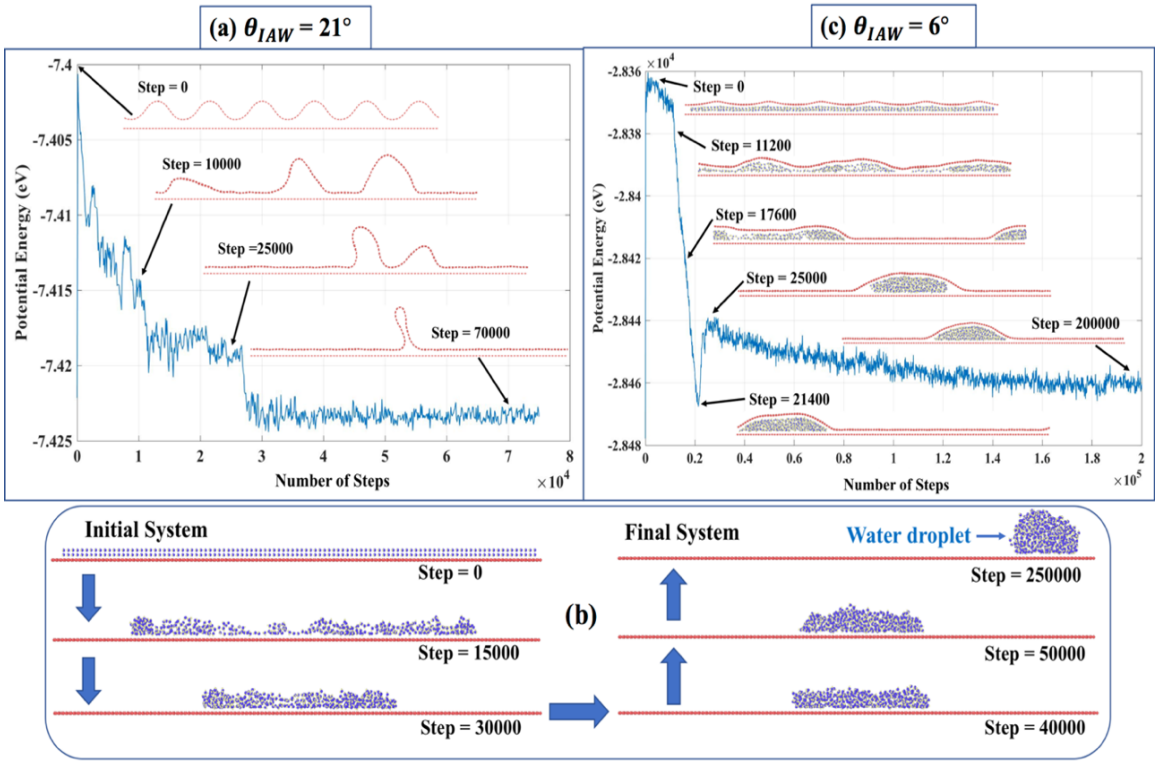

Figure 2.4: (a) Potential energy variation during the wrinkle amalgamation for θ_{IAW} =21° (no water case), (b) Formation of the water droplet on graphene, (c) Potential energy variation during wrinkle amalgamation (θ_{IAW} = 6° for two water layer case.). Simulation box is not visible.

Figure 2.4b represents a case-study where water molecules are initially placed on monolayer FG with no graphene sheet on top. The MD simulation shows that water molecules coalescence to form a water droplet because of the hydrophobicity of graphene[55] with a contact angle of 125°, which matches with the literature [56]. In Figure 2.4c, we considered a representative case of θ_{IAW} = 6° (two-layer water) to discuss how diffused water molecules inside GDW and FG influence the wrinkle evolution. The presence of diffused water causes 'competition' between two phenomena – (i) wrinkle

amalgamation, and (ii) droplet formation. The final localized wrinkle configuration is primarily determined by the dominant phenomenon. Figure A.1 (Appendix A) shows that for GDW with $\theta_{IAW} = 6°$, initial wrinkles tend to merge together to form a flat sheet. Figure 2.4b shows the water droplet formation starting from the initial water layer. When these phenomena, i.e., wrinkling formation and droplet formation interact with each other, the droplet formation process dominates. However, the final droplet shape in this case (Figure 2.4c) is not the same as in Figure 2.4b. Because in this case, the upper graphene sheet tries to compress the water droplet, as observed by S. McKenzie et al. [57]. However, since the droplet formation phenomenon is dominant here, the final wrinkle configuration is primarily determined by the water droplet.

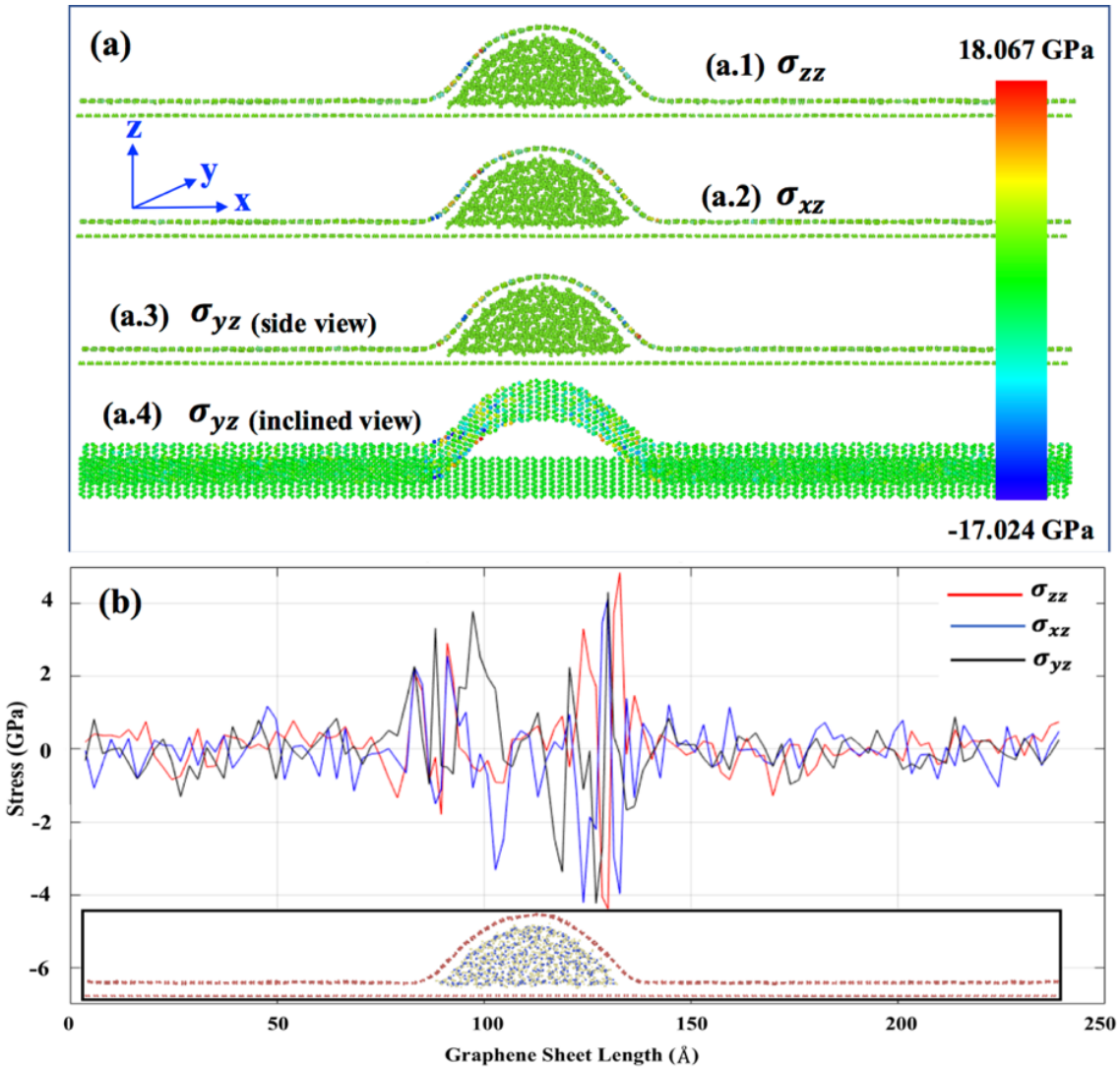

Figure 2.5 (a) Cauchy stress field distribution in the localized wrinkle graphene system for a particular time frame – [a.1] σ_{zz}, [a.2] σ_{xz}, [a.3] σ_{yz} - side view, [a.4] σ_{yz} - inclined view, (b) Stress distribution across the top wrinkled graphene sheet. Stresses are averaged upon the whole line of atoms along the y-axis. Simulation box is not visible.

Figure A.4-A.7 (Appendix A) show the final wrinkle configuration of graphene starting from the initial wrinkle angle of $\theta_{IAW} = 6°$, 11°, 16°, and 21°, respectively for 0-, 2-, 4-, and 6-layer water cases. The stress generated during the wrinkle formation is shown here. We considered a representative case of $\theta_{IAW} = 11°$ for the 2-layer water case (Figure A.5b in Appendix A) for analyzing the stress generation during the wrinkle formation.

Figure 2.5 shows the z-component of the Cauchy stress. Considering the stress-field in Figure 2.5a, we note that atoms in the flat regions and at the top of the wrinkle have no z-component stress. Only the sidewalls, i.e., the base of the localized wrinkle, are stressed. Figure 2.5b shows the distribution of the z-component of stress across the GLW (Graphene with Localized Wrinkle). Here, stresses are averaged upon the whole line of atoms along the periodic y-axis. We note that for all three stress cases ($\sigma_{zz}, \sigma_{xz}, \sigma_{yz}$), the stress is high in the sidewalls (the base) of the wrinkle as expected [58]. The maximum individual atomic stress, observed in the wrinkle, varies from around -17 GPa(compressive) to 18 GPa(Tensile) (Figure 2.5a). When averaged over the stripe of atoms along the periodic y-axis, the maximum magnitude of stress is around 4 GPa (Figure 2.5b). In summary, stress generation in graphene during the wrinkle formation is much lower than the stress that can cause plastic deformation [59,60]. Hence, water diffusion-induced wrinkle formation in graphene does not cause in-plane lattice-strain high enough to break the bonds and cause plasticity.

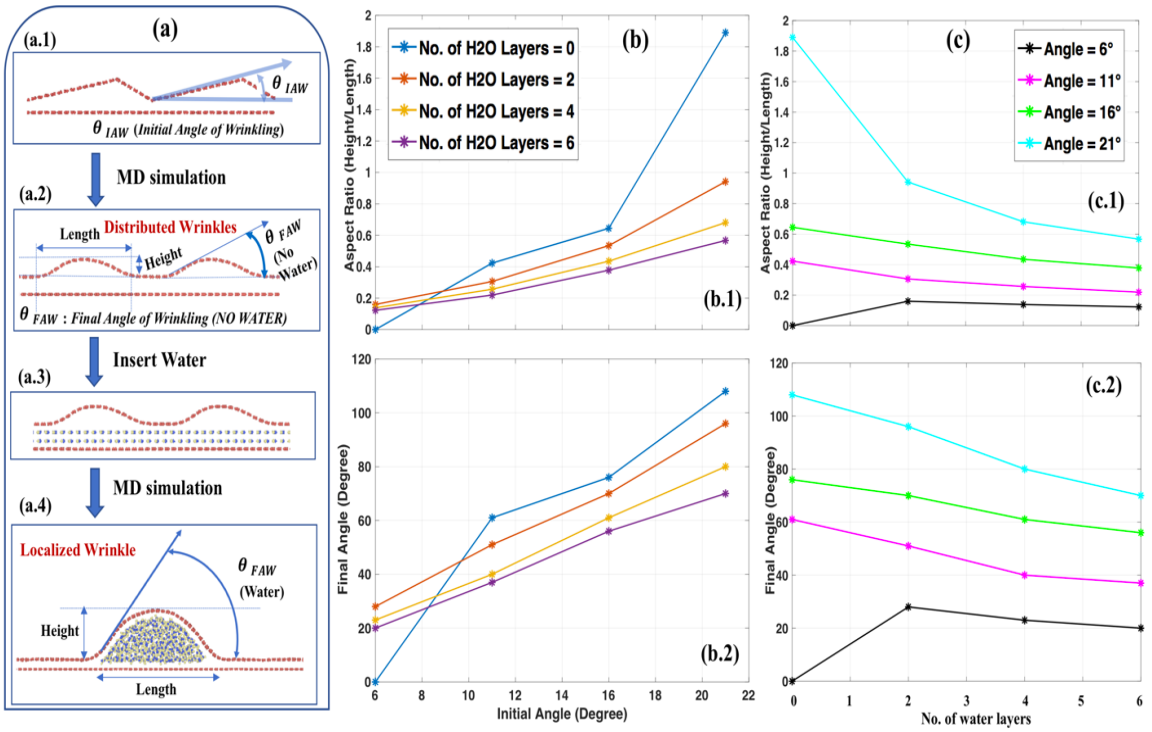

Figure 2.6 (a) Wrinkle configurations at different stages. [a.1] Model considered at the beginning of the simulation showing the 'Initial Angle of Wrinkle (θ_{IAW})'. [a.2] Wrinkle configuration obtained after MD simulation of Figure a.1 with specific height, length, and Final Angle of Water (θ_{FAW}) of the wrinkled structure (with no water). [a.3] Insertion of water molecules in the minimized wrinkled structure obtained in Figure a.2. [a.4] Final configuration (after MD simulation of Figure a.3) with final height, length, and θ_{FAW} of the wrinkled structure (with water). (b) Variation of the [b.1] aspect ratio (height/length), and [b.2] final angle (θ_{FAW}) of localized wrinkle obtained from different initial angles (θ_{IAW}). At each θ_{IAW}, we varied the number of water molecules inside the graphene bilayer. [c] The aspect ratio (AR) and final angle variation w.r.t. the no. of water layers. Simulation box is not visible.

As shown in Figure A.4-A.7 (Appendix A) , irrespective of the number of the diffused water layers (i.e., 2-, 4-, or 6-layer), the pattern of the final configuration is the same for all water layer cases. We define two new parameters (Figure 2.6a) – (1) *Aspect Ratio (AR)* as the ratio of the height of the wrinkle to its base length, and (2) '*Final Angle of Wrinkle*, θ_{FAW}'. If $AR = 0$, it means the sheet is flat (height = 0). The higher the value of *AR,* the lesser the radius of the curvature of wrinkle-vertex. Moreover, there is a directly

proportional relationship between AR and θ_{FAW}. Figure 2.6b,c show how AR and θ_{FAW} vary with θ_{IAW} (*initial angle of water*) for the differing number of the water layers. When there is no diffused water (Figure A.4a-A.7a in Appendix A), as θ_{IAW} increases from 6° to 21°, the final localized wrinkle becomes sharper. Therefore, the blue curve (*no water case*) in Figure 2.6b shows that the AR and θ_{FAW} increase as θ_{IAW} increases. As mentioned before, the presence of diffused water starts the complex interplay between the wrinkle amalgamation and droplet formation [61]. The final shape is the result of the interaction between two phenomena. For 2-, 4-, or 6-layer diffused water cases (Figure A.4b-d, A.5b-d, A.6b-d, A.7b-d in Appendix A), AR and θ_{FAW} linearly increases as θ_{IAW} increases from 6° to 21°. As shown in Figure A.4a (Appendix A), for $\theta_{IAW} = 6°$ case, the graphene sheet with initially distributed wrinkle flattens ($AR = 0$, $\theta_{FAW} = 0°$ in Figure 2.6b.1) for no water case. With the insertion of 2-, 4-, or 6-layer diffused water (Figure A.4b-d in appendix A), the droplet and wrinkle size increases. However, the decrease in AR for a different water-layer case for $\theta_{IAW} = 6°$ is not significant (*black* line in Figure 2.6c.1) as the length and height of the wrinkle increase almost proportionately. For the $\theta_{IAW} = 21°$ case (Figure A.7 in Appendix A), we have the spiker localized wrinkle for no-water case (Figure A.7a in Appendix A). The AR, in this case, is high (*blue* line in Figure 2.6b.1), since the base length of wrinkle is moderately short as compared to the height of the wrinkle. With the increase in diffused water amount, the base length of the wrinkle keeps increasing while the height is almost the same (Figure A.7b-d in Appendix A). Thus, AR and θ_{FAW} values drop significantly (*cyan curve* in Figure 2.6c).

In Phase I, it is observed that for all cases considered, distributed wrinkles evolve into a localized wrinkle. The way it appears is either the intra-attraction between water

molecules to make one droplet, and the vdW attraction between the wrinkle and water molecules that "drag" the graphene along with water droplet [62]. Another possibility is the vdW attraction between the upper graphene sheet and graphene substrate, causing that drag. The probability of the vdW attraction between walls of the same wrinkle, during evolution, are slim to none given the wrinkle wavelength. Furthermore, it may be a combination of all these factors, which may be the function of temporal and spatial variables as well. Though the detailed analysis is beyond the scope of this study, in Phase I, we tried to get an insight into the underlying mechanisms into the wrinkling formation and evolution kinetics.

2.3.2 Phase II: DFT Study of the Electronic Properties of Winkled Graphene

2.3.2.1 Crystal Orbitals (HOMO and LUMO). We performed the Molecular Orbital (MO) analysis of WGNR for all four angles ($6°, 11°, 16°, 21°$). We considered the localized wrinkle structure for four-layer of water cases shown in Figure A.4c-A.7c (Appendix A). We had considered coalesced wrinkle excluding the underlying substrate, i.e., free-standing WGNR (Figure 2.7). We considered the same number of atoms in all the cases, i.e., 120 atoms. The system is optimized with the MD code before performing electronic calculations with DFT. Figure 2.7 shows the isometric view and Figure A.11 (Appendix A) shows the front view. Crystal orbitals are demonstrated by the iso-surfaces with yellow color. A carbon atom has six electrons, out of which two lowest electrons are considered as core electrons, and the next four electrons are regarded as valence electrons. These valence electrons participate in the interaction with other atoms in the crystal. Consequently, we are considering these four electrons in the outmost shell in the DFT calculations.

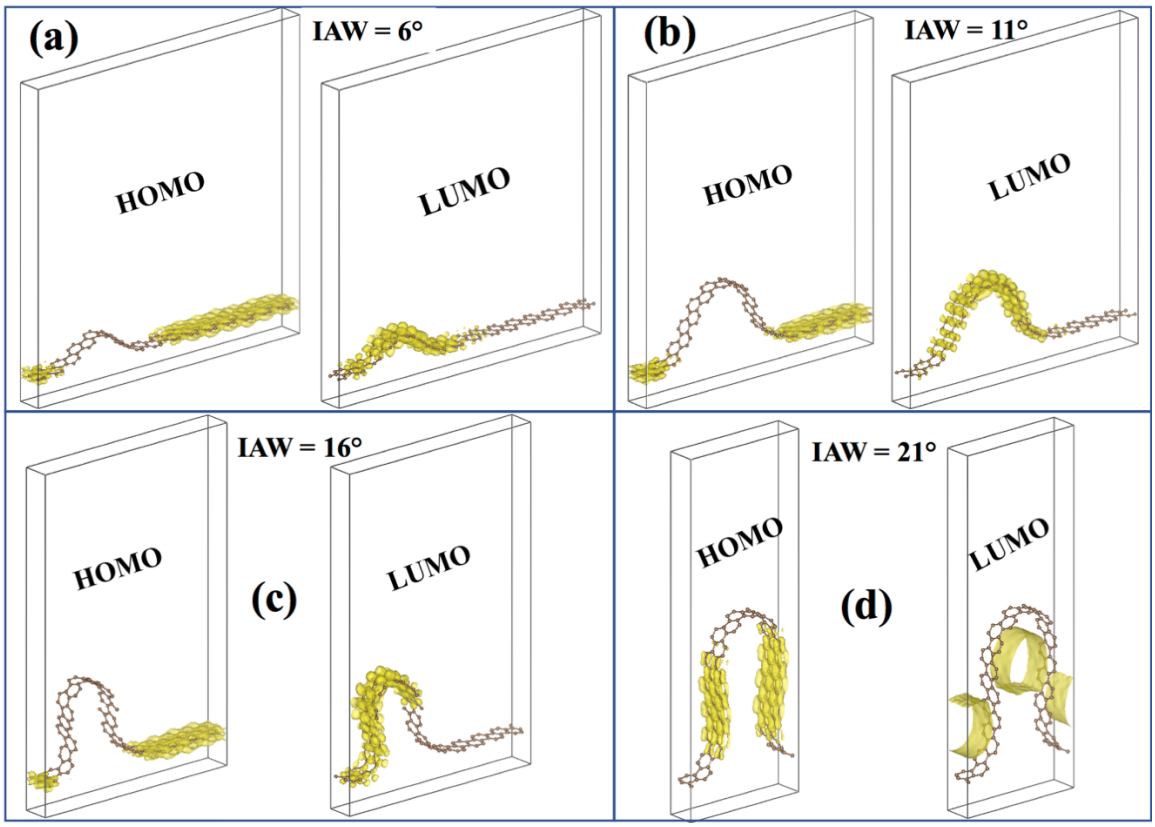

Figure 2.7 Isometric view of HOMO and LUMO for four localized wrinkles with Initial Angle of Wrinkle (IAW) of (a) 6°, (b) 11°, (c) 16°, and (d) 21°.

We observed the Highest Occupied Molecular Orbital (HOMO) at the portion of the WGNR, where the radius of curvature is high, i.e., the flat portion (Figure 2.7). For IAW of 6°, 11°, 16°, HOMO is observed to be only on the flat part of the GNR. This indicates that lattice distortion, present due to the wrinkle, is increasing the energy level of the molecular orbitals forming up the wrinkled portion of GNR. Hence, the electrons prefer to fill up the molecular orbitals formed by the flat portion of the GNR. The same phenomenon is observed in the sidewalls of the wrinkle for the highest angle considered (21°). In this case, the wrinkle is slender enough so that its sidewalls act like flat graphene and form the molecular orbitals having less energy. Consequently, electrons prefer to stay in the molecular orbitals formed by the sidewalls of the wrinkle instead of the vertex.

The Lowest Unoccupied Molecular Orbital (LUMO) is mostly observed in the portion of the GNR having high curvature (Figure 2.7). From IAW of 6° to 16°, LUMO can be found in the wrinkled section of the GNR and definitely not in the flat portion. It indicates that if the GNR gains an electron, then it happens by the atoms forming the wrinkle. The effect of curvature plays a dominant role when we increase the IAW beyond 16°. In the case of 21°, we observe LUMO in the form of tunnel shape [65]. The wrinkle is slender enough to confine the lowest unoccupied molecular orbital parallel to its direction. Further investigation is necessary to understand whether it's just the effect of curvature or the presence of HOMO along the sidewalls of the wrinkle or both of these factors contributing to some extent to the formation of "electron-tunnel"-LUMO. This observation proves that the presence of wrinkles and its slenderness plays a crucial role in the generation of "tunnel" LUMO orbital. It can be utilized to control the direction of electron flow in a (semi)conducting system, as observed by J.A Sulpizio et al. in the form of electron flow following a macro hydrodynamic flow pattern, i.e., Poiseuille flow [66].

Similar to these 'electron-tunnels', 'electron-channels' are obtained in the IAW values of 6°, 11°, 16°. The 'electron-channels' is the overlapping of the atomic orbitals of the same energy level forming an "electron-flow-channel" along the direction of wrinkle, which can act as a tunnel to the flow of every extra electron added to the system. Consequently, by controlling the course of these channels, the direction of electron-flow can also be controlled, which has multiple applications in the semiconductor industries. The studies aimed for similar outcomes are available in the literature [71,72]. For IAW of 16°, the asymmetricity is observed for LUMO. As shown in Figure 2.7c (Figure A.11c in Appendix A), the wrinkle is bent on one side (left). That causes the LUMO to only form

on the curved sidewall completely and partially on the right sidewall. There is a portion of the left sidewall of the wrinkle, where no LUMO or HOMO is observed (Figure A.11c in Appendix A). Further investigation is necessary to determine the energy level of the orbitals, possessed by the corresponding set of atoms forming the portion of the left sidewall of the wrinkle, where neither LUMO nor HOMO is obtained.

2.3.2.2 Band Structure. In Figure 2.8, band structures are plotted for localized wrinkled graphene structures shown in Figure 2.7. Each band structure is based upon the system consisting of 240 bands corresponding to 480 electrons constituting the crystal. The direct bandgap is observed for all of the cases. The observed bandgap values, based upon the difference between HOMO and LUMO, are 0.5492, 0.5453, 0.4801, and 0.5266 eV for the localized wrinkled structure corresponding to the IAW cases of 6°, 11°, 16°, 21°, respectively. Figure A.10 (Appendix A) shows the band structure of the flat pristine graphene. As expected, no bandgap is observed for this case.

The bandgap is observed to be decreasing linearly with IAW (6°, 11°, 16°), followed by sudden increase for 21°. This can be attributed to the observation made in Figure 2.7d for the 21° case, i.e., distortion of the HOMO-LUMO. As explained before, because of slenderness, the HOMO is observed on the sidewalls of the wrinkle. Moreover, because of high curvature, LUMO shifted from the tip to under the wrinkle to form an "electron tunnel". The delocalization of the HOMO and LUMO orbital for the highest angle case (21°) may be the reason behind non-linearity in the proportional relationship of IAW and bandgap.

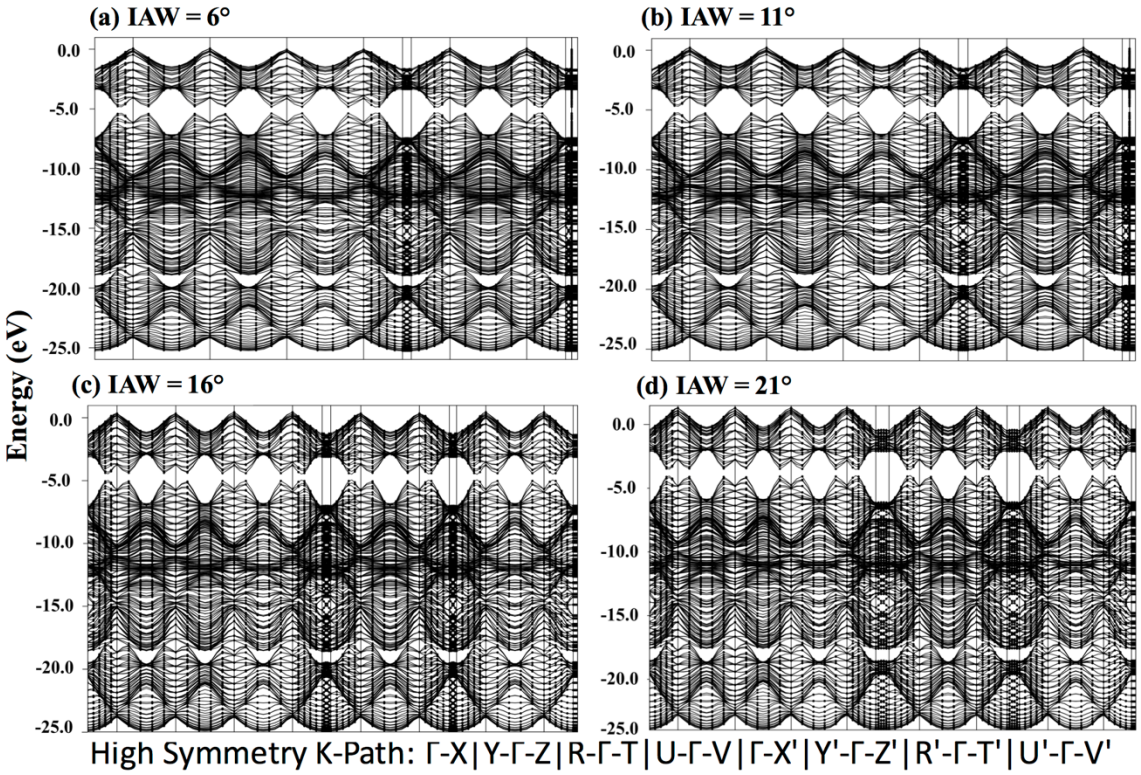

Figure 2.8 Band structure along high symmetry k-points for four localized wrinkles with Initial Angle of Wrinkle (IAW) of (a) 6°, (b) 11°, (c) 16°, and (d) 21°.

2.3.2.3 Density of States (DOS). In Figure 2.9, the density of states (DOS) is plotted for four wrinkled graphene structures mentioned in Figure 2.7. An inversely proportional relationship is observed between Fermi energy and the IAW. As IAW increases (6°, 11°, 16°, 21°), the magnitude of the Fermi energy decreases as -3.3651 eV, -3.2326 eV, -2.9825 eV, -2.0637 eV, respectively. The Fermi energy obtained for flat graphene is -2.3462 eV, which agrees with the values reported in the literature [68]. With the increase in IAW, the angle of curvature of final localized wrinkle decreases. It means that the wrinkled portion of GNR is denser (number of atoms/volume) than the flat portion of GNR and hence more stretched bonds.

Consequently, the strained lattice increases the energy levels of the localized crystal orbitals, which results in changing the Fermi energy as a function of IAW. In Figure 2.9, we notice two prominent peaks in DOS plots for all cases (IAW = 11°, 16°, 21°) except for the least IAW case (6°). We have the second peak in all the cases at around -2 eV to 0 eV, and the first peak at around -5 eV except for the least IAW case (6°). Further work can be conducted to find out the first value of IAW, which will generate the first peak in between IAW of 6° to 11° and results in two peaks.

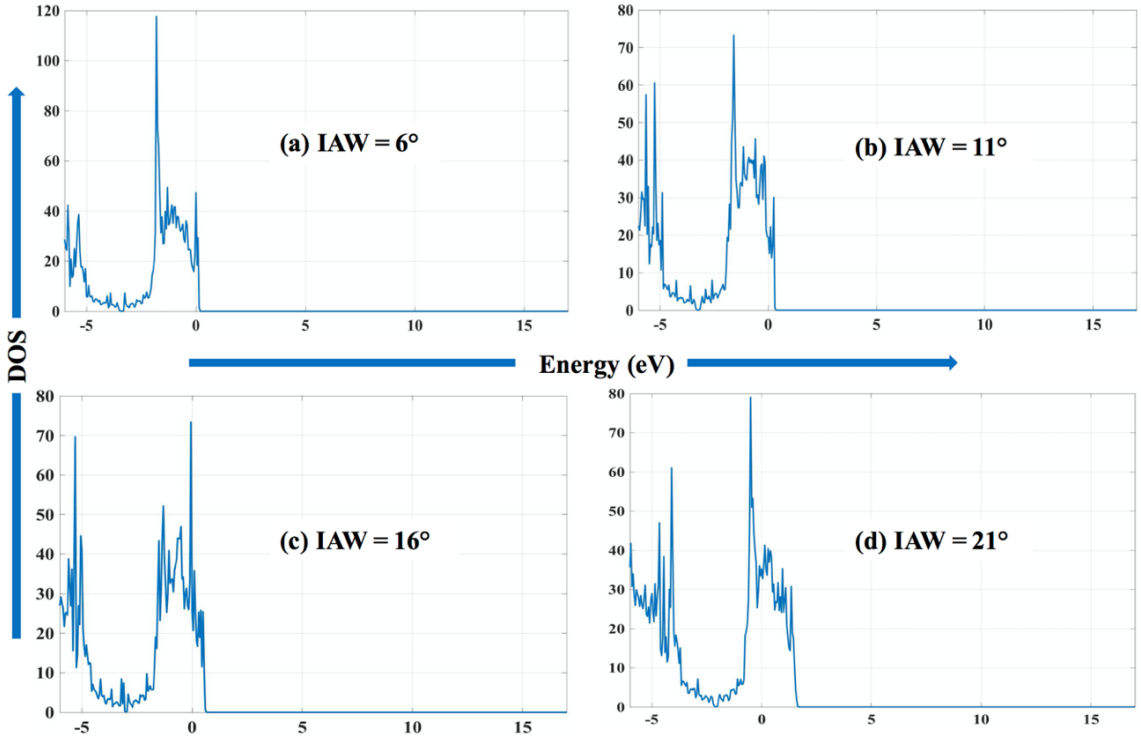

Figure 2.9 Density of states for four localized wrinkles with Initial Angle of Wrinkle (IAW) of (a) 6°, (b) 11°, (c) 16°, and (d) 21°.

As can be seen from potential energy plots (Figure A.1-A.4 in Appendix A), the local minima of potential energy increase (-7.427eV > -7.426eV > -7.424eV> -7.423eV) as the initial angle of wrinkle increases (6°>11°>16°>21°). The corresponding relationship can be observed in band structure plots while observing the Valence Band Maximum (VBM)

in Figure 2.8. As the initial angle of the wrinkle is increased, so does the VBM from approximately 0 eV to 1.5 eV. Synchronously, in total DOS plot in Figure 2.9, the energy corresponding to the highest energy state is also increased from ≈0 eV to ≈2 eV.

2.4 Conclusion

In conclusion, we have performed MD and DFT simulations to geometrically and electronically characterize the wrinkle formation, evolution, and collapse in graphene when water is diffused in between graphene and substrate. Our key findings are summarized below:

- The distributed wrinkles in graphene coalesce to form a 'localized wrinkle', whose configuration significantly depends on the initial pattern of distributed wrinkles and the amount of diffused water present in between the graphene and substrate.

- When water is distributed on a graphene sheet, due to hydrophobicity, distributed water molecules condense to form a water droplet. In the presence of diffused water, the final wrinkle configuration is the result of the competition between the water droplet formation process and the localized wrinkle formation process. For the lower initial angle of wrinkle, droplet formation is dominant, resulting in wrinkle with a high angle of curvature values i.e., non-sharp vertex. For higher initial wrinkle angle, wrinkle formation dominates, and the resulted localized wrinkle tends to possess a lower angle of curvature i.e., sharp vertex.

- The stress analysis reveals that the maximum stress is at the base of the wrinkle, and always below its plasticity limit. Therefore, wrinkle formation due to water diffusion does not cause any significant bond-breaking.

- "Electron-tunnel/channel" is observed along the vertex of the WGNR. By controlling the direction of WGNR, we can control the direction of the electron flow. This concept can be used in designing flexible electronics and optoelectronics.

- The direct bandgap is observed for all the wrinkle cases considered. The change in wrinkle geometry also generates lattice strains, which further changes the energy level of the crystal orbitals. The strain in lattice changes the Fermi energies as well as results in Fermi level modulations.

Our study addresses the fundamental questions regarding the wrinkle formation, evolution, and collapse due to water diffusion and its importance in flexible electronics.

CHAPTER 3

ENGINEERING FRICTIONAL CHARACTERISTICS OF MoS_2 STRUCTURE BY TUNING THICKNESS AND MORPHOLOGY- AN ATOMIC, ELECTRONIC STRUCTURE, AND EXCITON ANALYSIS

3.1 Introduction

Two-Dimensional (2D) materials are constituted of a few layers of atoms, and they are known for their cutting-edge applications in the domain of electronics, optics, and magnetics[69]. This work highlights their tribological properties and different approaches to tune them. Whenever a 2D material is used in a device, it will always form physical contact with another body, and consequently there will usually be relative motion across their surfaces and relative motion between surfaces yield friction. Friction could be desirable for an application, i.e., stopping a moving part, or non-desirable, i.e., supporting a moving part while offering minimum resistance to its motion, ideally none. This study primarily focuses on tuning the frictional characteristics of 2D materials by engineering the surface morphology and thickness[70][71]. While surveying the literature, we had discerned there were mainly two ways by which the tribological properties can be modified of the given layered materials with more importance being given to the former than the latter[72], i.e., a) introducing a structural change in the lattice geometry of material either by wrinkles or indents or folds or doping or functionalization or vacancy generation or straining, etc. and b) non-geometrical changes either by applying electric/magnetic/thermal field or annealing, irradiation, surrounding atmospheric conditions, etc. For tuning the surface morphology of 2D material, a favored mechanism was generating the wrinkles on the surface or other out-of-plane morphological deformations[73]. Since wrinkles usually acquire the shape of the waves, they can be controlled and modeled straightforwardly using

the parameters such as amplitude and wavelength. For example, the wrinkles' pattern change on Chemical Vapor Deposition(CVD) grown Graphene had been demonstrated to introduce frictional anisotropy[74].

Multiple experimental studies investigated interfacial strength [75], interface super-lubricity [76] and surface frictional [77] characteristics between Graphene, MoS_2, WS_2, WSe_2, and Atomic Force Microscopy (AFM) tip through Puckering Effect and at high pressure (1GPa) and humidity (51%) among other parameters. Furthermore, Graphene's tribological properties were tuned by fluorination-based surface corrugation in an experimental and MD (Molecular Dynamics) setup [78] and through hydrogenation and oxidation functionalization in an experimental and DFT (Density Functional Theory) framework[79]. Additionally, tribology-based aqueous and oil dispersion characteristics of carbon quantum dots(CQDs) decorated 2D materials (h-BN: MoS_2: $MoSe_2$: WS_2 and Graphene)[80], and interlayer and surface modification-dependent inorganic layers of Zirconium Phosphate[81] were observed, respectively. In other setups, 2D α-ZrP intercalated with multiple amines exhibited lubrication when dispersed in oil[82], and substitute for ambient conditions solid- and liquid-based lubricants were provided by synthesizing graphene-ionic liquid(IL) based on 1-butyl-3-methylimidazolium iodide, i.e., [BMIM][I] [83]. Moreover, models like spring-block, dashpot, 2D multi-atoms Prandtl-Tomlinson, and micro slip finite element were used to obtain correlations like the dependency of Friction Coefficient on the surface pattern of soft polymer, hierarchical complex and bulk materials [84][85][86], the curvature of multiwall hetero-nanotube complex[87], surface corrugations[88], and wrinkle's wavelength/amplitude in 2D/3D complex[89]. Furthermore, frictional characteristics were controlled by covering SrTiO3's

surface with molecular-monolayers[90], redistributing electrons in hexagonal boron-nitride bilayer through intercalation of fluorine atoms[91], and inserting Graphene against Silicon Force Microscopy(SFM) tip [78]. Similarly, another substitute of friction control was generating vacancies (which was more effective than C-O based add atoms functionalization) in Graphene for triboelectric NEMS/MEMS[92], and epitaxial Graphene on SiC, which becomes even more effective for bilayer due to electron-phonon coupling[93]. Additionally, Moiré superlattice seems to play a pivotal role in affecting the interfacial or surface frictional characteristics of multiple systems, i.e., Graphene on Ge(111) [94], Graphene flake subjected to area change and biaxial strain [95], fluorographene/MoS_2 [96], Graphene on Re(0001) and Pt(111) [97], and Graphene on Ru(0001) and Ir(111)[98]. In several studies multiple correlations regarding tribological characteristics were discovered including dependency of Graphene/Graphene; hBN/hBN; MoS_2/MoS_2; Graphene/hBN; H-graphene/h-BN system on atom's electronegativity[99], MoS_2 system on lattice orientation[100]. Similarly induced in-plane strain caused charge transfer[101], Graphite on Li^+ intercalation[102], MoS_2; WS_2; and WSe_2 on thickness[9], multi-layer Re intercalated homo MoS_2 on thickness due to enhanced phonon-electron interactions [103].

Another set of experimental/computational studies demonstrated friction tuning in electrochemically reduced graphene oxide(ERGO) can modify supercapacitor's charge storage [104], thickness controlled Zinc acetate ($Zn(Ac)_2$) derived boron nitride nanosheets (BNNSs) can reduce the friction coefficient of pure water[105]. Consonantly friction modification in BN/BN system by perturbing charge transfer caused by changing location of impurity atom[106] and achieving high-temperature lubricity by intercalating 11-

aminoundecanoic acid in protonated titanate $H_{1.07}Ti_{1.73}O_4$(organic/inorganic complex)[107]. Meanwhile, multiple studies used non-structural parameters as catalysis for affecting frictional characteristics including surface treatment and temperature variations[108], water intercalation and condensation for Graphene, Graphene Oxide, and SiO_2[109]. Likewise, ion-irradiation of Graphene and Diamond-like carbon in Nitrogen filled chamber[110], water and alcohol intercalated in Graphene/Mica[111], magnetic field between oxygen molecules layers on Nickel and gold substrate[112], and ambient humidity on the salt surface [113]. Furthermore, frictional characteristics were affected by the normal electric field on MoS_2[95], high pressure (46MPs) annealing of CVD-grown hBN monolayer[114], electronically engineering the ionic liquids between AFM tip and the electrode[115], condensed water from highly humid air between CVD MoS_2 and Silica substrate[116]. There were multiple applications utilizing frictional characteristics of layered materials, including quantifying friction exerted by the tip on organic composite[104], 0D/1D/2D materials based friction powered skin-mountable strain sensor[117], friction tuning graphene-oxide(GO)/poly(N-isopropyl-acrylamide)(pNIPAM) composite thermo-responsive hydrogels based Tweezers[118]. Comparably, interlayer-friction controlled photoresponsivity of MoS_2 based tribotronic-phototransistor[119], MoS_2-phototransistor with high ON/OFF ratio and drain-source current[120], interlocking friction in bi-layer MoS_2 system governing the fracture/crack propagation[121], black-phosphorous thickness/orientation controlled tribological NEMS[122]. Besides, new models and methods like conventional Prandtl-Tomlinson/DFT [123], electromagnetic field-based quantum chemistry[124], 2D Burridge-Knopoff [125], and nano-scratch and Raman spectroscopy[126] were used to find tribological correlations

for 2D electron-hole systems including Fluorographene, MoS_2, WO_2, and $WSe_2/MoSe_2$. Finally, phosphorene's tribological characteristics demonstrated dependency upon load applied on the tip, sliding direction, pre-strain of phosphorene, adhesion with the substrate, substrate's roughness, and bilayer arrangement[127]. Lastly, elastic conduct of TMDCs materials MX_2 (M= W, Mo; X= S, Se) was studied for the first time while modeling tribological properties[128].

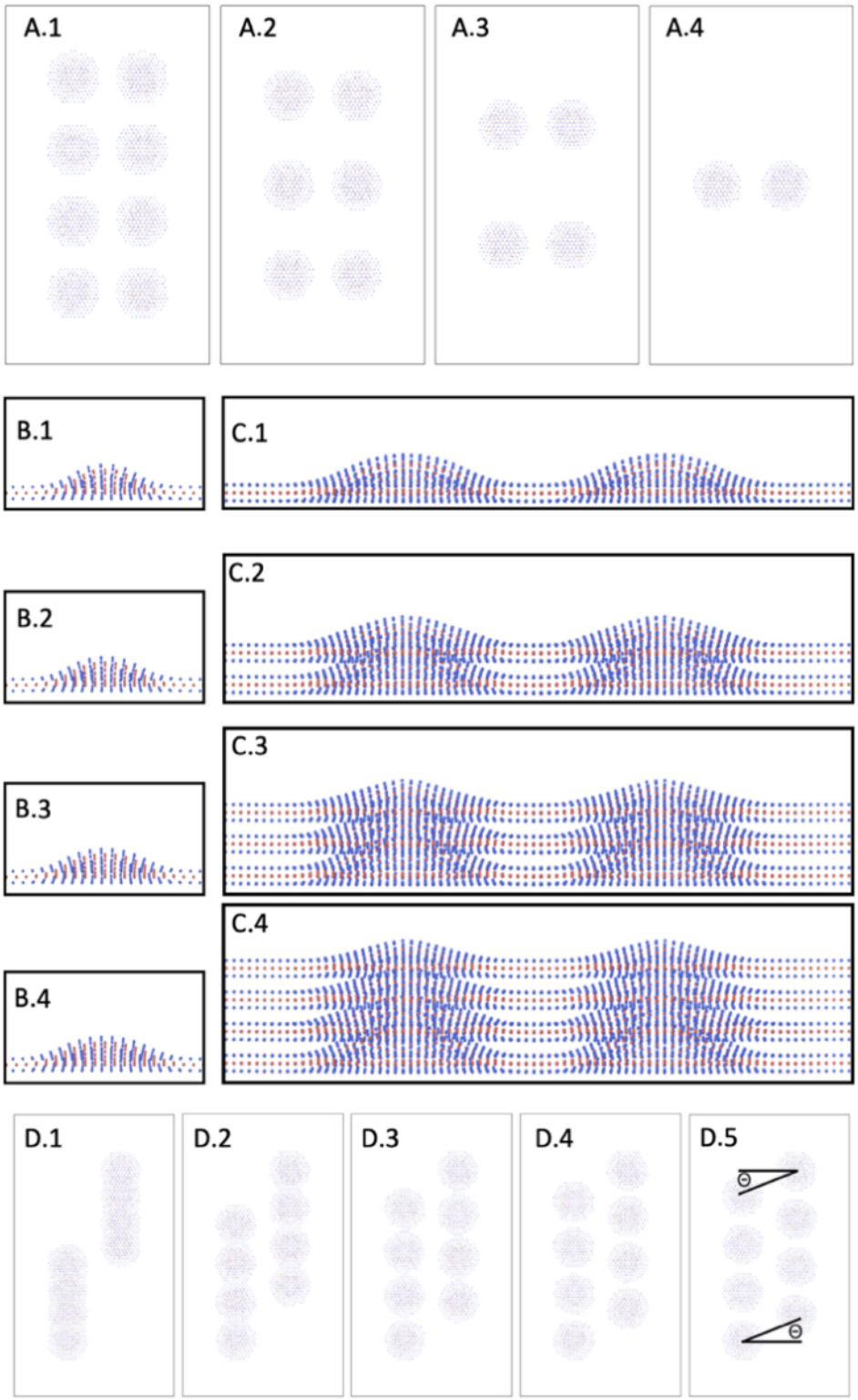

Figure 3.1 MoS_2 system models considered. A.1-A.4 Shows the change in number of indents (8, 6, 4, 2). B.1-B.4 Shows the change in radius of indents (12 Å, 16 Å, 20 Å, 24Å). C.1-C.4 Shows the change in number of layers (1, 2, 3, 4 layers). D.1-D.4 Shows the change in angles between adjecent indents (Θ=0°, 25°, 30°, 35°, 45°, 60°). For easy visualization, only indents are shown in A and D.

In this work, we had modeled the MoS_2 multilayered system by considering its nucleus degree of freedom in the Molecular Dynamics (MD) analysis phase, and electron's ground and excited states degree of freedom in the Density Functional Theory (DFT)/Time-Dependent Density Functional Theory (TD-DFT) analysis phase, respectively. We investigated the impact of morphological and thickness changes of a MoS_2 multilayered system on its tribological properties. We had considered 4 different cases, i.e., number of layers (1-4 layers), number of indents (2-8 indents), the radius of indents (12Å, 16Å, 20Å, 24Å), and the pattern of indents (0°, 25°, 30°, 35°, 45°, 60°) resulting into total 18 subcases (Figure 3.1). We used the Large-scale Atomic/Molecular Massively Parallel Simulator (LAMMPS) code to model the movement of an indenter's tip over the surface of the MoS_2 system. MD results show that changing the radius and number of indents in a MoS_2 system was the most effective way of tuning the frictional characteristics. While changing the number of layers and pattern was the least effective way. The ground-state study phase analysis shows that the number of stretched bonds in the systems increases with the number and radius of indents. This increases the Highest Occupied Molecular Orbital (HOMO) iso-surface volume, and TD-DFT analysis demonstrated that the tip might be responsible for the formation of the excitons in the system since Lowest Unoccupied Molecular Orbital (LUMO)'s volume was decreasing, which justifies the MD phase conclusion. Further, we had performed the in-depth electron-hole pair analysis of an oversimplified number of layer subcase to find the rationale behind the non-significant dependency of friction exhibited.

3.2 System Preparation and Methodology

The simulation cell size along X, Y, and Z directions were 159.581Å, 276.3Å, and 200Å for all cases except for the number of layers, where the Z dimension was: 200Å, 206.498Å, 212.996Å, 219.494Å in layers 1, 2, 3, 4 subcases, respectively. A spherical indenter tip of radius 10Å made from Carbon atoms was developed and relaxed in a separate MD simulation run.

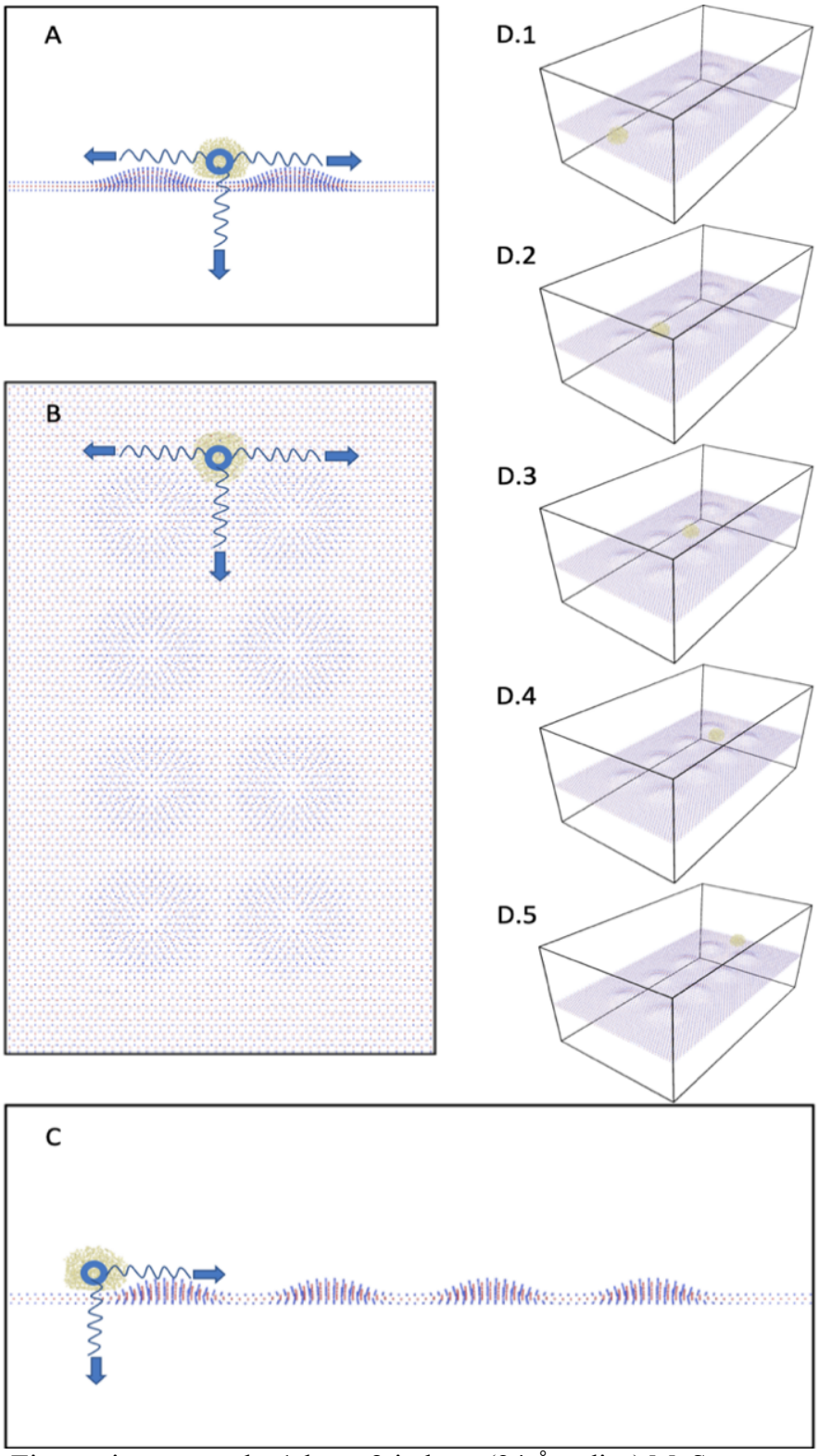

Figure 3.2 Tip moving across the 1-layer 8-indents (24 Å radius) MoS_2 system with Θ=0°. A, B, and C shows the front, top and side view, respectively. D.1-D.5 showing one full cycle of the movement of the tip from one end to another end of the MoS_2 sheet. Blue arrows are showing the direction of forces exerted by attached springs to the tip.

Consequently, the relaxed tip was placed 2Å above the top surface of the MoS_2 structure. First, the system was relaxed using gradient descent minimization to remove constrained/non-existent bonds. After this step, the tip and MoS_2 sheets were treated as rigid bodies for all simulation runs. For MoS_2 sheets to be treated as fixed, their atoms were assigned 0 m/s initial velocities, and forces were reset to 0 Kcal/mole-Angstrom at every step of all simulation runs. The next run was of 5000 steps NVT run for an equilibrium of the system at room temperature (300K). During this and subsequent runs, the tip was held with the springs. Two springs were tethered on opposite sides of the tip along the X-axis and centered at the center of the tip with spring stiffness of 10 eV/Å. A similar set of springs were installed along the Y-axis.

Only one spring was installed along Z-axis because the tip needed to be only pushed against the MoS_2 surface. The Spring constant of the Z spring was kept 5 eV/Å, lower than the other springs, since we just needed to gently push down the tip against the MoS_2 sheet with the least impact on the sheet's interaction with the tip. MoS_2 sheet works as a balancing spring, and the interaction between the tip and MoS_2 sheet counteracts the forces generated by the spring placed on the other side of the tip. These springs for the last run were kept stationary due to the fixed tip, while they were moved along with the tip for the next run. Once the system was visually inspected to not show any abnormal behavior during this equilibration run, the simulation was moved forward with the next run. The next and final run was a 100k steps NVT run (Figure 3.2). During this run, the tip was moved along with springs holding it in its place together (Figure 3.2(D.1-D.5)). The difference of springs from previous runs was the spring constant of X and Y springs was increased from 10 to 18 eV/Å, and there was only one spring along Y-axis used to pull the tip along Y direction

with a spring constant of 2 eV/Å, increased from previous 5 eV/Å. During this run, the X, Y, and Z components of the torque and force experienced by the tip were measured (Figure A.10-A.17 in Appendix A). For the force measurement, the force was measured on every atom of the tip, and then it was summed to a scalar value. For torque measurement, LAMMPS's inbuild torque measuring command was used.

The main objective of this project was to tune/engineer the forces acting along Y-direction on the tip. Given the morphological features introduced in the MoS_2 monolayer, all of them can be attributed to the change in Y-directional force in one way or the other. Since forces are often associated with a moment and hence torque, we had characterized the torques as well. Torque is a rotational effect a linear force had around an axis. In this system, more than one linear force produces the torque. Forces along the X and Z-axes produce the torque around the Y-axis, the Z and Y-axial forces produce torque around the X-axis, and X and Y-axial forces produce the torque around the Z-axis. Due to the interactions occurring at the atomic level, the significant part of the motion of the tip over the MoS_2 monolayer was the stick and slip nature. Consequently, we saw the fluctuations in the forces and torques plots in the MD phase of the study (Figure A.10-A.17 in Appendix A). This data noise was filtered out by averaging the forces and torques in the post-processing of the MD phase. Even though these fluctuations were detrimental to the overall data analysis, one can quickly pinpoint an MD step over the whole MD data plot, which can be studied in detail by itself and will help understand broader mechanistic detail about tip's overall motion. A wider perspective had emerged from averaging out similar MD steps. In our case, we had to pinpoint salient MD configurations that we believe had significant contributions to the overall perspective, and then we performed further studies

on those configurations using the first principle approaches. The ab-initio codes do not accept large systems considered in the MD phase. Therefore, we had to trim down the system just enough to be fed into DFT code and in a way that it should had maintained salient features of the geometry, if not all, which had contributed significantly to the MD force/torque plots. For all the cases, the number of atoms was kept constant except for the number of layer subcases since, implicitly, the number of atoms will change as the number of layers was changed.

We had implemented first-principles DFT with plane-wave basis sets and pseudopotentials to describe the electron-ion interactions as implemented in VASP. All calculations were done using the projector augmented wave (PAW) pseudopotentials and the Perdew–Burke–Ernzerhof (PBE) exchange-correlation functional. The plane-wave basis sets were used with a plane-wave cutoff energy of 300 eV. The convergence threshold of Kohn–Sham equations was set to $1e{-}06$ eV. The gamma-centered k-point sampling grids obtained using the Monkhorst–Pack method were $3 \times 3 \times 1$ with a zero offset for the graphene unit cell. The valence electrons for Mo belong to 4p5s4d orbitals, and S belongs to s2p4 orbitals. The Koopman theorem was used for calculating the HOMO and LUMO iso-surfaces of the systems, and the Bader charge program[129] was used to perform the atomic charge transfer analysis. Before DFT calculations, all atoms in the cell and the lattice dimensions and angles were relaxed to the equilibrium configurations using MD. For the band structure calculations, the symbols and coordinates of the high-symmetry points in the first Brillouin zone of the crystals were taken from the MaterialsCloud server[50]. MATLAB and VESTA codes were used for the post-processing of the results. Furthermore, for electron-hole (exciton) calculations, we computed the Bethe-Salpeter

Equations (BSE) using **exciting** code[130], which is a full-potential all-electron density-functional-theory package implementing the families of linearized augmented plane-wave methods. Since it's costly to perform such calculations, we must be conservative in selecting the system's size. As one indent in our systems contains 427 atoms and that was too big for BSE analysis, we had to consider only that case where analysis can be done without considering the indents. Given the technical constraints, we can afford to ignore indents only in one case out of four cases considered and still establish a meaningful correlation, i.e., the number of layers case. Therefore, we had considered primitive cell of MoS_2, having 6, 12, 18 and 24 atoms for 1, 2, 3, and 4 layers sub-cases alongside appropriate assumptions while explaining the rationale behind the results from the MD phase of the corresponding subcases.

3.3 Results

The net force acting on the diamond tip can be divided into three fundamental forces, i.e., X, Y, and Z-axis. Of these, only the Y-axis force was vital in studying the system's nano-frictional characteristics. As there may be situations where non-Y-axis forces contribute to the Y-axis force, due to which a brief analysis of all the components was needed in this study. Z-axis force is a direct normal reaction from the MoS_2 surface due to the diamond tip pressing against it. Any change in the surface morphology will directly impact its magnitude. Similarly, the Y-axis force is the direct reaction to the motion of the tip over the MoS_2 surface. Akin to the normal reaction in the case of Z-axis force, the velocity of the tip was maintained constant for all cases and was considered to be a standard reference for comparison purposes. In addition to these primary reasons for the forces to exist, there can be secondary reasons. Those were mainly due to the tip's highly stochastic stick and slip motion over the MoS_2 surface. The position of the tip with respect to its relaxed position at the time of the first MoS_2 surface morphological change experience by the tip highly influences these secondary reasons because this will set the tone for future movements of the tip and it was highly unpredictable. The secondary rationale for the Z-axis and Y-axis forces appear to had become the primary reason for the average X-axis forces experienced by the tip. That was why we had occasionally observed the average X-axis force, which does not agree with the hypothesis that supports the existence of the average Y-and Z-axis forces.

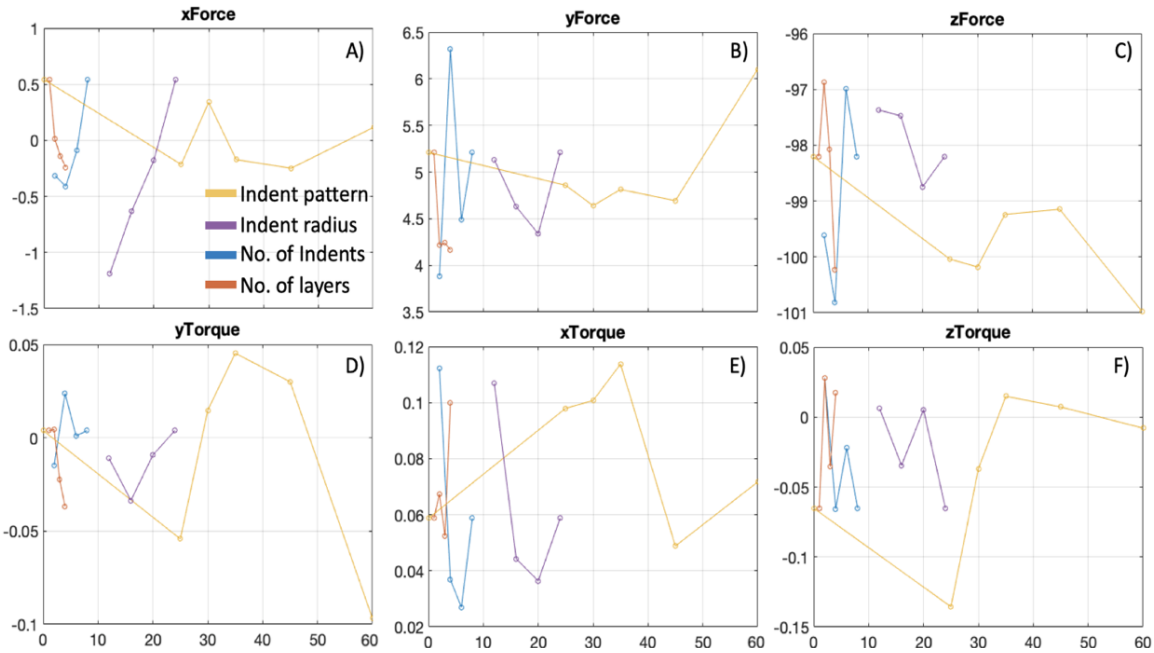

Figure 3.3 Average forces along X, Y, Z axes in A), B), C), respectively. Average torque about X, Y, and Z axes in D), E), and F), respectively. Legend is visible on A) for different line colors.

A plausible rationale for reactional forces to exist could be when the tip had its first interaction with the indent, the tip may had been present on the right-hand side about the centerline parallel to the Y-dimension of MoS_2 sheets due to the stick and slip phenomenon. Since it was already shifted to its right-hand side, the interaction of the tip further pushed it down the right-hand side so that it could not recover its initial position throughout the whole cycle of movement over the MoS_2 layer. A similar argument can be made for the left-hand side of the tip. On the other hand, the first interaction was probably strong enough to create the over-swinging pendulum motion of the tip, given the spring constant of springs holding the tip in its place. To make the movement of the tip more complicated, the resulting net motion of the tip could be either of these scenarios or any combination of them. Still a conclusion that can be made unequivocally is that this will be only possible in the average X-axis force and not for the Y and Z-axes forces. Because the wobbliness of

the tip was not "strong enough" to overcome the primary reasons, as outlined above, in the case of X and Y-axes forces. To avoid the data noise and given the Z-axis force (normal force) had a significant impact on the Y-axis force (frictional force) due to the Law of Friction[131], we shall focus our detailed discussion only on the number of indents and radius cases. Because only these two cases demonstrate significant linear correlation on the Y and Z-axes force plots (Figure 3.3). Furthermore, an increase in the number and radius of indents results in a higher population of stretched bonds in the whole system, leading to a significant change in the electronic structure and ultimately a corresponding transition in the mechanical behavior of the system. As opposed to the number of layers and indents pattern change subcases, where the changing the number of layer and indents angle doesn't produce a significant switch in the number of stretched bonds and hence the electronic structure in/of the whole system resulting in nonlinear changes on average Y and Z-axes force plots. Furthermore, Figure 3.3 shows that the first point of the orange curve and yellow curves, and the last points of the blue and magenta curve had the same Y-axis values on all of the MD plots since they were all the same structures, i.e., 1 layer having 8 indents of 24 Å radius with 0° indents' pattern.

3.3.1 Radius of Indents

As stated earlier, our primary focus will be the reaction force on the diamond tip along the Y and Z-axes since friction force (the Y-axis reaction force) is the function of the Z-axis reaction force. As the radius increases (Figure 3.3B), the Z and Y-axis average reactional forces decrease, considering the 24Å subcase as an outlier. The resultant force of these two forces was acting at an angle between 0° and 90°, opposite to the tip motion and spring pressing down the tip on the MoS_2 surface. As the radius of the indents increases, the

reaction forces exerted by the indents on the moving tip also increase since the tip moves with constant velocity among all the radii considered. The higher resultant reaction force was being split into the higher reaction force components along Y and Z-axes, resulting in the increased magnitude of the Y and Z-axes reactional components as the radius increases (Figure 3B). For discussion, we can call this resultant reactional force the sum of the upstream reactional force since it comes into existence when the tip touches the indent for the first time on its face-up and downstream reaction force, which was the force experienced by the tip while leaving the indent. This can be described by the superposition of all the forces in the Y-Z plane as we were not considering the X-axis reactional forces. Since the X-axis reactional forces were more indicative of the initial perturbation of the system when the tip touches the 1st indent of the surface rather than indicative of the reactional forces experienced by the tip throughout its overall trek over the MoS_2 sheets. Since these observations were made from force plots obtained by averaging the forces experienced by the tip throughout its complete motion cycle over the MoS_2 sheet, the upstream and downstream reactional forces had to add up to satisfy the proportionalities observed.

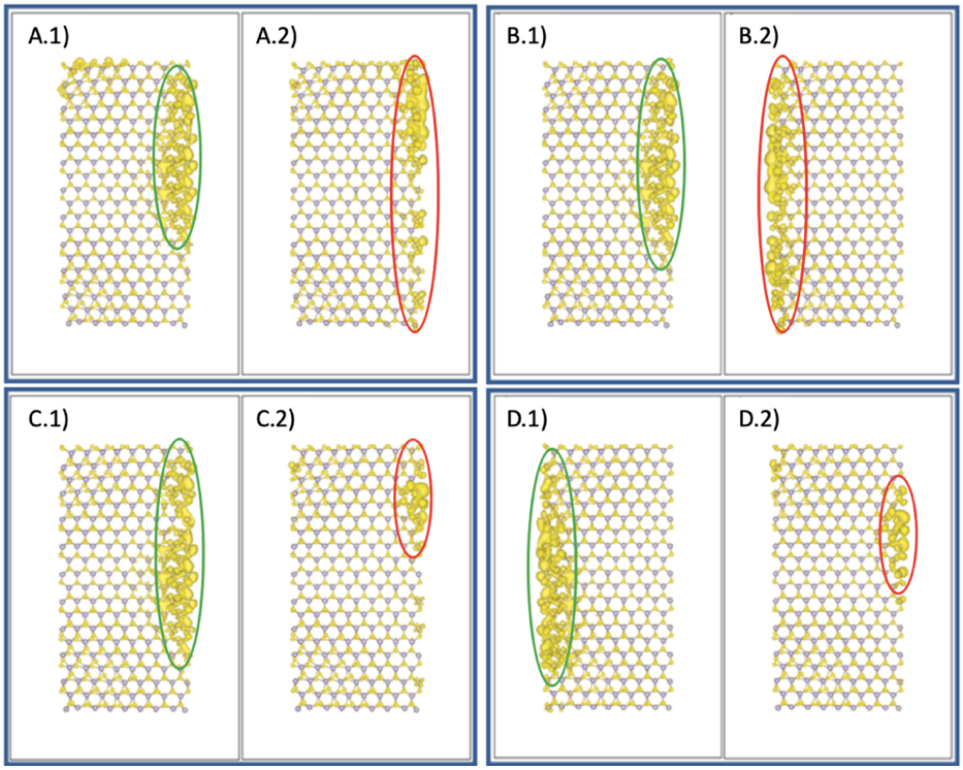

Figure 3.4 Molecular orbitals of radius sub-case. A), B), C), and D) shows the radius of 12Å, 16Å, 20Å, and 24Å, respectively. 1s(left) are HOMO and 2s(right) are LUMO iso-surfaces.

There could be two reasons that this Y-axis reactional force was emerging. First, as the radius increases, the Y-axis component of the force exerted by the indent on the tip increases. As this force rises, the Z-axis torque exerted on the tip increases. Comparing the Z-torque charts for radius and pattern change-subcases highlights a clear trend in the latter while not in the former. This can be attributed to the fact that in the case of pattern-subcase, the indents were placed asymmetrically, and if an indent exerts a torque on the tip, there was no indent on the other side to counteract, except in the inline subcase. However, this was not the situation for radius subcases. An indent on the other side counteracts the torque exerted by force generated by an indent on one side of the tip. On the flip side, the second mechanistic pathway may be the average Y-axis force on the tip could had resulted from the stiffness reaction exerted by the springs holding the tip. As the radius of the indents

increases, the negative Y-axis forces exerted on the tip increase. Once the tip gets past the indent, the reaction forces faced by the tip exerted by the springs holding the tip get leveraged and push the other side of the tip by the amount greater than the initial Y-axis force exerted by the indent on the tip. This also results in the same outcome, i.e., an average Y-axis reaction force increase while clear or unclear trend on the Z-torque for indent's pattern case or radius increase case, respectively (Figure 3.3F).

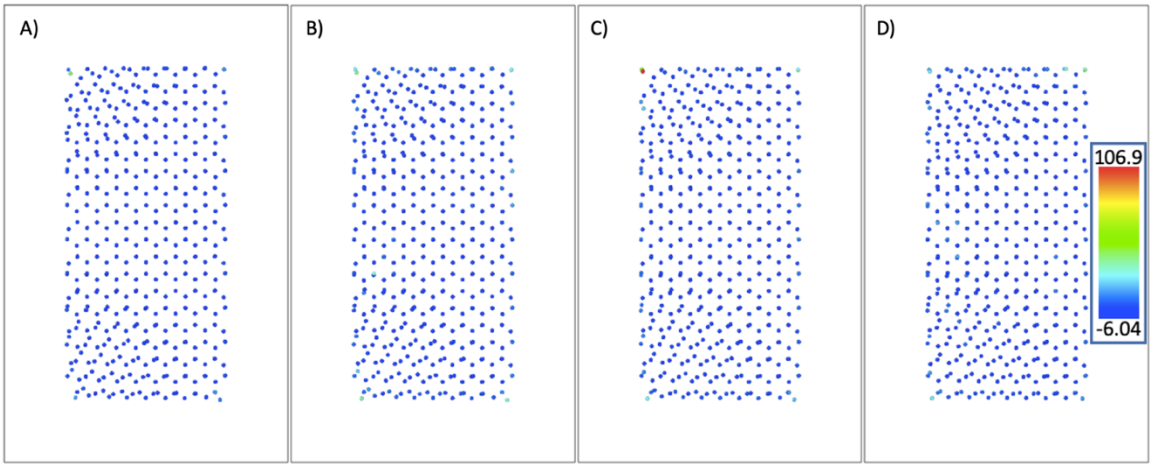

Figure 3.5 Bader charge transfer of the radius sub-case. A), B), C), and D) shows the radius of 12Å, 16Å, 20Å, and 24Å, respectively. Ligand with its end values is visible in inset of figure D in eV.

In electronic structure analysis, the volume covered by the HOMO-isosurface increases, and LUMO decreases as the indent's radius increases (Figure 3.4), which can be attributed to the bond stretches. As the radius of indents increases, more stretched bonds among Mo and S atoms in the system occur. The rise in HOMO volume dictates that the monolayer was willing to lose or share the electrons through a larger area. The decrease in the LUMO volume dictates that the lesser volume of layers was accepting the electrons. Since we already know from the MD force/torque results that as the radius increases, the Y and Z-axes reaction forces also decrease. That means the electronegative parts, i.e., the volume

occupied by HOMO of the monolayer, were less likely to lose/share its charge carriers with the other parts of the monolayer, i.e., the volume covered by the LUMO. However since the Y and Z-axes reaction forces were decreasing, the interlocking interaction between the tip and layer increases, i.e., the layer pulls down the tip with higher strength. This could be only possible if the greater HOMO-covered volume of the monolayer shares its charge carriers with the tip because the tip was the only other body contacting layer surface. Since we cannot model the whole system in ground-state DFT, it's difficult to prove it conclusively, still the Bader charge transfer analysis and the MD force analysis point to this possibility.

Additionally, the Bader charge transfer analysis (Figure 3.5) indicates the atoms of this system had a high charge transfer range compared to the range observed in the number of layers and indent pattern cases. The same holds for the number of indents case as well. The ranges were 112.94 eV, 98.97 eV, 34.75 eV, and 1.78 eV for indents' radius, number of indents, number of layers, and indents' pattern subcases. It agrees with the results obtained from HOMO/LUMO plots that due to significant change in the stretched bonds density and hence electronic structure, the radius and number of indents subcases were displaying a strong correlation with the resulting frictional force changes. This was not true for the number of layers and indents pattern cases because no significant change in the stretched bonds density occurs as the input parameters were changed, which was also visible in their Bader charge transfer plots, i.e., having a lesser charge transfer range. In Bader charge plots (Figure 3.5), it must be highlighted that the edge states tend to had electropositive behavior, and flat portions as electronegative behavior. This can be attributed to the highly stretched and/or dangling atomic bonds at edges due to trimming

the systems to accommodate the modeling within the available computational resources. Further, we had observed in the exciton calculation part for the multi-layer case (section 3.3.1) that electron-hole pseudo particles (excitons) were being formed between holes in the MoS_2 layer and electrons from the tip (Section 3.3.3.1).

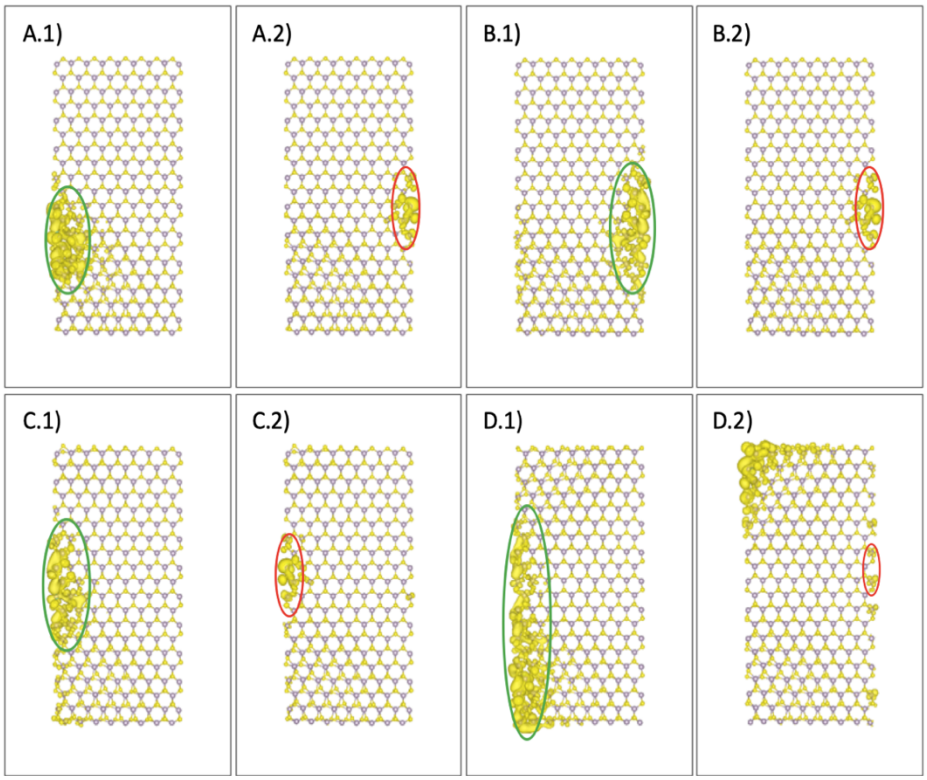

Figure 3.6 Molecular orbitals of number of indents sub-case. A), B), C), and D) shows the 2, 4, 6, and 8 indents sub-cases, respectively. 1s(left) are HOMO and 2s(right) are LUMO iso-surfaces.

This further supported the results observed in this section that as the radius of indents increases, more couplings occur between charge carriers across the layers and the tip, which results in the stronger interlocking between these two parts of the system resulting in a lower average Z and Y-axes reactive forces. To summarize, a change in the surface tribological properties will be pronounced and easier to detect in the reactional forces experienced by the moving tip if the surface and tip were "locked in" rigidly. It was

not observed for the number of layers and pattern change cases because of reasons already stated in section 3.1.

3.3.2 Number of Indents

In this section, we had investigated the frictional force dependency related to the number of indents. An increase in the number of indents in the MoS_2 monolayer increases the number of events that contribute to the interaction of the tip and an indent. As these events' occurrences increase, it skews the average force and torque calculations.

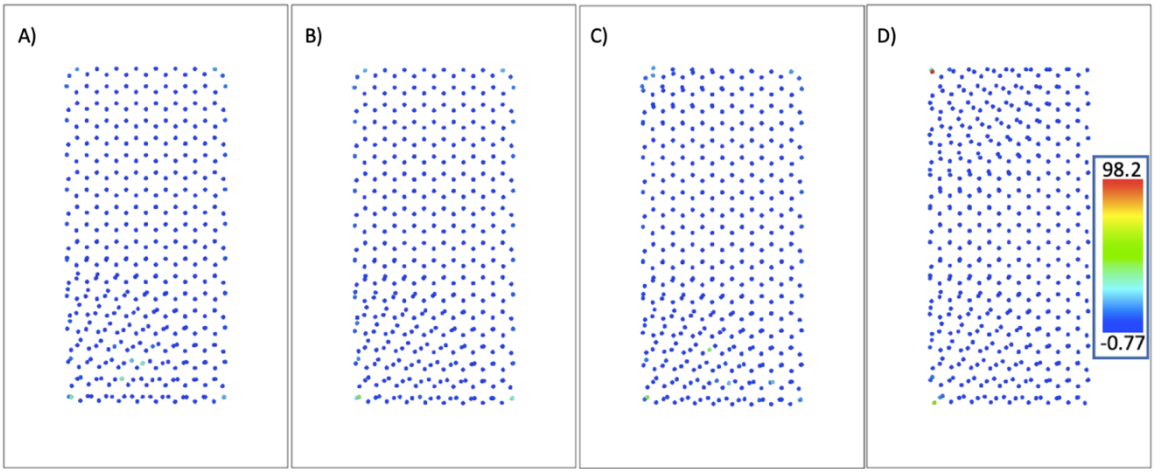

Figure 3.7 Bader charge transfer of the radius sub-case. A), B), C), and D) shows the 2, 4, 6, and 8 indents sub-cases, respectively. Ligand with its end values is visible in inset of figure D in eV).

Therefore, as building upon our previous argument of the generation of the average Y-axis reactional force, we can extend the opinion supported by the same hypothesis that as the tip was interacting with an indent in the monolayer, it experiences the net negative Y-axis force either as an act of the indent on tip or reaction of the springs holding the tip. Since one interaction between the tip and an indent increases the average negative Y-axis force, there shall be a linear relationship between these two, i.e., as the number of interactions increases between the tip and an indent, the average negative Y-axis reaction force will

increase. It was precisely what was observed on force plots in Figure 3.3B, as the number of indents was increased in the monolayer MoS_2 from 2 to 8 while considering 2 indents subcase as an outlier.

When the number of indents on the MoS_2 varies, the trend in reactional forces was not as straightforward as in the case of the radius subcase. For example, all four data points on the Z-axis reactional force plot were not displaying a line fit which was not observed for Y-axis reactional force (Figure 3.3B). An almost exact line fit exists if we consider the 2^{nd} data point as an outlier as we considered in the corresponding cases of radius subcase. Given the noise in data because of the highly unstable stick and slip motion of the tip over the MoS_2 surface, we can make an exception and cluster the last two and first two data points and consider the directly proportional relationship between the number of indents and Z-axis reactional force experienced by the tip. On the other hand, one can observe the increase in the Y-axis reactional force on the tip as the number of indents were increased, considering the 2^{nd} data point as an outlier. To summarize, we observed the increase in the indents was directly proportional to Z and Y-axes reactional forces. The resultant reaction force created by these two components of the reaction force experienced by the tip points along the positive Y-axis and negative Z-axis. Resulting in pushing the tip along its direction of motion while dragging it into the MoS_2 surface. As explained in the radius subcase section about upstream and downstream reaction force, in this case as the number of indents increases, the downstream reaction force acting along the positive Y and Z-axis also increases and by greater magnitude in comparison to the upstream reaction forces.

Additionally, the same phenomenon as of indent's radius case, was observed in electronic structure calculations. As the number of indents in the layers increases, the

number of stretched bonds increases in addition to increasing the stretchiness of already existing and new bonds. This results in higher volume covered by HOMO and lower volume covered by LUMO-isosurfaces (Figure 3.6) highlighted in green and red curves, respectively. A decrease in LUMO iso-surfaces dictates the intra-layer(s) bond formation was being deterred as the number of indents was increased. It means more layer surfaces area was available to share the charge carriers with a separate structure, i.e., tip in this case. However as described in the indent's radius case, the bonded interaction among electron-hole pseudo particles occurs as observed from excited-state calculations performed in the multi-layer subcase (Figure 3.10).

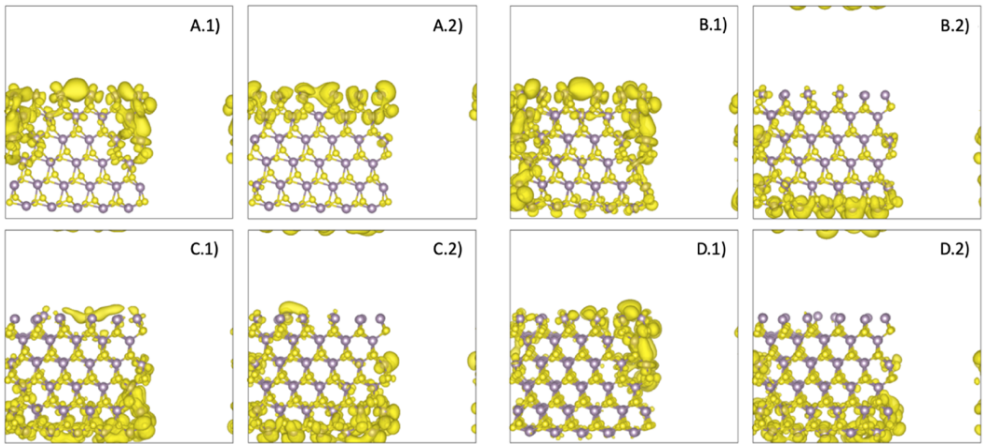

Figure 3.8 Molecular orbitals of number of number of layers sub-case. A), B), C), and D) shows the 1, 2, 3, and 4 layers sub-cases respectively. 1s(left) are HOMO and 2s(right) are LUMO iso-surfaces.

These bonded interactions use the higher HOMO volumes to form a stronger interlocking interaction among the layer and tip that results in a more "rigid transfer" of the changes in the electronic structure to the mechanical behavior, i.e., a higher number of indents leads to lower Y and Z-axes average reaction forces, respectively. Consequently, increasing the frictional force exhibited by the layered system. Similarly, the high range of Bader charge transfer was observed, i.e., ~100 eV in this subcase on par with the indent

radius subcase (Figure 3.7). This again agrees with our hypothesis that the number of stretched bonds was increasing in a similar trend as of indent's radius case, which was much higher than the number of layer and indent pattern cases.

3.3.3 Number of Layers

For number of layers case, we had observed that the average Y-axis reaction force was almost constant (Figure 3.3B). This can be attributed to two reasons: first, no force was experienced by the tip from the substrate, and second, the tip was experiencing forces and immediately an opposite force counterbalances it. It gives the illusion that the tip was experiencing no reactional force. We believe in the second rationale, which can be attributed to non-uniform X and Z-axes force curves in Figure 3.3B.

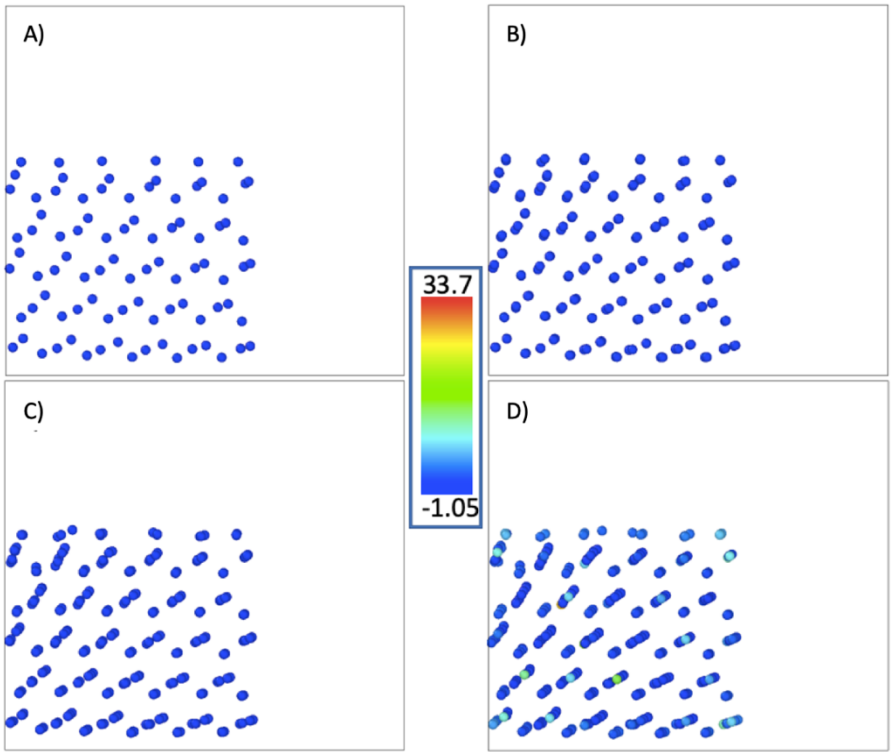

Figure 3.9 Bader charge transfer of the number of layers sub-case. A), B), C), and D) shows the 1, 2, 3, and 4 layers sub-cases respectively. Ligand with its end values is visible in center in eV.

If it was the former reason, i.e., the tip was not experiencing any force, the probability of average X and Z-axes forces having non-constant nature as we change the number of layers shall be acute. As the number of layers increases, the van der Waals interaction between the multi-layer system increases. We postulate that this was responsible for amplifying the average X, Y, and Z-axes forces exhibited by the substrate on the tip as the number of layers increases. Furthermore, increasing the number of layers increases the substrate's structural stability, augmenting the reaction forces experienced by the tip moving across the substrate/layers. As the number of layers increases, the tip's adherence to the morphological change shall become more rigid. The Y-axis force experienced by the tip while ascending an indent was almost the same as the force experienced while descending an indent and of precisely the opposite sign. There was nearly zero "hysteresis loss". Irrespective of number of indents the tip was moving over, it will always experience opposing forces along the Y-axis while ascending and descending the indent. That will result in almost zero accumulation of the net average Y-axis reaction force, supported by the Y-axis reaction plot showing the nearly horizontal line. Meanwhile, the average Y and Z-axes reactional forces were influenced by the increase in pull-down generated by the rise in the number of layers in the substrate. As the number of layers increases, the intensity of van der Waals interaction between substrate and tip also increases, which decreases the distance between the substrate, which now had a higher number of layers, and the tip. As the substrate cannot move towards the tip since it was fixed, the tip had to move closer to the substrate given an opportunity, and that opportunity was available whenever the equilibrium breaks due to the movement of the tip. In other words, the opportunity arises throughout the whole tip's movement period. The same

argument can be easily made for the average X-axis reactional force. In this case, the only difference was that due to the tip's wobbling motion, the tip drifted apart on such a side of the centerline so that the resulting reaction force on the tip was a net negative X-axis force. Which kept on increasing as the number of layers increased due to an increase in van der Waal interaction.

In addition to van der Waals interaction, bonded interaction can also demonstrate a significant role, as per HOMO/LUMO orbital plots and Bader charge analysis in Figure 3.8 and Figure 3.9, respectively. In this case, the FMO plot was not as helpful as the Bader charge plot. As the number of layers increases, the atoms with the less dark blue color appear, which indicates the losing/sharing of the electrons and hence the probability of bond formation. Moreover, there was no clear trend observable on X and Z-axes torque (Figure 3.3D-F), while there was a coherent decreasing trend on Y-axis torque (Figure 3.3E) as the number of layers were increased. Y-axis torque was produced by more than one force acting in the XZ plane (Figure 3.3E). Average X and Z-axes forces show an inverse trend with the number of layers. That results in these two forces trying to counterbalance the moment generated by each other since they were working in the same plane and around the same axis over the same range of the number of layers. Since the decrease in average Z-axis force was almost twice as big as the decrease in the average X-axis force, the moment generated by the Z-axis force was bigger, resulting in the net negative torque around Y-axis as the number of layers was increased. Furthermore, as explained in the previous two sections, the range of the Bader charge transfer was comparatively less than the last two subcases, i.e., 34.75 eV. This further supported our argument that the strong bonding between the surface and the tip accompanied by

counterbalance events was the rationale behind why we cannot observe a significant correlation on the Y-axis forces plots despite moderate changes in the electronic structure of the MoS_2 system for this subcase.

3.3.3.1 Quasi Particles in Multi-Layers Case – Excitons. We performed the excited-state calculation using the Bethe-Salpeter equation (BSE) model to explain the MD phase results further. Despite already trimming down the systems from MD step into DFT step analysis, the structure was cut further and over-simplified since the cost of the computations increases exponentially for excited states calculations with the BSE model. Consequently, we had only considered number of layers case subsystem, which demonstrated non-significant frictional characteristics. We had skipped the remaining 3 systems of pattern, radius, and the number of indents due to our inability to converge the systems within available computational resources.

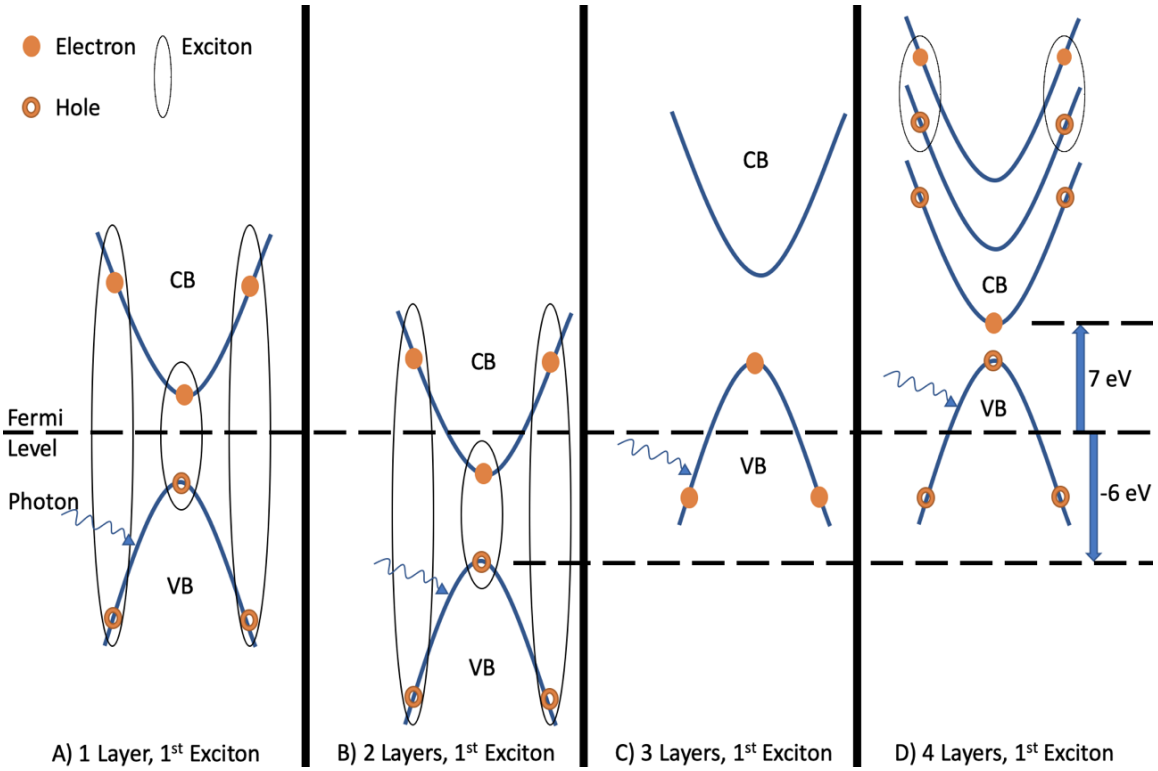

Figure 3.10 Schematic exciton visualization in k-space. A), B), C) and D) shows the excitons for the 1, 2, 3, and 4 layers subcases.

Excitons are electron-hole pairs that usually act as primary drivers for 2D materials' properties. Since exciton wavefunctions are 6-dimensional matrix objects, we need to reduce the dimensionality to handle the visualization by keeping one object fixed and plotting the cloud of another object in electron-hole couples. In this work, hole location was kept fixed while plotting the cloud density of the electron distribution for a given exciton. For one-layer system, hole located at x=0.02, y=0.02, z=0.5 scaled coordinates were fixed in the vicinity of a Mo atom located at x=0.0, y=0.0, z=0.5. An offset was provided to avoid the spurious effect generated in the real space exciton visualization due to the exact overlapping of the hole of a given exciton and an atom (Figure A.19). To provide the comparative analysis for the higher number of layers subcase, we need to keep a reference point to account for which the identity of the fixed hole was kept the same.

As Figure 3.10 and Figure A.19 (Appendix A) show, the excitons' energy increases as the number of layers increases if we consider the 1-layer (1L) case as an outlier. Furthermore, we observed from the fatband plots (Figure A.18 in Appendix A) that the coupling coefficients between electron-hole pairs decrease as the number of layers increases. We shall be careful about fatband plots since they were for highly simplified versions of the number of layers subcases. One of the major simplifications was that they include neither the tip nor the indents in the modeled system. Given that, we had attributed the non-significant change in frictional forces as the function of the number of layers to the two contributing factors mainly, i.e., the electron pair based covalent bond and electron-hole coupling. From the fatband plot, we can observe that the electron-hole coupling had an inverse relation with the number of layers in the case of a system containing only layers. However when the tip was introduced over the layers, then three outcomes were possible: as the number of layers was increased, i) the electron pair based covalent bonds and electron-hole couplings get strong among layers and tip, ii) the electron pair based covalent bonds gets weaker while the electron-hole coupling was getting stronger by greater magnitude among layers and tip and iii) the electron pair based covalent bonds was getting stronger while the electron-hole coupling was getting weaker by greater magnitude among layers and tip. Finally, the greater number of coupled particles and stronger coupling among these particles produces greater interaction between tip and layers, contributing to higher frictional characteristics as the number of layers was increased. From the Fatbands (Figure A.18 in Appendix A), delocalization of excitons over the K-space was observed, implying that they must be localized in real space (Figure A.19 in Appendix A). Real-space visualization shows the electron clouds getting stretched along the system's height as the

number of layers increases. For the 1-layer system, the electron cloud was localized over the Mo atom and less stretched in the Z dimension contrary to as the number of layers was increased the electron cloud starts getting stretched along the Z dimension and starts covering more of the S atoms of MoS_2 sheets and less of Mo atoms. As demonstrated in Figure 3.10, all of the excitons observed preferred intra-valley formations.

Increasing the number of layers decreases the excitonic effect (the interaction between electron and hole pair of an exciton). The excitonic effect dictates how strongly an electron and hole in a given exciton were paired. As the number of layers increases, the number of atoms also increases, making a bigger crystal size available for an electron cloud to spread over for a fixed hole in a given exciton. As the electron cloud for a given fixed hole in an exciton spreads over a bigger volume, it loses its binding strength with the attached hole than the electron cloud spread in a lesser crystal volume. It may hold true for all the excitons of the system instead of only 1^{st} exciton. As the tip was inserted in the system, we believe either no new excitons were being formed, or if they were being created, their generation rate was equivalent to their recombination rate. As discussed above, increasing the number of layers in the system increases the exciton energy, and it was comparatively accessible for an exciton of the layers to couple with the conduction band electron of the tip to form a negative trion or couple with a valence band hole to form a positive trion. Given a trion is a quasi-particle with three charged particles, it had a net tendency to hold components of a system together if the constituting electrons and holes belong to different components. That was why we can see a decrease in the average Z-axial reaction force plot from MD results as the number of layers increases in the system. That supports our hypothesis that the multi-layer system holds onto the tip more robustly as the

number of layers increases. Nonetheless the primary reaction force of this study, i.e., friction force, which was characterized by the Y-axis reaction force on the tip, was almost kept steady as seen from the Y-axis reaction force plot (Figure 3.3). This can be explained by the wobbliness motion of the tip that regardless of the number of layers the tip was stacked against, there will always be a balancing force against every negative Y-axis movement of the tip due to stick and slip motion. To summarize, we can see an increase in the Z-axis reaction forces felt by the tip traveling across a substrate due to the formation of the charge transfer exciton/trions while derivative of the Z-axis reactional forces, i.e., Y-axis reaction forces OR frictional force experienced by the tip moving across substrate was not modified. The latter overcome the former because of the stick and slip motion of the tip given the cavity spaces between atoms forming the tip and even bigger cavity spaces between the atoms forming the MoS_2 layer(s).

3.3.4 Pattern of Indents

In the case of pattern change, we investigated how the angle between the centerline of the substrate bisecting X dimension of the MoS_2 system and the center of the tip (Figure 3.1-D.5) affects the frictional force. Only two angles of 0° and 25° were considered for DFT calculations due to computational cost while considering all angles (0°, 25°, 30°, 35°, 45°, 60°) for MD analysis. To explain frictional dependency on indents' pattern, we believe as the density/congestion of the atoms increases under the tip, the tip follows any morphological changes in the substrate more swiftly. Or in other words, the link between the substrate and the tip becomes rigorous. Such was the reasoning in the number of layers case. As the density of atoms increases under the tip by any technique, the volume of the HOMO orbital becomes more distributed between Mo and S atoms (Figure 3.11), which

helps form the bonded/non-bonded interaction between the substrate and tip. Out of four cases considered in this work, we had observed such behavior only in two, i.e., the number of layers and pattern of indents. That means there was a critical value of density of atoms, below which the rigidity of bonding between substrate and tip was not rigid enough to "lock" the substrate with the tip. Studying the value of that critical volume of atoms is beyond the scope of this article, nonetheless we want to acknowledge that such a threshold shall exist. In this case, the rigidity of the bonding may be so strong that we had observed almost constant average forces along X, Y, and Z-axes. Which was only the Y-axis average force in the subcase of the number of layers increase due to lower rigidity compared to the pattern change case. As the pattern angle was increased, the overlap between the indents increases. This results in a higher density of atoms than usual under the tip, which makes the volume of the HOMO orbital moderately bigger and intricately intervened between Mo and S atoms than the one obtained in the highest number of layers, i.e., 4 layers, subcase. This phenomenon was attributed to the constant value of the average Y-axis reaction force (as in the case of the number of layers subcase) in addition to X and Z-axes reaction forces.

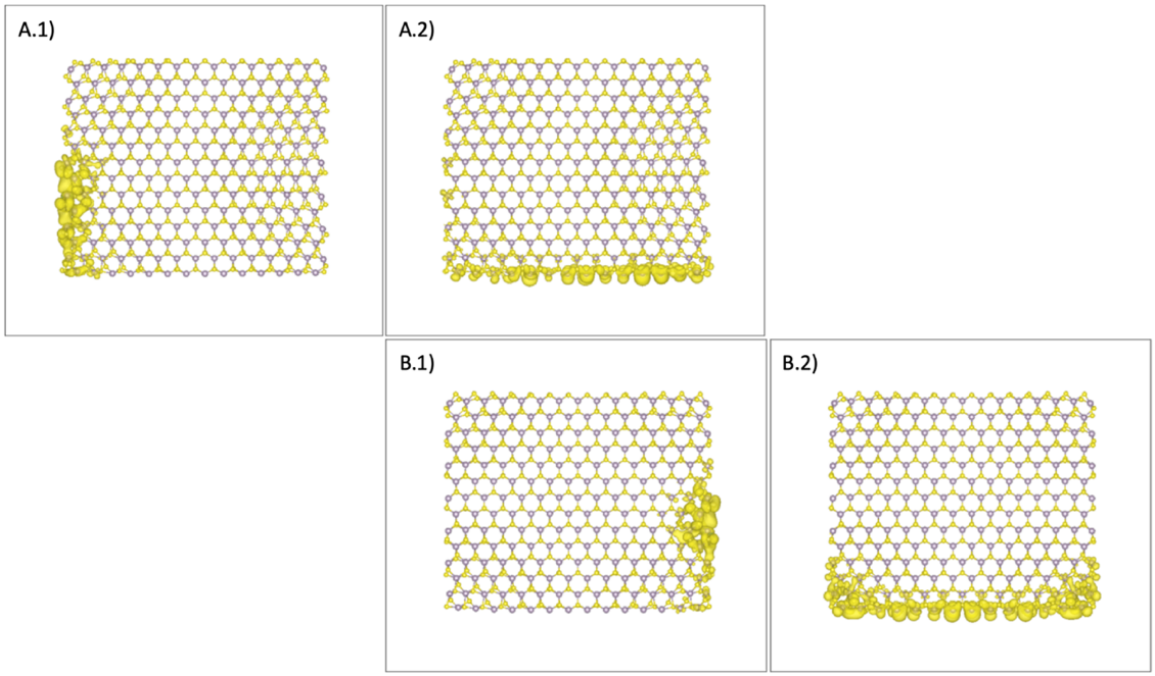

Figure 3.11 Molecular orbitals of indents' pattern sub-case. A), and B) shows the Θ=0°, 25° sub-cases, respectively. 1s(left) are HOMO and 2s(right) are LUMO iso-surfaces.

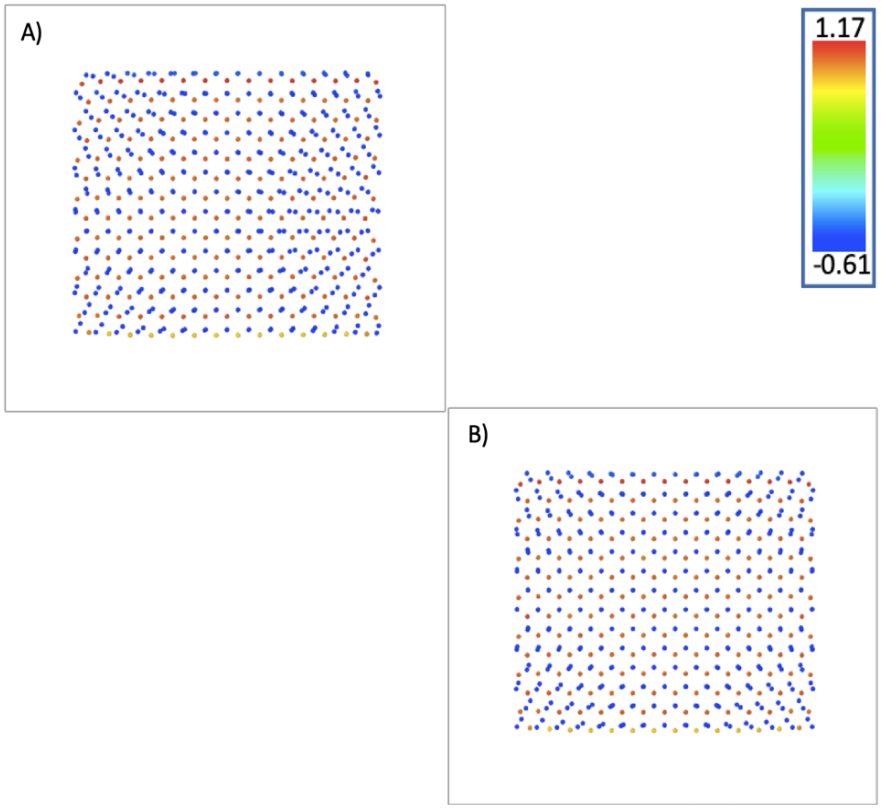

Figure 3.12 Bader charge transfer of indents' pattern sub-case. A), and B) shows the Θ=0°, 25° sub-cases, respectively. Ligand with its end values is visible in right top corner in eV.

We observed weak correlations on X, Y, and Z-axes torques; however, since forces are what causes the moments and hence torques, and there was an almost constant correlation for all three reaction forces, the probability of formation of correlations in the moments charts was significantly less. That makes a sturdy rationale that the weak patterns observed in the torque charts were not due to the correlations in the force data rather they were due to the data's noise due to the tip's wobbling motion. As the angle increases, the HOMO iso-surface volume diffused more evenly (Figure 3.11), and the probability of bond formation improves, which results in the counter movement for every active movement by the tip on the substrate. If there were negative Y-axis forces on the tip while ascending an indent, the equal and opposite force shall also present while descending the same indent. This suggests "hysteresis loss" was reducing as the pattern angle increases. The same argument can be made for forces along the X and Z-axes. This results in the average X, Y, and Z-axes forces and their respective moments/torques being constant. On the contrary, if we consider the range of Bader charge analysis, i.e., 1.78 eV (Figure 3.12), which was around 1-33% of the significant correlation subcases, i.e., radius and number of indents, respectively, it was equally justifiable to consider another rationale. That states the tip was displaying non-significant Y and Z-axes force correlation with the input parameters because the weak interlocking between the layer and tip instead of strong interlocking subjected to a counterbalancing movement for any given reaction along Y and Z-axes resulting in almost flat correlation on Y and Z-axes force plots or noisy correlation at best. With the Bader charge transfer analysis and the MD-based force plots data, our belief was skewed towards later rationale instead of the former, i.e., the tip was in weak interaction with the layers system.

3.4 Conclusion

In this study, we had performed atomic and electronic dynamics analysis to study the impact of morphological and thickness changes of a MoS_2 layered system on its tribological properties. We had considered 4 different cases, i.e., number of layers (1-4 layers), number of indents (2-8 indents), the radius of indents (12Å, 16Å, 20Å, 24Å), and pattern of indents (0°, 25°, 30°, 35°, 45°, 60°) resulting into 18 subcases in total. We used the LAMMPS MD code to model the movement of a tip over the surface of the MoS_2 system. The tip route was chosen in such a way to cover most of, if not all, the critical points covering the structural changes that appear as different systems were considered for analysis. Using the in-build algorithms in LAMMPS, we obtained torque and force experienced by the moving tip about and along X, Y and Z-axes, respectively. We had mainly focused on the Y-axis component of force experienced by the tip, either directly or indirectly. Since the highly stochastic stick and slip nature of the tip's motion results in significant noise in the data, we had averaged the data across the whole production MD run for each of the 18 subcases. It were these averaged values that we had based upon our complete analysis. From MD results, we observed that changing the radius and number of indents in a MoS_2 was the most effective way of tuning the frictional characteristics. MoS_2 layer tends to offer higher friction to a moving object along the armchair direction as the radius of indents increases and tends to provide lower friction as the number of indents increases. While changing the number of layers and pattern was the least effective way.

Additionally, we had performed ab-initio (VASP) based Bader charge transfer and molecular orbital analysis (HOMO LUMO) to find the rationale behind the results obtained in the molecular dynamics phase. Since the system's size varies from 15,859

atoms (smallest systems-1layer) to 60,859 atoms (biggest system-4layers), even the smallest system was too big to be analyzed in ab-initio code, the structures need to be trimmed. In the ground-state study phase, our analysis shows that as the number and radius of indents increase, the number of stretched bonds in the systems increases. Consequently, the volume covered by the HOMO iso-surface increases, and that of LUMO decreases. That makes higher area/volume available to lose/share charge carriers, resulting in stronger interlocking between layers and tip. From the BSE calculation, we had observed that not only the excitons were being formed, they were being formed across the interface of layers' surface and tip, i.e., interfacial excitons, which results in stronger interlocking despite the decrease in the LUMO iso-surface's volume. We believe these interlayer excitons result in higher average Z-axis reaction forces for the indents subcase and lower for the indents radius subcase as the number of indents and indents' radius increase. It further results in a decrease and increase in frictional forces exhibited for the number and radius of indents cases, respectively, since frictional force is the function of a surface's normal reaction (Z-axis). In the last phase of the study, we performed excited state analysis using BSE for an over-simplified replica of the number of layer subcases due to higher computational cost otherwise. As the number of layers increases, the electrons of a given electron-hole pair were delocalizing over a larger area resulting in weaker interfacial bonds. On the other side, the increase in the layers also increases the excitonic energy, resulting in stronger couplings that counterbalance the weaker interfacial bonds, and neither a significant increase nor a major decrease in the frictional force was observed as the number of layers was increased.

CHAPTER 4

DRUG REPURPOSING FOR SARS-COV-2: A HIGH-THROUGHPUT MOLECULAR DOCKING, MOLECULAR DYNAMICS, MACHINE LEARNING, AND DFT STUDY

4.1 Introduction

A worldwide global health emergency is posed due to a novel coronavirus(SARS-CoV-2) that is said first to appear and spread from Asia[132]. The World Health Organization (WHO) declared it as Public Health Emergency of International Concern(PHEIC) on 30th January 2020[133]. There are similar viruses that emerged in 2003 and 2012, known as severe acute respiratory syndrome coronavirus (SARS-CoV) and middle east respiratory syndrome coronavirus(MERS-CoV), respectively[134]. The new SARS-COV-2 causes a mortality rate of 2%-5% by causing severe acute respiratory syndrome(SARS)[135]. So far, there are known to be seven strains of human coronaviruses, which are broadly classified into two categories, i.e., Alpha coronaviruses and Beta coronavirus[134]. The Alpha coronaviruses are as: 229E, NL63 and Beta coronaviruses are OC43, HKU1, SARS, MERS, SARS-CoV-2. Until the SARS-CoV-2, the SARS and MERS were pathogenic strains with the highest mortality rate of 10% and 36% as per WHO[136]. The causative agent of COVID-19(Coronavirus disease-19) is a positive-sense single-stranded ribonucleic acid (ssRNA) virus encoding multiple proteins[137]. These proteins can be broadly classified into structural and non-structural proteins. The structural proteins include Nucleocapsid(N), Envelope(E), Spike(S), and Membrane(M) proteins. Non-structural proteins include non-structural protein 1-16, i.e., NSP1-NSP16. These proteins play a vital role in the functioning of the SARS-CoV-2, some more than others.

Consequently, some of these proteins are considered a potential target for full or partial inhibition of the SARS-CoV-2[138]. Inhibiting the SARS-CoV-2 by this approach will result in bio-molecules called drugs, and the procedure is known as drug therapy. However, the structures of these proteins can be modified to deactivate their functionality by using 2-dimensional materials-based devices, i.e., MEMS/NEMS[139]. These approaches are still in the proof-of-concept stage. At the pandemic's beginning, several research efforts resulted in publications citing already proven drugs for other viruses, i.e., Remdesivir, Ivermectin, Chloroquine, Hydroxychloroquine, Lopinavir, Azithromycin, Ritonavir as effective drug therapy for SARS-CoV-2[140]. However their clinical efficacy has been under question in lab trials containing a broader range of patients[141]. That motivated the researchers to reposition other drugs as improved drug therapy with constant efficacy. However, performing in-vivo experiments with new drugs is a very time-consuming and expensive way for drug repositioning. Discovering a new drug altogether can take more than a decade. That is why most in-vivo analyses preferred to focus on in-silico drug repurpose/repositioning before entering the in-vivo phase.

To take it one step further, different in-silico(computational) approaches are advised for drug repositioning/repurposing study[142]. The only constraint is the power of the fastest computer available globally. Agreeably, the results will not be as accurate as those obtained in the in-vivo studies. Nevertheless the trade-off between speed/money and accuracy justifies the efforts, especially when time can be sped up, i.e., the amount of time it takes to analyze 1000 drugs for repurposing in-silico is a fraction of what it takes for in-vivo studies of the same number of drugs. The number of drugs in the sample set can reach millions or even billions in in-silico studies which is unheard of in the case of in-vivo

studies[143]. Multiple in-silico studies were carried out for the given advantages, targeting one set of proteins in SARS-CoV-2 more than the other.

We started with 242,000 ligands from the ZINC database[144]. The database was selected to include ligands approved by FDA USA and match the LogP and weight of the previously partially successful candidate drugs i.e. Remdesivir, Ivermectin, Chloroquine, Hydroxychloroquine, Lopinavir, Azithromycin, and Ritonavir. Since working with an incorrect binding site even with the correct ligand can severely weaken the approach's efficacy, so we spend rigorous efforts to carefully select the binding sites solely based upon previous experimental studies instead of following an in-silico algorithm-based blind binding-site search. We had identified nine unique binding sites on six different proteins with ZINC ID as follows: 6LU7, 6M0J, 6M71, 6W9C, 6W63, 7BV2 and corresponding binding sites as follows: main protease/inhibitor N3, spike receptor-binding domain, RNA-dependent RNA polymerase, papain-like protease, main protease/inhibitor x77, and nsp12-nsp7/8 complex, Remdesivir and RNA binding sites of SARS-COV-2 system. Based upon docking and ADMET results, we have filtered down the sample set to 18 ligands, i.e., two ligands per binding site. From which, three ligands (ligand 12^{th}, 13^{th}, 18^{th}) were finally selected based upon the results of MD analysis, i.e., less than 1Å RMSD. They all attack the same protein (7BV2) through different binding sites resulting in multi-binding-site inhibitors. Further, we performed a multi-scale analysis by rationalizing the RMSD and hydrogen bonds formed with the electronic structure analysis obtained from ab-initio approaches. This conclusively proves that the ligand with low RMSD in complex tends to display a direct correlation between their hydrogen bond formations in complex form and the volume covering the frontier molecular orbitals (FMOs) and charge transfer potential

of atoms within that region. The same results were corroborated by using Molecular Mechanics Poisson-Boltzmann Surface Area (MMPBSA) derived free energy modeling and machine learning-based FMO energy gap values.

4.2 Models and Methodology

Our literature survey identified four unique binding sites on protein 7BV2 totaling nine unique binding sites spread over six proteins for the chosen set of 242000 ligands (Figure A.20 in Appendix A). Table B.6 (Appendix B) depicts the relationship between the complex/ligand/protein number used in this work and the complex/ligand/protein's standard identity. Additionally, we have used the same pipeline on Remdesivir in 7BV2 protein as a controlled experiment. Similar to other complexes, the system seems to be stable from 40 to 100 ns of the production run, and we have considered this part of the trajectory to measure the various MD parameters. This study is broadly divided into three major steps. Step-I performs molecular docking modeling, step-II performs molecular dynamics simulations of the filtered ligands in step-I. Step-III is an electronic structure study of the ligands used in step II and explains the ligands screened out in step-II. It must be highlighted that these three major steps are also associated with minor steps. Before performing step-I, all six proteins were minimized using a molecular dynamics code called YASARA software[145]. YASARA web-server supported by YASARA force fields[146] was used for this minor step and YASARA view for visual inspection[147]. Subsequently, performing high throughput screening-molecular docking of 242,000 ligands on nine different binding sites of 6 unique proteins resulted in more than 2 million distinctive binding-site/ligand combinations using AutoDock Vina software[148].

The top 10 ligands were chosen based upon the least binding energy calculated by the molecular docking method of Step-I. Multiple ligands appear in more than one complex's top 10 ligand list. This proves the robustness of the framework chosen in this study. Subsequently, only two ligands were picked from this list of 10 ligands. The absorption, distribution, metabolism, excretion, toxicity (ADMET) analysis was performed for all ten ligands. The first preference was given to the ligands that show zero violation of LIPSINKI's rules. For non-zero LIPSINKI's rules violations under a given ligand, there were either 1 or 2 violations that were both treated with the same preference, provided that the range from 1^{st} to 10^{th} ligand's binding energy was small for almost all the nine binding sites. In that case, simply the first and second ligand in order of their binding energy sequence was chosen for the next step, i.e., Step II.

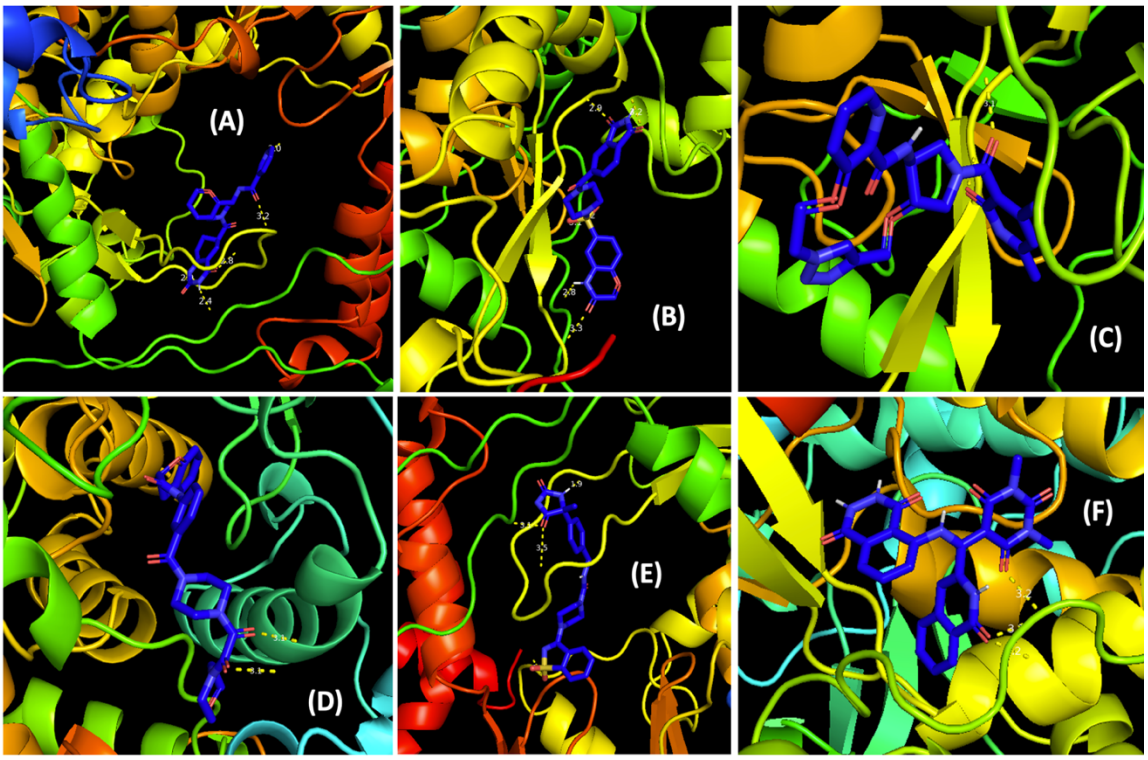

Figure 4.1 Docked complexes of ligands having extreme RMSD. (A, B, C) Lowest RMSD sub-group: 12th, 13th, and 18th ligands, (D, E, F) Highest RMSD sub-group: 5th, 11th, and 14th ligands. Proteins and ligands are shown in cartoon and sticks representation, respectively, with hydrogen bonds highlighted with dashed lines labeled with bonds lengths.

For Step II, molecular dynamics simulations were performed using AMBER20 code[149]. All the complexes were minimized before heating, equilibrating, and finally, a production simulation of 100 ns. In the analysis phase of Step II, root mean square distance (RMSD), root mean square fluctuation (RMSF), hydrogen bond analysis, solvent accessible surface area(SASA) of ligands, and radius of gyration (RoG) of protein and ligand was performed by using the CPPTRAJ[150] utility and python scripts associated with package AMBER20. Furthermore, MMPBSA.py subroutine was used to perform Molecular Mechanics Poisson-Boltzmann Surface Area (MMPBSA) free energy analysis of the complexes. We have selected three ligands with the highest RMSD (high RMSD subset) and three ligands with the lowest RMSD (low RMSD subset) for further in detail

investigation (Figure 4.1). In step III, VASP[151] was used to perform the following analysis: Bader charge[152], Highest occupied molecular orbital(HOMO), lowest occupied molecular orbital(LUMO), molecular electrostatic map(MEP). In addition, quantum chemical characteristics were calculated, which are various functions of HOMO and LUMO energies. Most of the analysis and discussion is focused on the high RMSD and low RMSD ligand subset while discussing the rest of the complexes when necessary.

4.2.1 Ligands and Proteins Preparation

We have downloaded all six protein structures from the RCSB protein data bank[153]. After downloading the structures, they were processed in the UCSF Chimera package[154]. All hetero-atoms were removed, i.e., co-crystallized ligands, ions, water molecules. In the case of multi-binding site protein 7BV2 protein, we removed the co-crystallized ligands/molecules based upon the binding site. For example, we pulled co-crystallized RNA strands to use the binding site of the RNA strand as the binding site of the potential ligand. We kept the RNA strand intact in the case of using the interface of NSP12/7 or NSP 12/8 as the binding site of the potential ligand. There is one exception to the framework of removing one co-crystallized molecule while keeping the other. Since this protein has Remdesivir co-crystallized, it was trimmed in case of using any four of the binding sites available on the protein for the potential ligand. This exception was made because out of four binding sites available on the protein 7BV2, only one binding site has the co-crystallized molecule, which works as an inhibitor, i.e., Remdesivir.

To avoid the existence of the dual molecules crystalized with the protein, which can act as an inhibitor, we removed Remdesivir from all four “allotropes” of protein 7BV2. Since the proteins had gone through trimming, which may lead to dangling bonds or steric

clashes between the chains, they were minimized using the conjugate gradient method implemented in YASARA. The proteins were minimized until the YASARA's Z score was achieved within an acceptable tolerance for all nine binding sites. Consequently, a thorough literature survey was conducted to find the binding sites of the proteins from experimental studies all over the world. Following the proteins minimization, a Linux bash shell script was developed to be used on the XSEDE supercomputing machine[155] to execute high throughput virtual screening in step-I, as described above. The ligands were not minimized before high-throughput screening since their structure was not modified as in the case of proteins. This drastically reduces our computational requirement and makes it feasible to perform molecular docking on 242,000*9= 2.178 million unique combinations of a protein-binding site and a ligand.

4.2.2 Molecular Dynamics

After completion of Step-I, two ligands were picked for all nine proteins. Those 18 combinations were processed through Step-II, i.e., Molecular Dynamics simulation. We used AMBER20 software for the MD simulations. The tasks performed in step II were minimization, heating(1ns), equilibration(10ns), production run(100ns), followed by post-production analysis. For the minimization run, we performed 10,000 steps. First, we computed 5000 steps of the steepest descent method followed by 5000 steps of the conjugate gradient method. For heating, we raised the temperature in a stepwise manner. In the first step, the temperature was increased from 0°C to 100°C during 0.3 ns followed by 100°C to 200°C during the next 0.3 ns before throttling it to the final 300°C for the remaining 0.4 ns. The last leg contains additional 0.1 ns compared to the 1st and 2nd leg of 0.3 ns to compensate temperature rise from a point which was highest among all beginning

temperatures among all three legs despite being raised by an equal amount, i.e., 100°C. A temperature coupling constant of 1.0ps was used for the heat bath for all legs. We used the NVT ensemble for this part of the MD step. For the equilibrium step, the system was equilibrated for 10ns with an NPT ensemble. This step helps stabilize the system while relaxing any compressed/stretched bonds raised due to the last stage of heating. Finally, the production run was implemented for 100ns with the NPT ensemble. Following settings applied for all MD simulations steps: SHAKE algorithm to constrain hydrogen bonds, step size of 2 fs, cutoff of 9.0 Å, restrain weight of 0.5. For MD analysis, we wrote every 1000^{th} frame to the trajectory file output of the production run of 50 million steps resulting in the trajectory file containing 50,000 frames. We performed the RMSD, RoG, SASA on every frame of the trajectory file and every 100^{th} frame for MMPBSA analysis. One frame should be considered equivalent to 2 fs for hydrogen bond analysis in this work.

4.2.3 Density Functional Theory

We used the VASP program to optimize the ground state geometries of all the 18 ligands before performing the ab-initio analysis. The density functional theory-based program used Becke3-Lee-Yang-Parr(B3-LYP) exchange functional, Lee-Yang-Parr (LYP) correlation functional with standard 6-311G basis set. The Koopman theorem was used for plotting the HOMO and LUMO of the ligands. Bader charge program was used to perform the atomic charge analysis[129]. Which was substituted for MEP maps highlighting the electron-rich and deficient areas at various points in the region surrounding the molecule and at equidistance from the molecular surface.

4.2.4 Drug-likeness Analysis

We used the SwissADME online web-server [156] to perform the drug-likeness analysis. Drug-likeness helps find the probability of a drug working as an oral consumption drug based upon its bioavailability. It is solely based upon the physicochemical and structural characteristics of the compounds. It is general practice in the pipeline for computer-aided drug design to screen the compounds according to pharmacokinetics. The SwissADME server gives access to five filters for drug-likeness screening based upon five unique methodologies to filter out the drugs based upon pharmacokinetics. Pharmaceutical companies mainly invented these filter methods to better their drug discovery pipelines. The five rules are Lipinski, Ghose, Veber, Egan, and Muegge; the corresponding inventor-corporation are Pfizer, Amgen, GSK, Pharmacia, and Bayer, respectively. Although all five filters can be used to find out the best combination for the given compounds, we primarily used Lipinski's rule of five. Since Lipinski's rule is the oldest among all five filters, it is most acceptable among the computational biology research community.

We considered Lipinski's rule as the primary filter and the remaining four filters as secondary collectively. Although we also measured the parameters from the rest of the four filters, their corresponding decision-making weight was less than Lipinski's rule. Lipinski's rule was over-ridden only when we encountered a severe breach of secondary filter for a given compound. In addition to the drug-likeness screener, we considered the following screeners supported by the same web server: Physicochemical properties, Lipophilicity, water-solubility, Pharmacokinetics, medicinal chemistry. Out of these, only drug-likeness was considered as the primary screener. Further, the Lipinski rule was regarded as the primary drug-likeness filter. Lipinski rule evaluates a compound based on

pharmacokinetics, absorption, distribution, metabolism, excretion. It has the following selection criteria: molecular mass is less than 500 daltons, octanol-water partition coefficient(logP) does not exceed 5, hydrogen bond donors(HBD) is less than 5, hydrogen bond acceptors(HBA) is not more than 10.

4.2.5 Machine Learning

We used GNN (graphical neural network) with two layers based upon Battaglia equations [157] using an applied ML book[158]. These equations are mostly used for bio-molecules training. The model was trained on a dataset known as QM9[159] containing 134,000 molecules/ligands/inhibitors/compounds. This neural network converts the distance between the atoms to an inverse pairwise distance. This inverse pairwise distance acts like the edges of the "graph" in Graphical Neural Network. It fits well with the framework that more weightage is assigned to the atomic pairs having less distance than atomic pairs having comparatively more distance to mimic the conditions of the more interaction between the atoms involved in the former case than the latter. Moreover, the limit conditions need to be satisfied, i.e., the weights shall never be zero and infinity. The model is designed so that the inverse pairwise distance cannot be zero and infinity. Our model is tweaked to assign zero weights if the pairwise inverse distance crosses a threshold. That is equivalent to assigning a cutoff value for force-field-based classical molecular dynamics approaches[73][160][161][162].

4.3 Results and Discussion

In the following in-depth discussion, Table 4.1 can be used as a reference aid in understanding the dependability among different parameters investigated in this work and discussed in the upcoming sections.

Table 4.1 Proportionality of Different Investigated Parameters with RMSD

Property	**Relationship with RMSD**
DFT parameters	
HOMO-LUMO gap (reactivity and stability)	Directly proportional
Ita (hardness)	Directly proportional
Omega (electrophilicity)	Inversely proportional
Sigma (local softness)	Inversely proportional
Zita (electronegativity)	Inversely proportional
MD Parameters	
Protein RoG	Directly proportional
Ligand RoG	Inversely proportional
SASA	Inversely proportional
Binding free energy of complexes	Directly proportional

4.3.1 Drug-likeness Analysis

We passed the top ten ligands sorted according to the binding energy obtained from the molecular docking analysis from each of the nine binding sites of six proteins through the SwissADME web-server[156] and then picked the two ligands from each of the binding

sites. The selection criteria were the binding energy and violation of Lipinski's rules. We made the following observations during this sub-step: 1) a violation of Lipinski's rule (if any) is not more than one; 2) only one protein(6M0J) does not have at least one ligand with zero Lipinski's violation; 3) two proteins (7bv2_nsp12-7 and 7bv2_rna) with only one ligand with zero Lipinski's rule violation. Except for the above-highlighted cases, every other case has at least two or more ligands with zero Lipinski's rule violations. This accounts for the efficacy of the drug discovery pipeline chosen in this work. Furthermore, in multiple cases, the same drug demonstrated good binding potential to various proteins in a selected set of nine unique binding sites from six proteins. For example, the compound ZINC000750965621 is present in the top 10 best binding ligands list of protein 6M0J and 7BV2_rna. Similarly, drug ZINC000587983851 is showed up in the list of 6M0J and 6M71_nsp_12_7_8. Such drugs may have a higher potential to be selected in the final pool of drugs to be synthesized, given they can target more than one binding site, increasing their inhibition ability. However in our cases, the binding energy of both the above drugs was less than the binding energy of other drugs having 0 Lipinski's rule violation, so we could not select these drugs for those proteins/binding sites, given the already specified rules.

4.3.2 Molecular Dynamics Study

4.3.2.1 RMSD Analysis. Following three ligands exhibit the least RMSD (<1Å) – Ligand 12th, 13th, 18th i.e. 7BV2_nsp12-7/ZINC001176619532, 7BV2_nsp12-8/ZINC000517580540, 7BV2_rna/ZINC000952 855827 as 0.6Å, 0.45Å, and 0.5Å, respectively (Figure 4.2). Since all the sub-1Å RMSD ligands docked to the same protein 7BV2 through different binding sites, future in-vivo tests shall be done in this protein, at least for selected ligands in this work. The HETAOMS removed in the first, second, and third cases are interaction sites of NSP12-7 interface (7BV2_nsp12-7), NSP12-8 interface(7BV2_nsp12-8), and template-primer RNA(7BV2_rna). Figure A.21-A.22 in Appendix A depicts the RMSD analysis of the rest of the complexes. Similarly, we selected a set of 3 ligands with the highest RMSD to juxtapose against the earlier set of least RMSD ligands. These ligands are 5th, 11th, 14^{th,} i.e., 6m71_nsp12_7_8 /ZINC000410177506, 7bv2_nsp12-7/ZINC000616537204, and 7bv2_nsp12-8/ZINC001180048431 with RMSD as follows: 4.1Å, 2.05Å, and 1.9Å. In this work, we had primarily discussed hydrogen bonding among all bonded interactions. However, we performed calculations considering all kinds of interaction a biological system undergoes, i.e., van der Waal, Coulomb interactions in MMPBSA analysis, etc.

We observed that a ligand tends to have lower RMSD if it: a) forms a greater number of hydrogen bonds with the binding site residues and b) maintains those bonds for longer simulation time. Among least RMSD sub-group, ligand 12 have RMSD of 0.6Å primarily because of stability acquired by forming a hydrogen bond with residues PHE362 through terminal pyrimidine as shown in 1st circle and ALA467 and ALA470 through hexahydroindan and double-bonded oxygen as shown in 1st and 2nd dip in 2nd circle in

Figure 4.3(a). Correspondingly, very high charge transfer values (Figure 4.8A) and HOMO/LUMO orbitals iso-surfaces (Figure 4.10A) over ligand can be seen in the region containing these residues, i.e., PHE362 and ALA470. The second ligand in the least RMSD sub-group is ligand 13, with an RMSD of 0.45Å. It forms hydrogen bonds with ALA478, THR485, ASN417, ASN 427, GLN461, ASN463. All these residues were encapsulated using a single closed curve in Figure 4.3(B). Out of all hydrogen-bonded residues, only ASN 427, GLN 461, ALA 478, ASN463 are covered by the iso-surfaces of HOMO/LUMO and extreme charge transfer values as shown in black closed curves in Figure 4.8(B) and Figure 410(B), respectively. The last ligand of the least RMSD sub-group is ligand 18, with an RMSD of 0.5Å. This ligand forms hydrogen bonds with THR485, ARG489, SER484 (first circle in Figure 4.3c), and ALA60 (highlighted by the second circle in Figure 4.3c). Furthermore, we observe a direct correlation of these hydrogen bonds formation with ab initio analysis (Figure 4.8c and Figure 4.10c), which further proves the rationale of these bonded interactions for the lower RMSD of these ligands.

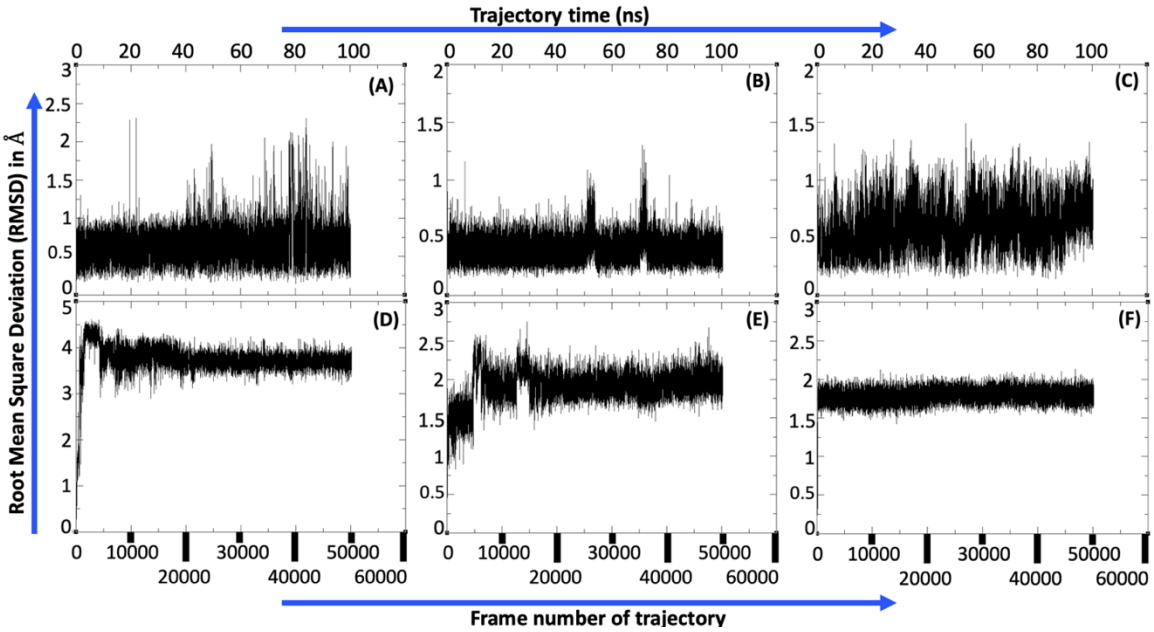

Figure 4.2 Root Mean Square Deviation (RMSD) of ligands having extreme RMSD. (A, B, C) Lowest RMSD sub-group: 12th, 13th, 18th ligands. (D, E, F) Highest RMSD sub-group: 5th, 11th, 14th ligands. The X-axis shows the frame number(bottom) and trajectory time(top) of the production run, and the y-axis is RMSD (Å).

Among the high RMSD ligand sub-group, ligand 5 has an RMSD of 4Å and significantly fewer bonded interactions with the protein binding site. The ligand has two sites for hydrogen bonds, i.e., ARG291 and PHE338. Both bonds are neither stable nor high frequent bonds (Table 1a). It can be attributed to comparatively less HOMO/LUMO iso-surfaces volume and lower extreme charge transfer values, as highlighted by closed black curves superimposed on Figure 4.8D and Figure 4.10D. The next ligand in the high RMSD group is ligand 11, with an RMSD of 2Å. This ligand has the largest number of hydrogen bond sites, where the bond exists for more than 1000 frames. It is ranked number 2 (according to RMSD) in the high RMSD ligand sub-group. We believe this complex exhibits this behavior because although the number of 1000s frames with hydrogen bond sites is five times the other ligands, it cannot retain those hydrogen bonds for an extended period. For example, the longest hydrogen bond in this ligand exists for 5634 frames (Table

4.1a), while this number is 30,000 frames on average (Table 4.1b) for the ligands in the low RMSD sub-group. This seems to be the primary reason for the high RMSD of this ligand in the complex.

The last ligand from the high RMSD sub-group is ligand 14 with 1.9Å RMSD. This ligand has every profile of a ligand belonging to the low RMSD sub-group, because of which it has the least RMSD among its sub-group. However there is one difference in terms of the HOMO/LUMO iso-surfaces region, i.e., as oppose to a ligand from the low RMSD sub-group, the HOMO/LUMO iso-surfaces of this ligand are not overlapping (Figure 4.10(F)). This makes it comparatively less stable in the binding site. The HOMO iso-surfaces cover the extreme right N-N bond edge of tetrahydro-3,6-pyridazinedione of 3,4-Diazabicyclo[4.4.0]decane-2,5-dione terminal, and LUMO iso-surfaces covers the 2,4(1H,3H)-Pyrimidinedione, dihydro-1,3-dimethyl attached in the middle of the ligand chain between azadecalinone and tetrahydro-3,6-pyridazinedione of 3,4-Diazabicyclo[4.4.0]decane-2,5-dione.

4.3.2.2 RMSF Analysis. We have focused on the RMSF of only those residues within 5 Å distance from the ligands. Those residues were identified and visually inspected (Figure A.34 in Appendix A) by PyMol, and investigated with the RMSF plot of that complex as generated by AMBER20's CPPTRAJ utility. For Ligand 12, the residues selected are VAL 330, HIS 359, PHE 360, PHE 361, PHE 362, ALA 363, GLN 364, LYS 465, TYR 466, ALA 467, ILE 468, SER 469, ALA 470, LYS 471, ASN 472, ARG 473, ALA 474, ARG 475, GLU 731, SER 734, ARG 756. All residues belong to main chain A of the protein.

For complex ligand 13, the selected residues are VAL 415, ASN 417, LEU 418, LYS 420, SER 421, ALA 422, ALA 432, TYR 436, GLN 461, MET 462, ASN 463, LEU 464, LYS 465, TYR 466, VAL 477, ALA 478, GLY 479, VAL 480, SER 481, ILE 482, THR 485, ARG 489, SER 602, GLY 603. All residues belong to main chain A of the protein.

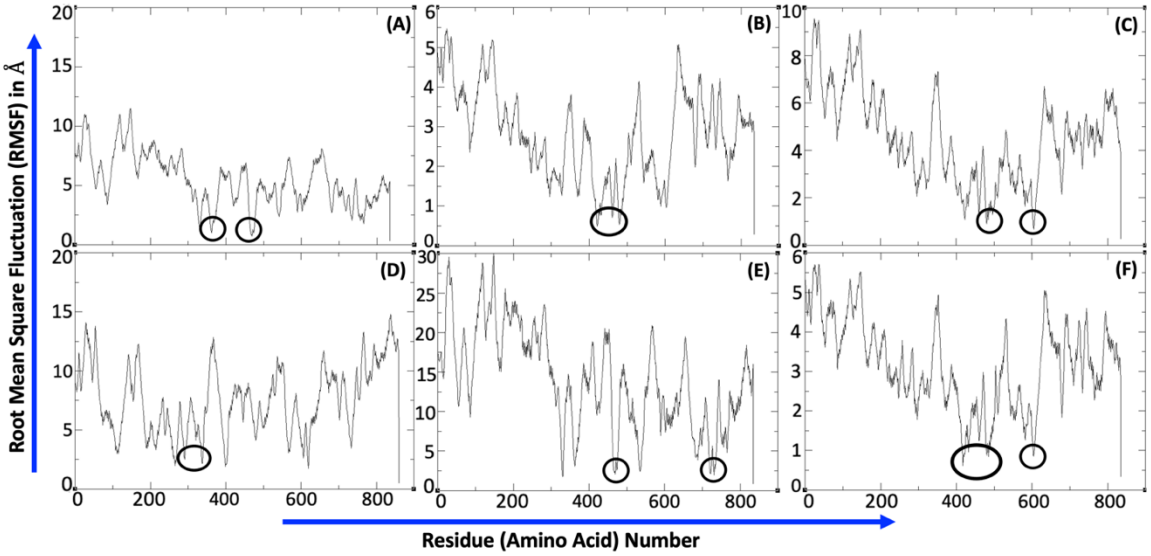

Figure 4.3 Root mean square fluctuation of ligands having extreme RMSD. (A,B,C) Lowest RMSD sub-group: 12th, 13th, 18th ligands. (D, E, F) Highest RMSD sub-group: 5th, 11th, 14th ligands. The X-axis shows the residue identification, and the y-axis is RMSF (Å).

For complex ligand 18, the following residues are selected- LYS 420, SER 421, ALA 478, GLY 479, VAL 480, THR 485, ARG 489, GLN 493, LEU 496, SER 602, GLY 603, ASP 604, ALA 605, ALA 608, TYR 609. All residues belong to main chain A of the protein. Figure A.23-A.24 (Appendix A) depicts the RMSF plots of the rest of the complexes.

The above-selected residues having hydrogen bond with ligands shows the least RMSF within corresponding selected ligand-protein complexes, i.e., ligand 12, 13 and 18 with the RMSF of 5.1 Å, 1.5 Å, and 2.2 Å. Furthermore, Figure 4.3 shows the RMSF plot for all low and high RMSD subset ligands with superimposing black closed curves

highlighting the residues forming the highest number of hydrogen bonds with the protein as determined by hydrogen bond analysis (described in next section). Among the low RMSD subset, the ligand 12 forms hydrogen bond for 2510 and 26418 frames with the N and O atoms of residue 2-Amino-3-phenylpropanal (PHE 362), respectively. Ligand 13th forms hydrogen bond for 679, 18673, 32391 frames with residues 3-Amino-4-oxobutanamide (ASN417), 2-Amino-3-oxobutanal (THR 485) and Propanal, 2-amino- (ALA 478) residues, respectively. Ligand 18th maintained hydrogen bonds for 25023 and 29790 frames with Propanal, 2-amino- (ALA 605), and 2-Amino-3-hydroxybutanal (THR 485) residues.

Among the high RMSD subset, ligand 5th has 6 and 8 hydrogen bonds with 2-Amino-3-phenylpropanal (PHE 338) and 2-(4-Amino-5-oxopentyl)guanidine (ARG 291) residues, respectively. Ligand 11th holds hydrogen bonds for 4031 and 15573 frames with Propanal, 2-amino- (ALA 467), and 2,6-Diaminohexanal (LYS 718) residues, respectively. Ligand 14th forming hydrogen bonds for 7510, 23435, 32130 frames with 2-Amino-3-(4-hydroxyphenyl) propanal (TYR 436), Propanal, 2-amino- (ALA 478), 2-Aminoacetaldehyde (GLY 603), respectively. The above information is used from the next section, and it shows justification of the RMSF characterization. Low RMSF residues have a relatively higher number of hydrogen bonds for stability, resulting in lower fluctuation than other residues of the protein.

4.3.2.3 Hydrogen Bond Analysis. We calculated the hydrogen bonds formed between the ligand and the protein using the hydrogen bond CPPTRAJ tool in the AMBER20 package. Consequently, we sorted out the output by the number of hydrogen bonds formed. Then we trimmed the data to show the highest among the following in Table 4.2a and 4.2b: (i) bottom-most five lines or (ii) the number of lines having hydrogen bonds existing over 1000 frames or (iii) the number of lines having the highest lifespan of a hydrogen bond in that complex to be visible in the selection.

Table 4.2a Calculated Hydrogen Bond Statistics for High RMSD Ligand Subset

Longest Lifespan	**Total Frames**	**Atoms/Residues Identity**
5th Ligand		
1	6	LIG_860@O4-PHE_338@N-H
1	8	LIG_860@O3-ARG_291@NH2-HH21
11th ligand		
132	1164	LIG_835@O2-SER_734@OG-HG
26	1235	LIG_835@O2-LYS_718@NZ-HZ3
30	1361	LIG_835@O2-LYS_718@NZ-HZ2
3	1612	SER_469@OG-LIG_835@N-H
9	2201	LIG_835@O3-PHE_362@N-H
10	3260	ILE_468@O-LIG_835@N-H
29	4031	ALA_467@O-LIG_835@N4-H1
28	4671	LIG_835@O1-LYS_718@NZ-HZ1
30	5268	LIG_835@O1-LYS_718@NZ-HZ2
32	5634	LIG_835@O1-LYS_718@NZ-HZ3
14th Ligand		
6	2590	LIG_835@O1-ASN_417@ND2-HD22
7	6132	ASN_417@O-LIG_835@N2-H
6	6593	LIG_835@O2-GLN_493@NE2-HE21
10	7510	LIG_835@O3-TYR_436@OH-HH
23	23435	ALA_478@O-LIG_835@N4-H2
25	32130	GLY_603@O-LIG_835@N5-H3

Table 4.2b Calculated Hydrogen Bond Statistics for Low RMSD Ligand Subset

Longest Lifespan	**Total Frames**	**Atoms/Residues Identity**
12th Ligand		
1	26	PHE_362@N-LIG_835@N1-H
2	108	LIG_835@O4-ALA_470@N-H
2	257	LIG_835@N2-ALA_467@N-H
4	2510	LIG_835@O3-PHE_362@N-H
19	26418	PHE_362@O-LIG_835@N1-H
13th Ligand		
13	319	LIG_835@O4-ASN_463@ND2-HD22
28	442	LIG_835@O3-ASN_463@ND2-HD22
8	570	LIG_835@O4-GLN_461@NE2-HE22
3	616	LIG_835@O3-ASN_427@ND2-HD21
3	679	LIG_835@O2-ASN_417@ND2-HD21
13	18673	THR_485@OG1-LIG_835@N2-H
20	32391	ALA_478@O-LIG_835@N3-H1
18th Ligand		
3	668	LIG_835@O4-SER_484@OG-HG
5	1060	LIG_835@O2-ARG_489@NH1-HH11
3	2340	LIG_835@N6-THR_485@OG1-HG1
18	25023	ALA_605@O-LIG_835@N1-H
28	27450	LIG_835@O4-THR_485@OG1-HG1

Table 4.2 displays hydrogen bond data among three columns. The first column is maximum lifespan, indicating the number of consecutive frames a hydrogen bond exists without breaking up between a given protein and ligand. The second column is the total number of frames the hydrogen bond exists between a given protein and ligand despite being non-consecutive frames. The third columns provide information about the exact identity of atoms involved in the hydrogen bond formation from protein and ligand structure, i.e., donors, acceptors, the hydrogen atom. The data from the first two columns in Table 4.2 support the results obtained in the RMSD section. To restate, the low RMSD sub-group has ligands $12^{th,}$ 13^{th}, 18^{th} with 0.6 Å, 0.45 Å, and 0.5 Å RMSD, respectively. We have obtained almost the same order from the first two columns of hydrogen bond formation (Table 4.2b). For the following analysis, lines of a table shall be read in reference to Table(4.2a,b). In the 13^{th} complex, due to the 1,2-Cyclohexanedicarboximide and Piperazine, the bottom two lines (Table 4.1b) have 18673 and 32391 frames with 13 and 20 frames of maximum lifespan. Due to the Piperidin-3-one and carbonyl group in the 18^{th} complex, the bottom two lines have 25023 and 27450 frames with 18 and 28 frames of maximum lifespan, respectively. Lastly, for the 12^{th} complex, the bottom two lines have 2510 and 26418 frames with a maximum lifespan of 4 and 19 frames, respectively, through 4a,5,6,7,8,8a-hexahydro-1H-quinazoline-2,4-dione in the ligand. In addition to the number of frames for hydrogen bond existence, it is also essential to know the maximum amount of period, in terms of frames, that the same bond did not break.

For complexes 13^{th} and 18^{th}, both columns have a high number for the bottom two lines in Table-4.2b than the complex 12. After sorting, if the bottom two lines in Table-(4.2a,2b) show fewer frames for a given hydrogen bond and the lesser maximum lifespan,

that will reflect in the RMSD value of the ligand compared to protein. The former will be inversely proportional to the latter. Therefore, we have a high number in the bottom two rows for the 13th and 18th complex and a lower number for the 12th complex since the 12th ligand has the maximum RMSD among the subset of lowest RMSD cases. An almost similar correlation was observed in the high RMSD ligand subset. The RMSD of the 5th, 11th, 14th ligands is 4 Å, 2 Å, and 1.9 Å, respectively. For the 5th ligand, carbonyl group and hexahydroindan contributed to the bottom two lines in Table-(4.2a) to have 6 and 8 frames with 1 and 1 frames of maximum lifespan. For the 11th complex, the bottom two lines are 5268 and 5634 frames, with 30 and 32 frames as maximum lifespan, respectively, due to Sulphur attached hexahydroindan. For the 3,4-Diazabicyclo[4.4.0]decane-2,5-dione in the 14th complex, the bottom two lines are 23435 and 32130 frames, with 23 and 25 frames as maximum lifespan, respectively. Hence, the combination of the number of frames a hydrogen bond exists and maximum lifespan correlates well with the ligand RMSD observed for that complex in Figure 4.3. Table B.4 (Appendix B) enlists the hydrogen bond analysis of the rest of the complexes.

4.3.2.4 Radius of Gyration (RoG). RoG measures the spread of the mass of a given molecule around its geometrical central axis. Comparing the RoG plot of a ligand and the corresponding docked protein reveals two aspects: the average value's relative difference and the fluctuation range's difference. For the former, the ligand RoG has values around 4-6 Å, while for the latter, the RoG ranges between 39 Å to 51 Å among all the 18 complexes considered. On average, the fluctuation range for the ligand and protein RoG are about 0.2 Å and 0.07 Å, respectively.

4.3.2.4.1 RoG of Ligands. A ligand with RMSD less than 1 Å helps the docked protein maintain its RoG, i.e., less fluctuation. For all that, it will have less impact on decreasing the RoG of a protein if it already has high RoG in the first place, to begin with. To elaborate, the 2 out of 3 given complexes with the highest, i.e., 5th, 11th, and 14th complexes, are showing such behavior. We can observe sudden jumps in RoG values from 0-2000th frame (6.2 Å to 4 Å) for the 5th complex (Figure 4.4d) and then multiple jumps on the RoG plot for the 11th complex between 5000th and 15000th frames with the range of 6.4 Å to 5.4 Å (Figure 4.4e). We considered the 14th complex as an outlier. Despite having high RMSD, it does not show such sudden jumps on the RoG plot.

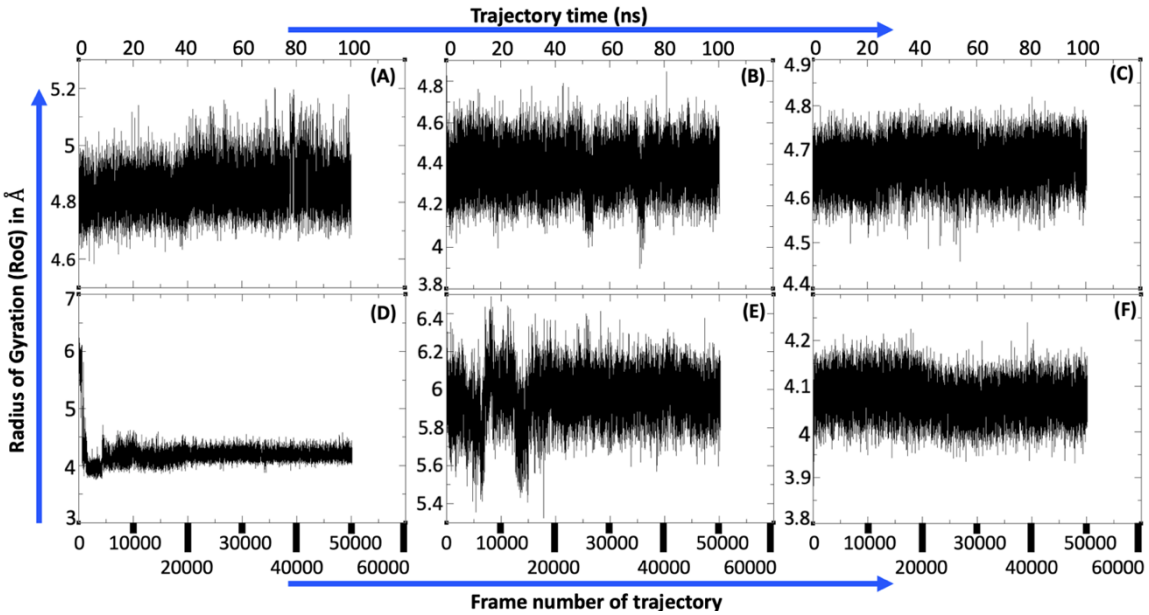

Figure 4.4 Radius of Gyration (RoG) of ligands having extreme RMSD. (A, B, C) Lowest RMSD sub-group: 12th, 13th, 18th ligands. (D, E, F) Highest RMSD sub-group: 5th, 11th, 14th ligands. The X-axis shows the frame number(bottom) and trajectory time(top) of the production run, and the y-axis is the ligand's RoG (Å).

The ligands with the least RMSD, i.e., 12th, 13th, 18th, show almost opposite behavior to those with higher RMSD ligands. There are no sudden jumps on the ligand RoG plots (Figure 4.4a, b, c) except a slight fluctuation for the 13th complex (Figure 4.4b).

However, we can consider it an outlier since the fluctuation only stays from 36000th to 37000th frames. Overall, for the three complexes with the lowest RMSD, the ligand RoG varies between 4.3 Å to 4.8 Å without any significant change in the RoG, i.e., step jump on the ligand RoG plot, during the production simulation. That indicates that the complexes' geometry remains stable, i.e., no drastic change in the distribution of the masses around the central axis. Furthermore, no drastic change in the complex's structure means no significant switch in the function of the complex since for biomolecules, their folding/unfolding dictates their behavior more than the atom constituting the biomolecule[163]. Figure A.25-A.26 (Appendix A) depicts the RoG plots of the rest of the ligands.

4.3.2.4.2 RoG of Proteins. We believe for proteins as well, it is more important to have a system with less RoG variation. The RoG of all 18 proteins has average values of around 50 Å (Figure 4.5), which is higher than the ligands. Therefore, we can follow the hypothesis mentioned above in all 6-complexes considered (3 high RMSD subset ligands+ 3 low RMSD subset ligands). Figure A.27-A.28 (Appendix A) depicts the RoG plots of the rest of the proteins. We have to follow the minimum protein RoG value to pick a winner. We hypothesize that a protein with higher RoG is less stable, which is not the case for ligands given a small range of RoG. For example, the protein RoG of the highest RMSD complexes subset is 50.25 Å, 48.75 Å, and 49.25 Å (Figure 4.5 d, e, f). The protein RoG values (Figure 4.5 a, b, c) for the lowest RMSD complexes subset are 48.80 Å, 49.35 Å, 49.25 Å. Here the sequence is the same as observed in the lowest RMSD subset order for ligand. Therefore, we perceive that the two of the complexes have the same value from high and low RMSD, while the 3rd complex has high RoG protein in case of the high RMSD sample

set and 3rd complex have low RoG protein in case of the low RMSD sample set. This helps us pick the winner because the set of complexes with the average high RMSD also have high average protein RoG, and the group of low average RMSD also has low average protein RoG.

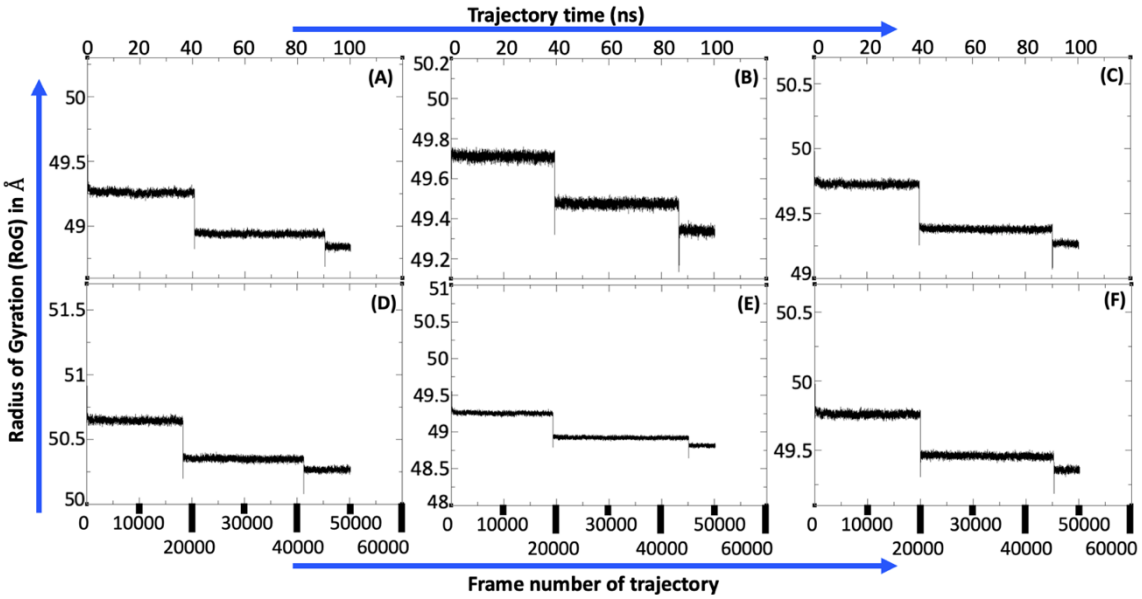

Figure 4.5 Radius of Gyration (RoG) of proteins' backbone having extreme RMSD. (A, B, C) Lowest RMSD sub-group: 12th, 13th, 18th ligands. (D, E, F) Highest RMSD sub-group: 5th, 11th, 14th ligands. The X-axis shows the frame number(bottom) and trajectory time(top) of the production run, and the y-axis is protein's RoG (Å).

4.3.2.5 Solvent Accessible Surface Area (SASA) Analyses. Solvent accessible surface area (SASA) measures how much fraction of the total surface area of the protein is accessible to the solvent. Since external molecules are integrated with solvent, the surface area exposure to solvent means exposure to external molecules. All SASA values are average SASA values observed over the entire MD production run of 100 ns. Usually, proteins have just high enough SASA to allow easy binding of a ligand/inhibitor except not higher, resulting in unstable protein. It means a fully unfolded ligand/protein along its backbone has the highest SASA among its conformations, albeit highest instability at the

same time. The ligands with the lowest RMSD, i.e., $12^{th,}$ 13^{th}, 18^{th}, do not have the highest SASA among all the complexes (Figure 4.6). Besides they have more than average SASA values, i.e., 12^{th}, 13^{th}, and 18^{th} ligands have 160 $Å^2$, 135 $Å^2$, 150 $Å^2$, respectively. Figure A.29-A.30 (Appendix A) depicts the SASA plots of the rest of the complexes. On the other hand, the ligands with the highest RMSD, i.e., 5^{th}, 11^{th}, $14^{th,}$ have the SASA as 70 $Å^2$, 130 $Å^2$, 160 $Å^2$, respectively. The second and third ligands for low- and high RMSD cases have almost the same SASA. The first ligand in the case of low RMSD ligands (12^{th}) has virtually double the SASA value than the first ligand of the high RMSD cases (5^{th}). Other complexes have even higher SASA values, i.e., the 5^{th} complex (6m71_nsp12_7_8/ZINC000410177506/) has a SASA value of around 200 $Å^2$. This is a positive characteristic from the point of view of SASA. Still, we had to filter the ligands based upon a holistic approach with RMSD characteristics as a primary consideration. Moreover, the 15^{th} complex (7BV2_remdesivir/ZINC 000596164676) has the lowest average SASA of 10 $Å^2$. The native inhibitor Remdesivir was removed and replaced by the ligand under consideration in this complex.

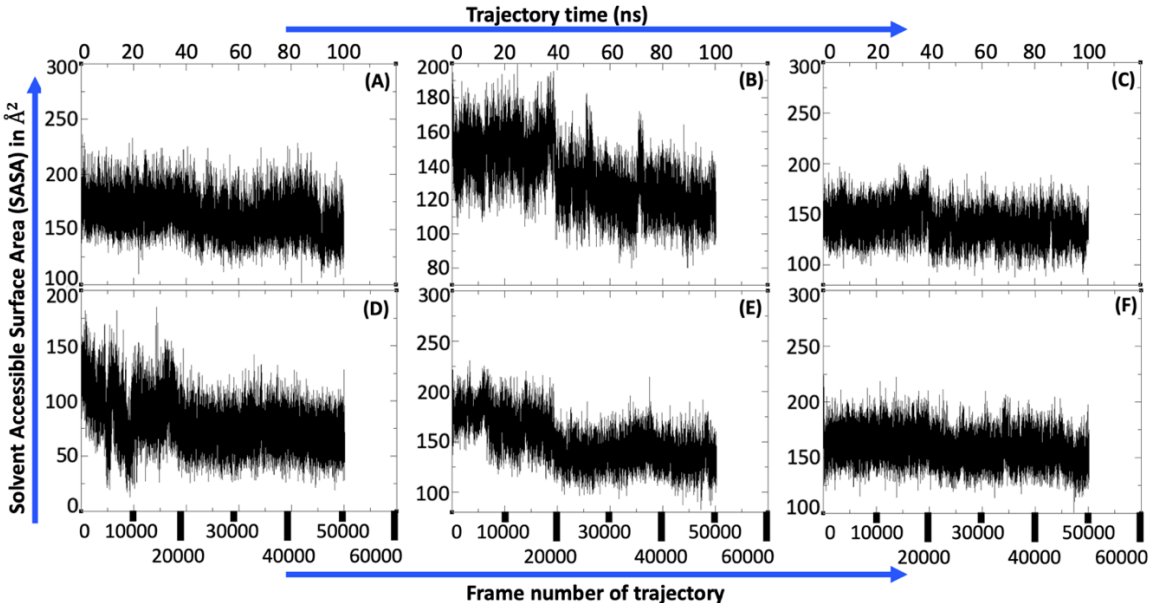

Figure 4.6 Solvent Accessible Surface Area (SASA) of ligands having extreme RMSD. (A, B, C) Lowest RMSD sub-group: 12th, 13th, 18th ligands. (D, E, F) Highest RMSD sub-group: 5th, 11th, 14th ligands The X-axis shows the frame number(bottom) and trajectory time(top) of the production run, and the y-axis is the protein's SASA ($Å^2$).

Finally, the protein's structural qualities, i.e., minimized structure's RMSD and MolProbity scores, are provided in Table B.7 (Appendix B). MolProbity and clash score of the proteins ranges from 91st percentile to 99th percentile, which supports the pipeline's integrity.

4.3.2.6 Molecular Mechanics Poisson-Boltzmann Surface Area (MMPBSA) Analyses.

We calculated the ligand and protein binding free energy using the Molecular Mechanics Poisson-Boltzmann Surface Area (MMPBSA) approach implemented in AMBER20's MMPBSA.py subroutine script. Due to high data fluctuation given its stochastic nature, we compared the binding energy values for the six highlighted cases (3 from low RMSD[Table 4.3a] + 3 from high RMSD subset[Table 4.3b] as defined in the RMSD section). The binding energies for the three high RMSD cases 5th, 11th, and 14th are -9.4409 kcal/mol, -0.5721 kcal/mol, and -9.8738 kcal/mol, respectively. The binding

energies for three low RMSD cases 12th, 13th, 18th are -6.5609 kcal/mol, -20.2606 kcal/mol, -4.5078 kcal/mol, respectively. We observed an almost direct correlation between the MMPBSA free binding energy and RMSD in the case of low and high RMSD ligand subsets. The ligands from the low RMSD ligand subset, on average, tend to have lower free energy than the average free binding energy of ligands from the high RMSD ligand subset. However, the 2nd and 3rd cases seem to be outliers in the case of high and low RMSD subsets, respectively. Binding free energy for the controlled complex of 7BV2/Remdesivir is calculated to be -20 eV.

Table 4.3a Binding Free Energy from MMPBSA Analysis for Low RMSD Ligand Subset

Ligand	12	13	18
Binding energy(eV)	-6.5609	-20.2606	-4.5078

Table 4.3b Binding Free Energy from MMPBSA Analysis for High RMSD Ligand Subset

Ligand	5	11	14
Binding energy(eV)	-9.4409	-0.5721	-9.8738

4.3.3 Density Functional Theory (DFT) Analyses

4.3.3.1 Molecular Electrostatic Map (MEP). We emphasize that all the ab-initio analyses were performed on systems containing only the ligands instead of the MD approach, which studied systems composing both proteins and ligands. From here onwards, we will primarily discuss connecting the ligand-only ab-initio results with the ligand/protein-complex MD results through various assumptions and hypotheses. In the MEP analysis, all six complexes appear to be covered with blue-iso-surfaces (Figure 4.7), indicating electron deficiency, i.e., bonded/unbonded interactions occur while the ligand gains an electron from the docked protein. This means the LUMO is more significant than the HOMOs in all the complexes to form bonded interaction and ultimately form hydrogen bonds and salt bridges. Figure A.31 (Appendix A) depicts the MEP plots of the rest of the complexes. In addition, we have performed Bader charge transfer analysis to probe charge dynamics further, as shown in the next section.

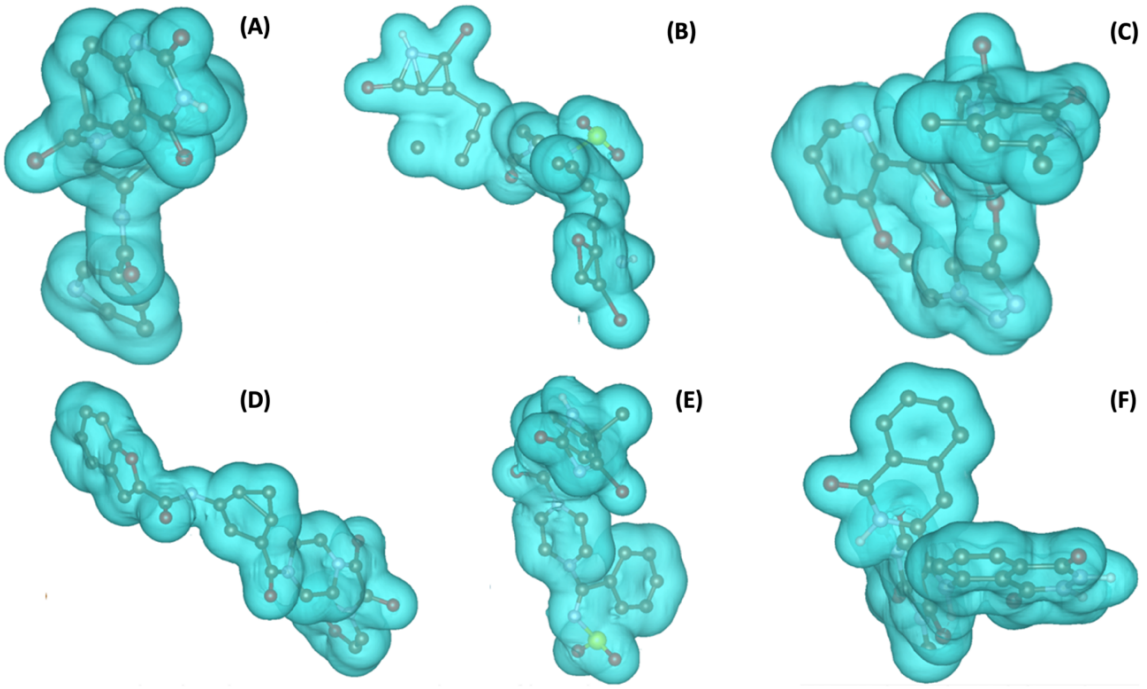

Figure 4.7 Molecular Electrostatic Potential (MEP) map of ligands having extreme RMSD. (A, B, C) Lowest RMSD sub-group: 12th, 13th, 18th ligands. (D, E, F) Highest RMSD sub-group: 5th, 11th, 14th ligands.

4.3.3.2 Bader Charge Analysis. We have further performed the Bader charge analysis to understand the charge potential of the individual atom/ion. We studied the same three complexes considered in the RMSD analysis having the least RMSD, i.e., 7bv2_nsp12-7/ZINC001176619532, 7bv2_nsp12-8/ZINC000517580540, and 7bv2_rna/ZINC000952855827. We notice the same observations in the Bader charge analysis (Figure 4.8) as in frontier molecular orbital analysis (Figure 4.10). The MEP plots denote that the ligand is more capable of accepting the electron than donating one. Consequently, one can see that the atoms residing in the volume overlapped by the LUMO (Figure 4.10) show negative Bader charge potentials as highlighted by black closed curves in Figure 4.8. This shows their receptivity of the electrons, resulting in bonded/unbonded interactions with the participating molecule/protein. Figure A.32 (Appendix A) depicts the Bader charge plots of the rest of the complexes' ligands. To further examine the extreme

Bader charge transfer values, we have visualized the residues bonded with ligands through hydrogen bonds (Figure 4.9) and highlighted them with white closed curves. For the 12th ligand, the extreme Bader charge values (-1.13 eV to 1.64 eV) appear to arise from the interaction between the Oxygen and Nitrogen of the ALA467 and PHE 362 of protein and the Nitrogen and Oxygen of the top benzene ring of the ligand's naphthalene. A similar observation can be seen for HOMO and LUMO (Figure 4.10). We superimposed the closed curves of the Bader charge plots as that for HOMO/LUMO plots. We could do that because the Bader charge displays the extreme values precisely in those areas having the HOMO/LUMO iso-surfaces. That proves the accuracy of our Bader charge analysis approach since it almost matches with FMOs analysis. For this ligand, the LUMO orbital is concentrated around both benzene rings of the naphthalene because of the presence of the ALA467 and PHE 362 nearby.

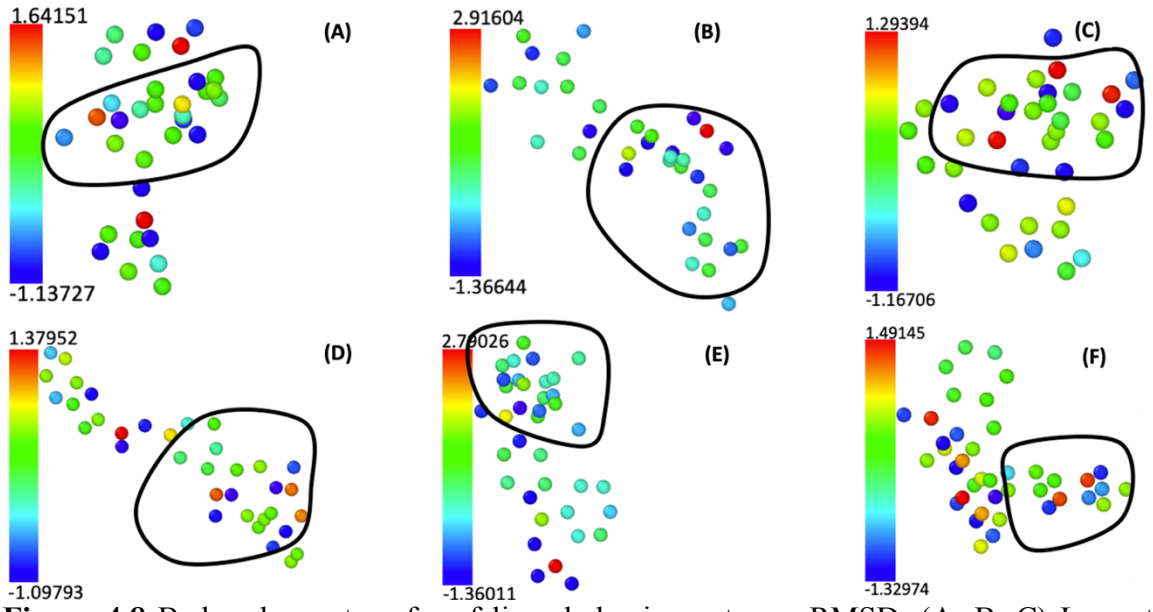

Figure 4.8 Bader charge transfer of ligands having extreme RMSD. (A, B, C) Lowest RMSD sub-group: 12th, 13th, 18th ligands. (D, E, F) Highest RMSD sub-group: 5th, 11th, 14th ligands.

For ligand 13th, the extreme values of the Bader charge analysis seem to be concentrated around volume containing S atom attached with two hydroxy functional groups and terminated with naphthalene on one end and Benzene heterocyclic ring on the other end. The benzene ring of naphthalene, further from the S atom, does have Oxygen and Nitrogen. The Nitrogen is balanced with an H atom and has a carbonyl group next to it. The other side of the S atom is terminated with a Benzene with 2 nitrogen atoms. These group S, hydroxy-functional group, carbonyl functionalized naphthalene interact with the nitrogen (ND2) and oxygen (OD1) atoms of residues ASN 436 and ASN 427. Out of which, oxygens are double bonded with the backbone of the residues. As shown in Figure 4.10b, most of the HOMO/LUMO volumes fall under the same closed curve highlighted on the Bader charge plot (Figure 4.8b). However, there appears to be LUMO covering the partial Benzene ring of hexahydroindan attached opposite to the Naphthalene terminal of the ligand. Finally, the 18th ligand is made primarily from 3 Benzene rings with a single heterocyclic Benzene ring attached as side chains through double bonds with terminal and middle Benzene rings of the backbone. Here most of the extreme Bader charge values (-1.16 to 1.29 eV) and HOMO/LUMO iso-surfaces appear to be concentrated over the region that contains the terminal Benzene that is not connected to the side chain benzene and the middle benzene ring. The terminal benzene ring has 1 nitrogen and is attached with 2 carbons through a single bond and 1 oxygen through a double bond. This ligand region appears to be the reason behind the formation of the most frequent hydrogen bond (27450 frames) with oxygen (OG1-HG1) of the residue THR 485 of the protein.

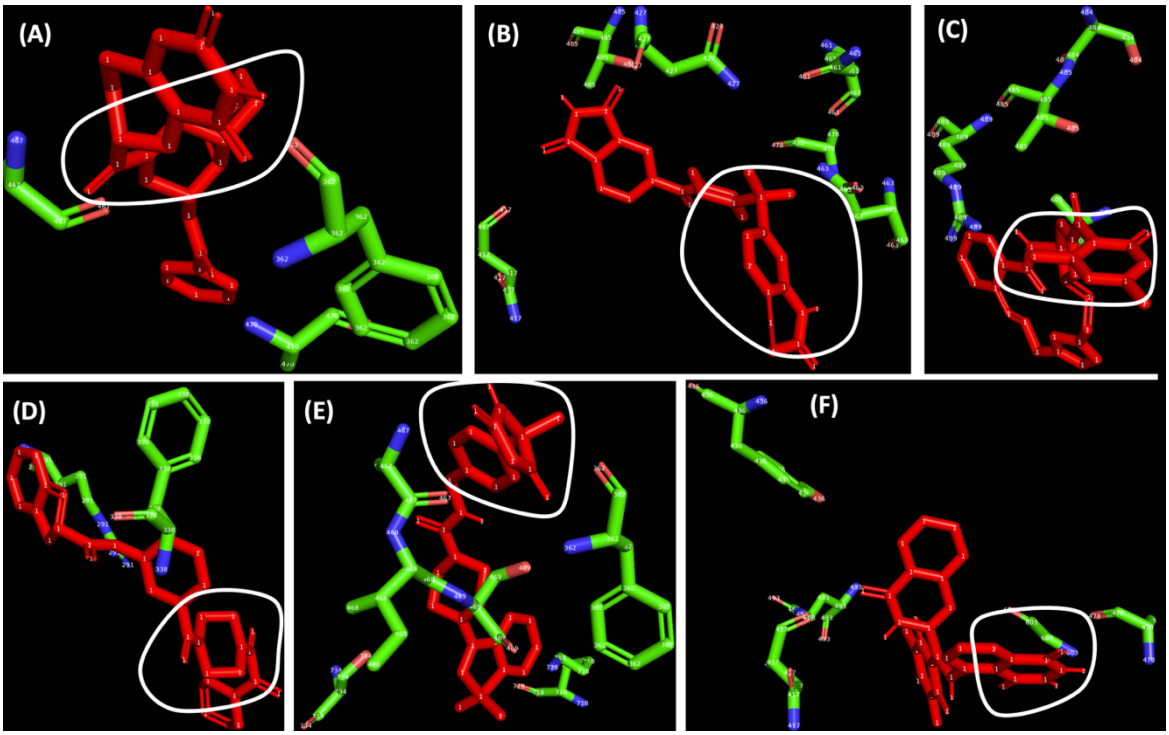

Figure 4.9 Stick representation of residues bonded with ligands through hydrogen bonds. (A, B, C) Lowest RMSD sub-group: 12th, 13th, 18th ligands. (D, E, F) Highest RMSD sub-group: 5th, 11th, 14th ligands. Ligand is represented in red.

The high RMSD ligand sub-group interacts with the protein binding site in such a way so that either the number of interactions are not enough or if they are large enough, then they are dispersed over the whole conformation of the ligand instead of being focused around a locale of the ligand, which displayed the iso-surfaces of HOMO/LUMO (Figure 4.10). Ligand 5 constitutes one hexahydroindan heterocyclic ring with an oxygen atom in cyclopentane. Furthermore, 1 benzene ring and 2 hetero-benzene rings, with one having 2 nitrogen atoms and the terminal benzene ring having a double-bonded oxygen atom, are attached through a nitrogen bond to the ligand's backbone. The conformation of the hetero-benzene rings makes them ideal candidates for the concentration of the HOMO/LUMO iso-surfaces. In this ligand, hydrogen bonds are formed only for two sets of residues and the ligand, i.e., ARG291@NH2–HH21···O3 and PHE338@N–H···O4. These residues are

not in close proximity to the hetero-benzene rings covered by HOMO/LUMO. This may be the prime reason this ligand falls under the category of high RMSD subset. Despite extreme values of the Bader charge transfer (-1.09 to 1.37 eV) in the same region covered by FMOs, there are some atoms of hexahydroindan, which exhibits high values for the Bader charge transfer because of the already cited hydrogen bonds. A similar phenomenon was observed for ligand 11, where a significant number of hydrogen bond interactions occur outside the region, overlapped by the HOMO/LUMO iso-surfaces. The compound had one hexahydroindan with a Sulphur atom in cyclopentane, 1 hetero-benzene, 1 benzene, and 1 hetero-Cyclopentane with 2 double-bonded attached oxygens. The majority of the high-frequency hydrogen bonds, i.e., 5634, 5268, 4671, 1361, 1235 frames, are formed between residue/ligand LYS718@NZ–HZ3···O1, –HZ2···O1, –HZ1···O1, –HZ2···O2, –HZ3···O2 respectively. They are further away from the LUMO/HOMO iso-surfaces among the hydrogen-bonded residues.

Furthermore, LIG835@N–H···ILE468@O is also a high-frequency bond and appears to be away from HOMO/LUMO overlapping volume, and so does the bond SER734@OG–HG ···O2. Conversely, the following bonds appear to be covered by the overlapping region of HOMO/LUMO iso-surfaces, i.e., LIG835@N4–HG ···ALA467@O, PHE362@N–H···O3, LIG835@N–H···SER469@OG. The Bader charge analysis agrees with the spatial distribution of the hydrogen bond formation. The highest positive value, i.e., 2.79 eV appears to be in the Sulphur atom interacting with residue LYS 718, and the highest negative value of -1.36 eV seems to be present in the atoms interacting with the residues LYS718, SER734, ILE 468, ALA 467. In ligand 14th, the two sets of hetero-hexahydroindan are linked through the hetero-benzene side chain. Out of which, one

hexahydroindan contains benzene with 1 nitrogen and one double oxygen, and another hexahydroindan has benzene with 2 nitrogen and 2 double bonded oxygens. The side chain benzene ring contains 2 nitrogen connected with carbons and 3 double bonded oxygens.

We discuss the hydrogen bonds in the decreasing order of their frequency. At the top, we observed LIG835@N5–H3···GLY603@O, with 32130 frames, hydrogen bond formed between double-bonded hydrogen of GLY603 and one of the NH group of the terminal benzene ring. We believe this bond results from the highest Bader charge values (-1.32 to 1.49eV) obtained within the closed curve in Figure 4.8F. The second highest frequent bond is LIG835@N4–H2···ALA478@O with 23435 frames. This bond appears to be originated from one of the HOMO lobes that cover the hydrogen atom attached to benzene nitrogen, shown in the highlighted closed curve area in Figure 4.10F. The next hydrogen bond with 7510 frames is TYR436@OH–HH ···LIG@O3, which forms between benzene linked OH group of residue TYR 436 and double-bonded oxygen of non-terminal benzene of one of the hetero-hexahydroindan. We observe the corresponding low Bader charge values(-1.32eV) on that double-bonded oxygen in Figure 4.8F. Followed by 3 hydrogen bonds GLN493@NE2–HE21···LIG@O2, LIG835@N2–H···ASN417@O, and ASN417@ND2–HD22···LIG@O1 with the frequency of 6593, 6132, and 2590 frames. The first of these three bonds are made between Nitrogen of residue GLN493 and oxygen of the side chain benzene ring. The 2nd and 3rd of these bonds are made between the same residue and benzene ring of the same hetero-hexahydroindan. Furthermore, the types of atoms involved are the same. The only difference is, in the 2nd bond, the donor is the ligand's nitrogen atom and the acceptor is the residue's oxygen atom, and this is reversed

in the 3rd bond, i.e., the donor is residue's nitrogen atom, and acceptor is ligand's oxygen atom.

Here, a trend can be observed, i.e., for a given ligand, if most high-frequency hydrogen bonds are observed, and corresponding extreme Bader charge transfer values occur in the region covered by the HOMO/LUMO iso-surfaces, it tends to belong to the low RMSD ligand subgroup. If the same majority do not fall under the region covered by the HOMO/LUMO iso-surfaces, it tends to belong to the high RMSD ligand subgroup.

4.3.3.3 Frontier Molecular Orbitals (FMO). One of the primary causes of interaction in a biological system is hydrogen bond formation. A hydrogen bond is formed when the probability of an electron transfer is highest between a residue and ligand. We assume the probability of an electron transfer depends upon the following factors: the shape of the ligand relative to the binding cavity in the protein, the shape/overlapping of the frontier molecular orbitals (FMO), overlapping of the FMOs over the interlocking part and the volume of the FMOs. One can counter-argue here about our consideration of the ligand's shape and its implicit incorporation in FMOs. To refute it, we can consider that for a single docked pose of a ligand, there could be multiple shapes/volumes of the FMOs, and for a single volume/shape of the FMO, there could be various ligand poses. Therefore, the separate considerations of these two variables are better to characterize the ligand's dynamic in the binding site.

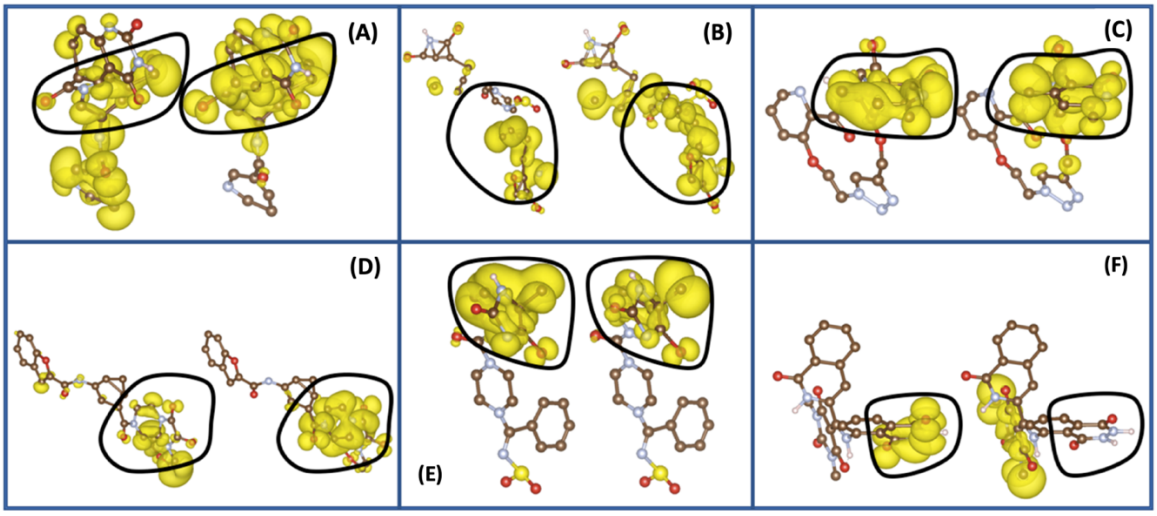

Figure 4.10 Frontier Molecular Orbitals (FMO) of ligands having extreme RMSD. (A, B, C) Lowest RMSD sub-group: 12th, 13th, 18th ligands. (D, E, F) Highest RMSD sub-group: 5th, 11th, 14th ligands. The left figure of each part shows the HOMO iso-surface, and the right figure shows the LUMO iso-surface.

We will be analyzing three complexes from high RMSD subgroup 6M71_nsp12_7_8/ZINC000410177506, 7BV2_nsp12-7/ZINC000616537204, 7BV2_nsp128/ZINC 001180048431, and three complexes from least RMSD ligand subgroup: 7bv2_nsp12-7/ZINC001176619532, 7bv2_nsp12-8/ZINC000517580540, 7bv2_rna/ZINC000952855827. Figure 4.10 shows the FMOs with 3D complex models for the previously mentioned six cases. Figure A.33 (Appendix A) depicts the FMO of the rest of the complexes. For the high RMSD ligand subset, the first complex has high RMSD because of the linear/non-interlocking geometry of the ligand in comparison to the binding pocket, despite having a significant FMO volume and their overlapping (Figure 4.10). The same holds for the second complex, despite having somewhat better inter-locking geometry of the ligand compared to the binding pocket, which is why this case has relatively higher RMSD than the first complex. Finally, the third case, even though it has an interlocking ligand profile, is not covered by either of the FMO orbitals. Moreover, the FMO orbitals do not overlap despite having decent volume.

On the other hand, in the case of the least RMSD ligands subset, the second complex has the least RMSD (0.45 Å) because of the better interlocking shape of the ligand with FMOs, covering that interlocking region in addition to overlapping orbitals despite having relatively lower orbitals volumes. Followed by second best, 3rd complex with RMSD (0.5 Å), which has the perfect combination of the FMOs overlapping each other and FMOs covering the whole ligand ring, which acts as an ideal interlocking geometry for a given binding site in a protein. Finally, the 1st case has the highest RMSD of 0.6 Å because of poor distribution/overlapping of the FMOs over the significant available interlocking area of the ligand and poor overlap of the FMOs despite having decent volume.

4.3.3.4 Quantum Characteristics. We had measured the quantum chemical characteristics for all the 18 complexes (Table B.5 (Appendix B)). However, we will discuss only the subset of the three highest and three lowest RMSD ligands (Table 4.4). The characteristics measures are as follows: the gap between HOMO and LUMO orbital's energy (a measure of the ligand's reactivity and thus stability), Ita(hardness), omega(electrophilicity), Sigma (local softness), Zita(electronegativity). Given the variation in data, we discussed the characteristics for the whole subset as one entity and then compared them among high and low RMSD subcases. The gap between the HOMO and LUMO orbital's energy for the high RMSD sub-group (5th, 11th, 14th ligands) is as follows: 1.3002 eV, 0.8070 eV, 1.1803 eV and same characteristics for low RMSD sub-group (12th 13th, 18th) is 0.8585 eV, 0.8337 eV, 1.0814 eV, respectively. We have observed a similar trend for hardness, i.e., the hardness tends to increase with the increase in RMSD of a molecule. For high RMSD subset the hardness measured is: 0.65010 eV, 0.40350 eV, 0.59015 eV and for low RMSD subset the hardness values are 0.42925 eV, 0.41685 eV,

0.54070 eV, respectively. We have observed the opposite trend in the case of electrophilicity. The electrophilicity decreases with the RMSD value of the ligand. The electrophilicity values of high RMSD group are 29.74 eV, 50.98 eV, 25.04 eV and as that for the low RMSD subgroup are 50.59 eV, 38.49 eV, 34.94 eV, respectively. A similar trend was obtained in the case of local softness, i.e., high RMSD tends to lower the local softness. The local softness for high RMSD subgroup are 1.53 eV^{-1}, 2.47 eV^{-1}, 1.69 eV^{-1} and for low RMSD group are 2.32 eV^{-1}, 2.39 eV^{-1} and 1.84 eV^{-1}, respectively. We observed an inverse relationship between electronegativity and RMSD. The electronegativities of the high RMSD group are: 6.21 eV, 6.41 eV, 5.43 eV and for low RMSD subgroup are: 6.59 eV, 5.66 eV and 6.14 eV, respectively. We have performed the same set of calculations for the controlled study case of Remdesivir against 7BV2, and corresponding values are shown in Table 4.4. The three lowest RMSD ligands exhibit better quantum chemical characteristics than the controlled case of Remdesivir.

Table 4.4 Quantum Chemical Characteristics from Ab-Initio Analysis for Low and High RMSD Ligand Subset

Ligand No.	**E_gap(eV)**	**Ita(eV)**	**Omega(eV)**	**Sigma(eV^{-1})**	**Zita(eV)**
5	1.3002	.65010	29.7471	1.5382	6.2191
11	.8070	.40350	50.9861	2.4783	6.4145
14	1.1803	.59015	25.0457	1.6944	5.4370
Remdesivir (Benchmark case)	.9493	.57465	36.8032	1.6691	5.2513
12	.8585	.42925	50.5960	2.3296	6.5906
13	.8337	.41685	38.4998	2.3989	5.6654
18	1.0814	.54070	34.9425	1.8494	6.1471

We can say from the collected data that the ligands with higher RMSD also tend to have high reactivity and lower stability. The electrophilicity helps us understand the reactivity, structural, and selectivity patterns in excited and ground states of the compounds. It highly correlates with the stabilization energy of the compound when it is saturated with electrons from docked virus protein enzyme. A high value of μ (chemical potential) and a low value of η (chemical hardness) indicate a better electrophile compound. Along with the HOMO-LUMO energy gap, the chemical hardness and chemical potential give important information about the reactivity of a compound. This combination also helps understand the charge transfer during the interaction between a compound and a protein. If a compound has a lower value of electrophilicity index, that means it has more probability of accepting electrons from its docked protein structure until it fills its frontier molecular orbitals. Besides, if a compound has a high electrophilicity

index value, they are less likely to absorb an electron from its docked protein, and hence they are less chemically reactive. In the sample set of 18 complexes, the subset of 3 ligands with the least RMSD has more electrophilicity index than the other subset of 3 high RMSD ligands with low electrophilicity index. This means ligands with high reactivity have higher RMSD and vice versa. As usual, this is expected as if a more reactive compound is more unstable, it shall have higher RMSD than another compound with lesser reactivity.

4.3.4 Machine Learning-Based HOMO–LUMO Energy Gap

As a representative case, we selected the HOMO LUMO energy gap (HLEG) to be predicted with a Machine Learning (ML) model. Unfortunately, due to the limitations of the training data and computational resources, we could not capture the absolute values of the HLEG. Still, we successfully captured the qualitative trend observed in the ab-initio calculations of HLEG from three extreme cases of the highest RMSD and lowest RMSD ligands subsets.

Table 4.5 Quantum Chemical Characteristics from Machine Learning Approach for Low and High RMSD Ligand Subset

Ligand	Machine Learning(eV)	DFT (eV)	% RMS Error
12	0.8013	0.8585	6.66
13	0.9307	0.8337	11.63
18	0.9711	1.0814	10.19
5	1.4083	1.3002	8.31
11	0.8578	0.8070	6.29
14	1.2874	1.1803	9.07

The qualitative trend obtained from ab-initio calculations is that the high RMSD sub-group of ligands, on average have high HLEG values, and the low RMSD sub-group of ligands, on average, have low HLEG values. This is the exact correlation obtained for the HLEG values obtained from the machine learning approach (Table 4.5). We believe the mismatch between the absolute values of HLG between ab-initio and machine learning approach can be attributed to one or any combination of the following: the difference between the source of the training data and production data, size of the training data, and the equation on which the model is based upon, i.e., Battaglia equations. In production codes, the first factor shall not exist because having the production data from the same source as the training data shall tend to eliminate the need to use machine learning in the first place. Except it becomes a significant aspect when the training data set is limited, which is the issue in our case. This leads us to the second variable that the dataset QM9 has only 134,000 molecules. That is

appropriate only for a limited set of scenarios. We believe this is the most significant parameter among all three behind missing the absolute values of HLEG. Lastly, the Battaglia equations are known to provide a good result for a beginner-level code, however the modification of the parameters is necessary to reduce the error, which is beyond the scope of this study. Therefore, we leave it for future work in these three variables of the machine learning analysis section of the article.

4.4 Conclusion

We studied more than 2 million unique protein-binding-site/ligand combinations, which were docked using high throughput virtual screening. These were filtered down to 90 complexes by selecting the top 10 binding energy complexes provided by the docking step for each of the nine proteins systems (binding site). They were further screened down to two ligands per binding site, resulting in 18 unique ligand/binding site complexes post ADMET analysis. Consequently, Molecular dynamics and first principle analysis were performed on these 18 unique complexes. Three complexes each for the lowest and highest ligand RMSD values were selected for the post MD simulation analysis based upon qualitative reasoning rationalized with MD and DFT computations. Ligands from the least RMSD subgroup are docked to the same protein (nsp12-7-8 complex) through three different binding sites (interface of nsp12/7, interface of NSP 12/8, and binding site of template-primer RNA). The least RMSD sub-group is ligand 12^{th}, 13^{th}, 18^{th} with RMSD as follows: 0.75Å, 0.4Å, 0.5Å and highest RMSD sub-group is ligand 5^{th}, 11^{th}, 14^{th} with RMSD as 4Å, 2Å, and 1.9 Å**.** The hydrogen bond analysis demonstrates the low RMSD ligand sub-group have either higher frequency hydrogen bonds or more stable hydrogen bonds than their counterparts in the high RMSD ligand sub-group. The hydrogen bond-

forming residues almost overlap with the corresponding RMSF plots of low and high RMSD ligand sub-group. We hypothesize that it is attributed to the location/volume of the iso-surfaces of FMOs and the extreme values of the charge transfer. We have observed an almost direct correlation between the extreme charge transfer values and hydrogen bonds.

Additionally, if the majority of the extreme charge values and thus hydrogen bonds are encapsulated by FMO's iso-surfaces, then that ligand tends to belong to the category of least RMSD ligand sub-group. If the majority of extreme charge values and thus hydrogen bonds are not encapsulated by FMO's iso-surfaces, then that ligand tends to belong to the high RMSD ligand sub-group. For example, from the low RMSD ligand sub-group, in the 18th ligand, most of the extreme Bader charge values (-1.16 to 1.29 eV) and HOMO/LUMO iso-surfaces appear to be concentrated over the region that contains the terminal benzene ring. This ligand region seems to be the reason behind the formation of the highest frequent hydrogen bond (27450 frames) with oxygen (OG1-HG1) of the residue THR 485 of the protein. On the other hand, similarly, ligand 14th from high RMSD ligand sub-case, hydrogen bond LIG835@N5–H3···GLY603@O is most frequent with 32130 frames. This bond is formed between double-bonded hydrogen of GLY603 and one of the NH groups of the terminal benzene ring. We have further performed MMPBSA based binding energy analysis, which agrees with our RMSD observation that the low RMSD ligand subgroup has lower binding energy on average than the group with high RMSD, i.e., -10.4431 VS. -6.6289 eV. HOMO-LUMO energy gap from the ab-initio method is modeled to be 0.85 eV to 1.08 eV for low RMSD ligand subgroup compared to high RMSD ligand subgroup's range of 0.80 eV to 1.3 eV. Our results support the hypothesis that ligand needs to be less reactive to have low RMSD, and it agrees with other quantum

characteristics. A GNN based machine learning model qualitatively supports these results. Our computational results provide insight into the drug repurposing for inhibition of different proteins of SARS-COV-2 and warrant further experimental investigations.

CHAPTER 5

CONCLUSION AND FUTURE WORK

5.1 Conclusion

We have found that structural perturbations like wrinkles and folds in 2D (no-biological) material and bio-logical material, respectively, plays important role in dictating their properties. In wrinkled Graphene exposed to the moister content, the wrinkle tends to coalesce with each other having final structural configuration significantly impacted by the configurational of initial wrinkles and diffused water amount. Further the wrinkles formation tends to depend upon the interplay between dynamics of interaction between sandwiched Graphene layers and the formation dynamics of water droplets. Maximum stress generated were observed to be at base of the wrinkles and never exceeded the plastic limit, which helps in the generation and control of the direction of "Electron-tunnel/channel" resulting in the applications of flexible electronic devices. The wrinkle caused strain tend to impact electronic structure i.e. Fermi energies/level, bandgap etc.

In next project, we have investigated the nano-friction properties as a result in the thickness and morphologic changes of MoS_2 layered material. Out of four parameters considered i.e. change in number of layers and indents, and radius and pattern of indents; change in radius and number of indents was found to be the most effective way to tune the nano-friction of the system. MoS_2 layer tend to offer high frictional force to a diamond tip moving along the armchair direction as result of increase in indents' radius and lower frictional exhibition as the indents' number decrease. The modeling methods used incorporated the atom's, electron's, hole's and excitons (electron-hole pair) dynamics.

Lastly this dissertation aims to study the structure-property relationship in biological system of ligand docked protein. Since in case of biological systems, two molecules can perform the same inhibitory action provided they have same folding configuration despite having different atomic composition which is impossible for non-bio materials without breaking constituting equation. We had taken SAR-CoV-2 as an example of the macromolecule and it was screened against ZINC drug library resulting in 242,000(ligands)*9(proteins)= 2.178 Million unique protein binding site/ligand combinations. Though 6 different sub-parts of the SARS-CoV-2 were investigated (6LU7, 6M0J, 6M71, 6W9C, 6W63, 7BV2) yet the resulting 3 drugs binds to the 7BV2 (nsp12-nsp7-nsp8 complex bound to the template-primer RNA and triphosphate form of Remdesivir) chain of the SARS-CoV-2 given this was only part of the SAR-CoV-2 spike protein that was docked by partially successful inhibitor (Remdesivir). This thesis is first project to the best of our knowledge to perform Bader charge analysis of the successful leads/drug along with the full computational pipeline in the order of: Molecule docking, ADMET/Toxicity, Molecular dynamics, machine learning and density functional theory-based analysis. By using this computational pipeline, most 3 promising drugs were filtered from the 2.178 Million unique protein binding-site/ligand combinations, and a number that was achieved by very few groups in the world at the time of submission of resulting publication.

5.2 Future Work

5.2.1 Neuromorphic Computing

The smallest structural dimension obtainable of complementary metal oxide semiconductor devices, i.e., transistors, and energy and area fingerprint cost of data transfer using von Neumann architecture are fundamental limitations of current digital computing power. However, this conventional computing paradigm (separate memory and logic operations architecture) can be replaced by advanced computing systems (Processing in Memory, PIM architecture) broadly classified under the umbrella term of neuromorphic computing.

Software-based artificial intelligence and machine learning are facing hardware-based bottlenecks [164] because data have to transfer from one part of the device to another to be stored and used for logic operations, which are fundamental building blocks of current computing systems. The increase in the data needed to run the current and future ML models is predicted to outpace the improvements in conventional computing hardware, which follows Moore's law.[165] Given the increasing demand for data, building more energy-efficient fundamental operations than CMOS transistors-based Boolean Logic is needed. These energy savings may not be justifiable for current computing needs, while they may be a significant chip designing constraint in the near future.

One electronic device that can help achieve neuromorphic computing is called Memristor. The first practical use of a Memristor was demonstrated in 1971 by using its property called memristance, which links the electric charge and magnetic flux. Memristors work on the principle of reversible resistance switching, where resistance correlates with the external electric field, which the applied voltage can control. In addition to Memristors,

advanced research in solid state physics led to newly observed degrees of freedom in 2D materials, i.e., spintronics in monolayer, Moiré lattice effect in multilayer systems, etc., which can be used for neuromorphic computing. For example, in spintronics, the electron's spin is used to store information bits in local magnetization, bundling the memory storage and data processing in the same step. Similarly, the Moiré lattice-based tunneling can be used as another degree of freedom in a similar approach to demonstrate the application in the neuromorphic computing device.

Neuromorphic computing can support the conventional machine learning algorithm such as Artificial Neural Network(ANN) as well the more advanced algorithm as well, such as Spiking Neural Network (SNN), recurrent neural network (RNN) based reservoir computing, etc.

5.2.1.1 Methodology. We have developed a monolayer 2D material system of different compositions, i.e., Graphene, MoS_2, and MXenes (Nb_4C_3). The SIESTA code is used to simulate the system with 20 x 10 x 100 Monkhorst-Pack mesh k-points. The non-linear green function (NLGF) subroutine of SIESTA was used to simulate the current-voltage (V/I) characteristics. SIESTA takes the device as a left electrode, a scattering region, and a right electrode (Figure 5.1). Left and right electrodes do not have to be of the same chemical composition and geometry, neverthless for preliminary results, both electrodes are considered to be the same, and they serve the same purpose as in the practical electronics transistors, i.e., source and drain. The scattering region is the part of the material across which the charges flow and scatter across the electrodes.

5.2.1.2 Results. A freestanding Graphene monolayer system displayed in Figure 5.1 was supplied with the bias voltage of 0.0 to 5.5 Volts, followed by the MoS_2 and an MXenes (Nb_4C_3). Due to the limited availability of computational resources, only the preliminary results of three materials were included in this dissertation. Referring to Figure 5.2, the current flow remains almost zero for all device materials until 1.5 Volts, followed by a significant rise. All materials follow the same pattern post 1.5 volts, i.e., inverted C curve. The highest point of that inverted C curve are as follows: 0.000.12, 0.00019, 0.000325 A for materials Graphene, MoS_2, and an MXenes (Nb_4C_3).

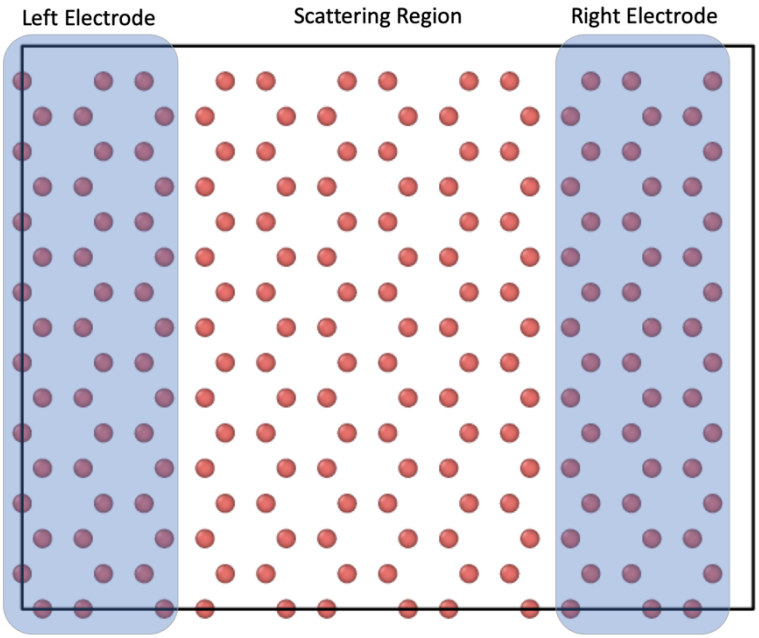

Figure 5.1 Schematic showing different parts of a typical field effect transistor with electrodes are highlighted in blue colors sandwiching the scattering region.

The endpoints on the VI curve were also in the same order of materials for values: 0.00006, 0.000155, 0.00025 A. Curves for Graphene and MXenes (Nb_4C_3) tend to be overlapping within 10% values of each other, as MoS_2 is an outlier. We believe this relative behavior in the curve is because of the bandgap of the materials, i.e., the bandgap of the

monolayers of Graphene and MXenes (Nb_4C_3) is zero, while the bandgap of MoS_2 is around 1.8 eV. Though this needs further investigation, we believe the density of states of the materials and HOMO/LUMO orbitals will have a significant role to play in VI characteristics curves. This correlation can be further investigated by studying exciton and trions dynamics as in section 3.3.3.1.

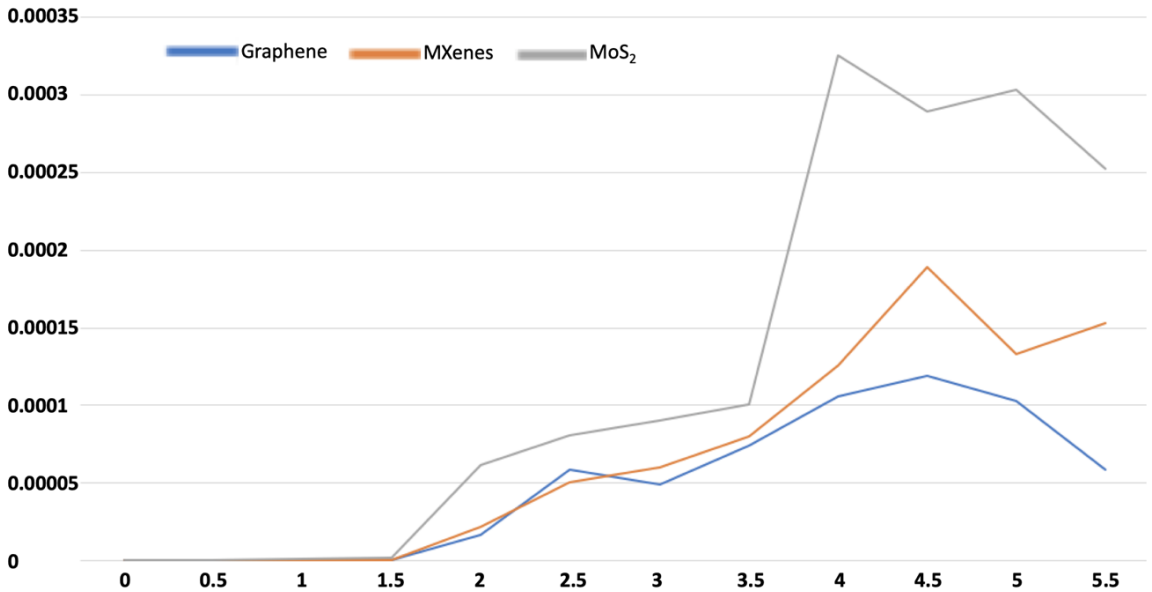

Figure 5.2 Voltage verses Current plots of different materials for electrode and scattering region area. Y-axis is showing the current in Amperes and X-axis is showing voltage in Volts.

5.2.2 Two-Dimensional Membrane DNA Sequencing

Another potential application of 2D materials is using them as a nanopore membrane to sense and/or translocate micro bio-material. A voltage applied across the membrane changes proportional to the ionic conductivity of the passing molecule. This change in voltage signal can help identify the molecule's identity passing through the membrane nanopore. Inspired by single molecule identification, recent studies have been published about detecting the single DNA bases by replacing them with the individual molecule in such devices.[166] Despite the success of using a 2D membrane to detect DNA bases, it

significantly suffers from error noise in the signals. Given the thinness of the 2D materials, they are always prone to be highly unstable given their solution-based structure, i.e., interaction with the H_2O molecules if in an aqueous solution. Every membrane instability will cause out-of-plane fluctuation, contributing to conductance change across the membranes, making it difficult to know whether the conductance change occurs because of molecular presence/translocation or membrane instability. This leads to solving the problem of synthesizing a new material or structure which will be thinnest without losing its structural stability. This section tries to answer this question in the dissertation by performing a comparative study among single planar 2D material (Graphene) and multiplanar 2D material (TMDs and MXenes).

5.2.2.1 Methodology. Since the nature of this system requires the large-scale movement of a group of atoms, so we decided to perform the machine learning force field-based molecular dynamics simulations. It can help attain ab-initio molecular dynamics accuracy without the need for the overhead of rich computational resources. DeepMDKit and VASP ML computational codes are used for this project. Given the more computational time needed for the former, only VASP ML-based results were included in this dissertation. The VASP ML's algorithm is given in Figure 5.3. It works on the methodology of continuing using an existing force field, if any, and randomly picks an MD step and performs first principles (FP) calculations, and measures the system properties. If that FP calculation-based properties are not within acceptable tolerance of the existing force field MD properties, then update the force field with the newly generated dataset. This cycle keeps repeating itself until the last step of MD simulation is achieved. Only the first steps changes in case there exists no force field before the first MD step, in that case,

the code first generates the multiple datasets based upon FP calculation and then creates the first force field of the simulation and keeps updating it in the subsequent steps as explained above (procedure of starting the simulation with an existing force field). Since the first steps need to perform multiple FP calculations, it is usually the most demanding step regarding computational time and resources.

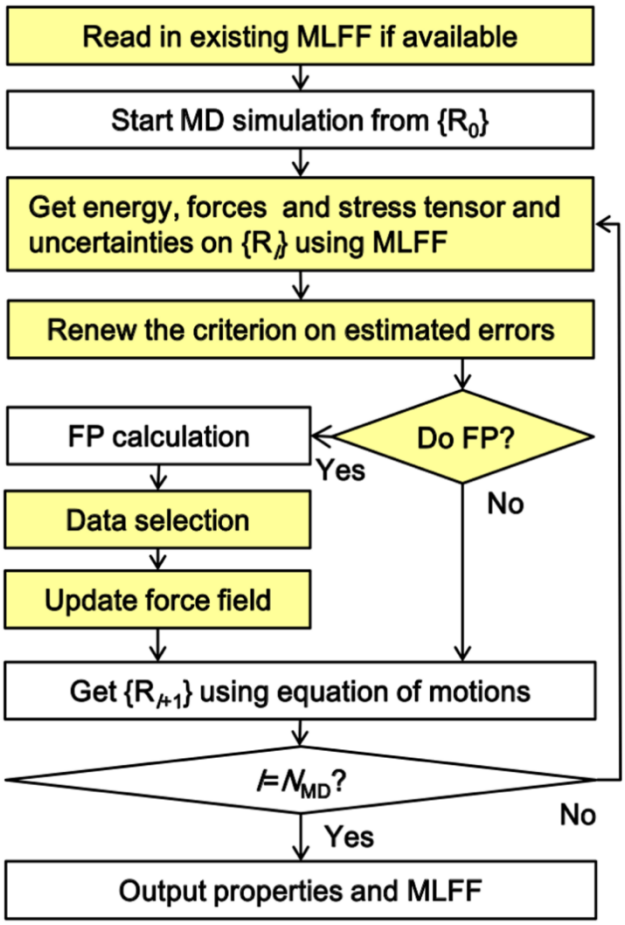

Figure 5.3 Flow-diagram of the machine learning force fields module of VASP.

Source: https://www.vasp.at/wiki/index.php/Machine_learning_force_field:_Theory
Retrieved on: 02/01/2022

5.2.2.2 Results. Adenine (A) is one of the four nucleotide bases in human DNA strain, with the remaining three beings: Thymine (T), Guanine (G), and Cytosine (C). This project aims to study the structural stability of the Adenine nucleotide while passing through a 2D material-based nanopore membrane. Different types of 2D materials, from semiconductor MoS2 to insulators MXenes allotropes (Ti_3C_2, Ti_2C, Nb_4C_3), were investigated to be used as the nanopore membrane (Figure 5.4). We have measured the root mean square deviation (RMSD as given in section 4.3.2.1) of the Adenine basis of human DNA strain with respect to the first frame, which will be an indicator of the structural stability of Adenine. While measuring the RMSD, the Adenine's atoms are not constrained in the spatial degree of freedom. Though this project aims to study the translocation of the Adenine from one end of the simulation box to another (including the vacuum), in this Chapter, only preliminary results are included, which focuses on the system dynamics after the Adenine is left freestanding in the plane of the membrane. The code was run in production mode for 10ns, and the average RMSD observed are as follows: 5.92 Å, 4.50 Å, 2.46 Å, 2.50 Å, 2.50 Å (Figure 5.5) for MoS_2 and MXenes allotropes (Ta_4C_3, Ti_3C_2, Ti_2C, Nb_4C_3), respectively. 2D materials tend to have most of their properties dictated by the only two critical electronic orbitals out of thousands of existing orbitals, i.e., HOMO and LUMO. An electronic bandgap measures the difference between HOMO and LUMO, which is 0 eV for MXenes and 1.46 eV for MoS_2 in the form of a freestanding monolayer. Adenine tends to show higher RMSD when placed in the center of the nanopore of higher bandgap monolayer material and tends to show lower RMSD when placed in the lower bandgap monolayer material.

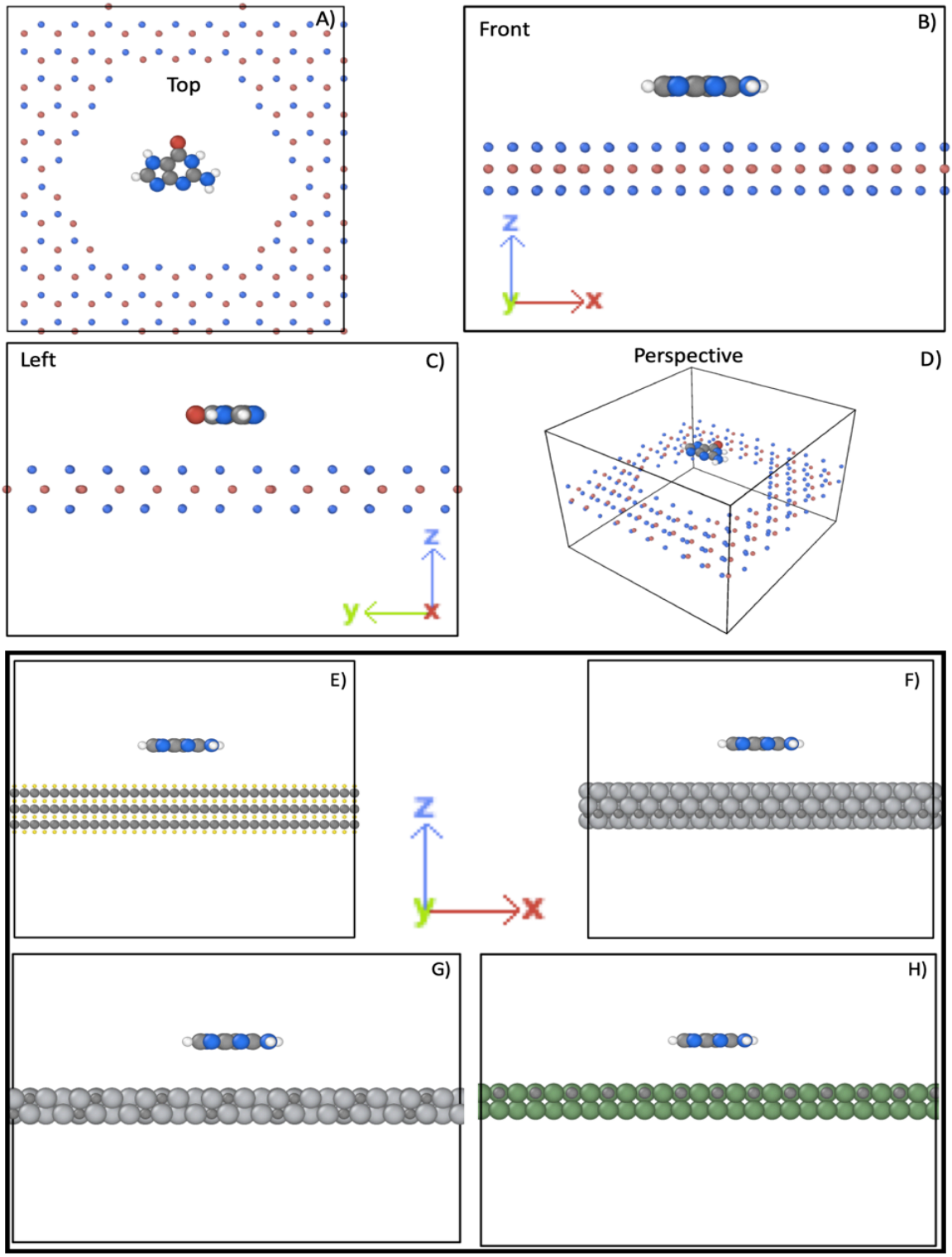

Figure 5.4 Structures of system containing Adenine nucleotide basis of DNA across nanopore of MoS_2 (A, B, C, D) and Ta_4C_3 (E), Ti_3C_2 (F), Ti_2C (G), Nb_4C_3(H) monolayers. Adenine is displaced along Z-axis for visualization purpose.

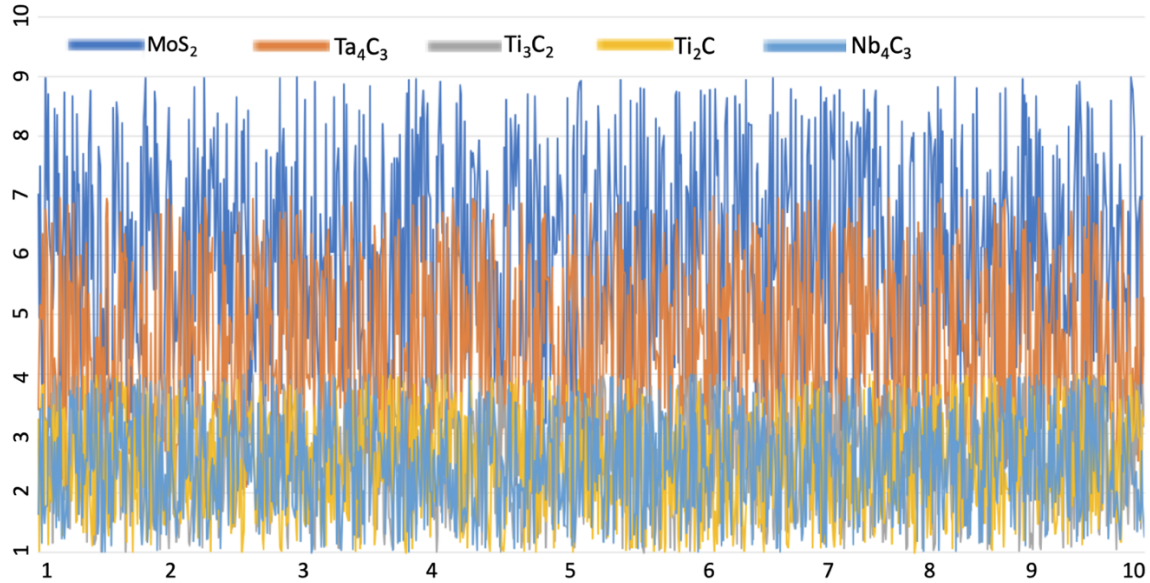

Figure 5.5 RMSD of Adenine basis of DNA in nanopore plane of MoS_2, Ta_4C_3, Ti_3C_2, Ti_2C, Nb_4C_3 monolayers. X-axis and Y-axis represents the time (ns) and RMSD (Å) Color legend is given at the top of the figure.

Though there appear to be a correlation between the RMSD of the passing molecule and the bandgap of the nanopore membrane's material nonetheless multiple set of additional studies must be performed to either support or refute this correlation

APPENDIX A

SUPPLIMENTARY FIGURES

Figure A.1 to A.34 show supplementary data cited with explanatory texts within the chapters.

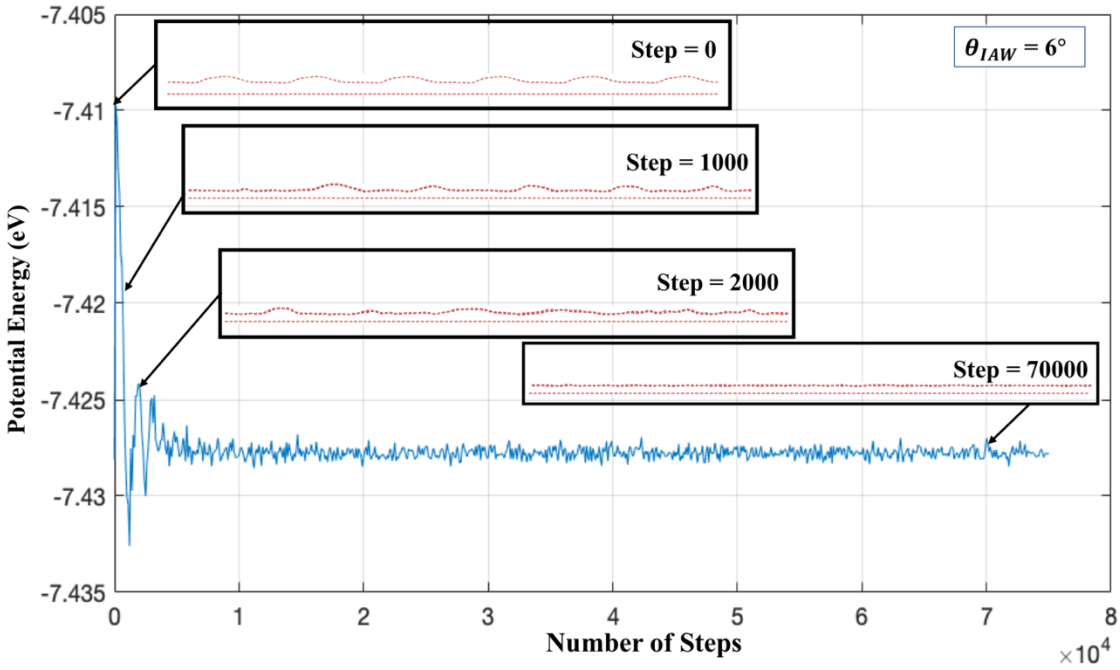

Figure A.1: Potential Energy variation for initial wrinkle angle of 6° (without water case).

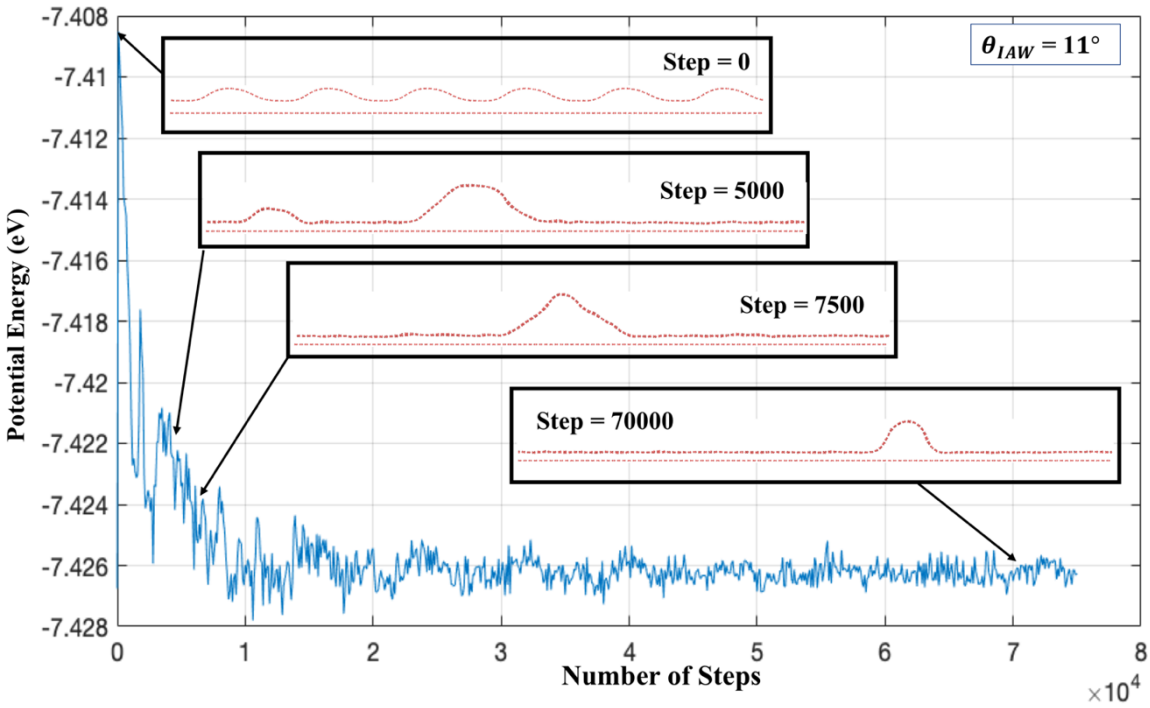

Figure A.2: Potential Energy variation for initial wrinkle angle of 11° (without water case).

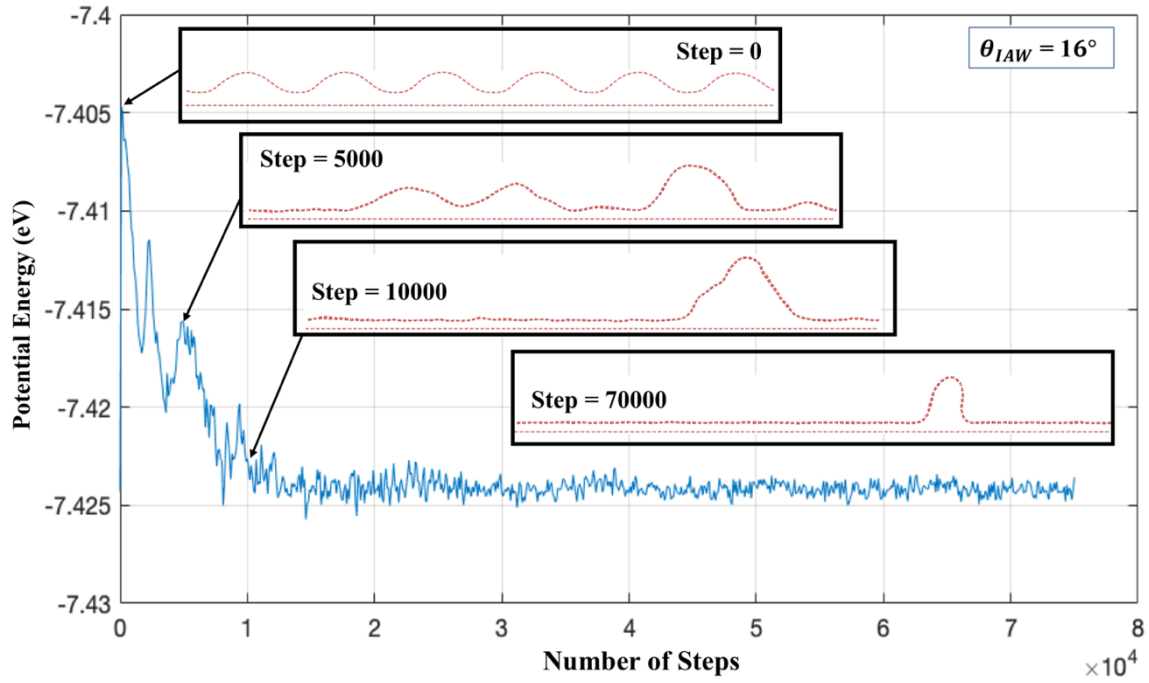

Figure A.3: Potential Energy variation for initial wrinkle angle of 16° (without water case).

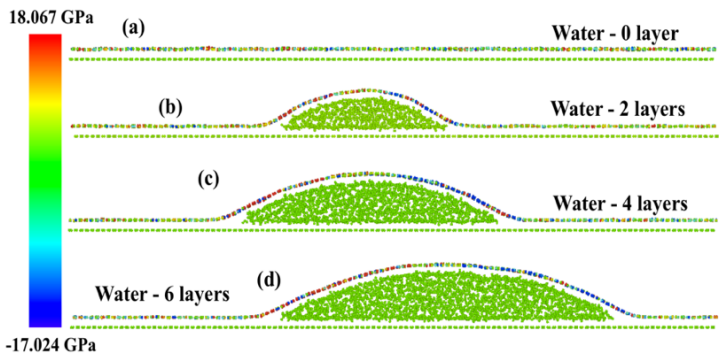

Height (z), Å	Length (x), Å	Aspect Ratio (z/x)	Angle (Degree)	Velocity
12.31	77	0.1598	28	yes
16.06	116	0.1384	23	yes
17.53	143	0.1225	20	yes
0	NA	0	0	NA

Figure A.4: Final equilibrium structure with stress profile starting from initial wrinkle angle of 6°.

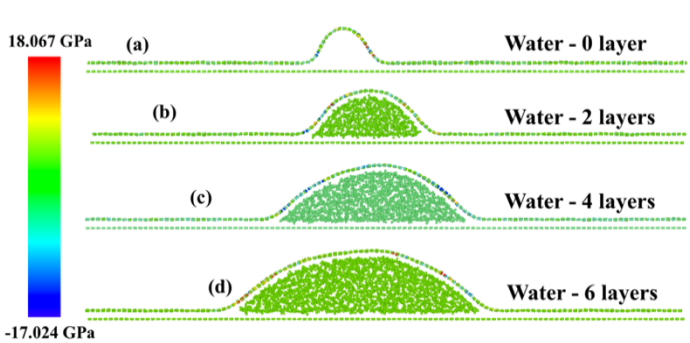

Height (z), Å	Length (x), Å	Aspect Ratio (z/x)	Angle (Degree)	Velocity
17.44	57	0.3059	51	yes
21.57	84	0.2567	40	yes
23.91	109	0.2193	37	yes
13.96	33	0.4230	61	yes

Figure A.5: Final equilibrium structure with stress profile starting from initial wrinkle angle of 11°.

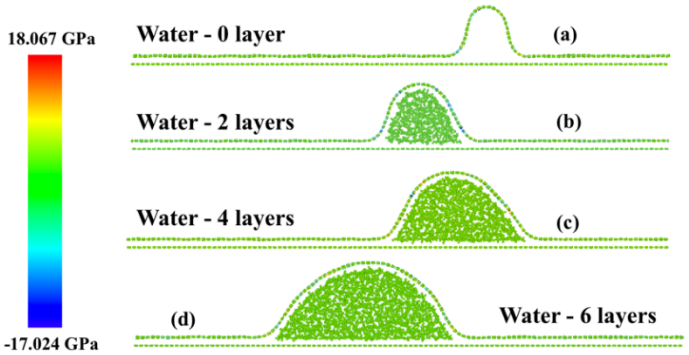

Height (z), Å	Length (x), Å	Aspect Ratio (z/x)	Angle (Degree)	Velocity
24.04	45	0.5342	70	yes
27.84	64	0.435	61	yes
30.98	82	0.3778	56	yes
20.63	32	0.6446	76	yes

Figure A.6: Final equilibrium structure with stress profile starting from initial wrinkle angle of 16°.

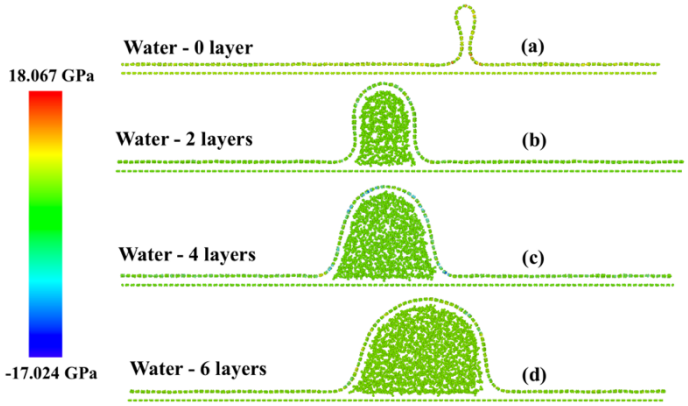

$\theta_{IAW} = 21°$

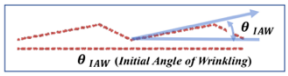

Height (z), Å	Length (x), Å	Aspect Ratio (z/x)	Angle (Degree)	Velocity
29.19	31	0.9416	96	yes
34.03	50	0.6806	80	yes
36.3	64	0.5671	70	yes
22.68	12	1.89	108	yes

Figure A.7: Final equilibrium structure with stress profile starting from initial wrinkle angle of 21°.

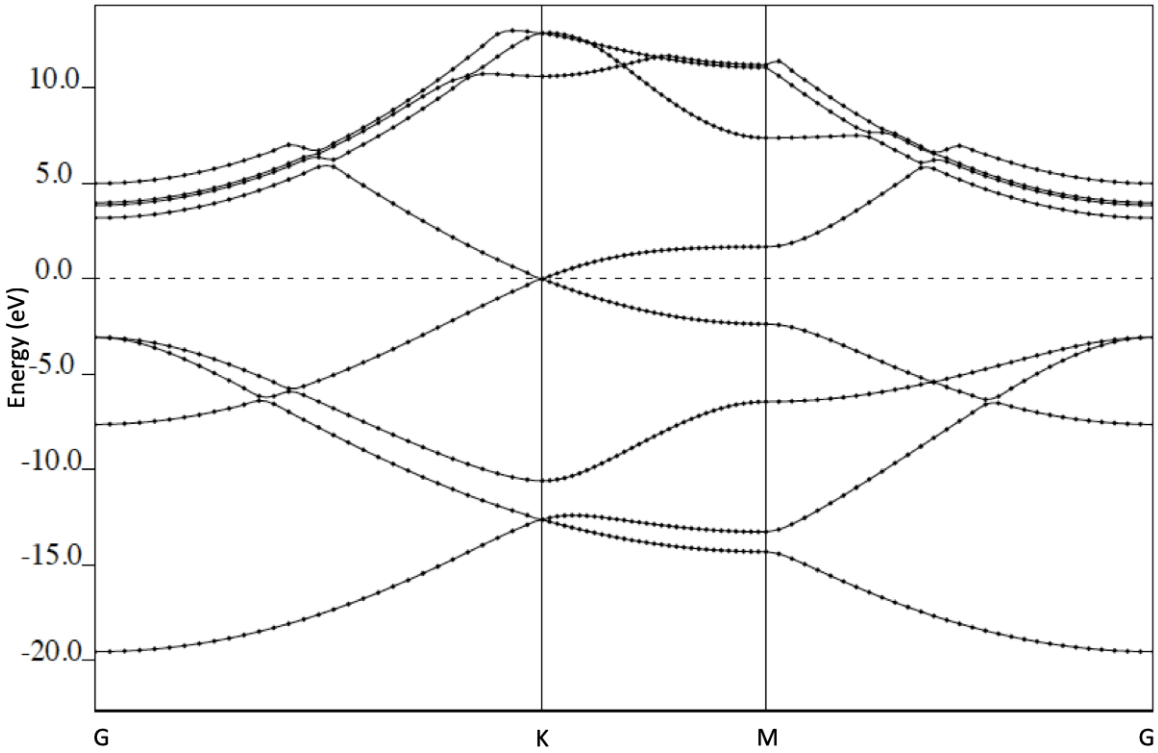

Figure A.8: Band structure of pristine flat graphene.

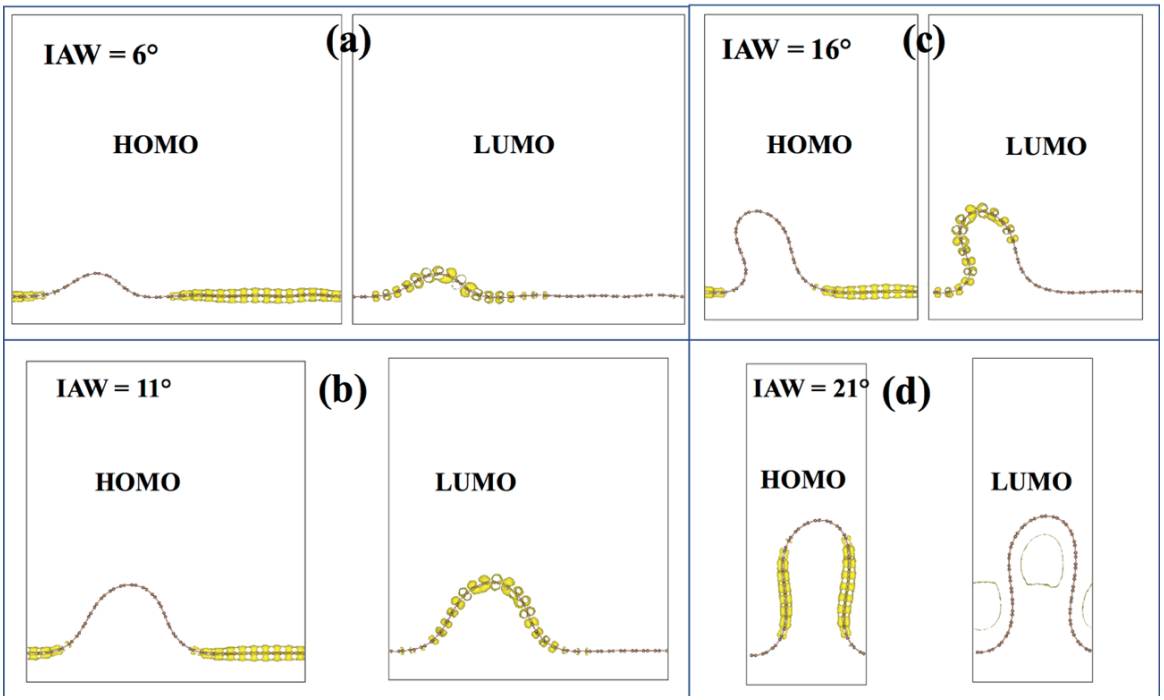

Figure A.9: Front view of HOMO and LUMO for four localized wrinkle obtained after complete wrinkled graphene (four water-layer case) with Initial Angle of Wrinkle (IAW) of (a) 6°, (b) 11°, (c) 16°, and (d) 21°.

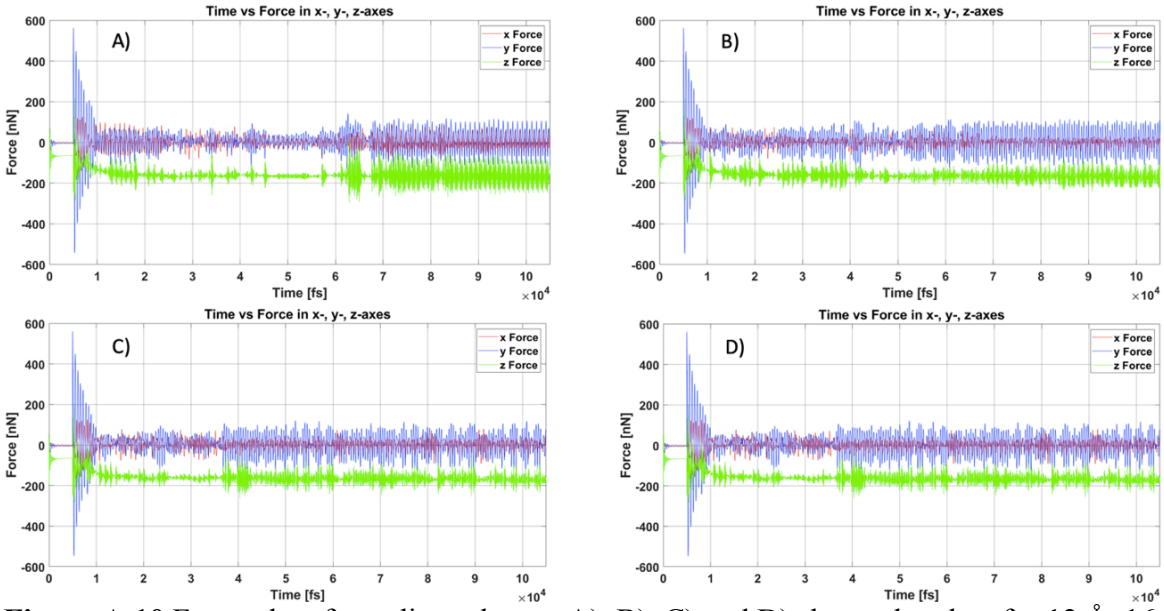

Figure A.10 Force plots for radius subcase. A), B), C) and D) shows the plots for 12 Å, 16 Å, 20 Å, and 24Å, respectively.

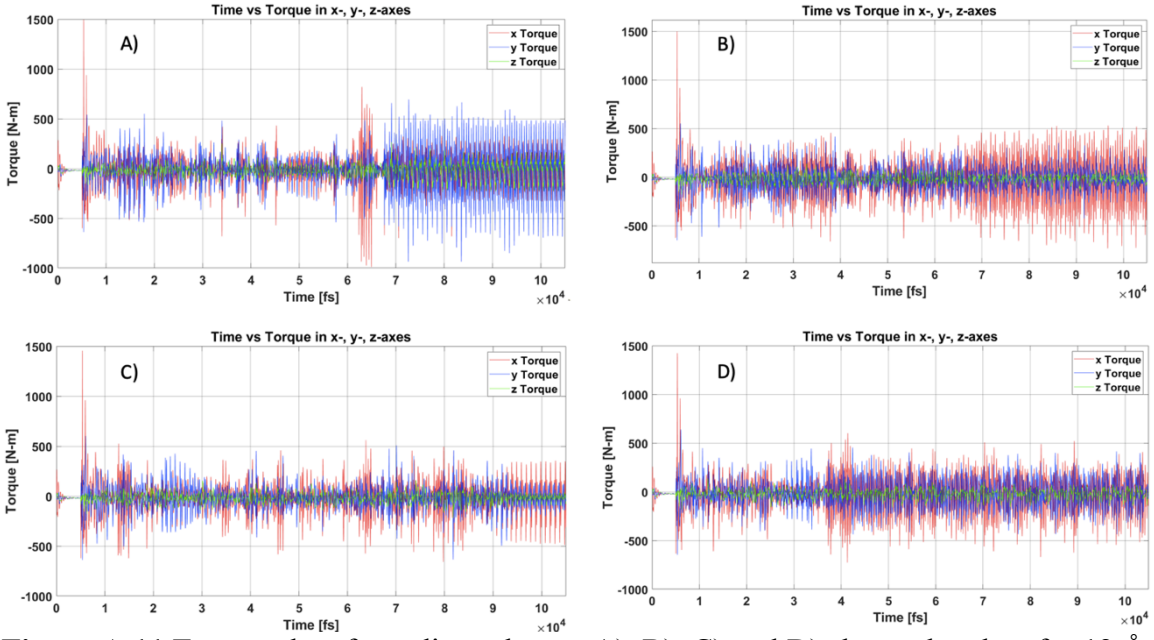

Figure A.11 Torque plots for radius subcase. A), B), C) and D) shows the plots for 12 Å, 16 Å, 20 Å, and 24Å respectively.

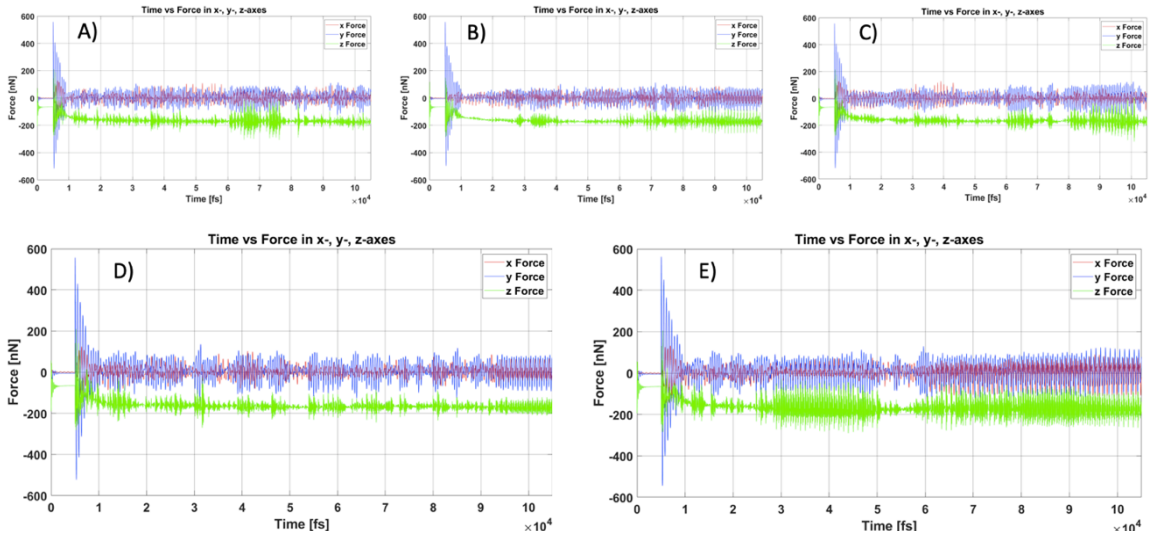

Figure A.12 Force plots for indents' pattern subcase. A), B), C), D) and E) shows the plots for Θ=0°, 25°, 30°, 35°, 45°, 60°, respectively.

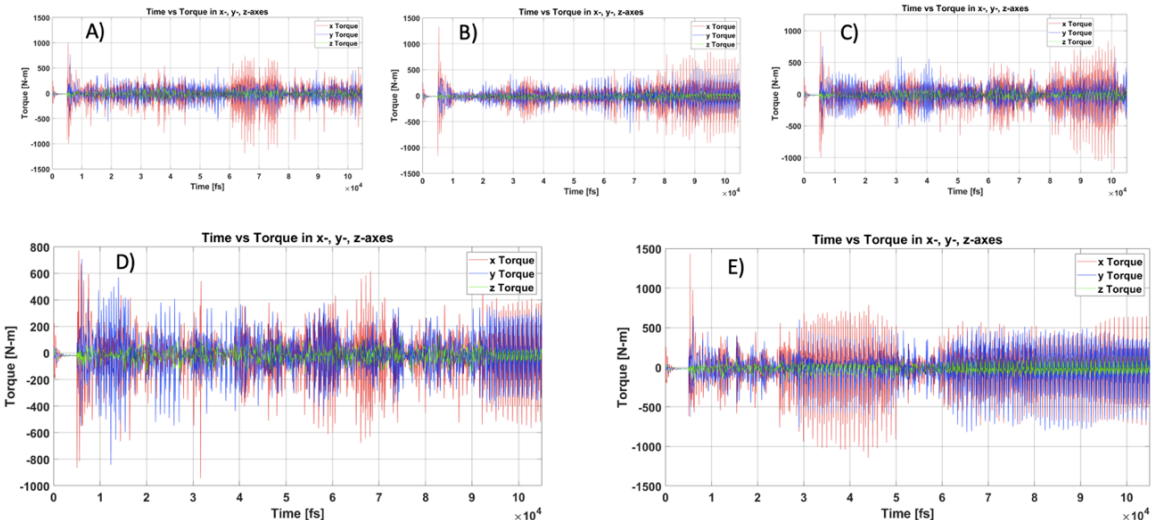

Figure A.13 Torque plots for indents' pattern subcase. A), B), C), D) and E) shows the plots for Θ=0°, 25°, 30°, 35°, 45°, 60°, respectively.

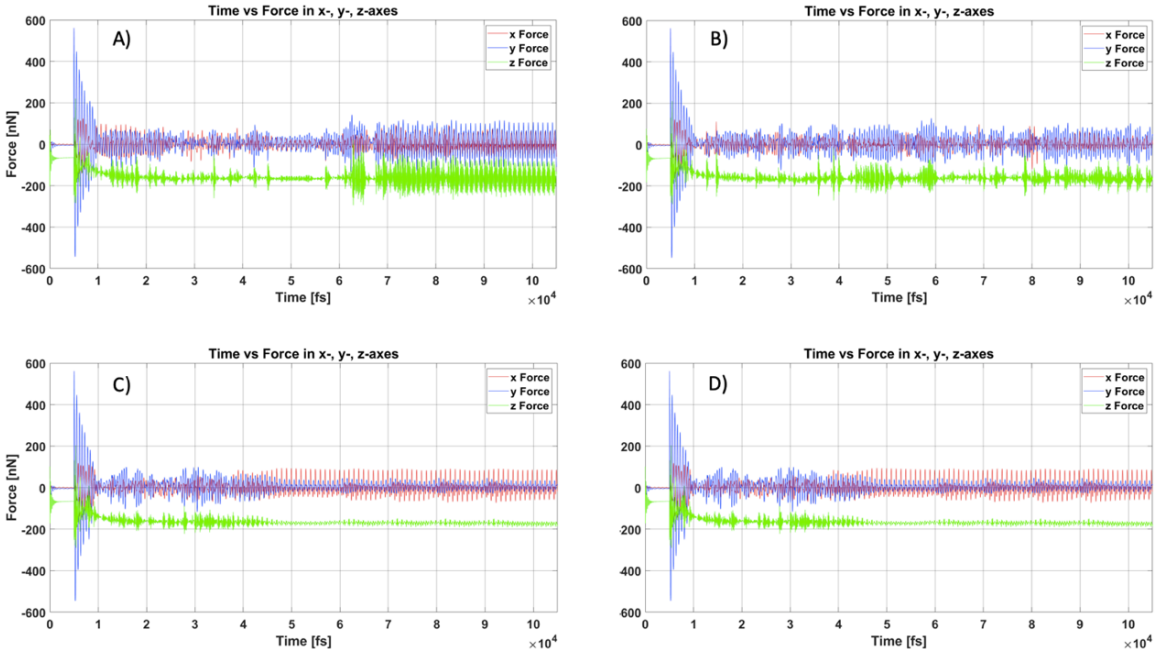

Figure A.14 Force plots for number of layers subcase. A), B), C) and D) shows the plots for 1, 2, 3, and 4 layers, respectively.

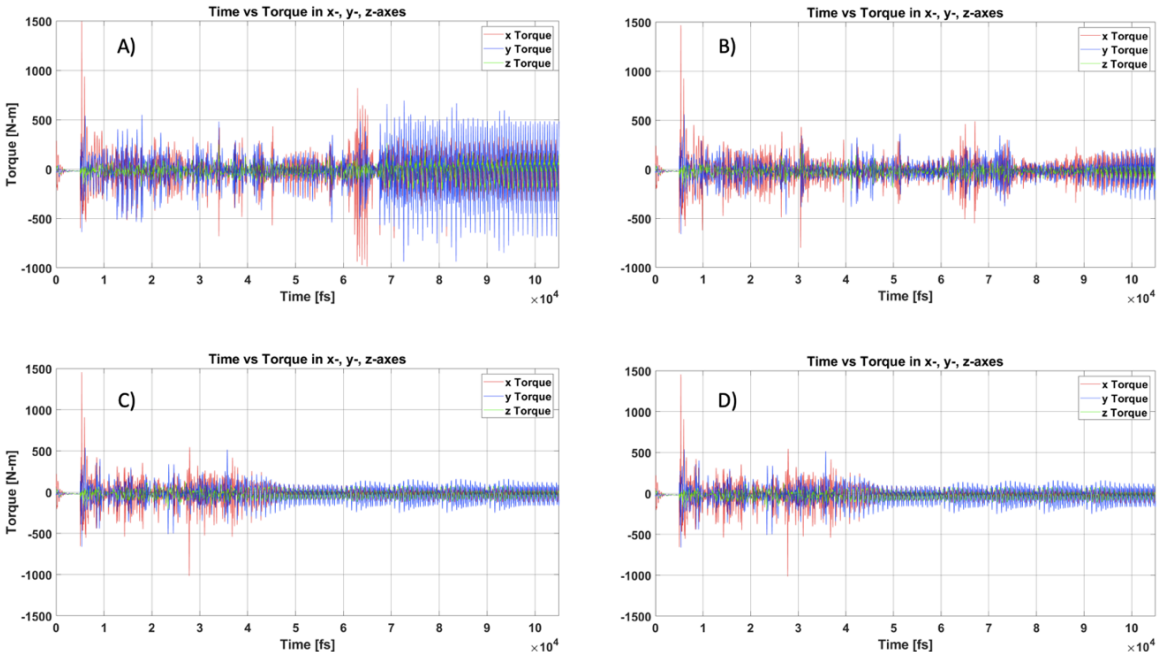

Figure A.15 Torque plots for number of layers subcase. A), B), C) and D) shows the plots for 1, 2, 3, and 4 layers, respectively.

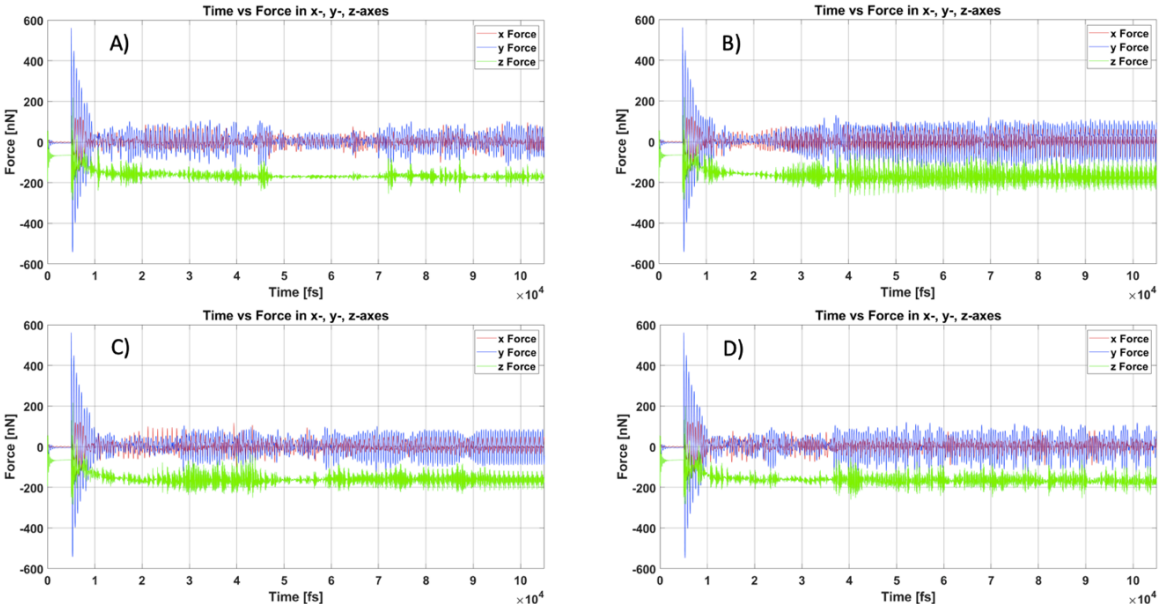

Figure A.16 Force plots for number of indents subcase. A), B), C) and D) shows the plots for 2, 4, 6, and 8 indents, respectively.

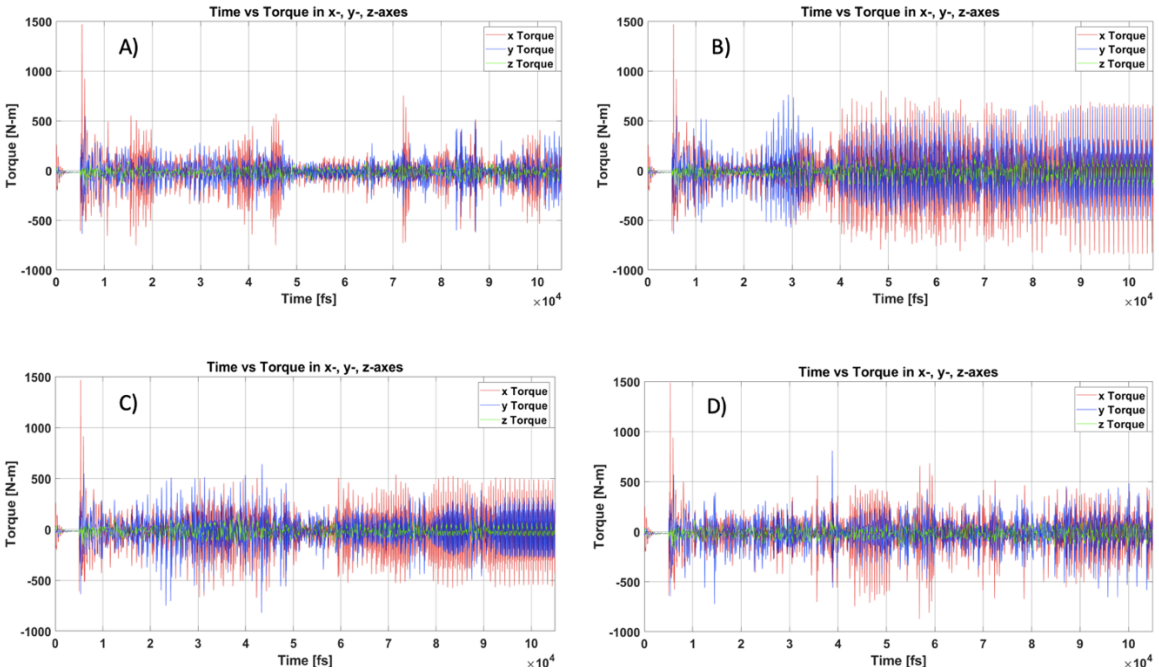

Figure A.17 Torque plots for number of indents subcase. A), B), C) and D) shows the plots for 2, 4, 6, and 8 indents, respectively.

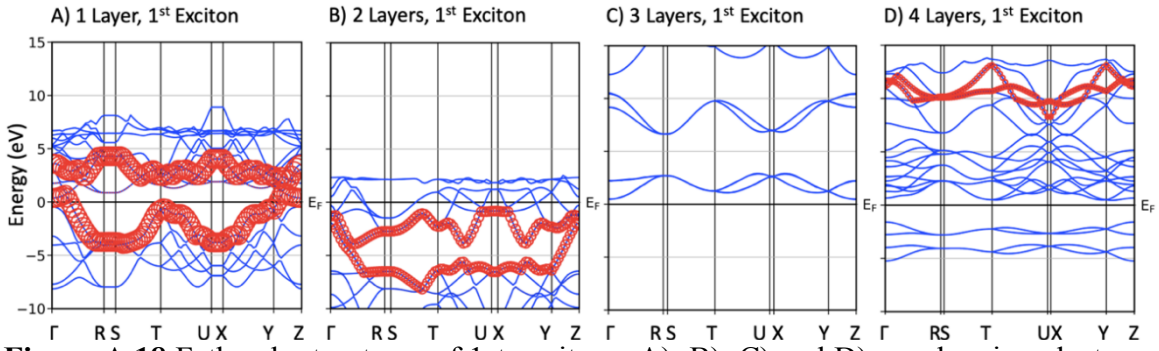

Figure A.18 Fatbands structures of 1st excitons. A), B), C) and D) are showing electron-hole couples for 1, 2, 3, and 4 layers cases, respectively.

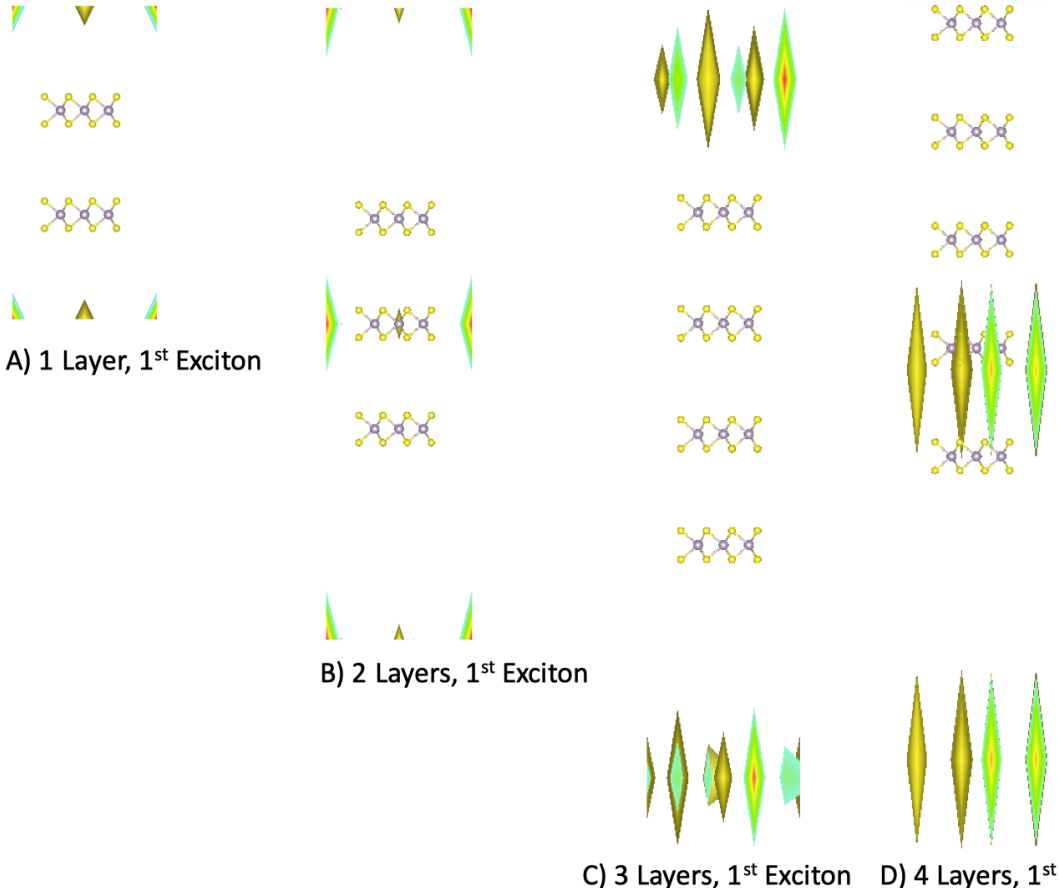

Figure A.19 Real space visualization of 1st excitons. A), B), C) and D) are showing electron-hole couples' clouds for 1, 2, 3, and 4 layers cases, respectively.

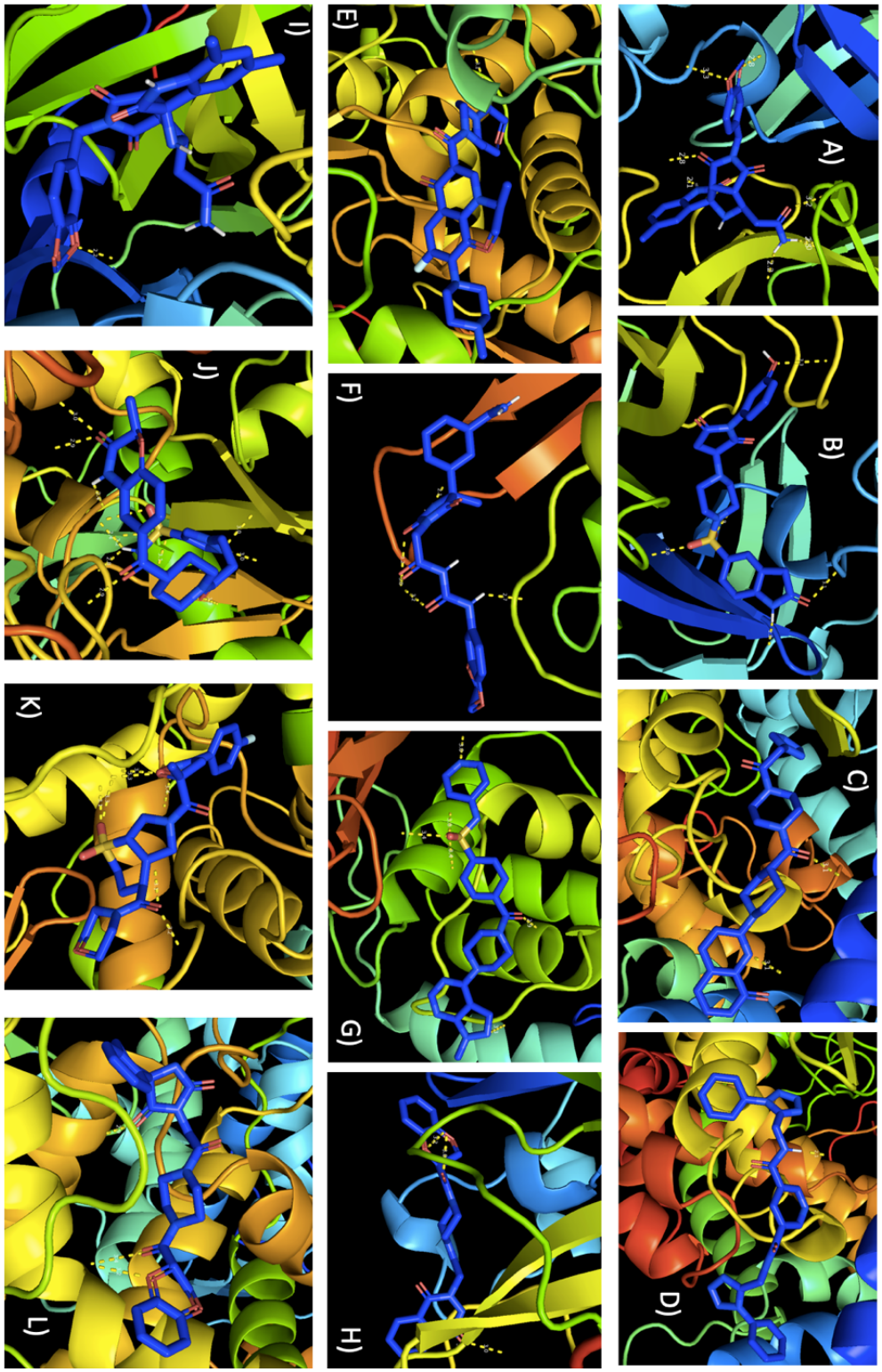

Figure A.20 Docked models of ligand and protein. A) to L) are showing systems from complex 1 to 18, except high RMSD and low RMSD ligand sub-groups. Proteins and ligands are shown in cartoon and sticks representation, respectively with hydrogen bonds highlighted with dashed lines labelled with bonds lengths.

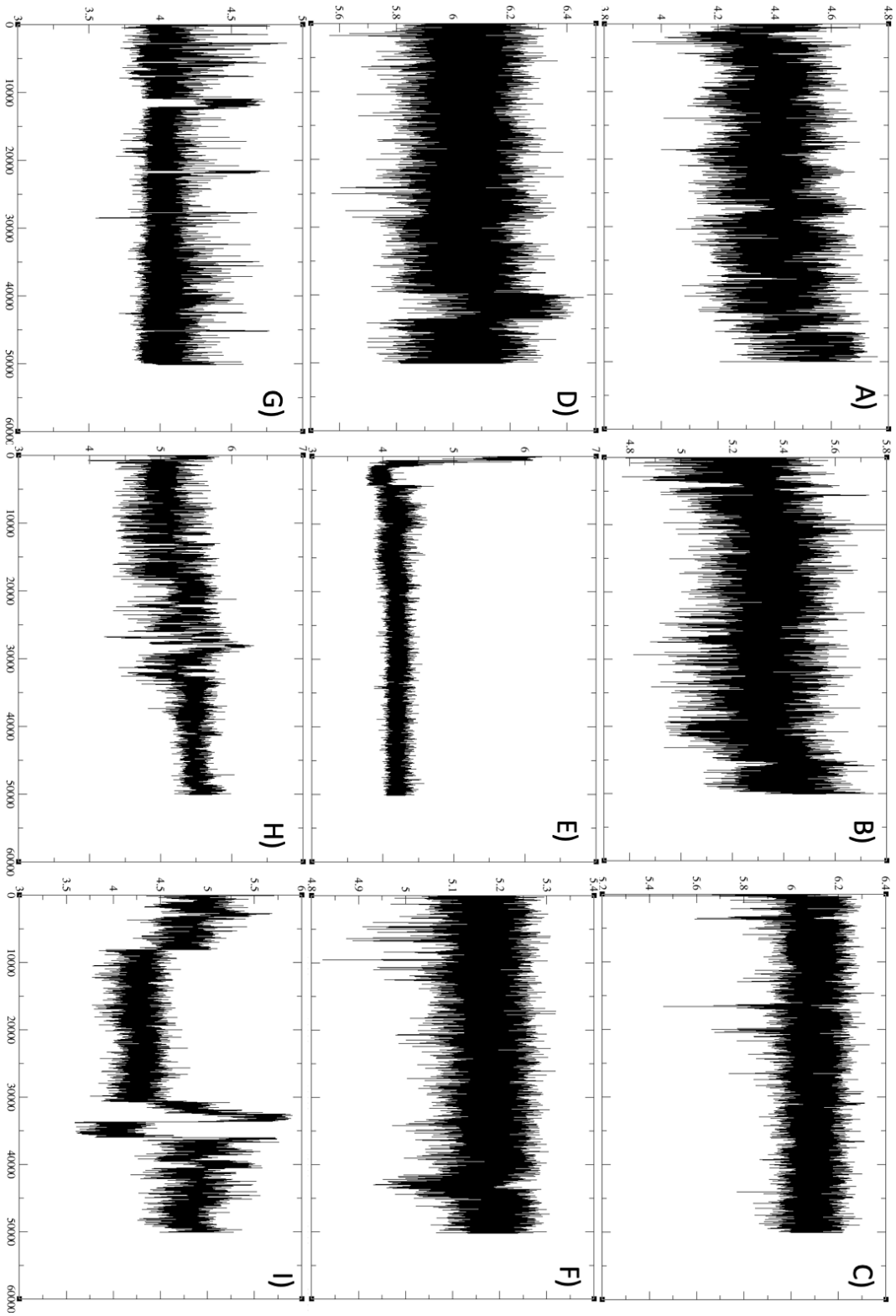

Figure A.21 Root mean square deviation of ligands under investigation. Plots A) to I) are showing RMSD from Ligand 1 to 9. Y-axis is showing RMSD in Å and X-axis is showing the frame number of the MD simulation trajectory.

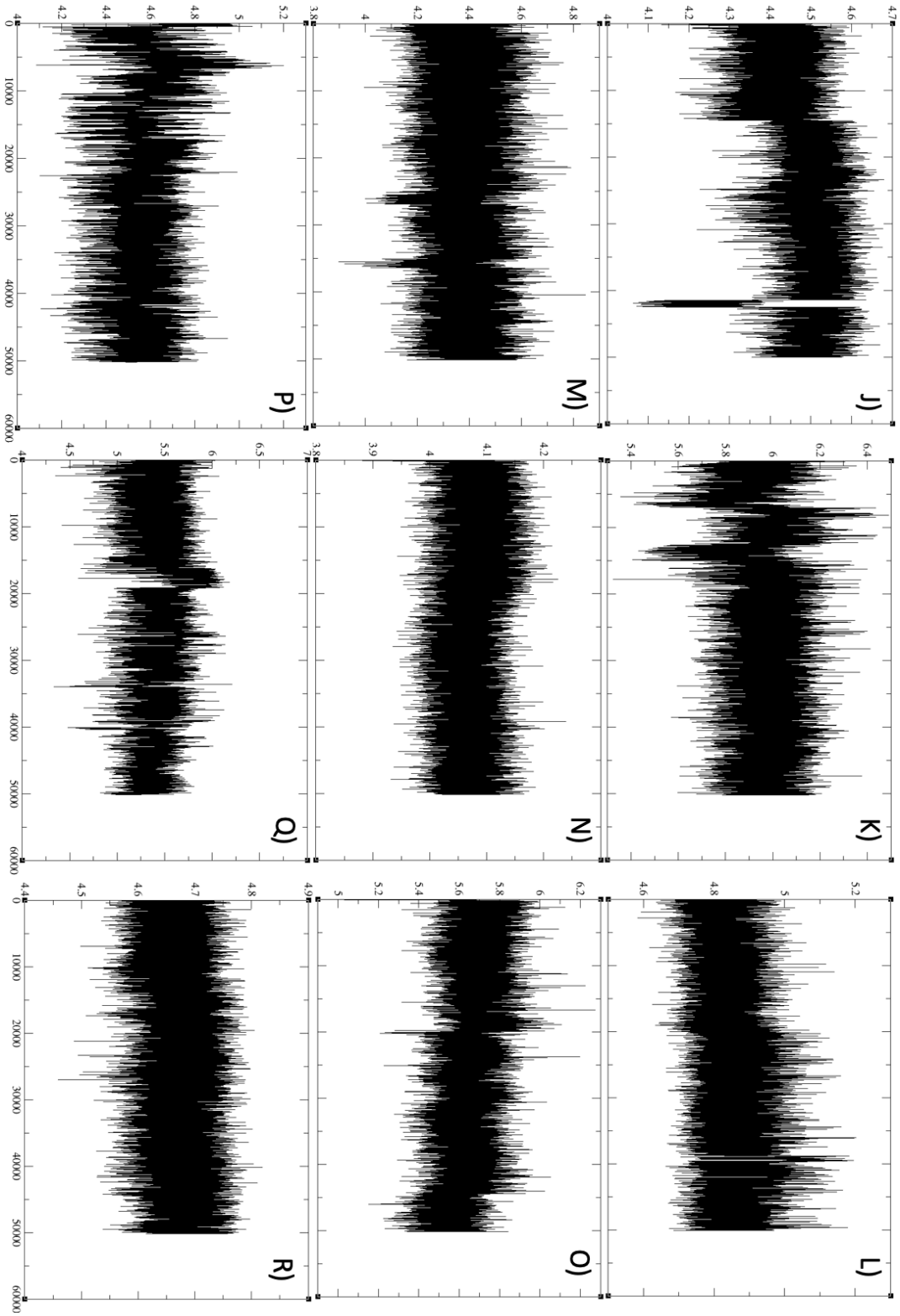

Figure A.22 Root mean square deviation of ligands under investigation. Plots J) to R) are showing RMSD from Ligand 10 to 18. Y-axis is showing RMSD in Å and X-axis is showing the frame number of the MD simulation trajectory.

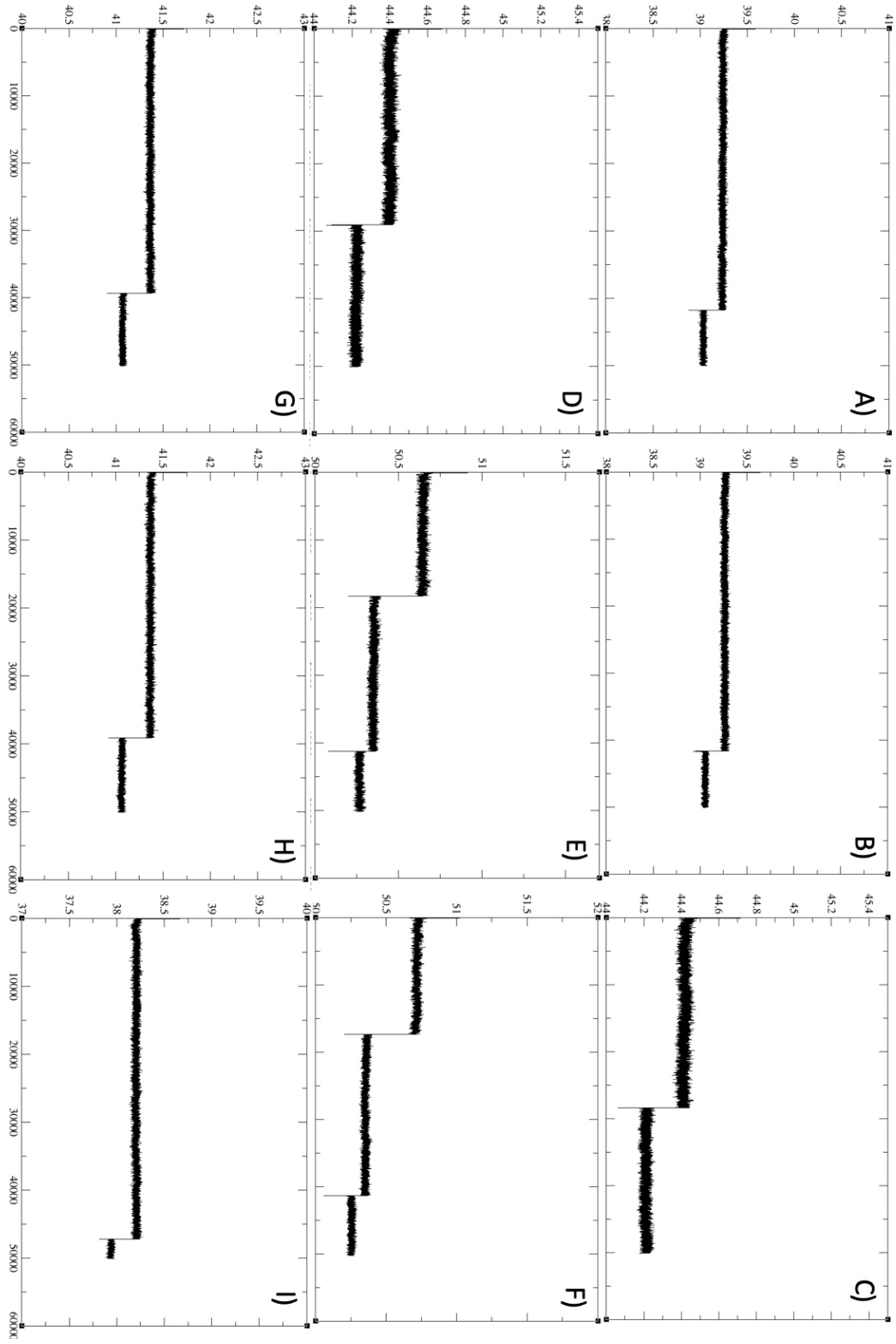

Figure A.23 Root mean square fluctuation of complexes under investigation. Plots A) to I) are showing RMSD from Ligand 1 to 9. Y-axis is showing RMSF in Å and X-axis is showing the residue number.

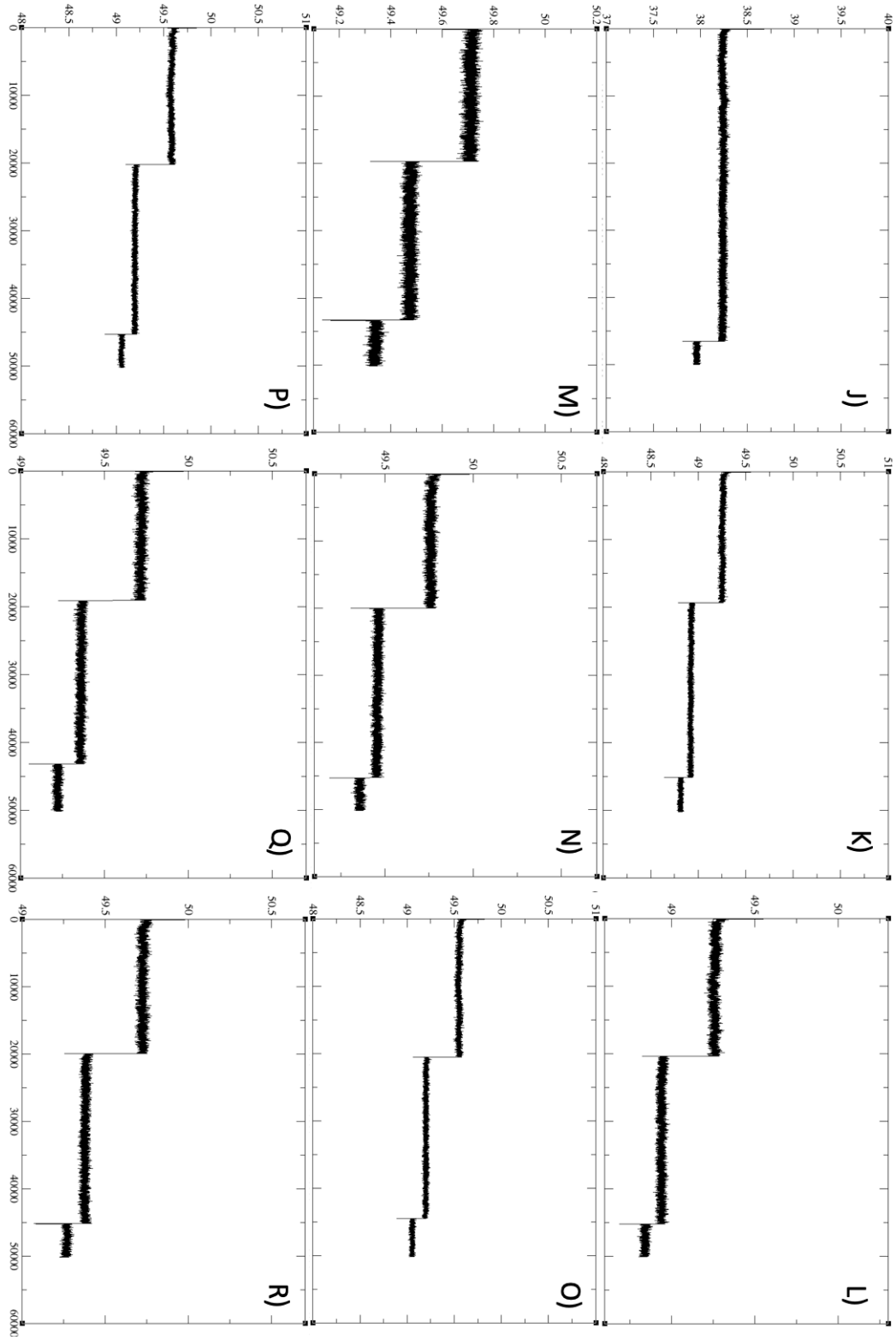

Figure A.24 Root mean square fluctuation of complexes under investigation. Plots J) to R) are showing RMSD from Ligand 10 to 18. Y-axis is showing RMSF in Å and X-axis is showing the residue number.

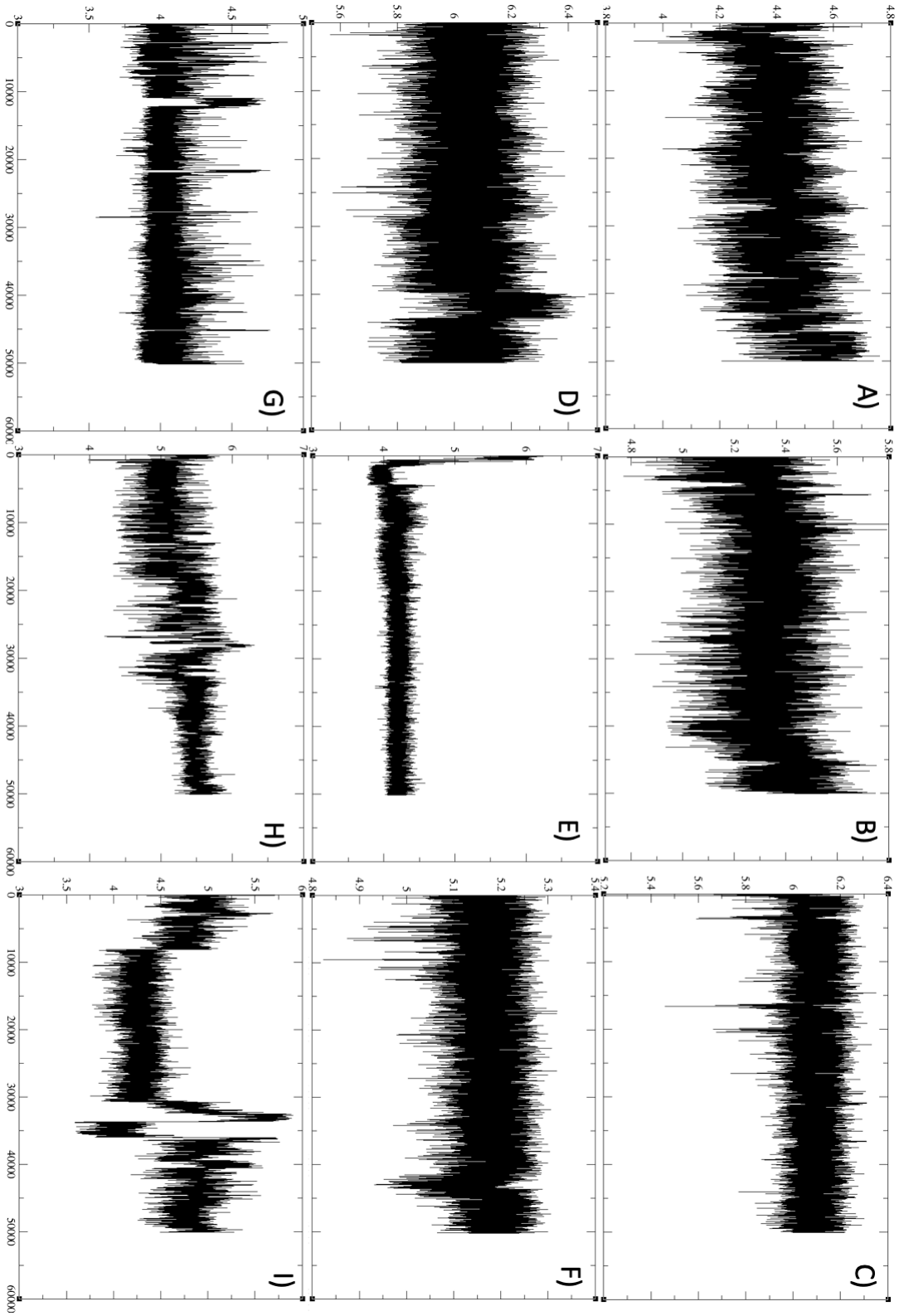

Figure A.25 Radius of Gyration of ligands under investigation. Plots A) to I) are showing RoG from Ligand 1 to 9. Y-axis is showing RoG in Å and X-axis is showing the frame number of the MD simulation trajectory.

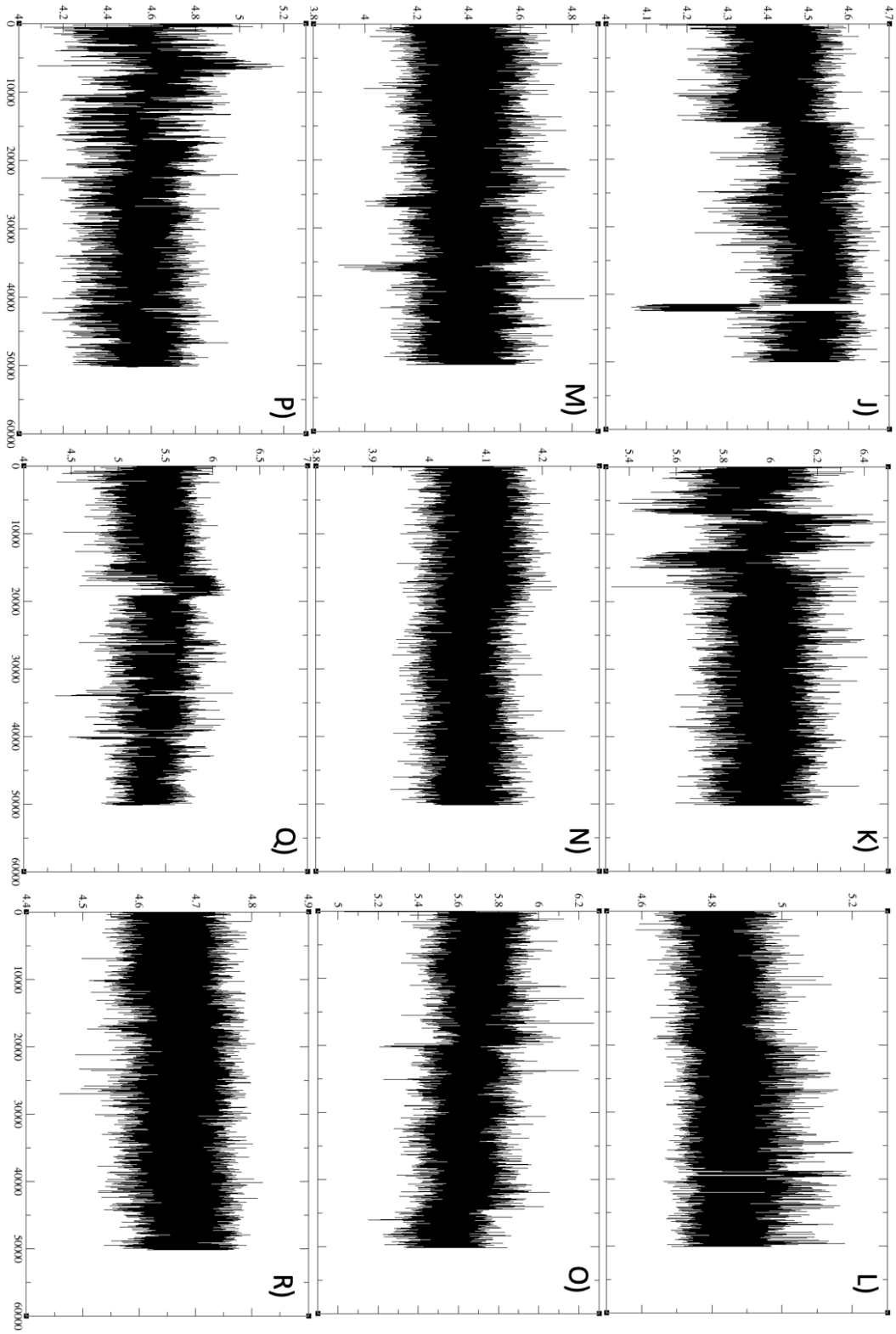

Figure A.26 Radius of Gyration of ligands under investigation. Plots J) to R) are showing RoG from Ligand 10 to 18. Y-axis is showing RoG in Å and X-axis is showing the frame number of the MD simulation trajectory.

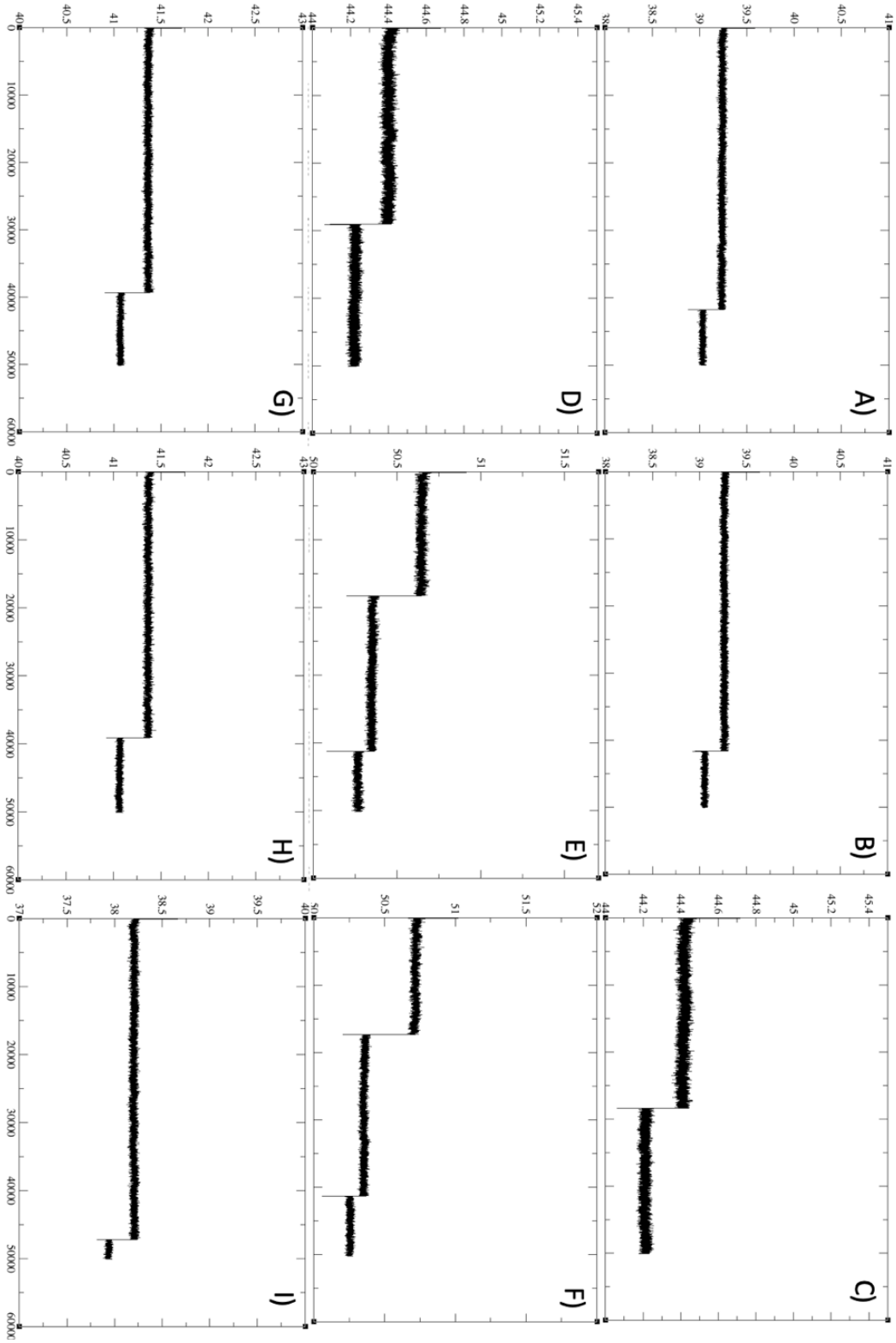

Figure A.27 Radius of Gyration of complexes under investigation. Plots A) to I) are showing RoG from complex 1 to 9. Y-axis is showing RoG in Å and X-axis is showing the frame number of the MD simulation trajectory.

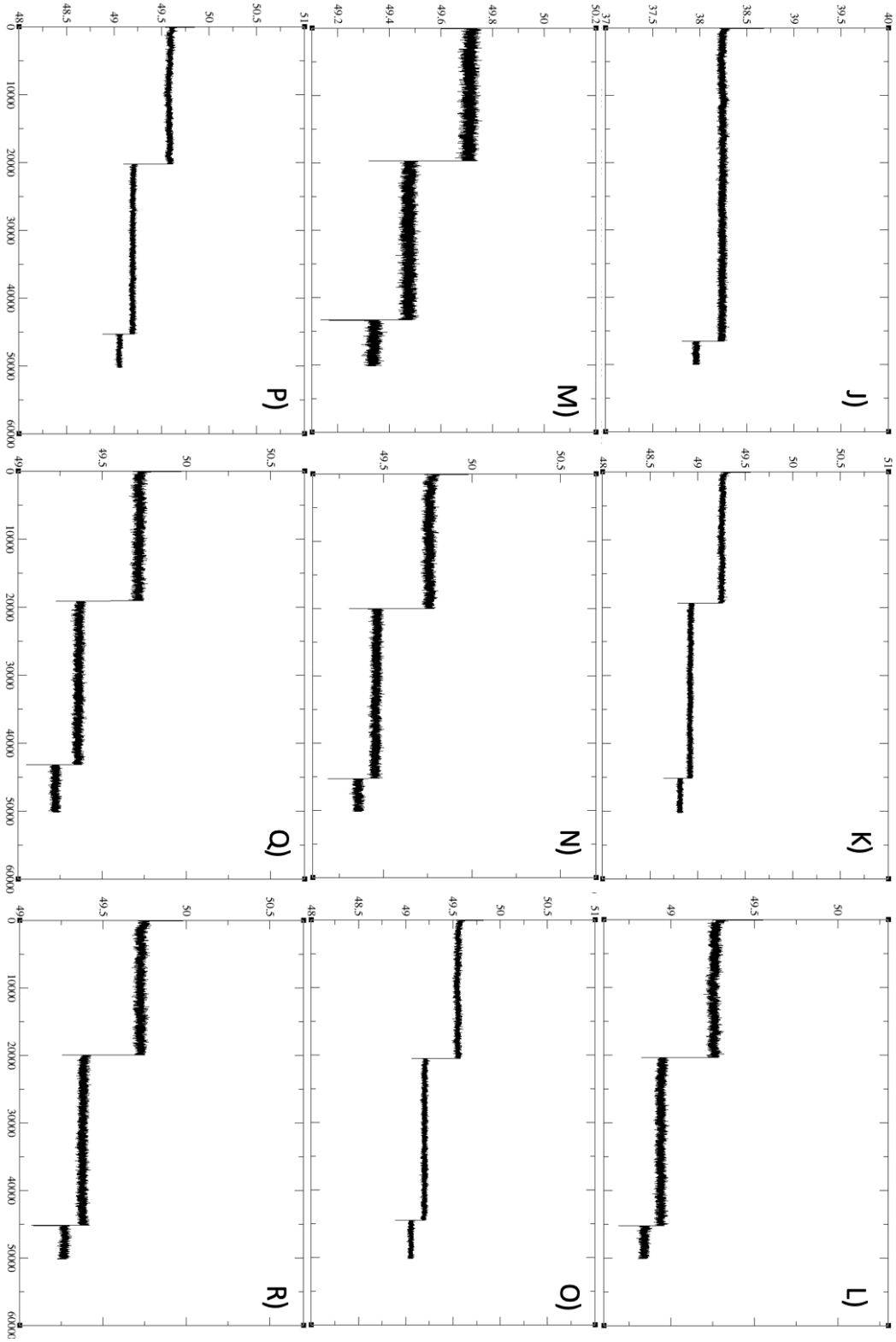

Figure A.28 Radius of Gyration of complexes under investigation. Plots J) to R) are showing RoG from complex 10 to 18. Y-axis is showing RoG in Å and X-axis is showing the frame number of the MD simulation trajectory.

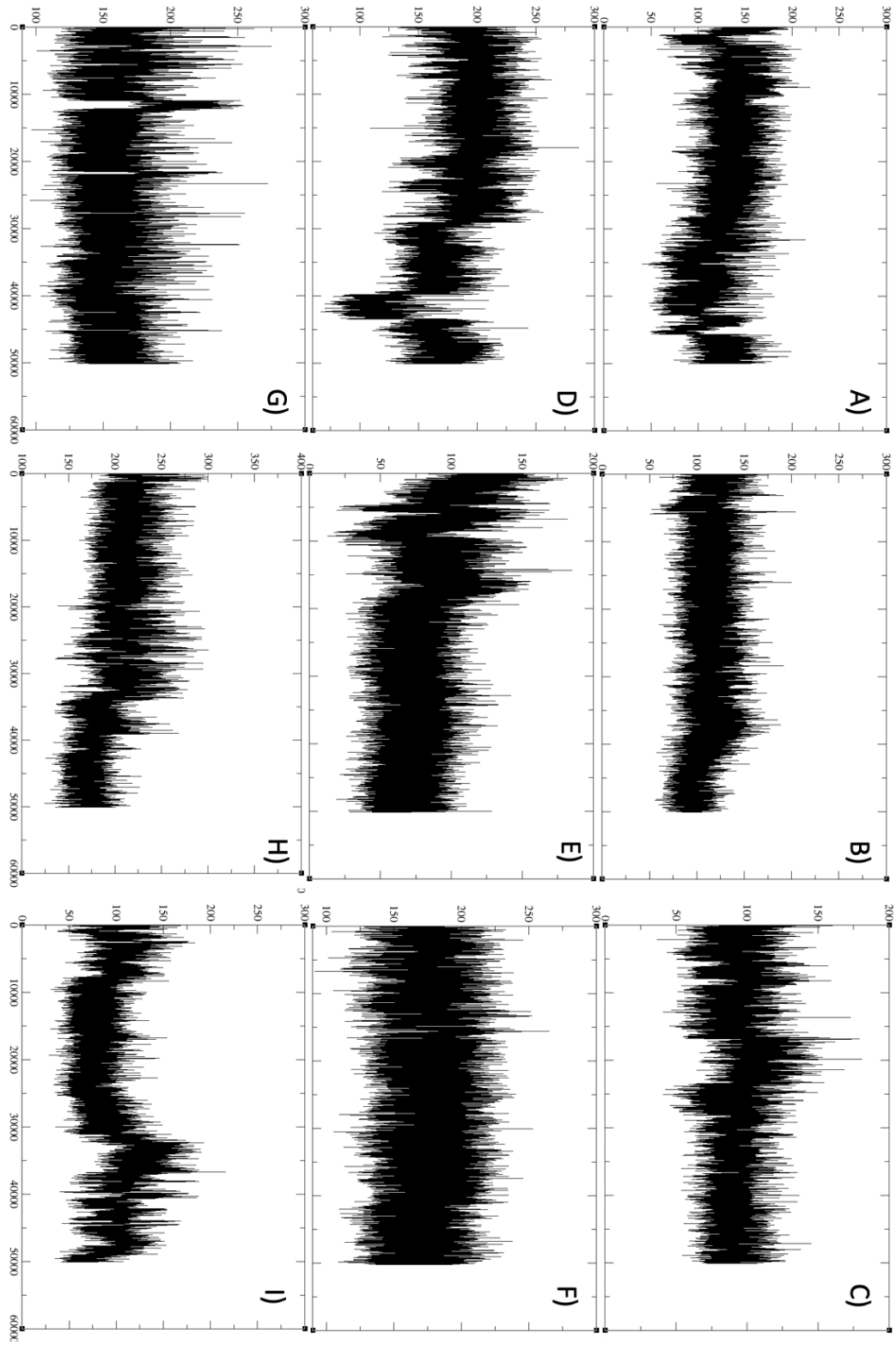

Figure A.29 Solvent accessible surface area (SASA) of complexes under investigation. Plots A) to I) are showing SASA from complex 1 to 9. Y-axis is showing SASA in $Å^2$ and X-axis is showing the frame number of the MD simulation trajectory.

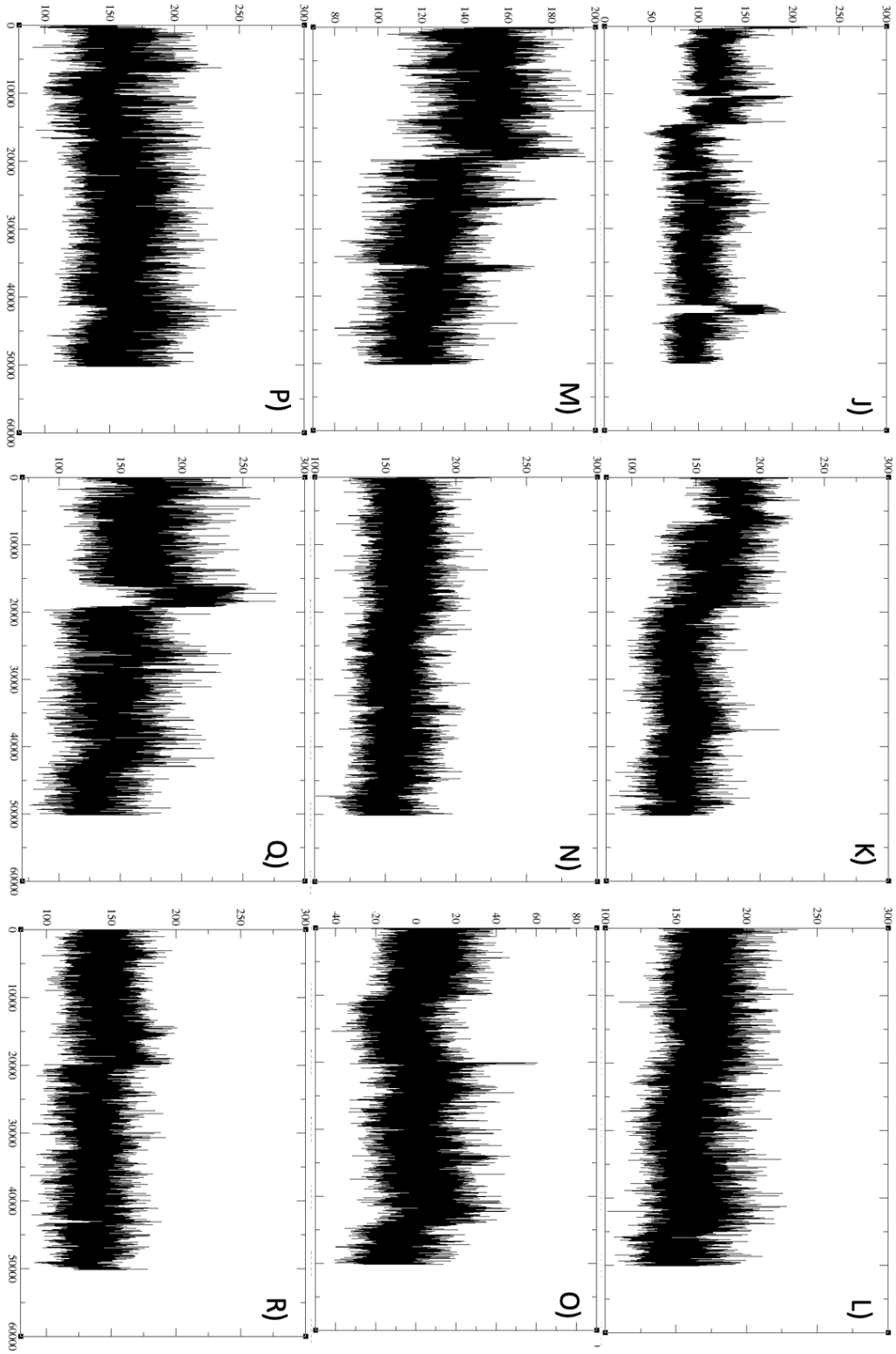

Figure A.30 Solvent accessible surface area (SASA) of complexes under investigation. Plots J) to R) are showing SASA from complex 10 to 18. Y-axis is showing SASA in $Å^2$ and X-axis is showing the frame number of the MD simulation trajectory.

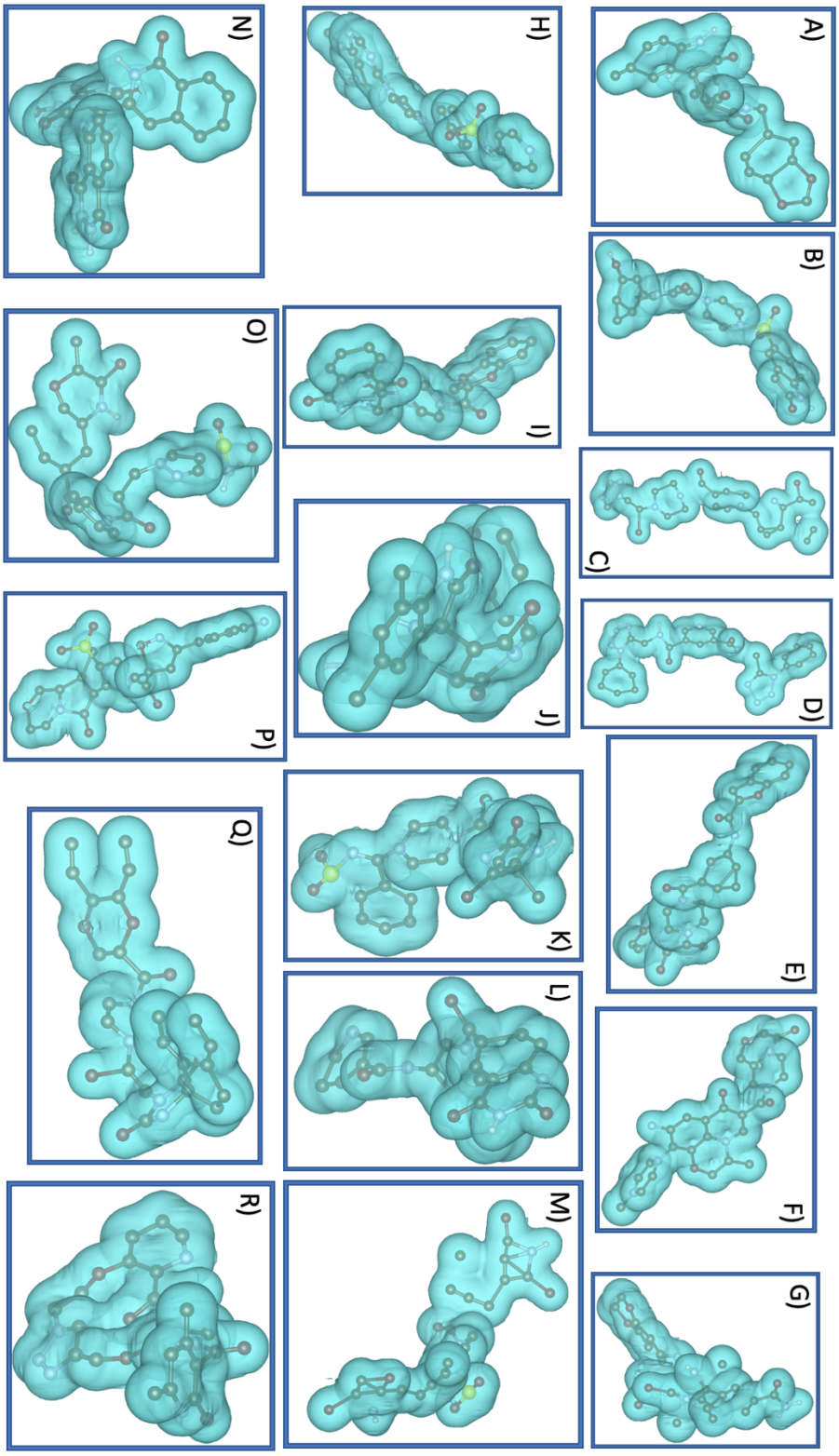

Figure A.31 Molecular electrostatic map analysis of all 18 Complexes under investigation. Plots A) to R) are showing complex 1 to 18. Blue color indicates electrons deficient and red means electrons rich areas/volumes.

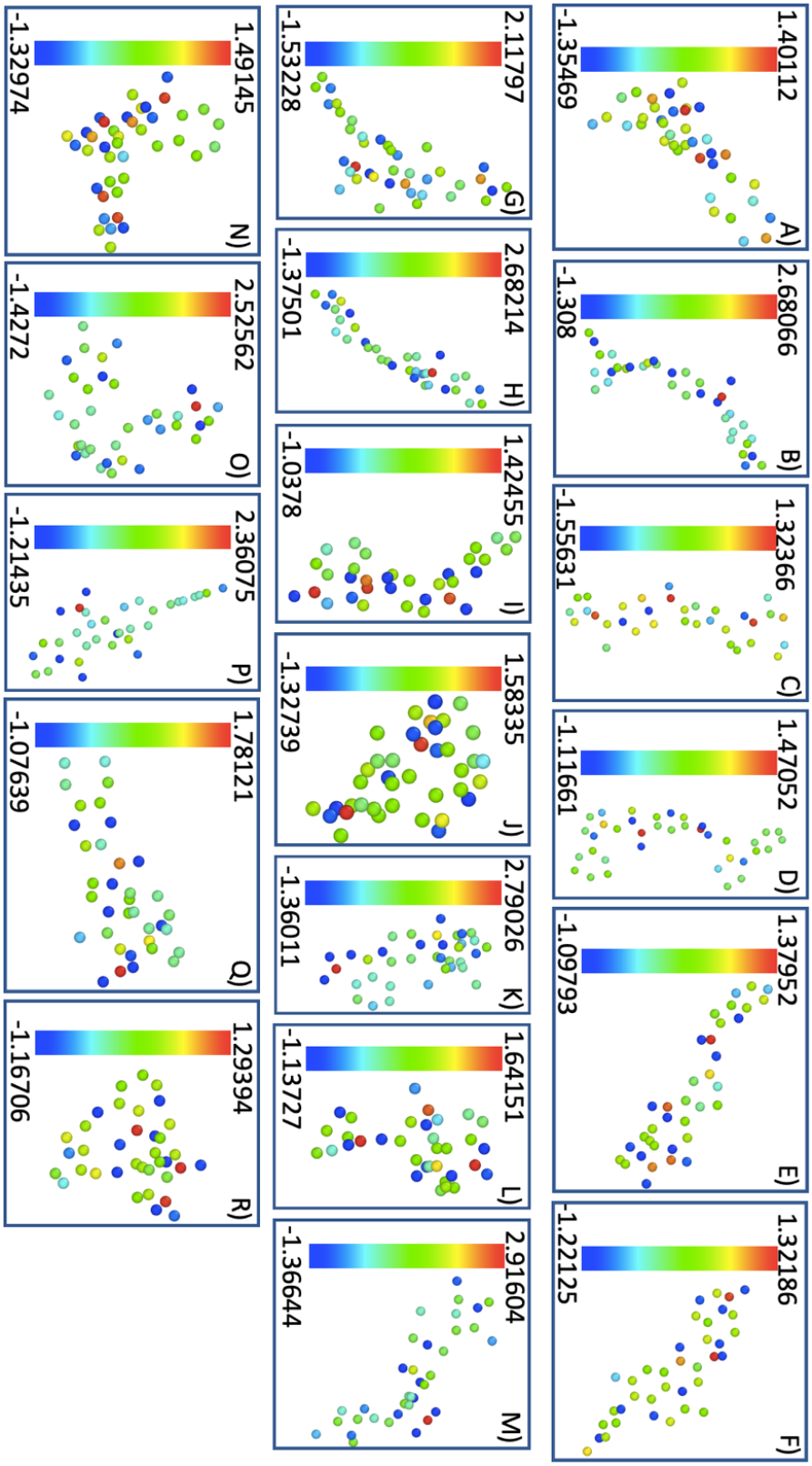

Figure A.32 Bader charge analysis of all 18 Complexes under investigation. Plots A) to R) are showing complex 1 to 18. Inset ligand is showing the charge transfer(eV).

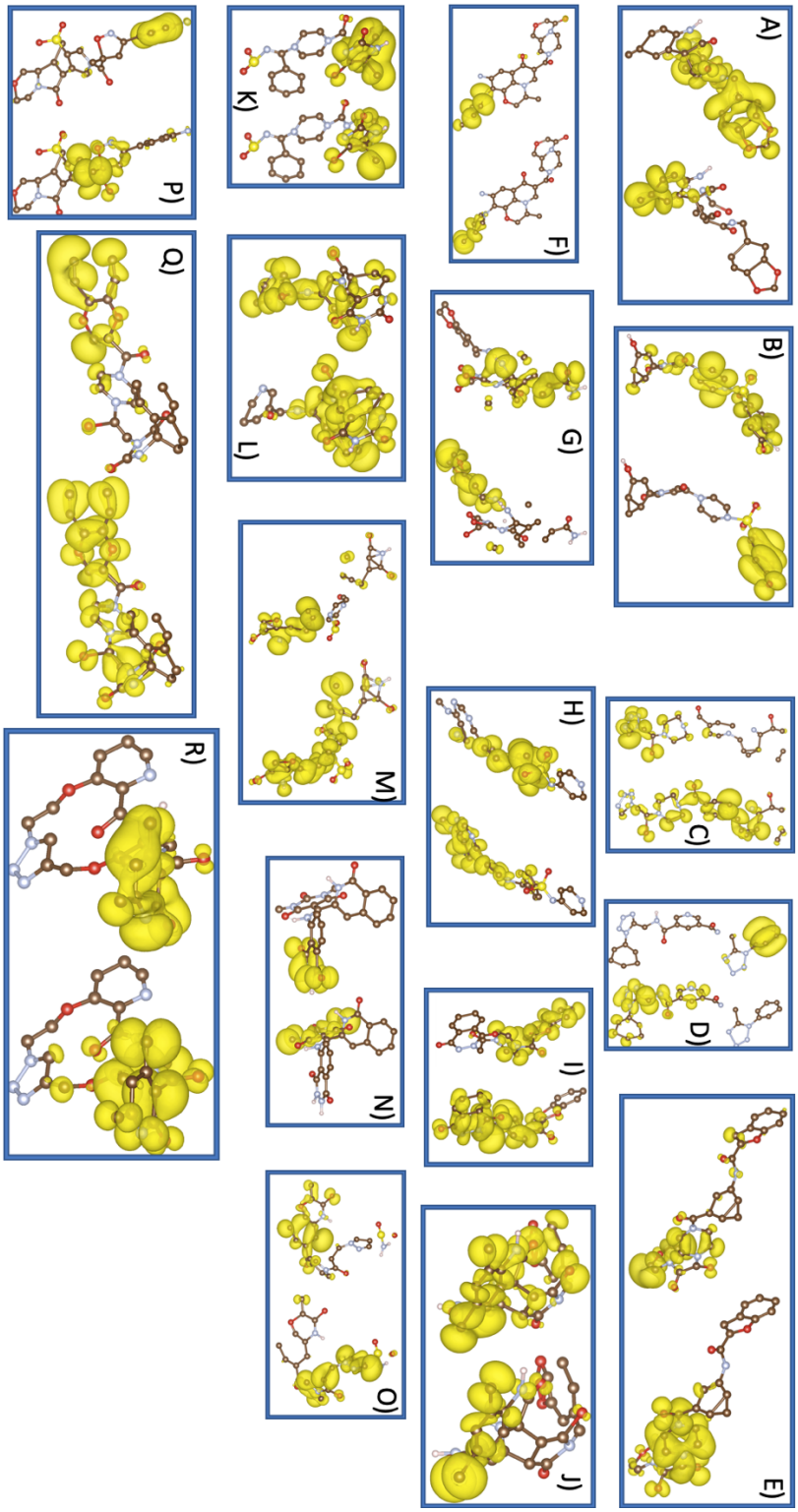

Figure A.33 Frontier molecular orbital analysis of all 18 Complexes under investigation. Plots A) to R) are showing complex 1 to 18. Left part of each figure shows HOMO-isofurfaces and right side shows LUMO-isosurfaces.

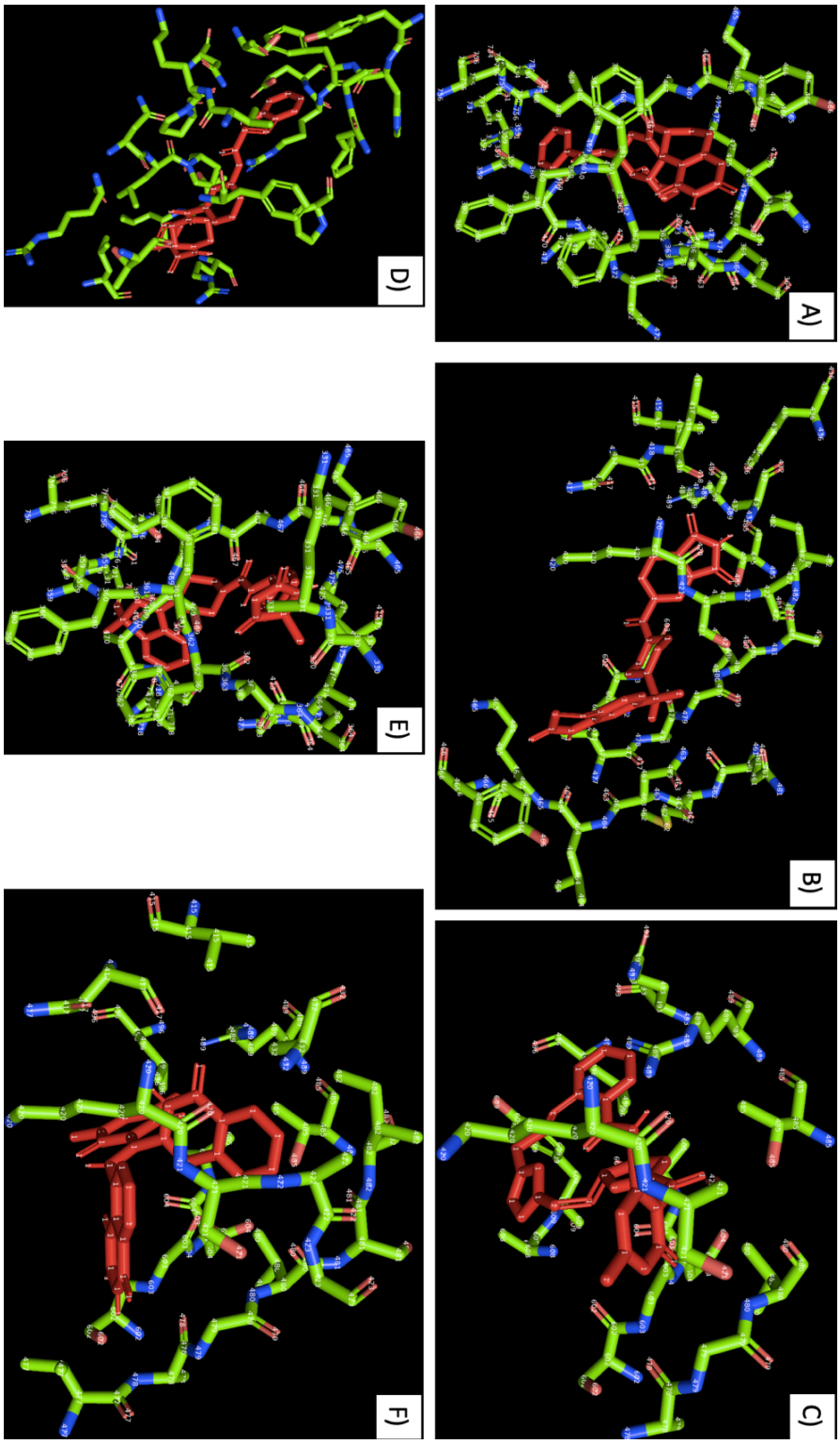

Figure A.34 Stick representation of residues within 5Å of ligands. 12th, 13th, 18th ligands (lowest RMSD sub-group) are shown in A), B), and C), respectively. 5th, 11th, 14th ligands (highest RMSD sub-group) are shown in D), E), and F), respectively. Ligand is represented in red.

APPENDIX B

SUPPLIMENTARY TABLES

Table B.1 to B.7 show supplementary data cited with explanatory texts within the chapters.

Table B.1 Number of Carbon Atoms in the Upper and Lower Graphene for Different θ_{IAW}

	$\theta_{IAW} = 6°$	$\theta_{IAW} = 11°$	$\theta_{IAW} = 16°$	$\theta_{IAW} = 21°$
Number of C in the Upper 'Graphene with Wrinkles'	1920	1920	1920	1920
Number of C in Lower Flat Graphene	1888	1824	1728	1600
Carbon Atom Ratio (CAR) between the Upper Graphene and Lower Graphene	1.0169	1.0526	1.1111	1.2000

Table B.2 Number of Water Molecules for Different Cases

Water Layer	$\theta_{IAW} = 6°$	$\theta_{IAW} = 11°$	$\theta_{IAW} = 16°$	$\theta_{IAW} = 21°$
0	0	0	0	0
2	384	368	352	320
4	768	736	704	640
6	1152	1104	1056	960

Table B.3 Angle of Curvature Measurements for 2-Layer Cases

IAW (θ_{IAW})	Initial angle	Final angle	% Change
6°	24.0365°	39.1605°	62.92
11°	50.4876°	63.4349°	25.64
16°	70.2189°	75.5792°	7.63
21°	93.1162°	97.8855°	-5.12

Table B.4 Hydrogen Bond Analysis from 1st o 18th Ligand. High RMSD and Low RMSD Ligands Sub-Groups Excluded from Below Table Because those are Given in Main Manuscript

Longest Lifespan	Total Frames	Atoms/Residues Identity
1st Ligand		
4	958	LIG_307@O5-SER_144@N-H
9	4090	LIG_307@O1-GLY_143@N-H
8	7445	LIG_307@O5-HIE_163@NE2-HE2
26	13168	ASP_187@O-LIG_307@N-H
26	29058	HIE_164@O-LIG_307@N1-H1
2nd Ligand		
4	1046	LIG_307@O1-GLN_189@NE2-HE22
30	1565	THR_190@O-LIG_307@O2-H
9	5083	THR_25@OG1-LIG_307@N3-H1
18	7277	GLU_166@O-LIG_307@O2-H
24	12314	ARG_188@O-LIG_307@O2-H
11	14543	LIG_307@O3-GLY_143@N-H
3rd Ligand		
2	61	LIG_598@N6-GLY_336@N-H
3	273	LIG_598@O-GLY_336@N-H
2	336	LIG_598@N5-GLY_334@N-H
5	475	LIG_598@O2-GLN_78@NE2-HE21
4	4719	LIG_598@N4-GLY_334@N-H
4th Ligand		
1	30	LIG_598@N-PHE_372@N-H
2	115	LIG_598@N5-GLY_336@N-H
2	351	LIG_598@N4-GLY_336@N-H
25	9455	GLU_19@OE1-LIG_598@N1-H
26	13267	GLU_19@OE2-LIG_598@N1-H
6th Ligand		
1	2	LIG_860@O2-TYR_288@OH-HH
1	8	LIG_860@O2-SER_606@OG-HG
8	6626	LIG_860@O1-PHE_338@N-H
7th Ligand		
5	1202	LIG_314@O4-GLN_267@NE2-HE22
12	1476	GLY_161@O-LIG_314@N3-H3
40	14604	GLU_165@OE2-LIG_314@N4-H4
21	18119	ASN_265@O-LIG_314@N-H
52	27436	GLU_165@OE1-LIG_314@N4-H4
8th Ligand		
1	76	LIG_314@N3-LEU_160@N-H
1	78	LIG_314@N4-LEU_160@N-H
7	87	LIG_314@O2-GLN_267@NE2-HE22
13	295	LIG_314@O2-TYR_271@OH-HH
19	7378	LIG_314@O2-TYR_262@OH-HH

Table B.4 Hydrogen Bond Analysis from 1st o 18th Ligand. High RMSD and Low RMSD Ligands Sub-Groups Excluded from Below Table Because those are Given in Main Manuscript

(Continue)

9th Ligand		
3	40	LIG_306@O4-GLN_189@NE2-HE22
2	43	LIG_306@O1-GLN_189@NE2-HE22
2	140	LIG_306@N3-GLN_192@NE2-HE22
4	1836	LIG_306@O4-THR_190@N-H
7	8232	LIG_306@O4-GLN_192@NE2-HE22
10th Ligand		
25	1029	GLN_189@OE1-LIG_306@N1-H1
4	1159	LIG_306@O3-HIE_163@NE2-HE2
7	3236	HIE_164@ND1-LIG_306@N3-H3
7	3268	HIE_164@ND1-LIG_306@N3-H2
18	3906	GLN_189@OE1-LIG_306@N-H
9	4038	HIE_164@O-LIG_306@N3-H3
13	4165	HIE_164@O-LIG_306@N3-H2
6	4577	ARG_188@O-LIG_306@N1-H1
20	14238	LIG_306@O1-HIE_41@NE2-HE2
15th Ligand		
5	1726	LIG_835@O4-ARG_544@NE-HE
3	1738	LIG_835@O-ARG_473@NH2-HH22
12	3272	ASP_538@OD1-LIG_835@N1-H
17	6081	ASP_538@OD2-LIG_835@N1-H
10	6604	LIG_835@O3-TYR_539@N-H
10	10279	LIG_835@N4-SER_602@N-H
217	46200	LIG_835@O4-ARG_544@NH2-HH21
16th Ligand		
5	305	LIG_835@O1-ARG_475@NE-HE
12	897	LIG_835@O1-ARG_475@NH2-HH22
22	2111	LIG_835@O1-ARG_475@NH1-HH11
4	2844	LIG_835@F-SER_602@N-H
68	34504	LIG_835@O-ASP_543@N-H
17th Ligand		
1	8	LIG_835@O1-ASN_416@ND2-HD21
2	17	LIG_835@O1-ALA_608@N-H
1	35	LIG_835@O5-ARG_489@NH2-HH21
6	227	LIG_835@O4-ARG_489@NH2-HH21
2	241	LIG_835@O-THR_607@OG1-HG1

Table B.5 Quantum Chemical Characteristics of All 18 Ligands Calculated with Ab-Initio Modelling

Ligand No.	E_gap(eV)	Ita(eV)	Omega(eV)	Sigma(eV^{-1})	Zita(eV)
1	.7236	.36180	38.9062	2.7639	5.3059
2	.9955	.49775	40.1998	2.0090	6.3260
3	.7562	.37810	47.5097	2.6448	5.9939
4	1.1517	.57585	35.3777	1.7365	6.3831
5	1.3002	.65010	29.7471	1.5382	6.2191
6	1.1835	.59175	33.5398	1.6899	6.3003
7	.9108	.45540	42.0849	2.1958	6.1912
8	.8463	.42315	50.1315	2.3632	6.5135
9	1.3228	.66140	25.5309	1.5119	5.8114
10	.8057	.40285	37.6987	2.4823	5.5112
11	.8070	.40350	50.9861	2.4783	6.4145
12	.8585	.42925	50.5960	2.3296	6.5906
13	.8337	.41685	38.4998	2.3989	5.6654
14	1.1803	.59015	25.0457	1.6944	5.4370
15	.8475	.42375	44.4492	2.3598	6.1376
16	.7568	.37840	51.1703	2.6427	6.2230
17	1.0553	.52765	44.8976	1.8951	6.8833
18	1.0814	.54070	34.9425	1.8494	6.1471

Table B.6 Relationship Between Complex/Ligand/Protein Number and Complex/Ligand/Protein's Identity Based Upon RCSB and ZINC Format along with RMSD of Optimized Ligand Structures from Known X-Ray Diffraction Solutions

Complex Number	**Complex Identity**	**RMSD with known diffraction solution (Å)**
1	6lu7_N3/ZINC000015959516	0.80
2	6lu7_N3/ZINC000596245498	1.29
3	6m0j_+/ZINC000590498462	0.74
4	6m0j_+/ZINC000593073653	1.50
5	6m71_nsp12_7_8/ZINC000410177506	0.47
6	6m71_nsp12_7_8/ZINC000495219491	0.95
7	6w9c_+/ZINC000004260192	0.98
8	6w9c_+/ZINC000916475592	0.77
9	6w63_x77/ZINC000012883288	0.68
10	6w63_x77/ZINC000015959596	0.81
11	7bv2_nsp12-7/ZINC000616537204	1.10
12	7bv2_nsp12-7/ZINC001176619532	0.83
13	7bv2_nsp12-8/ZINC000517580540	0.78
14	7bv2_nsp12-8/ZINC001180048431	0.64
15	7bv2_remdesivir/ZINC000596164676	0.73
16	7bv2_remdesivir/ZINC001180454492	0.84
17	7bv2_rna/ZINC000760123550	0.94
18	7bv2_rna/ZINC000952855827	0.54

Table B.7 RMSD of Minimized Proteins Structures and Structural Qualities by Using Molprobity Server

Complex Number	Complex Identity	Minimized protein RMS (Å)	Clashscore (MolProbity)	MolProbity score
1	6lu7_N3	8.6430E-02	0.86, 99th percentile	1.65, 91st percentile
2	6m0j_+	7.8446E-02	0.53, 99th percentile	1.48, 96th percentile
3	6m71_nsp12_7_8	1.6191E-01	0.07, 99th percentile	1.57, 93rd percentile
4	6w9c_+	7.6707E-02	0.2, 99th percentile	1.44, 96th percentile
5	6w63_x77	1.6915E-01	0, 100th percentile	1.24, 99th percentile
6	7bv2_nsp12-7	7.6304E-02	0.23, 99th percentile	1.54, 94th percentile
7	7bv2_nsp12-8	1.2998E-01	0.15, 99th percentile	1.60, 92nd percentile
8	7bv2_remdesivir	1.0331E-01	0.15, 99th percentile	1.61, 92nd percentile
9	7bv2_rna	8.2819E-02	0.38, 99th percentile	1.61, 92nd percentile

APPENDIX C

SUPPLEMENTARY MATERIALS

Additional research data and information recommended by the committee members.

Interaction between atoms for molecular dynamics approach was modeled using ReaxFF in LAMMPS (Chapter 2, 3) and General AMBER Force Fields (Chapter 4) in AMBER code. These codes use equation (A) for modeling interactions between any two atoms (bonds + angles+ dihedrals + non-bonded interactions) as explained by Wang et al. [167]. Here, r_{eq} and θ_{eq} are equilibration structural parameters; Kr, K_θ, and V_n are force constants; n is the multiplicity factor, and **the** torsional angle's phase is denoted by γ. The A, B, and q parameters characterize the nonbonded potentials.

$$E_{\text{pair}} = \sum_{\text{bonds}} k_r(r - r_{\text{eq}})^2 + \sum_{\text{angles}} k_\theta(\theta - \theta_{\text{eq}})^2 + \sum_{\text{dihedrals}} \frac{v_n}{2} \times [1 + \cos(n\phi - \gamma)] + \sum_{i<j} \left[\frac{A_{ij}}{R_{ij}^{12}} - \frac{B_{ij}}{R_{ij}^{6}} + \frac{q_i q_j}{\varepsilon R_{ij}}\right] \quad \text{Eq. (A)}$$

Additionally, all nine different binding sites of 6 proteins (Chapter 4) in this project were carefully selected from experimental works as cited in the main text of Chapter 4. As explained in Section 4.2.2, the AMBER code uses quantum mechanics to parameterize the force field of those atoms of the molecules for which experimental parametrization is not available. AMBER uses B3LYP/6-31g(d) based Kohn-Sham Density Functional Theory to parametrize the Eq (A) for unknown molecules. The primary shortcoming of the Density Functional Theory is the approximation of the Exchange Correlation energy functional, i.e.$V_{XC}(r)$ in [(Equation (B)].

$$\left(-\frac{h}{2m}\nabla^2 + V_{n-e}(r) + V_{e-e}(r) + V_{XC}(r)\right)\phi_i(r) = \in_i \quad \phi_i(r) \qquad \text{Eq. (B)}$$

Where, h = Planck's constant; m= electron mass, $V_{n\text{-}e}(r)$, $V_{e\text{-}e}(r)$, $V_{xc}(r)$ are nucleus-electron potential, electron-electron potential; and Φ (r) is a wavefunction and ε_i are eigen values of energy matrix.

Multiple phenomena are difficult to capture in the Exchange and Correlation Energies. Exchange energy is defined as energy produced when two identical sub-atomic particles, i.e., electrons, etc., with the same spin swap positions in a degenerate orbital of a subshell. Correlation energy measures the difference between true ground state energy and Hartree-Fock approximation-based ground state energy. Exchange Correlation functional is used in the Hamiltonian operator to predict Exchange and Correlation energies. Two famous Exchange-Correlational functions are Local Density Approximations (LDA) and Perdew–Burke–Ernzerhof (PBE).

Although effective for general problems, these functions are still not universally accurate. Along with other exchange correlational functionals, these functionals incorporate multiple errors that can be primarily streamlined into two sources, i.e., static correlation and delocalization error. These errors arrive from the self-interaction of the electron. When a distributed wavefunction representing the electron density interacts with electron density located locally around that same electron, it creates a repulsion force. This repulsion force shall not be present in the system since the electron cannot interact with itself in a physical setup. This force causes errors in calculating the bandgap (electronic and optical), binding energies, frontier molecule orbital energies, excitons energies, etc.

Exchange correlation functional tends to be non-variational, making them difficult to improve by incorporating additional variables due to self-countering tendency. While it is believed that there must exist an Exchange-Correlational functional that can produce correct results while capturing unknown variables of the true Hamiltonian but so far it has been only approximated by using semi-empirical approaches. Furthermore, DFT has a shortcoming in modeling the long-range noncovalent interactions, thus resulting in careful use of this model for large proteins or systems with dispersed small molecules. For instance, we have obtained +/- 5 percent deviation in the results for molecular dynamics trajectories for 100 nanoseconds which may be attributed to these limitations of the DFT functionals. Additionally, as mentioned in the Methodology section of Chapters 2 and 3, the ReaxFF force field shall be used carefully for high temperatures due to the complexity of real-time tracking of bond breakage and formation, which we believe has attributed to high deviations in MD trajectories obtained in NPT and NVT ensemble resulting into high simulation cell volumes as similar effects were observed by Li et al. [114].

REFERENCES

[1] Deng, S., and Berry, V., 2016, "Wrinkled, Rippled and Crumpled Graphene: An Overview of Formation Mechanism, Electronic Properties, and Applications," Mater. Today, **19**(4), pp. 197–212.

[2] Das Sarma, S., Adam, S., Hwang, E. H., and Rossi, E., 2011, "Electronic Transport in Two-Dimensional Graphene," Rev. Mod. Phys., **83**(2), pp. 407–470.

[3] Zang, J., Ryu, S., Pugno, N., Wang, Q., Tu, Q., Buehler, M. J., and Zhao, X., 2013, "Multifunctionality and Control of the Crumpling and Unfolding of Large-Area Graphene," Nat. Mater., **12**, p. 321.

[4] Kumar, K., Kim, Y.-S., and Yang, E.-H., 2013, "The Influence of Thermal Annealing to Remove Polymeric Residue on the Electronic Doping and Morphological Characteristics of Graphene," Carbon N. Y., **65**, pp. 35–45.

[5] Zhang, Y., Zhang, L., and Zhou, C., 2013, "Review of Chemical Vapor Deposition of Graphene and Related Applications," Acc. Chem. Res., **46**(10), pp. 2329–2339.

[6] Schniepp, H. C., Li, J.-L., McAllister, M. J., Sai, H., Herrera-Alonso, M., Adamson, D. H., Prud'homme, R. K., Car, R., Saville, D. A., and Aksay, I. A., 2006, "Functionalized Single Graphene Sheets Derived from Splitting Graphite Oxide," J. Phys. Chem. B, **110**(17), pp. 8535–8539.

[7] Becerril, H. A., Mao, J., Liu, Z., Stoltenberg, R. M., Bao, Z., and Chen, Y., 2008, "Evaluation of Solution-Processed Reduced Graphene Oxide Films as Transparent Conductors," ACS Nano, **2**(3), pp. 463–470.

[8] Schedin, F., Geim, A. K., Morozov, S. V, Hill, E. W., Blake, P., Katsnelson, M. I., and Novoselov, K. S., 2007, "Detection of Individual Gas Molecules Adsorbed on Graphene," Nat. Mater., **6**, p. 652.

[9] Nunna, B. B., Mandal, D., Lee, J. U., Singh, H., Zhuang, S., Misra, D., Bhuyian, M. N. U., and Lee, E. S., 2019, "Detection of Cancer Antigens (CA-125) Using Gold Nano Particles on Interdigitated Electrode-Based Microfluidic Biosensor," Nano Converg., **6**(1), p. 3.

[10] Pereira, V. M., Castro Neto, A. H., Liang, H. Y., and Mahadevan, L., 2010, "Geometry, Mechanics, and Electronics of Singular Structures and Wrinkles in Graphene," Phys. Rev. Lett., **105**(15), p. 156603.

[11] Oyewole, O. K., Yu, D., Du, J., Asare, J., Oyewole, D. O., Anye, V. C., Fashina, A., Zebaze Kana, M. G., and Soboyejo, W. O., 2015, "Micro-Wrinkling and Delamination-Induced Buckling of Stretchable Electronic Structures," J. Appl. Phys., **117**(23), p. 235501.

[12] Chae, S. H., Yu, W. J., Bae, J. J., Duong, D. L., Perello, D., Jeong, H. Y., Ta, Q. H., Ly, T. H., Vu, Q. A., Yun, M., Duan, X., and Lee, Y. H., 2013, "Transferred Wrinkled Al2O3 for Highly Stretchable and Transparent Graphene–Carbon Nanotube Transistors," Nat. Mater., **12**(5), pp. 403–409.

[13] Li, Y., 2016, "Reversible Wrinkles of Monolayer Graphene on a Polymer Substrate: Toward Stretchable and Flexible Electronics," Soft Matter, **12**(13), pp. 3202–3213.

[14] Raghav, N., Chakraborty, S., and Maiti, P. K., 2015, "Molecular Mechanism of Water Permeation in a Helium Impermeable Graphene and Graphene Oxide Membrane," Phys. Chem. Chem. Phys., **17**(32), pp. 20557–20562.

[15] Wang, Y., Yang, R., Shi, Z., Zhang, L., Shi, D., Wang, E., and Zhang, G., 2011, "Super-Elastic Graphene Ripples for Flexible Strain Sensors," ACS Nano, **5**(5), pp. 3645–3650.

[16] Yan, Z. G., Wang, B. L., and Wang, K. F., 2019, "Stretchability and Compressibility of a Novel Layout Design for Flexible Electronics Based on Bended Wrinkle Geometries," Compos. Part B Eng., **166**, pp. 65–73.

[17] Sakorikar, T., Vayalamkuzhi, P., and Jaiswal, M., 2020, "Geometry Dependent Performance Limits of Stretchable Reduced Graphene Oxide Interconnects: The Role of Wrinkles," Carbon N. Y., **158**, pp. 864–872.

[18] Polywka, A., Jakob, T., Stegers, L., Riedl, T., and Görrn, P., 2015, "Facile Preparation of High-Performance Elastically Stretchable Interconnects," Adv. Mater., **27**(25), pp. 3755–3759.

[19] Sharma, B. K., Jang, B., Lee, J. E., Bae, S.-H., Kim, T. W., Lee, H.-J., Kim, J.-H., and Ahn, J.-H., 2013, "Load-Controlled Roll Transfer of Oxide Transistors for Stretchable Electronics," Adv. Funct. Mater., **23**(16), pp. 2024–2032.

[20] Cantarella, G., Münzenrieder, N., Petti, L., Vogt, C., Büthe, L., Salvatore, G. A., Daus, A., and Tröster, G., 2015, "Flexible In–Ga–Zn–O Thin-Film Transistors on Elastomeric Substrate Bent to 2.3% Strain," IEEE Electron Device Lett., **36**(8), pp. 781–783.

[21] Feng, C., Yi, Z., Dumée, L. F., Garvey, C. J., She, F., Lin, B., Lucas, S., Schütz, J., Gao, W., Peng, Z., and Kong, L., 2015, "Shrinkage Induced Stretchable Micro-Wrinkled Reduced Graphene Oxide Composite with Recoverable Conductivity," Carbon N. Y., **93**, pp. 878–886.

[22] Oh, J., Kim, J. Y., Park, C. W., Jung, S. W., Na, B. S., Lee, K., Park, N., Lee, S. S., Koo, J. B., and Hwang, C., 2016, "Spontaneously Formed Wrinkled Substrates for Stretchable Electronics Using Intrinsically Rigid Materials," IEEE Electron Device Lett., **37**(5), pp. 588–590.

[23] Cantarella, G., Vogt, C., Hopf, R., Münzenrieder, N., Andrianakis, P., Petti, L., Daus, A., Knobelspies, S., Büthe, L., Tröster, G., and Salvatore, G. A., 2017, "Buckled Thin-Film Transistors and Circuits on Soft Elastomers for Stretchable Electronics," ACS Appl. Mater. Interfaces, **9**(34), pp. 28750–28757.

[24] Oh, J., Yoon, H. S., Kim, W. K., Kim, S. J., Lee, S. C., Jung, Y., Park, J. Y., and Jun, S. C., 2018, "Flexible Radio Frequency Interconnect of Reduced Graphene Oxide," 2D Mater., **5**(3), p. 35030.

[25] Nirmalraj, P. N., Thodkar, K., Guerin, S., Calame, M., and Thompson, D., 2018, "Graphene Wrinkle Effects on Molecular Resonance States," npj 2D Mater. Appl., **2**(1), p. 8.

[26] Hu, H.-W., Haider, G., Liao, Y.-M., Roy, P. K., Ravindranath, R., Chang, H.-T., Lu, C.-H., Tseng, C.-Y., Lin, T.-Y., Shih, W.-H., and Chen, Y.-F., 2017, "Wrinkled 2D Materials: A Versatile Platform for Low-Threshold Stretchable Random Lasers," Adv. Mater., **29**(43), p. 1703549.

[27] Chang, T.-H., Tian, Y., Li, C., Gu, X., Li, K., Yang, H., Sanghani, P., Lim, C. M., Ren, H., and Chen, P.-Y., 2019, "Stretchable Graphene Pressure Sensors with Shar-Pei-like Hierarchical Wrinkles for Collision-Aware Surgical Robotics," ACS Appl. Mater. Interfaces, **11**(10), pp. 10226–10236.

[28] Jia, J., Huang, G., Deng, J., and Pan, K., 2019, "Skin-Inspired Flexible and High-Sensitivity Pressure Sensors Based on RGO Films with Continuous-Gradient Wrinkles," Nanoscale, **11**(10), pp. 4258–4266.

[29] Sun, H., Dai, K., Zhai, W., Zhou, Y., Li, J., Zheng, G., Li, B., Liu, C., and Shen, C., 2019, "A Highly Sensitive and Stretchable Yarn Strain Sensor for Human Motion Tracking Utilizing a Wrinkle-Assisted Crack Structure," ACS Appl. Mater. Interfaces, **11**(39), pp. 36052–36062.

[30] Xue, P., Chen, C., and Diao, D., 2019, "Ultra-Sensitive Flexible Strain Sensor Based on Graphene Nanocrystallite Carbon Film with Wrinkle Structures," Carbon N. Y., **147**, pp. 227–235.

[31] Yang, S., Khare, K., and Lin, P.-C., 2010, "Harnessing Surface Wrinkle Patterns in Soft Matter," Adv. Funct. Mater., **20**(16), pp. 2550–2564.

[32] Li, H., Zhan, Q., Liu, Y., Liu, L., Yang, H., Zuo, Z., Shang, T., Wang, B., and Li, R.-W., 2016, "Stretchable Spin Valve with Stable Magnetic Field Sensitivity by Ribbon-Patterned Periodic Wrinkles," ACS Nano, **10**(4), pp. 4403–4409.

[33] Melzer, M., Makarov, D., Calvimontes, A., Karnaushenko, D., Baunack, S., Kaltofen, R., Mei, Y., and Schmidt, O. G., 2011, "Stretchable Magnetoelectronics," Nano Lett., **11**(6), pp. 2522–2526.

[34] Cheng, W., Zhou, Z., Pan, M., Yang, H., Xie, Y., Wang, B., Zhan, Q., and Li, R.-W., 2018, "Stretchable Spin Valve with Strain-Engineered Wrinkles Grown on Elastomeric Polydimethylsiloxane," J. Phys. D. Appl. Phys., **52**(9), p. 95003.

[35] Yuan, W., Yang, J., Yin, F., Li, Y., and Yuan, Y., 2020, "Flexible and Stretchable MXene/Polyurethane Fabrics with Delicate Wrinkle Structure Design for Effective Electromagnetic Interference Shielding at a Dynamic Stretching Process," Compos. Commun., **19**, pp. 90–98.

[36] Zang, J., Cao, C., Feng, Y., Liu, J., and Zhao, X., 2014, "Stretchable and High-Performance Supercapacitors with Crumpled Graphene Papers," Sci. Rep., **4**(1), p. 6492.

[37] Qi, D., Liu, Z., Liu, Y., Leow, W. R., Zhu, B., Yang, H., Yu, J., Wang, W., Wang, H., Yin, S., and Chen, X., 2015, "Suspended Wavy Graphene Microribbons for Highly Stretchable Microsupercapacitors," Adv. Mater., **27**(37), pp. 5559–5566.

[38] Ji, B., Wang, M., Ge, C., Xie, Z., Guo, Z., Hong, W., Gu, X., Wang, L., Yi, Z., Jiang, C., Yang, B., Wang, X., Li, X., Li, C., and Liu, J., 2019, "Flexible Bioelectrodes with Enhanced Wrinkle Microstructures for Reliable Electrochemical Modification and Neuromodulation in Vivo," Biosens. Bioelectron., **135**, pp. 181–191.

[39] Ma, Y., Jang, K.-I., Wang, L., Jung, H. N., Kwak, J. W., Xue, Y., Chen, H., Yang, Y., Shi, D., Feng, X., Rogers, J. A., and Huang, Y., 2016, "Design of Strain-Limiting Substrate Materials for Stretchable and Flexible Electronics," Adv. Funct. Mater., **26**(29), pp. 5345–5351.

[40] Lee, M. J., Choi, J. S., Kim, J.-S., Byun, I.-S., Lee, D. H., Ryu, S., Lee, C., and Park, B. H., 2012, "Characteristics and Effects of Diffused Water between Graphene and a SiO2 Substrate," Nano Res., **5**(10), pp. 710–717.

[41] Im, S. H., and Huang, R., 2005, "Evolution of Wrinkles in Elastic-Viscoelastic Bilayer Thin Films," J. Appl. Mech., **72**(6), pp. 955–961.

[42] Sinnott, D. W. B. and O. A. S. and J. A. H. and S. J. S. and B. N. and S. B., 2002, "A Second-Generation Reactive Empirical Bond Order (REBO) Potential Energy Expression for Hydrocarbons," J. Phys. Condens. Matter, **14**(4), p. 783.

[43] "LAMMPS Molecular Dynamics Simulator" [Online]. Available: https://lammps.sandia.gov Retrieved on: 06/06/2020

[44] Jorgensen, W. L., Chandrasekhar, J., Madura, J. D., Impey, R. W., and Klein, M. L., 1983, "Comparison of Simple Potential Functions for Simulating Liquid Water," J. Chem. Phys., **79**(2), pp. 926–935.

[45] Walther, J. H., Jaffe, R. L., Kotsalis, E. M., Werder, T., Halicioglu, T., and Koumoutsakos, P., 2004, "Hydrophobic Hydration of C60 and Carbon Nanotubes in Water," Carbon N. Y., **42**(5), pp. 1185–1194.

[46] Berendsen, H. J. C., Postma, J. P. M., van Gunsteren, W. F., DiNola, A., and Haak, J. R., 1984, "Molecular Dynamics with Coupling to an External Bath," J. Chem. Phys., **81**(8), pp. 3684–3690.

[47] Thompson, A. P., Plimpton, S. J., and Mattson, W., 2009, "General Formulation of Pressure and Stress Tensor for Arbitrary Many-Body Interaction Potentials under Periodic Boundary Conditions," J. Chem. Phys., **131**(15), p. 154107.

[48] Wentzcovitch, P. G. and S. B. and N. B. and M. C. and R. C. and C. C. and D. C. and G. L. C. and M. C. and I. D. and A. D. C. and S. de G. and S. F., 2009, "QUANTUM ESPRESSO: A Modular and Open-Source Software Project for Quantum Simulations of Materials," J. Phys. Condens. Matter, **21**(39), p. 395502.

[49] Hammer, B., Hansen, L. B., and Nørskov, J. K., 1999, "Improved Adsorption Energetics within Density-Functional Theory Using Revised Perdew-Burke-Ernzerhof Functionals," Phys. Rev. B, **59**(11), pp. 7413–7421.

[50] Hinuma, Y., Pizzi, G., Kumagai, Y., Oba, F., and Tanaka, I., 2017, "Band Structure Diagram Paths Based on Crystallography," Comput. Mater. Sci., **128**, pp. 140–184.

[51] Chae, S. J., Güneş, F., Kim, K. K., Kim, E. S., Han, G. H., Kim, S. M., Shin, H.-J., Yoon, S.-M., Choi, J.-Y., Park, M. H., Yang, C. W., Pribat, D., and Lee, Y. H., "Synthesis of Large-Area Graphene Layers on Poly-Nickel Substrate by Chemical Vapor Deposition: Wrinkle Formation," Adv. Mater., **21**(22), pp. 2328–2333.

[52] Liu, N., Pan, Z., Fu, L., Zhang, C., Dai, B., and Liu, Z., 2011, "The Origin of Wrinkles on Transferred Graphene," Nano Res., **4**(10), p. 996.

[53] Frank, F. C., 1949, "On the Equations of Motion of Crystal Dislocations," Proc. Phys. Soc. Sect. A, **62**(2), pp. 131–134.

[54] Kushima, A., Qian, X., Zhao, P., Zhang, S., and Li, J., 2015, "Ripplocations in van Der Waals Layers," Nano Lett., **15**(2), pp. 1302–1308.

[55] Chen, Y., Guo, F., Jachak, A., Kim, S.-P., Datta, D., Liu, J., Kulaots, I., Vaslet, C., Jang, H. D., Huang, J., Kane, A., Shenoy, V. B., and Hurt, R. H., 2012, "Aerosol Synthesis of Cargo-Filled Graphene Nanosacks," Nano Lett., **12**(4), pp. 1996–2002.

[56] Taherian, F., Marcon, V., van der Vegt, N. F. A., and Leroy, F., 2013, "What Is the Contact Angle of Water on Graphene?," Langmuir, **29**(5), pp. 1457–1465.

[57] McKenzie, S., and Kang, H. C., 2014, "Squeezing Water Clusters between Graphene Sheets: Energetics, Structure, and Intermolecular Interactions," Phys. Chem. Chem. Phys., **16**(47), pp. 26004–26015.

[58] Breid, D., and Crosby, A. J., 2011, "Effect of Stress State on Wrinkle Morphology," Soft Matter, **7**(9), pp. 4490–4496.

[59] Wei, X., Mao, L., Soler-Crespo, R. A., Paci, J. T., Huang, J., Nguyen, S. T., and Espinosa, H. D., 2015, "Plasticity and Ductility in Graphene Oxide through a Mechanochemically Induced Damage Tolerance Mechanism," Nat. Commun., **6**, p. 8029.

[60] Vinod, S., Tiwary, C. S., Machado, L. D., Ozden, S., Cho, J., Shaw, P., Vajtai, R., Galvão, D. S., and Ajayan, P. M., 2016, "Strain Rate Dependent Shear Plasticity in Graphite Oxide," Nano Lett., **16**(2), pp. 1127–1131.

[61] Choudhury, N., and Pettitt, B. M., 2005, "Dynamics of Water Trapped between Hydrophobic Solutes," J. Phys. Chem. B, **109**(13), pp. 6422–6429.

[62] Khestanova, E., Guinea, F., Fumagalli, L., Geim, A. K., and Grigorieva, I. V, 2016, "Universal Shape and Pressure inside Bubbles Appearing in van Der Waals Heterostructures," Nat. Commun., **7**(1), p. 12587.

[63] Calado, V. E., Schneider, G. F., Theulings, A. M. M. G., Dekker, C., and Vandersypen, L. M. K., 2012, "Formation and Control of Wrinkles in Graphene by the Wedging Transfer Method," Appl. Phys. Lett., **101**(10), p. 103116.

[64] "Open Visualization Tool" [Online]. Available: www.ovito.org Retrieved on: 06/06/2017

[65] Weinhold, F., 2001, "A New Twist on Molecular Shape," Nature, **411**(6837), pp. 539–541.

[66] Sulpizio, J. A., Ella, L., Rozen, A., Birkbeck, J., Perello, D. J., Dutta, D., Ben-Shalom, M., Taniguchi, T., Watanabe, K., Holder, T., Queiroz, R., Principi, A., Stern, A., Scaffidi, T., Geim, A. K., and Ilani, S., 2019, "Visualizing Poiseuille Flow of Hydrodynamic Electrons," Nature, **576**(7785), pp. 75–79.

[67] Xiong, W., Du, L., Lo, K. C., Shi, H., Takaya, T., Iwata, K., Chan, W. K., and Phillips, D. L., 2018, "Control of Electron Flow Direction in Photoexcited Cycloplatinated Complex Containing Conjugated Polymer–Single-Walled Carbon Nanotube Hybrids," J. Phys. Chem. Lett., **9**(14), pp. 3819–3824.

[68] Polini, M., Tomadin, A., Asgari, R., and MacDonald, A. H., 2008, "Density Functional Theory of Graphene Sheets," Phys. Rev. B, **78**(11), p. 115426.

[69] Tan, J., Li, S., Liu, B., and Cheng, H.-M., 2021, "Structure, Preparation, and Applications of 2D Material-Based Metal–Semiconductor Heterostructures," Small Struct., **2**(1), p. 2000093.

[70] Gupta, K., Mukhopadhyay, T., Roy, L., and Dey, S., 2022, "High-Velocity Ballistics of Twisted Bilayer Graphene under Stochastic Disorder."

[71] Gupta, K. K., Mukhopadhyay, T., Roy, A., Roy, L., and Dey, S., 2021, "Sparse Machine Learning Assisted Deep Computational Insights on the Mechanical Properties of Graphene with Intrinsic Defects and Doping," J. Phys. Chem. Solids, **155**, p. 110111.

[72] Zhang, S., Ma, T., Erdemir, A., and Li, Q., 2019, "Tribology of Two-Dimensional Materials: From Mechanisms to Modulating Strategies," Mater. Today, **26**, pp. 67–86.

[73] Kashyap, J., Yang, E.-H., and Datta, D., 2020, "Computational Study of the Water-Driven Graphene Wrinkle Life-Cycle towards Applications in Flexible Electronics," Sci. Rep., **10**(1), p. 1648.

[74] Long, F., Yasaei, P., Yao, W., Salehi-Khojin, A., and Shahbazian-Yassar, R., 2017, "Anisotropic Friction of Wrinkled Graphene Grown by Chemical Vapor Deposition," ACS Appl. Mater. Interfaces, **9**(24), pp. 20922–20927.

[75] Elinski, M. B., Menard, B. D., Liu, Z., and Batteas, J. D., 2017, "Adhesion and Friction at Graphene/Self-Assembled Monolayer Interfaces Investigated by Atomic Force Microscopy," J. Phys. Chem. C, **121**(10), pp. 5635–5641.

[76] Liu, S.-W., Wang, H.-P., Xu, Q., Ma, T.-B., Yu, G., Zhang, C., Geng, D., Yu, Z., Zhang, S., Wang, W., Hu, Y.-Z., Wang, H., and Luo, J., 2017, "Robust Microscale Superlubricity under High Contact Pressure Enabled by Graphene-Coated Microsphere," Nat. Commun., **8**(1), p. 14029.

[77] Fang, L., Liu, D.-M., Guo, Y., Liao, Z.-M., Luo, J.-B., and Wen, S.-Z., 2017, "Thickness Dependent Friction on Few-Layer MoS2, WS2, and WSe2," Nanotechnology, **28**(24), p. 245703.

[78] Li, Q., Liu, X.-Z., Kim, S.-P., Shenoy, V. B., Sheehan, P. E., Robinson, J. T., and Carpick, R. W., 2014, "Fluorination of Graphene Enhances Friction Due to Increased Corrugation," Nano Lett., **14**(9), pp. 5212–5217.

[79] Ko, J.-H., Kwon, S., Byun, I.-S., Choi, J. S., Park, B. H., Kim, Y.-H., and Park, J. Y., 2013, "Nanotribological Properties of Fluorinated, Hydrogenated, and Oxidized Graphenes," Tribol. Lett., **50**(2), pp. 137–144.

[80] Zhang, W., Cao, Y., Tian, P., Guo, F., Tian, Y., Zheng, W., Ji, X., and Liu, J., 2016, "Soluble, Exfoliated Two-Dimensional Nanosheets as Excellent Aqueous Lubricants," ACS Appl. Mater. Interfaces, **8**(47), pp. 32440–32449.

[81] Han, X., Yong, H., and Sun, D., 2017, "Tuning Tribological Performance of Layered Zirconium Phosphate Nanoplatelets in Oil by Surface and Interlayer Modifications," Nanoscale Res. Lett., **12**(1), p. 542.

[82] Jiang, F., Sun, H., Chen, L., Lei, F., and Sun, D., 2020, "Dispersion-Tribological Property Relationship in Mineral Oils Containing 2D Layered α-Zirconium Phosphate Nanoplatelets," Friction, **8**(4), pp. 695–707.

[83] Khare, V., Pham, M.-Q., Kumari, N., Yoon, H.-S., Kim, C.-S., Park, J.-I., and Ahn, S.-H., 2013, "Graphene–Ionic Liquid Based Hybrid Nanomaterials as Novel Lubricant for Low Friction and Wear," ACS Appl. Mater. Interfaces, **5**(10), pp. 4063–4075.

[84] Berardo, A., Costagliola, G., Ghio, S., Boscardin, M., Bosia, F., and Pugno, N. M., 2019, "An Experimental-Numerical Study of the Adhesive Static and Dynamic Friction of Micro-Patterned Soft Polymer Surfaces," Mater. Des., **181**, p. 107930.

[85] Costagliola, G., Bosia, F., and Pugno, N. M., 2017, "Tuning Friction with Composite Hierarchical Surfaces," Tribol. Int., **115**, pp. 261–267.

[86] Costagliola, G., Bosia, F., and Pugno, N. M., 2016, "Static and Dynamic Friction of Hierarchical Surfaces," Phys. Rev. E, **94**(6), p. 63003.

[87] Niguès, A., Siria, A., Vincent, P., Poncharal, P., and Bocquet, L., 2014, "Ultrahigh Interlayer Friction in Multiwalled Boron Nitride Nanotubes," Nat. Mater., **13**(7), pp. 688–693.

[88] Dong, Y., Vadakkepatt, A., and Martini, A., 2011, "Analytical Models for Atomic Friction," Tribol. Lett., **44**(3), p. 367.

[89] Liu, L., and Eriten, M., 2016, “Frictional Energy Dissipation in Wavy Surfaces,” J. Appl. Mech., **83**(12).

[90] Paradinas, M., Garzón, L., Sánchez, F., Bachelet, R., Amabilino, D. B., Fontcuberta, J., and Ocal, C., 2010, “Tuning the Local Frictional and Electrostatic Responses of Nanostructured SrTiO3—Surfaces by Self-Assembled Molecular Monolayers,” Phys. Chem. Chem. Phys., **12**(17), pp. 4452–4458.

[91] Zhang, J., Bai, Y., An, L., Zhang, B., Zhang, J., Yu, Y., and Wang, C.-M., 2019, “Reduction of Interlayer Friction between Bilayer Hexagonal Boron Nitride Nanosheets Induced by Electron Redistribution,” J. Appl. Phys., **126**(3), p. 35104.

[92] Gajurel, P., Kim, M., Wang, Q., Dai, W., Liu, H., and Cen, C., 2017, “Vacancy-Controlled Contact Friction in Graphene,” Adv. Funct. Mater., **27**(47), p. 1702832.

[93] Filleter, T., McChesney, J. L., Bostwick, A., Rotenberg, E., Emtsev, K. V, Seyller, T., Horn, K., and Bennewitz, R., 2009, “Friction and Dissipation in Epitaxial Graphene Films,” Phys. Rev. Lett., **102**(8), p. 86102.

[94] Zheng, X., Gao, L., Yao, Q., Li, Q., Zhang, M., Xie, X., Qiao, S., Wang, G., Ma, T., Di, Z., Luo, J., and Wang, X., 2016, “Robust Ultra-Low-Friction State of Graphene via Moiré Superlattice Confinement,” Nat. Commun., **7**(1), p. 13204.

[95] Zeng, Y., He, F., Wang, Q., Yan, X., and Xie, G., 2018, “Friction and Wear Behaviors of Molybdenum Disulfide Nanosheets under Normal Electric Field,” Appl. Surf. Sci., **455**, pp. 527–532.

[96] Wang, L.-F., Ma, T.-B., Hu, Y.-Z., Zheng, Q., Wang, H., and Luo, J., 2014, “Superlubricity of Two-Dimensional Fluorographene/MoS2heterostructure: A First-Principles Study,” Nanotechnology, **25**(38), p. 385701.

[97] Gao, L., Chen, X., Ma, Y., Yan, Y., Ma, T., Su, Y., and Qiao, L., 2018, “Origin of the Moiré Superlattice Scale Lateral Force Modulation of Graphene on a Transition Metal Substrate,” Nanoscale, **10**(22), pp. 10576–10583.

[98] Shi, R., Gao, L., Lu, H., Li, Q., Ma, T.-B., Guo, H., Du, S., Feng, X.-Q., Zhang, S., Liu, Y., Cheng, P., Hu, Y.-Z., Gao, H.-J., and Luo, J., 2017, “Moiré Superlattice-Level Stick-Slip Instability Originated from Geometrically Corrugated Graphene on a Strongly Interacting Substrate,” 2D Mater., **4**(2), p. 25079.

[99] Wang, J., Tiwari, A., Huang, Y., Jia, Y., and Persson, B. N. J., 2020, “Dependency of Sliding Friction for Two Dimensional Systems on Electronegativity.”

[100] Li, M., Shi, J., Liu, L., Yu, P., Xi, N., and Wang, Y., 2016, “Experimental Study and Modeling of Atomic-Scale Friction in Zigzag and Armchair Lattice Orientations of MoS2,” Sci. Technol. Adv. Mater., **17**(1), pp. 189–199.

[101] Wang, C., Li, H., Zhang, Y., Sun, Q., and Jia, Y., 2014, "Effect of Strain on Atomic-Scale Friction in Layered MoS2," Tribol. Int., **77**, pp. 211–217.

[102] Pang, Z., Wan, J., Lu, A., Dai, J., Hu, L., and Li, T., 2020, "Giant Tunability of Interlayer Friction in Graphite via Ion Intercalation," Extrem. Mech. Lett., **35**, p. 100616.

[103] Acikgoz, O., Yanilmaz, A., Dagdeviren, O. E., Çelebi, C., and Baykara, M. Z., 2020, "Inverse Layer Dependence of Friction on Chemically Doped MoS_{2}."

[104] Terada, H., Imai, H., and Oaki, Y., 2018, "Visualization and Quantitative Detection of Friction Force by Self-Organized Organic Layered Composites," Adv. Mater., **30**(27), p. 1801121.

[105] E, S., Ye, X., Zhu, Z., Lu, W., Li, C., and Yao, Y., 2019, "Tuning the Structures of Boron Nitride Nanosheets by Template Synthesis and Their Application as Lubrication Additives in Water," Appl. Surf. Sci., **479**, pp. 119–127.

[106] Cheng, Z., Zhang, G., Zhang, B., Ma, F., and Lu, Z., 2018, "Tuning the Electronic Structure of Hexagonal Boron Nitride by Carbon Atom Modification: A Feasible Strategy to Reduce Sliding Friction," Mater. Res. Express, **6**(3), p. 36306.

[107] Rodriguez, P. G., Lubbers, R., Veldhuis, S. A., Narygina, O., Lette, W., Schipper, D. J., and ten Elshof, J. E., 2017, "Tuning the Structure and Ionic Interactions in a Thermochemically Stable Hybrid Layered Titanate-Based Nanocomposite for High Temperature Solid Lubrication," Adv. Mater. Interfaces, **4**(14), p. 1700047.

[108] Dickrell, P. L., Pal, S. K., Bourne, G. R., Muratore, C., Voevodin, A. A., Ajayan, P. M., Schadler, L. S., and Sawyer, W. G., 2006, "Tunable Friction Behavior of Oriented Carbon Nanotube Films," Tribol. Lett., **24**(1), pp. 85–90.

[109] Arif, T., Colas, G., and Filleter, T., 2018, "Effect of Humidity and Water Intercalation on the Tribological Behavior of Graphene and Graphene Oxide," ACS Appl. Mater. Interfaces, **10**(26), pp. 22537–22544.

[110] Gongyang, Y., Ouyang, W., Qu, C., Urbakh, M., Quan, B., Ma, M., and Zheng, Q., 2020, "Temperature and Velocity Dependent Friction of a Microscale Graphite-DLC Heterostructure," Friction, **8**(2), pp. 462–470.

[111] Dollekamp, E., Bampoulis, P., Siekman, M. H., Kooij, E. S., and Zandvliet, H. J. W., 2019, "Tuning the Friction of Graphene on Mica by Alcohol Intercalation," Langmuir, **35**(14), pp. 4886–4892.

[112] Fredricks, Z. B., Stevens, K. M., Kenny, S. G., Acharya, B., and Krim, J., 2019, "Tuning Nanoscale Friction by Applying Weak Magnetic Fields to Reorient Adsorbed Oxygen Molecules," Condens. Matter , **4**(1).

[113] Strelcov, E., Kumar, R., Bocharova, V., Sumpter, B. G., Tselev, A., and Kalinin, S. V, 2015, "Nanoscale Lubrication of Ionic Surfaces Controlled via a Strong Electric Field," Sci. Rep., **5**(1), p. 8049.

[114] Li, X., Yin, J., Zhou, J., and Guo, W., 2014, "Large Area Hexagonal Boron Nitride Monolayer as Efficient Atomically Thick Insulating Coating against Friction and Oxidation," Nanotechnology, **25**(10), p. 105701.

[115] Pivnic, K., Fajardo, O. Y., Bresme, F., Kornyshev, A. A., and Urbakh, M., 2018, "Mechanisms of Electrotunable Friction in Friction Force Microscopy Experiments with Ionic Liquids," J. Phys. Chem. C, **122**(9), pp. 5004–5012.

[116] Lee, H., Jeong, H., Suh, J., Doh, W. H., Baik, J., Shin, H.-J., Ko, J.-H., Wu, J., Kim, Y.-H., and Park, J. Y., 2019, "Nanoscale Friction on Confined Water Layers Intercalated between MoS2 Flakes and Silica," J. Phys. Chem. C, **123**(14), pp. 8827–8835.

[117] Shi, X., Liu, S., Sun, Y., Liang, J., and Chen, Y., 2018, "Lowering Internal Friction of 0D–1D–2D Ternary Nanocomposite-Based Strain Sensor by Fullerene to Boost the Sensing Performance," Adv. Funct. Mater., **28**(22), p. 1800850.

[118] Wu, Y., Cai, M., Pei, X., Liang, Y., and Zhou, F., 2013, "Switching Friction with Thermal- Responsive Gels," Macromol. Rapid Commun., **34**(22), pp. 1785–1790.

[119] Pang, Y., Xue, F., Wang, L., Chen, J., Luo, J., Jiang, T., Zhang, C., and Wang, Z. L., 2016, "Tribotronic Enhanced Photoresponsivity of a MoS2 Phototransistor," Adv. Sci., **3**(6), p. 1500419.

[120] Xue, F., Chen, L., Wang, L., Pang, Y., Chen, J., Zhang, C., and Wang, Z. L., 2016, "MoS2 Tribotronic Transistor for Smart Tactile Switch," Adv. Funct. Mater., **26**(13), pp. 2104–2109.

[121] Jung, G. S., Wang, S., Qin, Z., Martin-Martinez, F. J., Warner, J. H., and Buehler, M. J., 2018, "Interlocking Friction Governs the Mechanical Fracture of Bilayer MoS2," ACS Nano, **12**(4), pp. 3600–3608.

[122] Cui, Z., Xie, G., He, F., Wang, W., Guo, D., and Wang, W., 2017, "Atomic-Scale Friction of Black Phosphorus: Effect of Thickness and Anisotropic Behavior," Adv. Mater. Interfaces, **4**(23), p. 1700998.

[123] Cahangirov, S., Ataca, C., Topsakal, M., Sahin, H., and Ciraci, S., 2012, "Frictional Figures of Merit for Single Layered Nanostructures," Phys. Rev. Lett., **108**(12), p. 126103.

[124] Volokitin, A. I., and Persson, B. N. J., 2007, "Near-Field Radiative Heat Transfer and Noncontact Friction," Rev. Mod. Phys., **79**(4), pp. 1291–1329.

[125] Giacco, F., Ciamarra, M. P., Saggese, L., de Arcangelis, L., and Lippiello, E., 2014, "Non-Monotonic Dependence of the Friction Coefficient on Heterogeneous Stiffness," Sci. Rep., **4**(1), p. 6772.

[126] Manimunda, P., Nakanishi, Y., Jaques, Y. M., Susarla, S., Woellner, C. F., Bhowmick, S., Asif, S. A. S., Galvão, D. S., Tiwary, C. S., and Ajayan, P. M., 2017, "Nanoscale Deformation and Friction Characteristics of Atomically Thin WSe 2 and Heterostructure Using Nanoscratch and Raman Spectroscopy," 2D Mater., **4**(4), p. 45005.

[127] Bai, L., Liu, B., Srikanth, N., Tian, Y., and Zhou, K., 2017, "Nano-Friction Behavior of Phosphorene," Nanotechnology, **28**(35), p. 355704.

[128] Zhou, X., Liu, Y., Hu, X., Fang, L., Song, Y., Liu, D., and Luo, J., 2020, "Influence of Elastic Property on the Friction between Atomic Force Microscope Tips and 2D Materials," Nanotechnology, **31**(28), p. 285710.

[129] Tang, W., Sanville, E., and Henkelman, G., 2009, "A Grid-Based Bader Analysis Algorithm without Lattice Bias," J. Phys. Condens. Matter, **21**(8), p. 84204.

[130] Gulans, A., Kontur, S., Meisenbichler, C., Nabok, D., Pavone, P., Rigamonti, S., Sagmeister, S., Werner, U., and Draxl, C., 2014, "Exciting: A Full-Potential All-Electron Package Implementing Density-Functional Theory and Many-Body Perturbation Theory," J. Phys. Condens. Matter, **26**(36), p. 363202.

[131] Archard, J. F., and Allibone, T. E., 1957, "Elastic Deformation and the Laws of Friction," Proc. R. Soc. London. Ser. A. Math. Phys. Sci., **243**(1233), pp. 190–205.

[132] Lai, C.-C., Shih, T.-P., Ko, W.-C., Tang, H.-J., and Hsueh, P.-R., 2020, "Severe Acute Respiratory Syndrome Coronavirus 2 (SARS-CoV-2) and Coronavirus Disease-2019 (COVID-19): The Epidemic and the Challenges," Int. J. Antimicrob. Agents, **55**(3), p. 105924.

[133] "WHO Chief Media Conference for Pandemic Declaration." - www.who.int /director-general/speeches, Retrieved on: 03/11/2020

[134] Cui, J., Li, F., and Shi, Z.-L., 2019, "Origin and Evolution of Pathogenic Coronaviruses," Nat. Rev. Microbiol., **17**(3), pp. 181–192.

[135] Rabi, F. A., Al Zoubi, M. S., Kasasbeh, G. A., Salameh, D. M., and Al-Nasser, A. D., 2020, "SARS-CoV-2 and Coronavirus Disease 2019: What We Know So Far," Pathog. , **9**(3).

[136] Paules, C. I., Marston, H. D., and Fauci, A. S., 2020, "Coronavirus Infections—More Than Just the Common Cold," Journal of the American Medical Association, **323**(8), pp. 707–708.

[137] Astuti, I., and Ysrafil, 2020, "Severe Acute Respiratory Syndrome Coronavirus 2 (SARS-CoV-2): An Overview of Viral Structure and Host Response," Diabetes Metab. Syndr. Clin. Res. Rev., **14**(4), pp. 407–412.

[138] Yang, J., Petitjean, S. J. L., Koehler, M., Zhang, Q., Dumitru, A. C., Chen, W., Derclaye, S., Vincent, S. P., Soumillion, P., and Alsteens, D., 2020, "Molecular Interaction and Inhibition of SARS-CoV-2 Binding to the ACE2 Receptor," Nat. Commun., **11**(1), p. 4541.

[139] Kashyap, J., Nagesh, S., Narayan, K., and Pattnaik, P. K., 2016, "Design and Simulation of a Novel 3D MEMS Fabrication/Micro Cutting Facility by Thermally Actuated MEMS Device," *IEEE Region 10 Annual International Conference, Proceedings/TENCON*.

[140] Siemieniuk, R. A. C., Bartoszko, J. J., Ge, L., Zeraatkar, D., Izcovich, A., Kum, E., Pardo-Hernandez, H., Qasim, A., Martinez, J. P. D., Rochwerg, B., Lamontagne, F., Han, M. A., Liu, Q., Agarwal, A., Agoritsas, T., Chu, D. K., Couban, R., Cusano, E., Darzi, A., Devji, T., Fang, B., Fang, C., Flottorp, S. A., Foroutan, F., Ghadimi, M., Heels-Ansdell, D., Honarmand, K., Hou, L., Hou, X., Ibrahim, Q., Khamis, A., Lam, B., Loeb, M., Marcucci, M., McLeod, S. L., Motaghi, S., Murthy, S., Mustafa, R. A., Neary, J. D., Rada, G., Riaz, I. Bin, Sadeghirad, B., Sekercioglu, N., Sheng, L., Sreekanta, A., Switzer, C., Tendal, B., Thabane, L., Tomlinson, G., Turner, T., Vandvik, P. O., Vernooij, R. W. M., Viteri-García, A., Wang, Y., Yao, L., Ye, Z., Guyatt, G. H., and Brignardello-Petersen, R., 2020, "Drug Treatments for Covid-19: Living Systematic Review and Network Meta-Analysis," British Medical Journal, **370**, p. m2980.

[141] Maciorowski, D., Idrissi, S. Z. El, Gupta, Y., Medernach, B. J., Burns, M. B., Becker, D. P., Durvasula, R., and Kempaiah, P., 2020, "A Review of the Preclinical and Clinical Efficacy of Remdesivir, Hydroxychloroquine, and Lopinavir-Ritonavir Treatments against COVID-19," SLAS Discov. Adv. Sci. Drug Discov., **25**(10), pp. 1108–1122.

[142] Terstappen, G. C., and Reggiani, A., 2001, "In Silico Research in Drug Discovery," Trends Pharmacol. Sci., **22**(1), pp. 23–26.

[143] Ton, A.-T., Gentile, F., Hsing, M., Ban, F., and Cherkasov, A., 2020, "Rapid Identification of Potential Inhibitors of SARS-CoV-2 Main Protease by Deep Docking of 1.3 Billion Compounds," Mol. Inform., **39**(8), p. 2000028.

[144] Irwin, J. J., Sterling, T., Mysinger, M. M., Bolstad, E. S., and Coleman, R. G., 2012, "ZINC: A Free Tool to Discover Chemistry for Biology," J. Chem. Inf. Model., **52**(7), pp. 1757–1768.

[145] Krieger, E., and Vriend, G., 2015, "New Ways to Boost Molecular Dynamics Simulations.," J. Comput. Chem., **36**(13), pp. 996–1007.

[146] Krieger, E., Koraimann, G., and Vriend, G., 2002, "Increasing the Precision of Comparative Models with YASARA NOVA—a Self-Parameterizing Force Field," Proteins Struct. Funct. Bioinforma., **47**(3), pp. 393–402.

[147] Krieger, E., and Vriend, G., 2014, "YASARA View—Molecular Graphics for All Devices—from Smartphones to Workstations," Bioinformatics, **30**(20), pp. 2981–2982.

[148] Trott, O., and Olson, A. J., 2010, "AutoDock Vina: Improving the Speed and Accuracy of Docking with a New Scoring Function, Efficient Optimization, and Multithreading," J. Comput. Chem., **31**(2), pp. 455–461.

[149] Case, D. A., Cheatham III, T. E., Darden, T., Gohlke, H., Luo, R., Merz Jr., K. M., Onufriev, A., Simmerling, C., Wang, B., and Woods, R. J., 2005, "The Amber Biomolecular Simulation Programs," J. Comput. Chem., **26**(16), pp. 1668–1688.

[150] Roe, D. R., and Cheatham, T. E., 2013, "PTRAJ and CPPTRAJ: Software for Processing and Analysis of Molecular Dynamics Trajectory Data," J. Chem. Theory Comput., **9**(7), pp. 3084–3095.

[151] Hafner, J., 2008, "Ab-Initio Simulations of Materials Using VASP: Density-Functional Theory and Beyond," J. Comput. Chem., **29**(13), pp. 2044–2078.

[152] Henkelman, G., and Jónsson, H., 1999, "A Dimer Method for Finding Saddle Points on High Dimensional Potential Surfaces Using Only First Derivatives," J. Chem. Phys., **111**(15), pp. 7010–7022.

[153] Rose, P. W., Prlić, A., Altunkaya, A., Bi, C., Bradley, A. R., Christie, C. H., Costanzo, L. Di, Duarte, J. M., Dutta, S., Feng, Z., Green, R. K., Goodsell, D. S., Hudson, B., Kalro, T., Lowe, R., Peisach, E., Randle, C., Rose, A. S., Shao, C., Tao, Y.-P., Valasatava, Y., Voigt, M., Westbrook, J. D., Woo, J., Yang, H., Young, J. Y., Zardecki, C., Berman, H. M., and Burley, S. K., 2017, "The RCSB Protein Data Bank: Integrative View of Protein, Gene and 3D Structural Information," Nucleic Acids Res., **45**(D1), pp. D271–D281.

[154] Pettersen, E. F., Goddard, T. D., Huang, C. C., Couch, G. S., Greenblatt, D. M., Meng, E. C., and Ferrin, T. E., 2004, "UCSF Chimera—A Visualization System for Exploratory Research and Analysis," J. Comput. Chem., **25**(13), pp. 1605–1612.

[155] Towns, J., Cockerill, T., Dahan, M., Foster, I., Gaither, K., Grimshaw, A., Hazlewood, V., Lathrop, S., Lifka, D., Peterson, G. D., Roskies, R., Scott, J. R., and Wilkins-Diehr, N., 2014, "XSEDE: Accelerating Scientific Discovery," Comput. Sci. Eng., **16**(5), pp. 62–74.

[156] Daina, A., Michielin, O., and Zoete, V., 2017, "SwissADME: A Free Web Tool to Evaluate Pharmacokinetics, Drug-Likeness and Medicinal Chemistry Friendliness of Small Molecules," Sci. Rep., **7**(1), p. 42717.

[157] Battaglia, P. W., Hamrick, J. B., Bapst, V., Sanchez-Gonzalez, A., Zambaldi, V., Malinowski, M., Tacchetti, A., Raposo, D., Santoro, A., Faulkner, R., Gulcehre, C., Song, F., Ballard, A., Gilmer, J., Dahl, G., Vaswani, A., Allen, K., Nash, C., Langston, V., Dyer, C., Heess, N., Wierstra, D., Kohli, P., Botvinick, M., Vinyals, O., Li, Y., and Pascanu, R., 2018, "Relational Inductive Biases, Deep Learning, and Graph Networks."

[158] White, A. D., 2022, "Deep Learning for Molecules and Materials," Living J. Comput. Mol. Sci., **3**(1 SE-Articles), p. 1499.

[159] Liang, J., Xu, Y., Liu, R., and Zhu, X., 2019, "QM-Sym, a Symmetrized Quantum Chemistry Database of 135 Kilo Molecules," Sci. Data, **6**(1), p. 213.

[160] Solanky, P., Sharma, V., Ghatak, K., Kashyap, J., and Datta, D., 2019, "The Inherent Behavior of Graphene Flakes in Water: A Molecular Dynamics Study," Comput. Mater. Sci., **162**, pp. 140–147.

[161] Ghatak, K., Datta, D., Kashyap, J., and Team, K. G., 2019, "Growth Physics of MoS2 Layer on the MoS2 Surface: A Monte Carlo Approach," *American Physical Society March Meeting Abstracts*, p. F13.009.

[162] Kashyap, J., Ghatak, K., Datta D., 2019, "Characterizing the Morphology of the Different Grown Homo/Hetero TMD Structures By Controlling Parameters – a Multiscale Computational Approach," The Electrochemical Society Meet. Abstr.

[163] Anfinsen, C. B., 1973, "Principles That Govern the Folding of Protein Chains," Science (80-.)., **181**(4096), pp. 223–230.

[164] 2018, "Does AI Have a Hardware Problem?," Nat. Electron., **1**(4), p. 205.

[165] Mehonic, A., and Kenyon, A. J., 2022, "Brain-Inspired Computing Needs a Master Plan," Nature, **604**(7905), pp. 255–260.

[166] Mojtabavi, M., VahidMohammadi, A., Liang, W., Beidaghi, M., and Wanunu, M., 2019, "Single-Molecule Sensing Using Nanopores in Two-Dimensional Transition Metal Carbide (MXene) Membranes," ACS Nano, **13**(3), pp. 3042–3053.

[167] Wang, J., Wolf, R. M., Caldwell, J. W., Kollman, P. A., and Case, D. A., 2004, "Development and Testing of a General Amber Force Field," J. Comput. Chem., **25**(9), pp. 1157–1174.